Investigating The Data Rate in Reconfigurable Intelligent Surfaces Assisted Wireless Communication

Saber I.H.Hassouna

Submitted in fulfilment of the requirements for the
Degree of Doctor of Philosophy

School of Engineering
College of Science and Engineering
University of Glasgow

February 2024

Abstract

In the realm of wireless communications, reconfigurable intelligent surfaces (RIS) offer network providers the capability to manage the behaviour of electromagnetic signals, encompassing their scattering, reflection, and refraction properties. Numerous research findings have underscored RIS's effectiveness in controlling wireless wave attributes, such as amplitude and phase, without necessitating intricate equalization and decoding at the receiver's end. However, it's crucial to note that configuring the surface in practical scenarios with frequency-selective fading channels should be carefully addressed across the entire bandwidth. This entails considering a wideband orthogonal frequency division multiplexing (OFDM) communication system that is based on a practical RIS configuration, involving distinct phase shifts for each element on the surface.

In this thesis, we propose a communication setup to investigate the user data rate enhancement with the aid of RIS surface using practical phase shift model for multi-bit RIS phase resolutions. It is observed that the achievable data rate enhances with higher bit resolutions but the cost of hardware complexity. The effects of mutual coupling (MC) due to the large RIS surface and the electromagnetic interference (EMI) due to the unavoidable signals from external sources are well investigated on the performance data rate. The MC and EMI degrade the achievable rate so, the RIS must be aware of such signal impairment parameters.

Furthermore, we have extended the study of the performance of the achievable data rate for multi-users in single-input-single-output (SISO) wideband based-RIS system with single antenna at the access point (AP) and each user. The propagation environment was assumed to have both line-of-sight (LoS) and non-line-of-sight (NLoS) channels so, it is more realistic and practical. Different RIS algorithms are studied in both LoS and NLoS channels scenarios taking into considerations the computational complexity and run time. The semidefinite relaxation scheme shows higher performance than the other schems but at the cost of computational complexity and run time consequently, the thesis proposes low complex with comparable performance iterative power method that adopts codebook approach.

The RIS demonstrated significant performance data rate not only in communication but also in localization. The RIS-enabled localization has been investigated in the near and far-field regimes using realistic RIS phase shift model that considers the phase and amplitude variations. We introduced an analysis of Fisher information using a straightforward expression for the Fisher information matrix (FIM), illustrating how the position error bound (PEB) is influenced by the phase profiles of RIS. We employed three types of RIS phase profiles—random, direc-

tional, and positional configurations—to showcase the impact of RIS on localization and communication within the near-field range. These profiles were designed considering both the amplitude and phase responses of the RIS, utilizing a practical phase-dependent amplitude model. The random profile ensures a uniform signal-to-noise ratio (SNR) across the deployment area, while the directional and positional profiles enhance SNR towards the user's location. Additionally, we devised a straightforward localization scheme to simplify the maximum likelihood (ML) estimator's complexity. In the near-field region, the achievable data rate diminishes with distance, mirroring the gradual increase in localization error as distance from the RIS grows. Both the achievable data rate and localization error exhibit subpar performance when employing the RIS phase-dependent amplitude model with amplitude values less than one. Consequently, the widespread assumption of unity amplitude in the RIS phase shift model, as commonly seen in literature, leads to overly optimistic and inaccurate results in localization and communication performance.

Simulation results have shown the importance of utilizing RIS technology in both communication and localization. Finally, we have carried out RIS measurements field in the mast lab to configure the test bed hardware of 64×64 RIS elements in order to show the capability of such new technology in improving the signal strength and coverage.

List of Publications

A. *Articles*

(1) **Hassouna S**, Jamshed MA, Rains J, Kazim JU, Rehman MU, Abualhayja M, Mohjazi L, Cui TJ, Imran MA, Abbasi QH. A survey on reconfigurable intelligent surfaces: Wireless communication perspective. *IET Communications*. 2023 Mar;17(5):497-537.

(2) **Hassouna S**, Jamshed MA, Ur-Rehman M, Imran MA, Abbasi QH. Configuring reconfigurable intelligent surfaces using a practical codebook approach. *Scientific Reports*. 2023 Jul 22;13(1):11869.

(3) **Hassouna S**, Jamshed MA, Rehman MU, Imran MA, Abbasi QH. Rate optimization using low complex methods with reconfigurable intelligent surfaces. *Journal of Information and Intelligence*. 2023 Sep 1;1(3):267-80.

(4) **Hassouna S**, Jamshed MA, Ur-Rehman M, Imran MA, Abbasi QH. RIS-assisted near-field localization using practical phase shift model. Scientific Reports. 2024 Feb 22;14(1):4350.

B. *Conference Proceedings*

(1) **Hassouna S**, Jamshed MA, Ur-Rehman M, Imran MA, Abbasi QH. Investigating the Data Rate of Intelligent Reflecting Surfaces with Mutual Coupling and EMI. In2023 IEEE Wireless Communications and Networking Conference (WCNC) 2023 Mar 26 (pp. 1-6). IEEE.

(2) **Hassouna S**, Jamshed MA, Ur-Rehman M, Imran MA, Abbasi QH. Reconfigurable Intelligent Surfaces Aided Wireless Communications with Electromagnetic Interference. In 2023 17th European Conference on Antennas and Propagation (EuCAP) 2023 Mar 26 (pp. 1-5). IEEE.

(3) **Hassouna S**, Jamshed MA, Ur Rehman M, Imran MA, Abbasi QH. RIS-Enabled Near-Field Localization with EMI. In 2024 18th European Conference on Antennas and Propagation (EuCAP).

(4) **Hassouna S**, Rains J, Kazim JR, Rehman MU, Imran M, Abbasi QH. Discrete Phase Shifts for Intelligent Reflecting Surfaces in OFDM Communications. In2022 International Workshop on Antenna Technology (iWAT) 2022 May 16 (pp. 128-131). IEEE.

(5) **Hassouna S**, Rains J, Kazim JU, Rehman MU, Imran M, Abbasi QH. Investigating The data rate of Intelligent Reflecting Surface Under Different Deployments. In2022 IEEE International Symposium on Antennas and Propagation and USNC-URSI Radio Science Meeting (AP-S/URSI) 2022 Jul 10 (pp. 1578-1579). IEEE.

(6) **Hassouna S**, Kazim JU, Rains J, Jamshed MA, Rehman MU, Imran MA, Abbasi QH. Indoor Field Trials for RIS-Aided Wireless Communications. In2023 IEEE International Symposium on Antennas and Propagation and USNC-URSI Radio Science Meeting (USNC-URSI) 2023 Jul 23 (pp. 75-76). IEEE

(7) **Hassouna S**, Jamshed, M. A., Ur-Rehman, M. , Imran, M. A. and Abbasi, Q. H. (2024) Rate Optimization and Power Allocation in RIS-assisted Multi-user OFDM Communication. IEEE Wireless Communications and Networking Conference (WCNC2024) workshops

(8) **Hassouna S**, Kaur J, Jamshed, M. A., Rehman MU, Imran M, Abbasi QH. Data Rate Performance of RIS in the Near-Field Regime Incorporating the Presence of EMI. Submitted to In2024 IEEE International Symposium on Antennas and Propagation and USNC-URSI Radio Science Meeting (AP-S/URSI) 2024 Jul 10 and it is still under review.

C. *Book chapters*

(1) Abualhayjaa M, **Hassouna S**, Centeno A, Abbasi QH, Ur Rehman M, Imran MA, Mohjazi L. Intelligent reflective surfaces (IRSs) for green networks.

Contents

List of Tables

List of Figures

List of Acronyms

AWGN additive white Gaussian noise

AO alternating optimization

AP access point

AoA angle-of-arrival

AoD angle-of-departure

ASER average symbol error probability

AAR average achievable rate

AmBC ambient backscatter communication

AF amplify and forward

BCD block coordinate descent

BS base station

BADV AMP bilinear adaptive vector approximate message passing

BER bit error rate

BPSK binary phase shift keying

B5G beyond 5G

BnB branch and bound

BADVAMP bilinear adaptive vector approximate message passing

CSI channel state information

CFR channel frequency response

CIR channel impulse response

CNN convolution neural network

CR cognitive radio

CE channel estimate

CRLB Cramer–Rao lower bound

CSCG circularly symmetric complex Gaussian

CS compressive sensing

CMOS complementary metal–oxide–semiconductor

DC direct current

DL deep learning

DFT discrete Fourier transform

DF decode and forward

DE deterministic equivalent

DSP digital signal processors

EMI electromagnetic interference

EM electromagnetic

EE energy efficiency

FFT fast Fourier transform

FSS frequency selective surface

FDD frequency division duplexing

FSO free-space optical

FIM Fisher information matrix

FD full duplex

FPGA field programmable gate array

GMD geometric mean decomposition

GPS global positioning system

Gbps gigabit per second

HIS high impedance surfaces

HWI hardware impairments

IID independent and identically distributed

IoT internet-of-things

IDFT inverse discrete Fourier transform

IWW intelligent wireless wall

JBF-MC joint bilinear factorization and matrix completion

LIS large intelligent surfaces

LEO low earth orbit

LoS line-of-sight

LS least square

ML maximum likelihood

MIMO multiple-input multiple-output

MMSE minimum mean-square error

MEC mobile edge computing

MU multiuser

MRC maximum ratio combining

MRC maximal ratio combining

MEMS microelectromechanical systems

MRT maximum ratio transmission

MAC multiple access channel

MISO multiple-input-single-output

mm-Wave millimeter wave

m-MIMO massive MIMO

MC mutual coupling

MSE mean square error

NLoS non-line-of-sight

NOMA non-orthogonal multiple access

OFDMA orthogonal frequency-division multiple access

OFDM orthogonal frequency-division multiplexing

PWE programmable wireless environments

PGM projected gradient method

PDF probability density function

PIN positive-intrinsic-negative

PSD power spectral density

PARAFAC parallel factor

PEC Perfect electric conductor

PWE programmable wireless environments

PU primary users

PIN positive-intrinsic-negative

PD photo detector

PRESS programmable radio environment for smart spaces

PEB position error bound

PIS passive intelligent surface

PB power beacon

QAM quadrature amplitude modulation

QoS quality of service

QCQP quadratically constrained quadratic program

QUBO Quadratic unconstrained binary optimization

RBM reflecting beamforming matrices

RFF radio frequency fingerprinting

RIS reconfigurable intelligent surface

RSS received signal strength

RM-AO riemannian manifold based alternating optimization

Rx receiver

RLC resistor-inductor-capacitor

RMSE root mean square error

RF Radio Frequency

SCA successive convex approximation

SNR signal-to-noise ratio

SISO single-input-single-output

SDR semidefinite relaxations

SRE smart radio environments

SIMO single-input-multiple-output

SMM spatial microwave modulators

SINR signal-to-interference-plus-noise ratio

SeUCE sequential user channel estimation

SiUCE simultaneous user channel estimation

STM strongest tap maximization

SEP symbol error probability

SE spectral efficiency

SU secondary users

SIC successive interference cancellation

SIMO single-input and multiple-output

SER symbol error probability

SCM strongest-CIR maximization

SDP standard convex semidefinite program

SMM spatial microwave modulators

TDD time division duplex

Tx transmitter

TDD time division duplexing

ToA time-of-arrival

TDoA three-time difference of arrival

UE user equipment

USRP universal software radio peripheral

URLLC ultra-reliable low latency communications

UAV unmanned aerial vehicle

VBLAST vertical bell labs layered space time

WSN wireless sensor network

WS wireless sensor

WPT wireless power transfer

WSR weighted sum rate

WPSN wireless powered sensor networks

ZF zero forcing

2D two-dimensional

3D three-dimensional

4G fourth-generation

5G fifth-generation

6G sixth-generation

Notations and Symbols

Symbol/Notation	Description
j	Imaginary unit ($\sqrt{-1}$)
$[\mathbf{A}]_{m,n}$	Element in the mth row and nth column of matrix $\mathbf{A}$
$[\mathbf{A}]_{i:j,m:n}$	Returns a matrix comprising rows i through j and columns m through n from $\mathbf{A}$
$(\cdot)^\top$	Vector and matrix transpose operator
$(\cdot)^{\mathrm{H}}$	Vector and matrix complex conjugate transpose operator
$\det(\mathbf{A})$	Determinant of a square matrix $\mathbf{A}$
$\mathrm{diag}(\mathbf{A})$	Diagonal of a square matrix $\mathbf{A}$
$\mathrm{Tr}(\mathbf{A})$	Trace of a square matrix $\mathbf{A}$
$\|\cdot\|$	ℓ_2 norm of a vector
$\|\cdot\|_{\mathrm{F}}$	Frobenius norm of a matrix
$\mathbf{0}_N$	All-zeros column vector of length N
$\mathbf{0}_{N\times N}$	All-zeros matrix of size $N \times N$
$\mathbf{I}_N$	All-ones column vector of length N
$\mathbf{1}_{N\times N}$	All-ones matrix of size $N \times N$
$\mathbf{I}_N$	Identity matrix of size $N \times N$
$\mathbb{E}\{\cdot\}$	Expectation operator
$\Re\{\cdot\}$	Real part
$\Im\{\cdot\}$	Imaginary part
$\odot$	Hadamard product
$\otimes$	Kronecker product
$\dagger$	Pseudo-inverse of a matrix
$\mathbb{R}^N$	N-dimensional real vector space
$\mathbb{R}^{N\times M}$	$N \times M$ dimensional real matrix space
$\mathbb{C}^N$	N-dimensional complex vector space
$\mathbb{C}^{N\times M}$	$N \times M$ dimensional complex matrix space
λ	Wavelength
c	Speed of light

ϑ	Elevation angle measure w.r.t positive z-axis
φ	Azimuth angle measure w.r.t positive x-axis
$a(\vartheta, \varphi)$	Array response vector in the direction (ϑ, φ)
N_0	Noise power spectral density
$\mathcal{K}(\vartheta, \varphi)$	Wavenumber vector in the direction (ϑ, φ)
r_t	Received signal vector at the receiver
x_t	Transmitted signal vector
$J(\Upsilon)$	Fisher Information Matrix of Υ
$f(d)$	Probability density function of a random variable d
w_θ	RIS reflection coefficients

Acknowledgements

Above all, I give thanks to God, who has consistently provided guidance, patience, and endurance throughout my journey. I am also indebted to numerous individuals whose support made this endeavor possible. I want to express my appreciation and acknowledge each of them:

- Prof. Qammer H. Abbasi, my primary supervisor, for his continuous guidance and support during the creation of this thesis. His commitment, expertise, and assistance proved indispensable in navigating through my challenging PhD journey. I acknowledge and appreciate his unwavering support, extending from the inception of my PhD application to the conclusion of my thesis. His belief in my capabilities and the autonomy he granted me as an independent researcher have been truly invaluable. I not only acquired knowledge from formal lab meetings but also gained wisdom through informal tea chats with him.

- Prof. Muhammad Ali Imran and Dr. Masood Ur Rehman merit gratitude for their substantial contributions, feedback, and insightful discussions during my doctoral studies.

- Dr. Muhammad Ali Jamshed provided thought-provoking opinions and constructive criticism, offering alternative perspectives on my work.

- I would like to extend my appreciation to the James Watt School of Engineering, specifically Prof. Marc Sorel, for their financial support that facilitated the completion of this research. Without your assistance, this project would not have come to fruition, and I am genuinely thankful for the investment you've made in my work.

- Colleagues Dr. Jalil ur Rehman Kazim, James Rains, and Mahmoud Ahmed Shawky Ahmed served as sources of inspiration and advice when needed.

- My parents, Ibrahim and Mokarram, stand out for their unconditional love, unyielding support, and high expectations, urging me to excel in every task.

- Finally, my deepest gratitude goes to the love of my life, Jawaher, and our two children, Mokarram and Mecca. Their love, encouragement, patience, and understanding have been constant motivators, acting as "angel" co-authors in the creation of this thesis.

Statement of Originality

Name: Saber I.H. Hassouna
Registration Number:

I certify that the thesis presented here for examination for a PhD degree of the University of Glasgow is solely my own work other than where I have clearly indicated that it is the work of others (in which case the extent of any work carried out jointly by me and any other person is clearly identified in it) and that the thesis has not been edited by a third party beyond what is permitted by the University's PGR Code of Practice.

The copyright of this thesis rests with the author. No quotation from it is permitted without full acknowledgment. I declare that the thesis does not include work forming part of a thesis presented successfully for another degree.

I declare that this thesis has been produced in accordance with the University of Glasgow's Code of Good Practice in Research.

I acknowledge that if any issues are raised regarding good research practice based on the review of the thesis, the examination may be postponed pending the outcome of any investigation of the issues.

Signature: Saber Hassouna
Date: 04-01-2024

Chapter 1

Introduction

This chapter provides an overview of the background and research motivation that form the basis of this thesis. It explores the objectives and primary contributions of the research and outlines the structure of the thesis.

1.1 Background and Motivation

While the evolutionary progress of fifth-generation (5G) has gained considerable momentum, the envisioned revolutionary scenario of 5G, characterized by a system predominantly operating at millimeter wave (mm-Wave) frequencies and facilitating a range of internet-of-things (IoT) services, has yet to materialize [1,2]. Although the 5G wireless network is still deployed around the world, both academia and industry are excited about the future beyond 5G (B5G) which seeks to satisfy more demanding requirements than 5G, such as ultra-high data rates, e.g., gigabit per second (Gbps), energy efficiency (EE), global coverage and connectivity, spectral efficiency (SE) as well as high reliability and low air latency [2, 3]. Figure 1.1 shows the vision and the expectation for the sixth-generation (6G) [4] key performance requirements in comparison with 5G. Compared to 5G, 6G must offer a much higher data rate. While the peak data rate for 5G was intended to be 20 Gbps, the goal for 6G is to deliver a peak data rate of 1000 Gbps and a user experience data rate of 1 Gbps. The entire network performance must be enhanced in order to deliver advanced multimedia services to a large number of users, for example, by aiming to achieve spectral efficiency that is twice as high as 5G. As a result, it is critical to developing sustainably new and inventive technologies to enable future wireless network capacity increase at a moderate and manageable budget, complexities and power consumption with the widespread adoption of user devices that will form the future of IoT.

On the other hand, because of user mobility, time-varying wireless channels are a major challenge in building ultra-reliable wireless communications. Traditional ways to address this problem are either by using different modulation, coding and diversity plans to compensate for channel fading, or adjusting to it using modified power, rate management, and beamforming

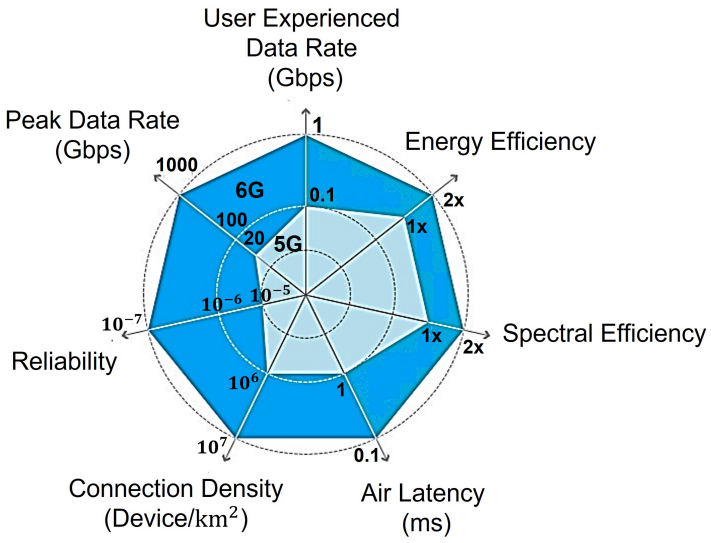

Figure 1.1: Comparison between 5G and 6G.

methods [5]. However, they require extra costs and have a restricted amount of influence over the essentially random nature of wireless channels, making the basic obstacle to establishing wireless communications with high capacity and reliability insurmountable. Moreover, signal transmission is subject to reflections, diffractions, and scattering before arriving at the destination, resulting in a plethora of arbitrarily degraded and deferred extra versions of the source waves along various paths owing to the unpredictability of the radio environment. This channel fading change becomes a fundamental restricting element in wireless network EE and SE performance optimization.

The existing modern physical layer solutions are insufficient, and overall progress is still modest, necessitating new and radical physical layer solutions. There is attracting attention in new communication patterns that exploit the propagation environment's extreme randomness to achieve the target of the simplicity of the transceiver components and the quality of service (QoS). The reconfigurable intelligent surface (RIS) has recently been added in the wireless communications by the academic researchers [6]. The RIS is a fundamental facilitator for achieving the concept of smart radio environments (SRE)s by rendering the wireless environment configurable and adjustable as per Fig. 1.2.

RIS refers to a cost-effective, flexible surface, like a smart and lightweight composite layer, capable of manipulating incoming wireless signals. This manipulation can be configured and adjusted through external inputs. As a result, one of the most important characteristics of RISs is their flexibility to be reconfigured after being deployed in a wireless environment. RIS is a metasurface, which is a two-dimensional (2D) electromagnetic (EM) material surface constitutes of multiple passive scattering units. Each unit in the surface can be modified in a method specified by software to change the EM characteristics of the incident signal's reflection on the scattering units. By heavily placing RISs in wireless networks and intelligently organizing their reflections, the propagating signals in wireless channels between sources and destinations can

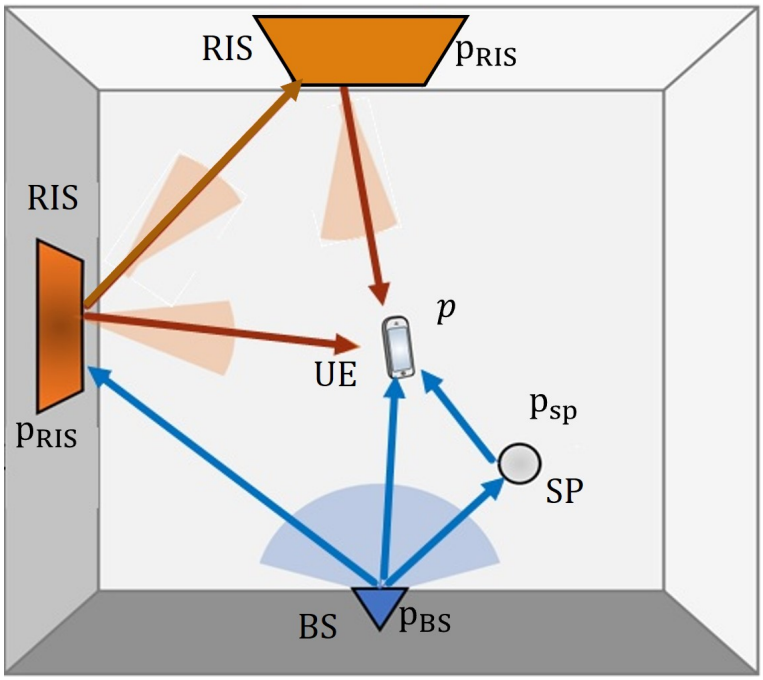

Figure 1.2: RIS in Communication and localization

be freely reconfigured to obtain targeted realizations and distributions. Consequently, they introduce a better way to essentially address the fading channel deficiency, interference problem and potentially gives a practical solution.

RIS's aided future wireless networks have recently prompted substantial research. In the literature, a few publications have provided an overview of research on RIS and its variants from various perspectives. Realistic simulations and tests have shown the SRE's potential to increase transmission performance in a variety of wireless networks by using the RIS's tunability. The author in [7] described the active wall, and how it works by manipulating the wireless environment via an active frequency selective surface (FSS). The intelligent wall's major objective is to switch the active FSS on and off dynamically to modify its EM properties, which affects the propagation environment and hence, the system performance. More interestingly, in [8] the authors proved the advantages of deploying the low-cost devices into a building's walls to transmit and reflect wireless waves actively and passively respectively. The paper [9] provides a novel technique for controlling the behavior of wireless environments that is predictable and programmable. The major enabler is the hypersurface tile, a novel class of planar meta-materials that can engage with encroaching EM radiation in a manageable way. EM waves may be re-engineered in many ways using hypersurface tiles, including total absorption, polarisation manipulation, and more. Multiple tiles are used to cover items in both indoor and outdoor conditions, such as facades of the buildings and other items. To better meet the demands of communication devices, an external software service determines and delivers the ideal interaction types per tile. Simulations are used to evaluate the new concept's potential. The researchers in [10] implement and evaluate many physical layer building-block solutions for a

configurable wireless network and proposed the KPCONFIG method which is a new way to setting the programmable wireless environments (PWE), allowing for multi-user support and flexibility in expressing resource sharing policies and user communication goals. Furthermore, it uses an accessible model based on well-known ray-tracing principles to illustrate the underlying physics of hypersurfaces' unique ray-manipulation capabilities. The incident Radio Frequency (RF) waves may be configured with the desired response by regulating the distribution of the current over the hypersurfaces, resulting in a reconfigurable wireless environment. The programmable wireless environment can improve the performance of transmission relating to signal strength, communication coverage, EE, and SE performance by reducing signal pathloss, multi-path fading, and co-channel interference. Rather than using hypersurfaces, the authors in [11] proposed Scatter-multiple-input multiple-output (MIMO), which employs a smart surface to maximize the scattering in the surroundings to give MIMO spatial multiplexing gain.

Wireless networks aided by the RIS are expected to change the existing network optimization patterns by incorporating the smart wireless environment into network optimization issues and are predicted to take a proactive role in the future wireless networks [12].

The incorporation of a RIS introduces various possibilities for localization enhancement [14, 15]. These include the introduction of synchronized location references and configurability to optimize localization performance. Additionally, each RIS contributes to the generation of new geometric measurements, thereby enhancing both accuracy and coverage in localization. An RIS can be viewed as a synchronized multi-antenna base station (BS) equipped with a phased array, contributing to localization enhancement. Strategic placement of the RIS can lead to significant improvements in location coverage, even in scenarios involving a single-antenna user and BS. The RIS configuration can be customized for the specific user location, but it differs significantly from the optimal configuration for communication purposes. While many RIS elements are necessary for communication to enhance signal-to-noise ratio (SNR), localization demands broader bandwidths, and the RIS can be smaller since its primary role is to introduce new dimensions for resolving identifiability issues. Furthermore, unlike communication scenarios where the RIS provides limited gains in the presence of line-of-sight (LoS) path, both paths are valuable for localization, offering useful and necessary information. By encoding RIS configurations with a global code, it becomes possible to separate controlled and uncontrolled channels, supporting the implementation of multiple non-interfering RISs [12].

1.2 Research Scope and Overview

The next generations of mobile communication systems (beyond 5G and 6G) are expected to provide an excellent platform of a wide range applications of RIS-based communication and localization. In this context, RIS-based communication and localization can be seen as a key enabler of such systems. Although RIS-assisted Communication and localization techniques

have been an actively researched topic over the past decades, there are still many open problems which researchers have not solved or understood yet. With focus on RIS theory, this thesis contributes to the wireless field by providing applied and fundamental research results that address open areas of RIS-based technology with more focus on the realistic and practical channel and phase shift models in addition to the signal impairments like mutual coupling (MC) and electromagnetic interference (EMI). The thesis studies RIS-based communications in various outdoor environments of conventional communication and localization systems (sub-6 GHz). It explores fundamental performance of achievable data rate and bounds of location estimation and provides a deep understanding of the factors that together affect these performances and bounds and shows how this understanding can be exploited to better design 5G and 6G communication systems and localization algorithms. The main contribution this thesis provides is a fundamental understanding of how the RIS technology can enable extremely better achievable data rate performance and accurate localization in the near-field regime. By studying theoretical performance bounds, we aim to provide insights on the feasibility and the factors that need to be considered when designing localization and communication systems in order to achieve the required high location accuracy and better data rate for the users.

1.2.1 Research Questions

The research presented in this thesis seeks to address the following research questions:

1. Q_1: In sub-6 GHz, when operating in an environment characterized by a specific level of scattering richness, what performance can be anticipated as optimal? How can we effectively utilize non-line-of-sight (NLoS) propagation models to enhance the design of localization and communication algorithms, aiming for performance levels that closely resemble the best achievable outcomes?

2. Q_2: In communication system design, is it more advantageous to opt for a one-bit RIS or a multi-bit RIS? What constitutes the optimal deployment scenario for RIS – near the transmitter, the receiver, or equidistantly between them?

3. Q_3: The literature is saturated with algorithms and schemes investigating the behaviour of communication and localization systems based on RIS. What computational complexities and runtime considerations are associated with these algorithms? Do these algorithms demonstrate effective functionality in NLoS channels?

4. Q_4: The literature is filled with assumptions and overly optimistic simulation outcomes for communication and localization systems. To what extent does the oversight of inevitable parameters like EMI, RIS MC, and practical amplitude variation models align with the realistic performance of data rates or targeted localization accuracy?

1.2.2 Research Objectives

The primary research objectives encompass the following:

- *Objective 1*: This thesis delves into the investigation of the achievable data rate for a single and multi-users assisted RIS communication considering the LoS and NLoS channels. The perfromance is verified using multi-bit RIS and practical phase model which considers both amplitude and phase variations.

- *Objective 2*: Investigating the performance of different RIS algorithms taking into consideration the reflection coefficients phase shift tuning and fair power allocations for all number of subcarriers. This thesis proposes iterative power algorithm which adopts codebook approach for selecting the best RIS configuration and waterfilling technique to dedicate power fairly into all subcarriers considering their channel gain status. The iterative power method shows comparable performance with low computational complexity and run time.

- *Objective 3*: This thesis explores the effects of mutual coupling and electromagnetic interference on the achievable data rate performance. It is observed that the achievable rate degrades when considering both effects consequently, the RIS has to be aware of the mutual coupling and electromagnetic interference.

- *Objective 4*: The thesis focuses on investigating 3D localization using a simplified design of RIS elements. This design integrates adjustable RIS lenses and a single antenna connected to a receiving radio frequency (RF) chain. We address the challenge of RIS-assisted geometric near-field localization in scenarios where LoS blockage occurs. To address this challenge, we conducted Fisher information analysis and derived a closed-form expression of the Fisher information matrix (FIM), demonstrating how the position error bound (PEB) depends on the RIS phase profiles. We utilized three types of RIS phase profiles – random, directional, and positional configurations – to illustrate the role of RIS in both localization and communication in the near-field region. These phase profiles are designed considering the amplitude and phase responses of the RIS, incorporating a practical phase-dependent amplitude model. The random profile ensures a uniform signal-to-noise ratio (SNR) across the deployment area, while the directional and positional profiles enhance the SNR towards the user's location. Additionally, we propose a simplified localization scheme to reduce the complexity of the maximum likelihood (ML) estimator. The achievable data rate decreases with distance in the near-field region, which correlates with the gradual increase in localization error as distance from the RIS increases. Both the achievable data rate and localization error exhibit poorer performance when the RIS phase-dependent amplitude model assumes an amplitude value less than one. Thus, the common assumption of unity amplitude for the RIS phase shift model, widely used in

the literature, leads to overly optimistic and inaccurate results regarding localization and communication performance.

- *Objective 5*: While there has been extensive theoretical research on modeling RIS, there remains a scarcity of test-bed systems designed to evaluate RIS functionality in real-world scenarios. This thesis addresses this gap by developing and testing a novel feedback-based adaptive optimization algorithm for adjusting reflection coefficients, facilitating intelligent reflection without necessitating changes to existing communication standards. Through indoor NLoS field trials, a notable 18 dB channel gain improvement was observed compared to a reference case involving a metal plate. This underscores the substantial benefits achievable through the implementation of RIS in real-world environments.

1.2.3 Thesis Overview

The remainder of this thesis is organized as follows:

- *Chapter 2* provides the background necessary to understand the thesis. This includes a brief revision of relevant RIS theory from the RIS architecture and control mechanism, a review of performance analysis and optimization, a review of channel estimation, a review of the RIS deployment scenarios, future research directions and finally, a summary for the chapter.

- *Chapter 3* studies the achievable data rate obtained by using different RIS based-schemes. The chapter explores the behaviour of these techniques in the LoS and NLoS channels in addition to the computational complexities and run time for the diferent methods.

- *Chapter 4* takes into consideration the effects of MC and EMI on RIS performance. According to our knowledge, we notice that the literature is lacking such important parameters and most of the research obtained results are overoptimistic. We have investigated RIS setup to look at the effect on the data rate for both the users who have LoS and NLoS scenarios under MC and EMI in a single-input-single-output (SISO) multi-user orthogonal frequency-division multiplexing (OFDM) communication Setup.

- *Chapter 5* studies the near-field localization using an RIS practical amplitude variations model. We have estimated the user location in three-dimensional (3D) by developing a three stage localization algorithm. The Fisher information matrix analysis is presented and the position error bound is derived in order to calculate the localization accuracy. We have also adopted the RIS amplitude variation model to the calculation of the achievable data rate in the near-field regime to study its effect on the performance data rate.

- *Chapter 6* Shows the RIS field measurements. The RIS measuremnts have been taken in our Mast lab. We have measured the received signal power when the RIS is tuned by using

the DFT codebook and compare the results with the RIS surface when it is unconfigured. The perfromance gap shows the importance of RIS technology.

- *Chapter 7* gives conclusion and predicts the future directions and challenges.

Chapter 2

RIS Literature Review

This chapter presents the RIS hardware and functionality, including signal and channel models, hardware design, and control mechanisms. By examining the strengths and limitations of each approach and technique, this chapter aims to provide a comprehensive overview of the performance analysis and optimization of RIS-assisted wireless systems. It explores various approaches for RIS channel estimates which can be applied to a variety of RIS topologies and communication settings considering RIS deployment at both link and network level. Finally, chapter 2 is concluded by describing the challenges and research challenges. in Section 2.1, RIS hardware and functionality is presented. Performance analysis and optimization, Channel estimation and RIS deployment are thoroughly studied in sections 2.2, 2.3 and 2.4 respectively. The limitations and challenges are discussed in section 2.5 while 2.6 gives summary for the chapter. Finally, the publications resulted from this chapter is listed in Section **??**

2.1 RIS Hardware and Functionality

In this section, we cover the fundamentals of RIS-assisted wireless communication, including the major RIS architecture, hardware, and control mechanism, as well as the signal and channel models presented in the existing works of literature.

2.1.1 RIS Architecture and Control Mechanism

Snell's law and the Fresnel equations control the intensities and directions of reflected and diffracted waves [16]. When the wave collides with a metasurface, the situation changes. A shifting in the resonance frequency and, as a result, changes in the boundary conditions might emerge from the periodic arrangement of the scattering components. Hence, extra phase shifts will be carried by the reflected and diffracted waves. The EM characteristics of the metasurface will be fixed once it is produced with a certain physical structure, allowing it to be utilized for a given aim, such as an ideal absorber working at a specific frequency. The RIS is made up

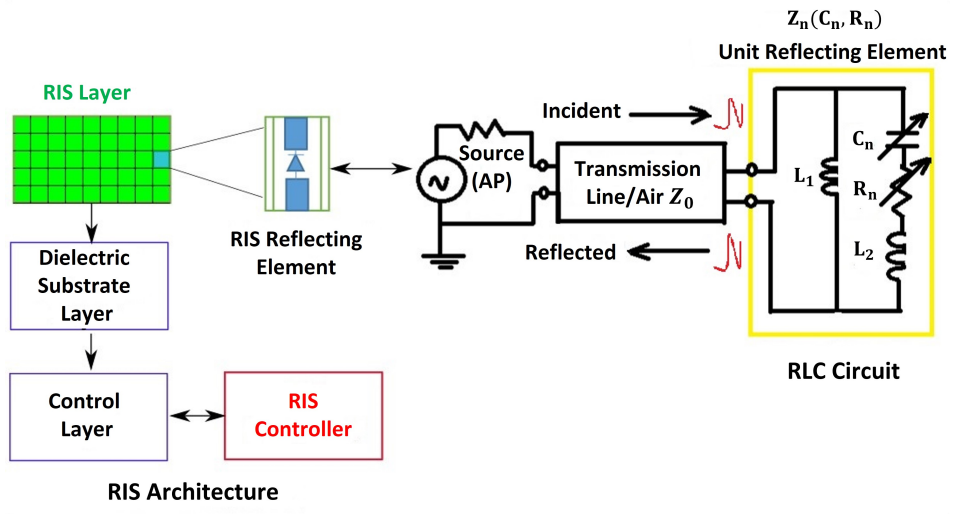

(a)

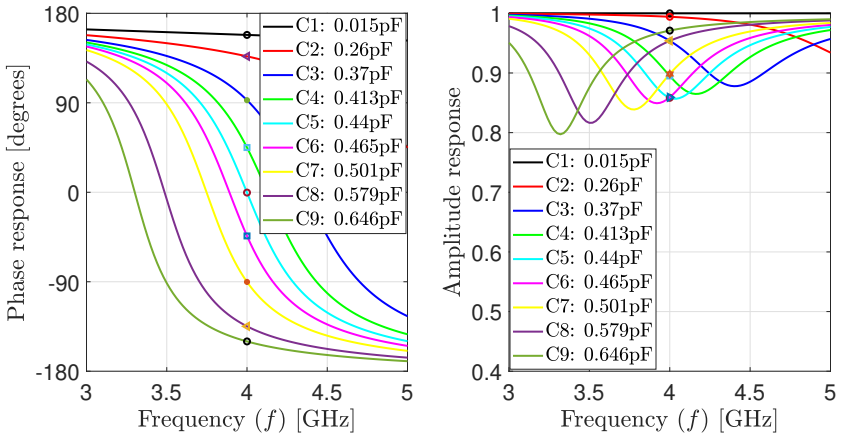

(b)

Figure 2.1: a) Structure of the RIS including its reflecting element and the equivalent RLC circuit model and b) Amplitude and phase responses for different elements and their corresponding capacitance values.

of a programmable metasurface that can completely regulate the phase changes that individual scattering components experience. This can be accomplished by applying outside stimulus to the scattering components, causing their physical characteristics to alter, resulting in a change in the metasurface's EM properties without refabrication [17].

Figure 2.1a depicts a typical RIS design, which includes three layers and a smart controller. The first layer (RIS layer) is made up of a dielectric substrate with several tunable and reconfigurable metallic patches put on it to directly regulate incoming waves. A copper substance is typically used in the second layer to avoid transmission power losses due to RIS reflection. The third layer is a control integrated board that is in charge of both excitation and real-time control of the reflecting elements' reflection amplitudes and phase shifts. Moreover, a smart controller linked to each RIS also activates and decides reflection adaptation, which may be done with a

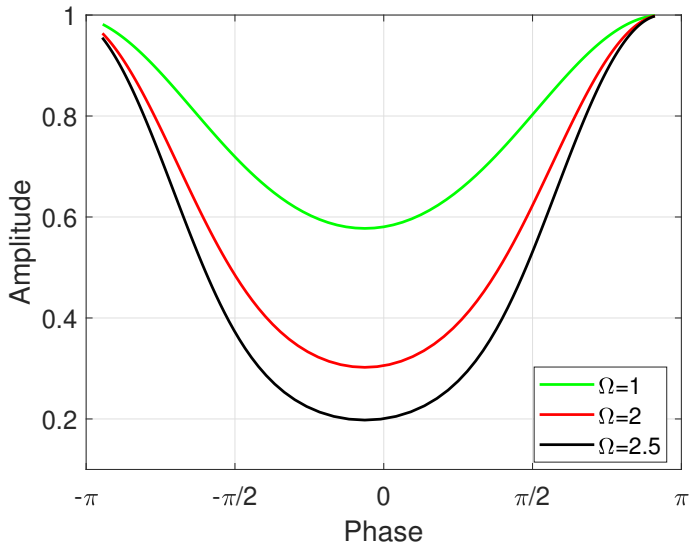

Figure 2.2: Reflected amplitude vs. phase shift for RIS element

field programmable gate array (FPGA). Another network components such as BSs, and user terminals can link to each other over wired or wireless backhaul and control lines thanks to the RIS controller's role as a gateway. In practice, dedicated sensors can be deployed in the first layer, for example, interlaced with the RIS's reflecting elements, to detect the surrounding radio signals of interest and assist the smart controller in designing the reflection coefficients, to enhance RIS's environmental learning capability [3]. There are three basic categories for the different tuning processes that have been proven in the literature namely:

1. Circuit tuning comprises the integration or modification of individual impedance into the unit cell circuit model using changeable capacitors and switches inside and between unit cells.

2. Geometric tuning refers to techniques that change the form of the unit cell physically, causing the accompanying circuit model to change dramatically.

3. Material tuning is the process of modifying the material properties of a substrate or small section of a unit cell to change the responsiveness and characteristics of the substrate layer or small component of the unit cell.

Circuit Tuning

The EM behaviour of actual, passive transmission lines, antennas, and metamaterials may be modelled as a lumped inductive, capacitive, and resistive equivalent circuit. This way of breaking down complex geometric shapes into a known circuit model is highly useful for predicting how updated designs would behave. Metamaterial circuit tuning is described as methods for

introducing, altering, and controlling specific components in the metamaterial's equivalent circuit. Due to their ease of combination into a variety of metamaterials, varactor diodes are the most often used tuning method [18]. The incorporation of a varactor in a metamaterial design is frequently referred to as active metamaterial despite the fact that the device remains inactive for RFs and is only active in its desire for a direct current (DC) bias [19].

The varactors in most cases have been considered as perfect or nearly ideal linear capacitors with good accuracy, although numerous researches have looked at the nonlinearity aspect of the varactor at various power levels [20]. In terms of applicability and simplicity of integration, the use of positive-intrinsic-negative (PIN) diodes [21] in a metamaterial is comparable to the use of varactors, although these actuators influence resistance rather than capacitance. In practice, independent amplitude and phase shift control of every RIS element are preferable for superior reflection design, but this needs more intricate architectural patterns and design elements [22] than those listed above for their independent control alone. While continually adjusting the reflection coefficient is advantageous for improving communication performance, it is challenging to put into practice because better quality reflective components need not only more expensive but also more complicated hardware architecture. For instance, at least $\log_2(8) = 3$ PIN diodes are required to allow 8 levels of phase changes per RIS unit. By properly quantizing the intervals $[0,1]$ and $[0,2\pi]$, we can calculate the discrete amplitude and phase-shift values, respectively. Even though phase-shift control or phase beamforming can achieve better passive beamforming performance than amplitude control or amplitude beamforming, phase-shift control or phase beamforming for RIS is more expensive to construct when the number of control bits and discrete levels for each reflective element are the same. The authors in [23] proposed a practical reflection model by simulating every reflective component as a resonant circuit with specific inductance, capacitance, and resistance values and depending on his prototype, it was discovered that the reflecting element's amplitude response and phase shift are in general non-linearly linked, and hence are not separately controllable. The reflection amplitude achieves a minimum value at zero phase shift, as shown in Fig. 2.2, but rises uniformly as the phase shift approaches 180 or -180, asymptotically approaching one.

Geometrical Tuning

Many metamaterials depend on conductive components that may combine with encroaching EM signals to produce the required electric or magnetic resonance or other beneficial behaviour. Because metamaterial characteristics are generally influenced by the form, size, direction, and closeness of conducting components, methods that change the geometric features of the conductive elements can be a powerful tool for adjusting or switching metamaterial response. By shifting conducting components in respect to each other, metamaterials may be geometrically adjusted. The microelectromechanical systems (MEMS) are often used in THz metamaterials to accomplish the mechanical movement of conducting components. The coupling between con-

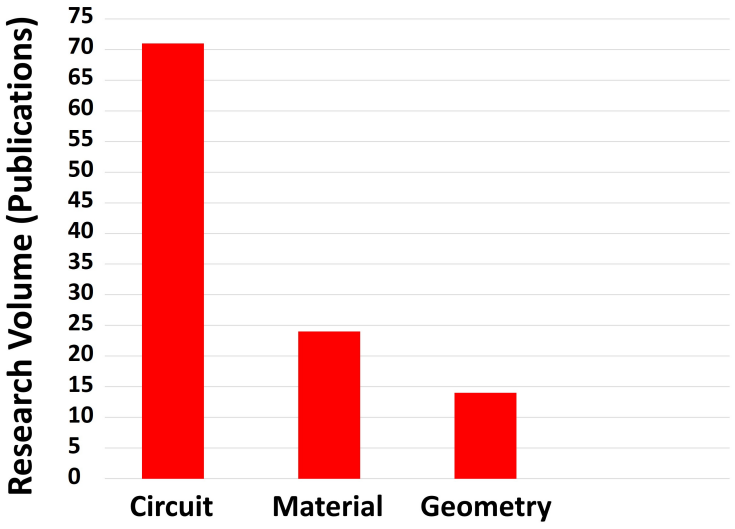

Figure 2.3: Tuning mechanism comparison

ducting components varies when they are pushed closer or farther away, resulting in variations in resonance frequency or resonance strength. Moving conducting elements can also alter the shape of the element. Stretching the substrate to further separate the elements on the substrate, resulting in significant variations in the resonance frequency of the elements, is a unique approach for moving conducting components in a metamaterial. Several tunable high impedance surfaces (HIS) have been shown to alter the phase of the reflected wave by mechanically sliding an upper plate of elements along the surface or vertically [18]. Geometrical tuning may result in substantial variations in metamaterial features since the geometry of the conducting elements has such a large influence on the related resonant frequency. Geometrical tuning, on the other hand, is difficult to execute since it necessitates a physical control mechanism.

Material Tuning

While changing the structure of resonant components provides for a number of tuning possibilities, the metamaterial's properties are ultimately determined by the constituent materials used to create the unit cell. Various constituent materials have been examined and used in the literature for tuning metamaterials by changing the permittivity, permeability, and conductivity of unit cell sections. Several candidate materials, such as $Ba_{0.5}Sr_{0.5}TiO_3$ (BST) ferroelectric films, liquid crystal, and Ga-Sb-Te (GST) phase-change materials, have been used to tune the permittivity of metamaterials. More details about the material tuning subject can be found in [18, 34, 35].

The purpose of presenting the three tuning approaches in this review study is to mention that due to its rapid reaction time, minimal reflection loss, low power consumption and cheap equipment price, the first technique (circuit tuning) has been widely used in actual applications and implementations. Fig. 2.1a depicts an example of a reflecting element and its corresponding resistor-inductor-capacitor (RLC) circuit based on a PIN diode installed in the centre of the

Table 2.1: List of publications related to RIS from the SRE perspective

Ref.	Surface Architecture	Control Mechanism	System Setup	Achievement
[7]	Active FSS with PIN diodes connecting metal parts of the FSS	ON-OFF PIN Diodes	multiuser (MU) wideband indoor downlink orthogonal frequency-division multiple access (OFDMA) system	Surfaces that are fully reflected with proper coverage and can boost system performance by up to 80%
[8]	programmable radio environment for smart spaces (PRESS) Low-Cost antenna elements connected to passive loads and embedded in the walls of a building	Prototype PRESS elements equipped with (SP4T) RF switches change phase of each antenna by $\pi/2$	Multi-client's wideband system	Passively reflect or actively transmit radio waves, and so attenuate or enhance signal strength by up to 26 dB, to reconfigure multipath propagation
[9]	Hypersurface tile equipped with physical switch elements	Switch element Controllable state (ON/OFF)	12 receivers, in both microwave and mm-Wave frequency bands, are uniformly distributed in indoor space and are evaluated using a map-based ray-tracer	Re-engineering EM waves, including steering in any direction, complete absorption, polarisation modification, and other techniques. With maximum and minimum received power of 32.5 dBm and 12.4 dBm, respectively, and an average received power of 20.6 dBm, the results demonstrate good coverage.
[24]	spatial microwave modulators (SMM) equipped with102 controllable EM reflectors	Two states of resonant elements (the reflector and the parasitic strip), π state and 0 state	Two antennas source and receiver connected to network analyzer are located in a room that the spatial microwave modulator can be placed on the walls of the room	Increasing or cancelling the wireless transmission amplitude between two antennas (Shaping complex microwave field). SMM can perform wave front shaping and concealing the field around one single antenna on a correlation length wide area (6 cm at 2.4 GHz)
[91]	Reflect-array panel with totally 48 reflector units and its peripheral circuits and varactors	Each reflector is controlled by a bias voltage to tune the varactors $(0.6-8\text{pF})$ for changing the capacitance and hence the phase of each unit	Two pairs of wireless users in a conference room where smart reflect array hung on the walls	Controlling the phase shift of each reflect-array element. The interference has been eliminated, and the signal-to-interference-plus-noise ratio (SINR) has been enhanced to around 30 dB, according to the achieved results
[26]	Intelligent receiving antenna array	the information transfer capabilities of an intelligent surface for every m^2 deployed surface area	Multi-user narrow band system with ideal free space propagation	Active surface for transmission and reception. Consequently, the limit of the normalized capacity is enhanced when the wavelength approaches zero
[27]	Hypersurface tile with controllers that regulate the metasurface's switch components	Dynamic meta-atoms include phase switching components like MEMS, complementary metal–oxide–semiconductor (CMOS) transistors, or microfluidic switches that can change the structure of the meta-atom	mm-Wave setups that include a receiver (Rx)-transmitter (Tx) pair situated in NLoS over a defined floorplan and walls covered with hypersurface	New physical layer security features can help avoid eavesdropping. Pathloss and multipath fading mitigation, as well as eavesdropping security, were proven in the 2.4 and 60 GHz configurations
[28]	Plasmonic antenna elements at each transceiver side	New intelligent plasmonic antenna arrays that can function in transmission, reception, reflection, and waveguiding, the mm-Wave and THz-bands	Ultra-Massive MIMO	In the mm-Wave and THz-bands, new intelligent plasmonic antenna arrays capable of communications and waveguiding have been developed. The results demonstrate a significant increase in transmission distance and data rate
[29]	RIS-assisted free-space optical (FSO) systems	Comparable mirror-assisted technology, which can be used to create a phase-shift profile that spans the RIS	A FSO communication system consists of a Tx with a Gaussian beam-emitting laser source, an RIS, and a Rx with a lens and a photo detector (PD)	FSO systems with RIS assistance can compensate the need for a LoS between Tx and Rx. The effect on the end-to-end channel varies depending on where Tx, RIS, and Rx are in relation to each other
[30]	102 phase-binary components make up the metasurface	The phase shift of the reflected wave may be electrically controlled for each element using a PIN diode bias voltage from an arduino microcontroller to be either 0 or π	The transfer of an RGB colour image across a 3-3 MIMO system was simulated using wireless image transmission in an office room	The benefit of shaping wireless channels. Physical shaping of propagation media with simple metasurfaces may achieve complete orthogonality of wireless channels and excellent channel diversity and low crosstalk
[31]	RIS with 16 elements	A method of encoding information in both the sent signal and the RIS configuration	single-input and multiple-output (SIMO) over a quasi-static fading channel	To boost capacity, a method is utilised that encodes data in the sent signal as well as the RIS configuration. Three times quicker than max-SNR encoding is the joint encoding.
[32]	RIS with large reflecting elements	The best RIS phase shift configuration	Multiple antennas at the transmitter and receiver in a point-to-point RIS-based system	Developing an overhead-aware resource allocation framework where RIS used to improve the performance SE/EE of the system
[33]	256 unit cell programmable surfaces based on varactor diodes	A digital to analogue converter generates an external control signal that controls the phase response of the unit cell	RIS-assisted MIMO wireless system	The proposed prototype implements real-time RIS based MIMO-QAM wireless communication with less power consumption and achievable data rate 20 Mbps

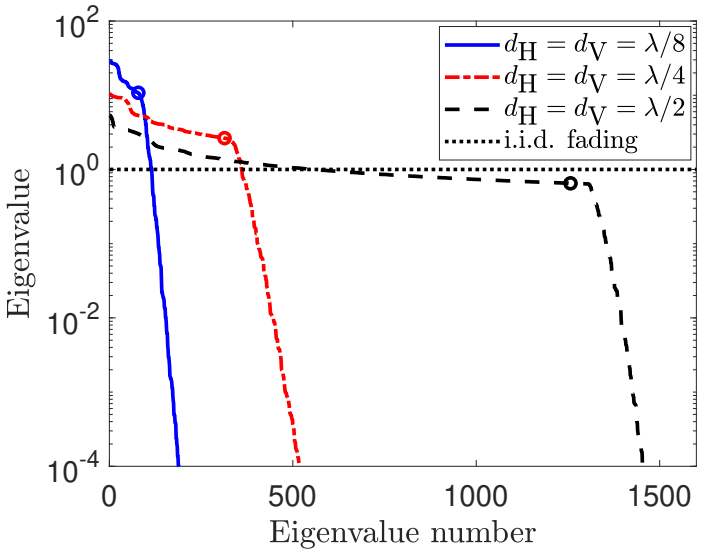

Figure 2.4: Eigenvalues of spatial correlation for an RIS with number of elements N = 1600 and different element spacing $d_H = d_V$. please, refer to [37] for simulation parameters

element. Such illustrations of RLC circuit equivalence have been used widely in the literature. Table 2.1 provides an overview of the most updated and recent concepts and realizations for a smart radio environment taking into account essential parameters such as surface architecture, control mechanisms, system setup and ending with the outcomes and work achievements. We noticed that high volume of researches depend on the circuit tuning more than the other two tuning methods which coincides with Fig. 2.3 survey.

2.1.2 Signal and Channel Model

Channel Fading

RIS can be coated on the front of buildings in the wireless environment, such as solid structures and top surfaces of rooms, or carried on aerial vehicles, such as balloons in the air and unmanned aerial vehicle (UAV) [36], to achieve the idea of the smart radio environment. As a result, for modelling and performance analysis of RIS-aided wireless communication, scientific analysis models that consider the geographical placements of RIS elements, the RIS's EM characteristics, and the wave modifications utilized by adjacent RIS elements in the environment are necessary. A transmitted radio signal in a typical wireless communication environment contacts many objects along the route, resulting in duplicates of the transmitted wave which comes across reflection, diffraction, and dispersion. Multipath components are signal copies that reach the receiver with randomly and unexpectedly different amplitudes, phase shifts, and signal delays, causing considerable distortions in the received signal due to their relative constructive or destructive addition. This is termed as fading in wireless communication systems, and it is a critical parameter in existing and future wireless communication systems.

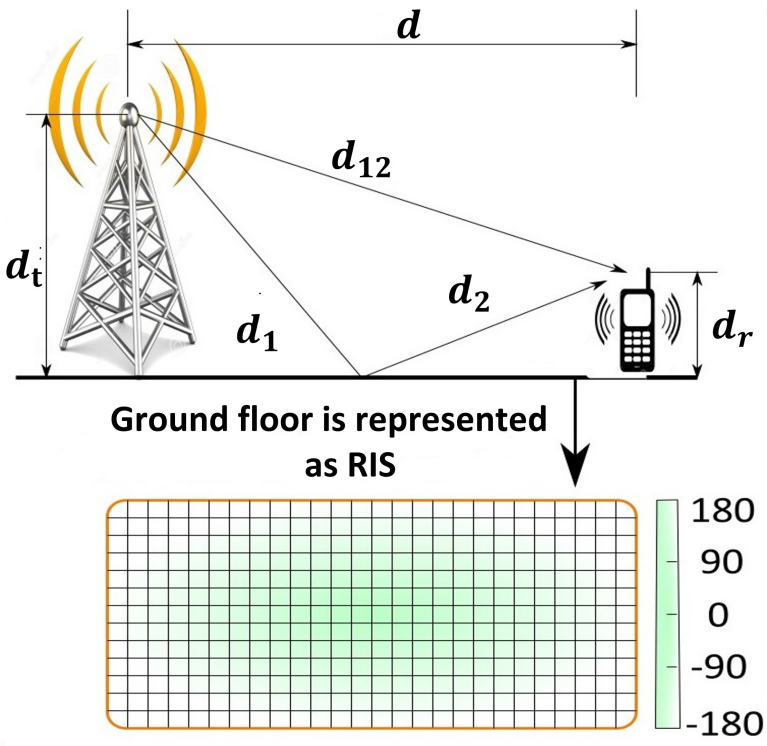

Figure 2.5: Illustration of the pathloss of two rays' propagation model

The basic goal of RIS is to establish a controllable wireless communication in which the extremely unpredictable radio channel is turned into a controllable space by carefully modifying EM signal propagation in a software-controlled manner. A channel model that captures the key characteristics of any wireless technology is required for an accurate performance assessment. The most theoretical work on wireless systems technologies in scattering conditions has been and continues to be based on the independent and identically distributed (IID) distributed Rayleigh fading channel model [45] [46] [47]. When using a rectangular RIS, the authors in [37] shows that such a paradigm does not exist realistically, and present an equivalent physically valid Rayleigh fading model that may be used as a reference for evaluating RIS-assisted communications. The received signal $r \in \mathbb{C}$ can be represented as in literature:

$$r = \left(G^{\top} w_{\theta} H + h_d\right) x + e, \tag{2.1}$$

where, x is the transmitted signal with power $p = \mathbb{E}\{|x|^2\}$ and $e \sim \mathcal{N}_{\mathbb{C}}\left(0, \sigma_e^2\right)$ is the noise variance. The configuration of the RIS is given by the diagonal matrix $w_{\theta} = \Gamma\Phi$ with $\Phi = \text{diag}\left(e^{-j\emptyset_1}, \ldots, e^{-j\emptyset_N}\right)$ and $\Gamma = \text{diag}\left(\gamma_1, \ldots, \gamma_N\right)$. The direct path $h_d \in \mathbb{C}$ has a Rayleigh fading distribution. However, the fading distribution of the channels $G \in \mathbb{C}^N$ and $H \in \mathbb{C}^N$ is independent and distributed as $G \sim \mathcal{N}_{\mathbb{C}}\left(0, A\mathbb{B}_G R\right)$ and $H \sim \mathcal{N}_{\mathbb{C}}\left(0, A\mathbb{B}_H R\right)$ where A is the area of the RIS element, $\mathbb{B}$ is the average attenuation intensity and R is the spatial correlation matrix. Figure 2.4 shows that non of the cases $d_{\text{H}} = d_{\text{V}} = \{\lambda/8, \lambda/4, \lambda/2\}$ resemble the IID Rayleigh fading.

More details can be found in [37].

Pathloss

The authors [38] evaluated the two-ray channel model as per Fig. 2.5. In the most perfect propagation scenario, with no user movement and no unanticipated environmental consequences, a single uncontrolled ground reflection might cause substantial signal degradation. The authors assumes that a changeable metasurface covers the whole ground. The RIS may be thought of as a perfect phase shifter, designed to change the reflected signal phase such that the LoS and reflected radiations add up constructively, increasing signal strength. It has been shown that the usage of programmable intelligent surfaces has the possibility to change the scaling rule that regulates the received signal power with distance. Despite the results concluded by [38] are promising, they are not realistic and practical because they were based on several assumptions including the ability to tune the reflected phases without any analogue to digital conversion error and for any incident and scattered angle, as well as the lack of reflection impairments and comprehensive awareness of the phases status at the RIS. Furthermore, for more actual system models, optimizing the phases is typically not a simple process.

By researching the physics and EM characteristics of RISs, the author in [92] developed a free-space pathloss models for RIS-assisted wireless communications for various circumstances which can be divided into two groups: RIS-assisted beamforming and RIS-assisted broadcasting. The proposed models reveal the relations between the free-space pathloss of RIS and distances from both the transmitter and receiver to the RIS. To explain the free-space pathloss of RIS-assisted beamforming and broadcasting, three perceptive free-space pathloss models were developed: the far and near fields beamforming equations and the near-field broadcasting equation. The authors in [48] improved the pathloss models derived in [92] by formulating joint radiation pattern of antennas and unit cells in addition to clarifying the relation between the scattering gain of the unit cell and its size.

The authors in [40] calculates the far-field pathloss using physical optics methods and explain why the surface consists of multiple reconfigurable elements that individually behaves as diffuse scatterers but may collectively beamform the signal in a desirable direction with a certain beamwidth. As a result, an RIS can be thought of as an array of sub-λ-sized diffuse scatterers that aiming the phase of their reflected signals at the receiver, resulting in anomalous reflection. Figure 2.6 depicts the pathloss as a function of observation angle for various RIS sizes. The main beamwidth narrows as the RIS surface area grows. The RIS virtually functions as a diffuse scatterer when the dimension is sub-wavelength (less than $\lambda/2$). The authors proved that the power of the received signal is proportional to the square of the RIS area and to $1/(d_1 d_2)^2$, where d_1 is the distance between the transmitter and the RIS and d_2 is the distance between the RIS and the receiver. This refutes [38] hypothesis that the received power is proportional to $1/(d_1 + d_2)^2$. To compensate for the enormous power loss caused by twofold attenuation, a

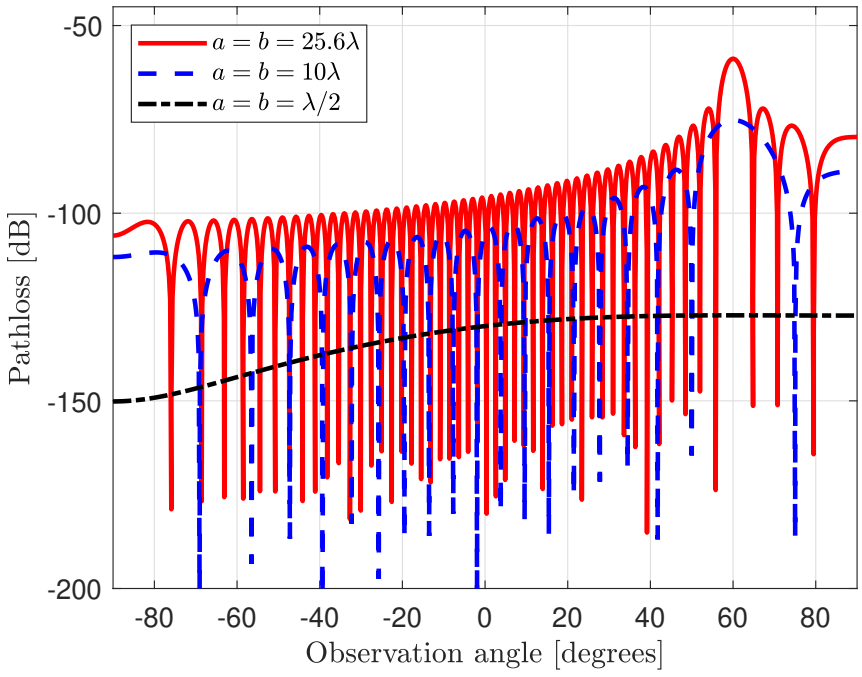

Figure 2.6: Pathloss of the reflected path. Please, refer to [40] for simulations parameters

significant number of RIS reflecting components must be employed to combine their reflection magnitude and phases to obtain higher passive beamforming gains. RIS is made up of several sub-wavelength components that scatter incident waves with distinct phase shifts in order to perform constructive beamforming in a certain direction.

Using the scalar theory of diffraction and the Huygens-Fresnel principle, the authors in [41] describe pathloss in RISs in both the near and far fields. RISs are represented as homogenous sheets of EM material with negligible depth. The authors reveal the regimes in which the pathloss relies on the summation and multiplication of the distances between the RIS and the source, as well as the RIS and the destination, using the stationary phase technique. The analytical technique provided is proven to be sufficiently generic for use with a consistent reflecting surface, anomalously behaving reflectors, and lenses with highly concentrating and reflecting features.

The authors in [42] have provided a viewpoint that unites RIS opposing behaviour as a scatterer and as a mirror. It has been proven that the RIS may be seen as a zero, one, or two-dimensional object, depending on its size and distance and its radiated power exhibits a dependency on the fourth, third, or second power of the distance, respectively. In addition, the Fresnel zone decomposition is used to gain a better understanding of how the various variables interact. More precisely, the importance of phase in determining the eventual pathloss exponent is discovered and demonstrated how free space propagation may be outperformed via smart dephasing. The findings are calculated numerically, and the received signal in terms of distance has no clear analytical meaning. [43] reports similar observations.

2.1.3 Discussions and Insightful Prospect for Section 2.1

- Figure 2.3 shows the volume of research (paper publications) using the three approaches of tuning however in this chapter we will not list the publications [18] to avoid repeating what other authors have done and worth mentioning that the reasons stated above for the more widespread usage of the first approach is not enough and more research still has to be conducted on the other two approaches to be parallel with the circuit tuning method.

- We have noticed a disagreement between the authors in [40] and the authors in [38] regarding the reflected power in the far-field region as a function of the distance between the transmitter to the RIS and the RIS to the receiver while other researches are in agreement with [40] . Moreover, the correlation fading revealed in [37] clarifies that using the IID fading channel is not encouraged to be modelled in the RIS wireless systems analysis which opens the door for reconsidering previous works depending on the IID fading models. Table 2.2 offer a comparison for different pathloss models in the existing literature. The purpose of narrating the previous work is to investigate the pathloss derivations based on strong foundation presenting all the scenarios bearing in mind that pathloss due to distance, large- and small-scale shadowing and multipath fading are all factors that affect channel coefficients. The pathloss of an RIS reflected channel, in particular, represents the average power of the channel and is therefore critical for link budget analysis and performance assessment of RIS-assisted wireless systems.

2.2 Performance Analysis and Optimization

This section is divided into two parts. In the first part, we present the performance analysis of the RIS using different performance metrics like bit error probability and sum rate for evaluating the overall behaviour of the wireless systems aided RIS and under various channels and environments. Furthermore, the second part will concentrate on the RIS reflection optimization techniques and algorithms.

2.2.1 Performance Analysis

In this chapter, we will present the RIS advantages and performance comparisons with other wireless systems. furthermore, we show the behaviour and the usage of the RIS as reflector, receiver and transmitter taking into consideration the performance metrics proposed in the literature for RIS supported wireless communication systems like coverage or outage probability, bit error probability, Ergodic capacity, and achievable data rate.

Table 2.2: Pathloss comparison for the existing literature

Ref.	Concept	Field	Goal	Notes
[38]	LoS and ground-reflected rays in a two-ray propagation model	Far-field regime	Beamforming	The received signal power is proportional to the square of the RIS area N^2 and inversely proportional to the square sum of the distances between the Tx and the RIS and the RIS and the Rx $1/(d_1+d_2)^2$
[92]	The physics and the EM nature of the RIS	Far and near field regime	Beamforming and broadcasting	The received signal power is proportional to the square of the RIS area and inversely proportional to the square product $1/d_1^2 d_2^2$ of the distances between transmitter and RIS and between RIS and receiver
[40]	Physical optics techniques and Antenna Theory	Far-field regime	Beamforming	The received signal power is proportional to the square of the RIS area and inversely proportional to the square product $1/(d_1 d_2)^2$ of the distances between transmitter and RIS and between RIS and receiver
[41]	The Huygens-Fresnel concept and generalized scalar diffraction theory	Far and near field regime	Anomalous mirrors and scatterers	RISs act like anomalous mirrors in the short distance domain while they behave as scatterers in the long-distance regime.
[42]	The Fresnel zone decomposition	Far and near field regime	Anomalous mirrors and scatterers	The RIS can be seen as a zero, one, or two-dimensional object, depending on its size and distance, and its radiated power exhibits a dependency with the fourth, third, or second power of the distance, accordingly.
[44]	Metallic reflectors using measurements, analytical expressions, and ray-tracing simulations	Near field regime	Anomalous mirror	Over the same link distance, the reflected received power is the same as the LoS free space received power for millimetre wave communications

RISs Versus Relay Networks and Random Phase Surfaces

We first present the following unique advantages of RIS-assisted wireless communications:

- **Densely Deployed and Sustainable Operation:**

If RISs are formed of smart metasurfaces, there are a lot of subwavelength unit cells in them. Such sub-wavelength heavy installations of small sub-wavelength dispersing devices are not typically used in radio communications, where MC among the reflecting elements is frequently prevented by design, by confirming that the scattering units are sufficiently far apart. This paves the way for the development of novel wave and propagation scenarios that may have an impact on wireless networks' ultimate performance limits, as well as the introduction of new scenarios in design in which wireless systems are built to be mutual coupling fully cognizant. RIS is easily applied and removed from a variety of surfaces, including front of buildings, interior walls, and top ceilings. The RIS can be battery-free and remotely powered thanks to RF-based energy harvesting, which eliminates the need for active equipments that require signal processing methods and power consumption.

- **New Signal Processing is not required for RIS-aided Communication:**
  The semi-passive feature of RISs opens new possibilities for re-defining communication, allowing data to be transferred without the use of EM waves, instead of reprocessing existing EM signals. This may be extremely useful in terms of minimizing EM pollution and lowering human EM exposure, which is often raised by deploying more network equipment and utilizing more spectra. This might be crucial for the effective installations of wireless technology in areas that are vulnerable to EM fields (e.g., in hospitals).

- **Highly Focusing Capabilities:**
  This high focusing capability could be used for a variety of purposes, including firstly, it enables interference-free communication in densely populated areas, secondly, enabling accurate radio identifications of users and environment modelling, and lastly, fill the batteries of limited power equipment by means of transfer the power wirelessly. The intelligent wireless wall (IWW) is a real-world example of this high focusing characteristic. The IWW consists of a RIS that does beam steering and beamforming, as well as machine learning algorithms that can accurately and automatically identify human activity [49].

- **Flexible Reconfiguration and Enhanced Capacity:**
  The RIS may be used to configure the wireless channel to provide a larger link capacity while consuming less power for point-to-point communications. When the RIS is used, interference reduction becomes more effective, resulting in improved signal performance for end users at the cell's edge. Scattering components in multi-user cellular networks can be separated and shared to optimise data transfer for multiple users. As a consequence, the RIS-assisted wireless network may be able to improve QoS provisioning as well as sum-rate performance or max-min fairness amongst users.

- **Investigating of New Wireless Application:**
  The RIS's advancement is likely to open the door for new and exciting research avenues. The RIS, for example, was recently presented as a unique technique for avoiding wireless eavesdropping assaults by regulating the transfer at the source and the optimized reflections at the RIS at the same time. The achievable secrecy rate is greatly enhanced by deploying the RISs close to the legitimate or eavesdropping user and appropriately configuring the RIS passive beamforming to raise or lower the achievable rate of the legitimate or eavesdropping user [50]. Despite the said feature in RIS-aided secrecy communication, the channel state information (CSI) is still needed between the TX and eavesdroppers as well as between the RIS and the eavesdropper. The challenge is obvious when the eavesdroppers intentionally continue to be covert, secret or hidden due to the fact that their CSI link cannot be estimated properly from their signal leakage, and thus requires new channel estimation methods and robust RIS beamforming taking into account the imperfect CSI of the eavesdropper [51]. Furthermore, in large-scale secrecy wireless communication networks with thousands of users whether legitimate or eavesdropper as well as highly dense RIS deployments, RIS is a key to increase the network security throughput and enhance the physical layer security for future 6G wireless modern systems where $1000\times$, as per Fig. 1.1 , increase in the data rates yielding a target of 1 Terabit/sec is required. Consequently, meeting these challenges of channel estimations and robust RIS beamforming in 6G massive networks deserve further investigations. Many other developing research fields, including wireless power transfer, UAV communications, and mobile edge computing (MEC) take the advantages of RIS technology.

In order to assess the advantages of RISs technology, it should be compared with different types of relay networks and surfaces which are not coated with RIS. The SNR for RIS and decode and forward (DF) relay as per Fig. 2.7 can be represented as follows:

$$SNR_{RIS} = \frac{p}{BN_0}\left|h_d + G^{\top} w_{\theta} H\right|^2, \tag{2.2}$$

$$SNR_{DF} = \min\left(\frac{p_1 G}{\sigma_e^2}, \frac{p_1 h_d}{\sigma_e^2} + \frac{p_2 H}{\sigma_e^2}\right), \tag{2.3}$$

where, p is the transmit power, B is the bandwidth and N_0 is the noise power spectral density. Consequently, the spectral efficiency ζ can be calculated for RIS and relay supported network as follows:

$$\zeta_{RIS/DF} = \log_2\left(1 + SNR_{RIS/DF}\right). \tag{2.4}$$

Figure 2.7a shows a typical RIS-assisted wireless communication system model. An RIS controller is used to program the RIS reflecting elements. Furthermore, the controller communicates with the BS by another wireless signal in order for the BS to control the RIS reflections by creating a phase shift matrix w_{θ} that results from modifying huge cheap passive reflecting

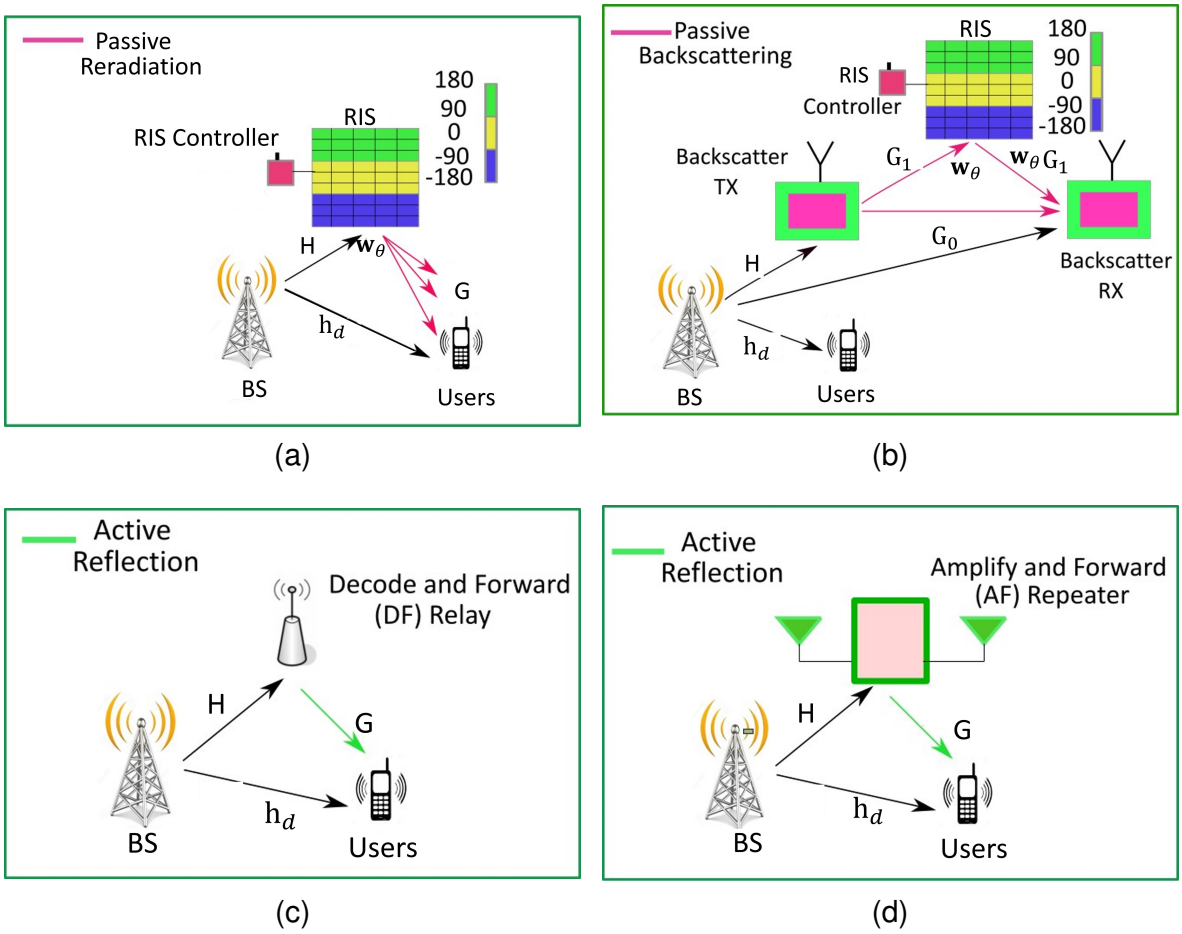

Figure 2.7: Comparison of different wireless systems. (a) RIS assisted wireless communication,(b) Wirless backscatter communication, (c) DF relay assited wireless communication, (d) AF repeater assisted wireless communication. H, h_d, and G represent the BS-RIS, BS-users, and RIS-users channels, respectively. Finaly, the RIS reflection coefficients is represented by $\mathbf{w}_\theta$

.

elements to configure the channel, and thus the concept of passive signal reflections is introduced in the research. As per Fig. 2.7d, amplify and forward (AF) repeater simply amplifies and sends the received RF signal ,including noise, to the users located in a dead spot by introducing amplifying channel coefficients. Repeaters are commonly employed in places where signal coverage is a problem and to extend the cell coverage however, it has a drawback of amplifying the noise as well which by return will degrade the received SINR. Repeaters work in the AF mode, whereas relays work in DF mode. In comparison to AF repeaters, DF relays, as per Fig. 2.7c, can provide superior noise immunity and intercell interference mitigation. The DF relay, on the other hand, necessitates a complex transceiver and might add to the transmission latency [266, 267]. In RIS-assisted and AF/DF relay-assisted communications, the receiver decodes the source information symbols, but in wireless backscatter communications, it seeks to decode the piggybacked information symbols from the strong interference signal. Backscatter, as per Fig. 2.7b, reflects an incoming RF signal while also modifying and modulating it

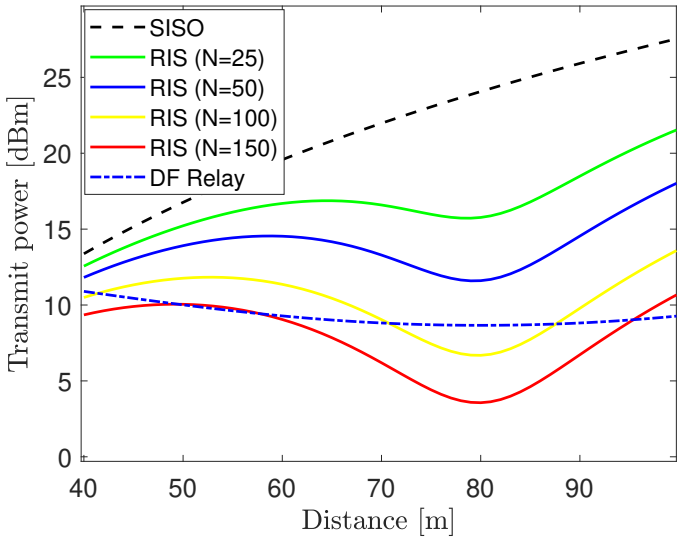

Figure 2.8: Transmit power to achieve the rate 6 bit/s/Hz [52]

for secondary transmission, or backscatter. There is no need to deploy and maintain separate RF sources because already-available RF sources are used, resulting in cost and power savings. Impedance mismatching is the fundamental concept behind altering and reflecting RF signals [56]. It uses the impedance of an antenna to encode data into previously existing waves, however it has low data rate transmission speeds and lacks data security. Massive backscatter communication [54] is a new idea that uses a programmable metasurface to alter the propagation environment of stray ambient waves. The metasurface's huge aperture and many degrees of freedom allow for exceptional signal control and, as a result, safe and high-speed data transmission. The proposed backscatter wireless communication strategy in which the transmitter depends on a programmable metasurface to modulate the propagation environment rather than a single or a few impedance-modulated dipole antennas open the door for significantly larger control over the wave. More interestingly, ambient backscatter communication (AmBC) was designed to solve communication and power consumption concerns in indoor and limited power IoT technologies. The authors in [55] presents a novel ambient backscatter communication approach in the frequency domain using ambient OFDM subcarriers in combination with the RIS. The higher performance in terms of bit error rate (BER) and data rate is demonstrated by analytical and numerical analyses.

The comparison between the RIS and relay assisted networks has been studied in the literature. The power transmission needed for achieving a certain rate has been studied in [52, 53] and a comparison between the RIS and the DF relay was investigated. Figure 2.8 Shows that the transmit power required in the RIS case reduces as the number of elements grows, and the distance to the DF relaying scenario is lowest when the receiver is either near to the transmitter or the RIS. When the distance is 80 (Mtrs), the RIS must have around or fewer than 100 elements to outperform DF relaying, demonstrating the RIS importance technology in future

wireless generations.

Measurable Metric Performance of RISs: The State-of-the Art

The authors in [57], with the help of RISs, has proposed new models for MIMO systems. The schemes of vertical bell labs layered space time (VBLAST) and Alamouti have been presented. Both schemes have shown improved BER performance gains and spectral efficiency and do not require significant changes to existing MIMO models, particularly in their receiver design, making them workable and viable options for future wireless communications. However, the authors did not consider a workable phase-shift setup, which take into considerations phase-dependent amplitude differences, in the model of the suggested schemes.

The authors in [58] determined the precise probability that a randomly located RIS may reflect for a certain transceiver using generalised rules of reflection. The analytical findings reveal that the length of a randomly positioned reflector has no effect on the possibility of reflecting. This approach, however, implies that all RISs have the same length, which does not reflect the real-world network situation. Furthermore, the authors focus just on reflection likelihood, with no assessment of how the large-scale RIS can increase transmission performance.

The researchers in [59–63] studied the outage probability of RIS-assisted wireless systems. The first authors proposed that The RIS could be used to increase the LoS likelihood for indoor mm-Wave setups. The authors derive a formula for the outage probability and then optimizes the RIS's deployment position to further reduce the outage probability while the second authors mentioned that for NLoS components, the outage performance is initially assessed and optimized in the slow fading scenario. The optimal outage probability declines with the size of the RIS when the LoS components are bigger than the NLoS components. The authors next describe the asymptotically ideal outage probability in the high SNR zone, showing that it decreases as the LoS component powers grow.

Unlike the authors in [59], who look at point-to-point mm-Wave communications, the authors in [61] consider a generalized mm-Wave downlink cellular network with random barriers and reflectors. According to the findings, only the placement of high-density reflectors can result in a considerable increase in mm-Wave coverage while reflected signals must travel greater distances than direct signals in low-density networks, and coverage probability does not differ from that of blockages. A restriction on this work is that the authors did not take into consideration the optimized deployment for the reflectors consequently, the performance coverage of the network was not promising.

The performance of outage probability in RIS-assisted vehicular communication networks is examined in [63]. Using series expansion and the central limit theorem, the authors derived the expression for outage probability. The RIS can greatly lower the probability of outages for vehicles in its area, according to numerical results. However, the authors in [62] investigated the outage probability of intelligent reflecting surface aided full duplex two-way communication

systems which characterizes the performance of overcoming transmitted data loss induced by extended deep fades. The authors computed the probability distribution of the cascaded end-to-end equivalent channel using an RIS beamformer of his choice. The number of reflecting components has a considerable influence on system reliability, according to both authors [62,63]. A shortcoming of their work is that the analysis was shown under the assumption of continuous amplitude and phase shifts.

For calculating the BER of the large intelligent surfaces (LIS)-assisted systems, the authors in [64] suggested an approximation and upper bound equation. Under the influence of Nakagami-m fading channels, the author looked at binary phase shift keying (BPSK) and M-quadrature amplitude modulation (QAM) modulations. For number of elements $N < 4$, the authors derived the exact distribution of the channel coefficient and used a Gaussian approximation for the in-phase and quadrature components because the exact calculation becomes too complicated for large values of N. However, the exact derivation for the BER was only for two and three elements and the scenario is more sophisticated when the number of elements is huge.

Unlike the authors in [64], the researchers in [65] established a broad mathematical model for calculating the symbol error probability (SEP) by determining the distribution of the received SNR, and the number of elements used in the simulations was in terms of hundred. On the other hand, the exact BER analysis of a two-user non-orthogonal multiple access (NOMA) system utilizing square QAM is discussed in [66]. Unlike previous work, there are no restrictions on the modulation order of QAM symbols for any user. In Raleigh fading channels, closed-form formulas for the BER of the successive interference cancellation (SIC) receiver are developed. The BER performance of an RIS-assisted NOMA downlink system is derived in closed form in [67].

In [68], the researchers examine an RIS-aided wireless system with and without a direct link between the AP and the user, using a finite number of RIS elements. The authors give a BER and average achievable rate (AAR) study of RIS-based systems, assuming maximum received power. The authors construct a closed-form BER approximation that allows forecasting asymptotic performance variation as SNRs and RIS elements increase. Simulation results show more accurate BERs than previous studies [65]. However, the performance of RIS-assisted wireless communications over Rician fading channels is discussed in [69]. For numerous performance metrics, such as outage probability, average SEP, and channel capacity, the authors construct new accurate closed-form approximations. Asymptotic equations for the outage probability at high SNR levels, as well as closed-form formulations for the system diversity order and coding gain are provided to give a better explanation of the system behaviour. The performance analysis in the previous works did not consider practical implementations like imperfect CSI.

The asymptotic optimality of achievable rate in a downlink RIS system is investigated in [70], which takes place in a real-world RIS environment with all of its limitations. Under practical reflection coefficients, a passive beamformer is proposed that can attain asymptotic optimal

performance by manipulating the incident wave characteristics. To enhance the feasible system sum-rate, a modulating mechanism that may be applied in a RIS without interacting with current users is provided, and its average symbol error rate is asymptotically determined. Simulation findings show that the proposed methods are in close agreement with their upper bounds in the presence of multiple RIS references. An obvious concern about this work that a RIS cannot coherently align with all users connected to BS via RIS.

In an RIS-assisted mm-Wave MIMO system, the authors in [71] define the RIS's ideal phase shifts based on limited feedback from the mobile user to describe the possible data rate from the BS to the user. In addition to improving data throughput, simulation results demonstrate that by deploying the RIS with perfect CSI, the positioning and orientation error bounds can both be decreased while the authors in [72] show the way that RIS can be employed and optimized to boost the rank of the channel matrix, resulting in significant capacity improvements. Because the previous works make use of a perfect RIS with unlimited phase resolution, the capacity related study that arises has an undefined mismatch with practical systems. The authors in [73] produce an approximation of the feasible data rate and discuss performance deterioration when a practical RIS is implemented with constrained phase shifts.

The authors in [74] employ a basic receiver architecture to explore the deterioration of attainable rate and discuss the correlation design of equipment deficiencies as a function of the distance between reflective elements. The authors in [184] specified the spatial throughput of a single-cell multiuser system supported by numerous RISs that are randomly placed in the cell, in contrast to earlier works that concentrate on link-level performance optimization for RIS-aided wireless applications. When the number of RISs surpasses a specific value, the simulations show the analysis is correct, and the RIS-aided system outperforms the full-duplex relay-aided counterpart system in terms of spatial throughput. Furthermore, it is demonstrated that alternative deploying procedures for RISs and active relays should be used to maximize their respective throughput. It is discovered that when fewer RISs are deployed, each with more reflecting elements, the system spatial throughput increases, but at the cost of greater spatially varied user rates and this is met with the research article in [185] when the author deployed one RIS only consisting of 4096 elements to enhance the communication data rate for 50 users distributed randomly in a room of $13(\text{ Mtrs }) \times 14(\text{ Mtrs })$ and far from the RIS $16.5(\text{Mtrs})$.

The authors in [74] studied the hardware impairments and its impact on the performance data rate while in [185] the authors analyzed in his system model the effect of MC between the adjacent reflecting elements on the achievable data rate per each user as per Fig. 2.9 and then the authors represented the MC per RIS elements statistically as follows:

$$C_n = \sum_{i=1}^{N} C_{i,\theta}^{\sim} \frac{100^{\frac{-d_{n,i}}{\lambda}}}{\sum_{j=1}^{N} 100^{\frac{-d_{n,i}}{\lambda}}} \tag{2.5}$$

where $d_{n,i}$ is the distance between element n and element i, $C_{i,\theta}^{\sim}$ is the capacitance that we assign

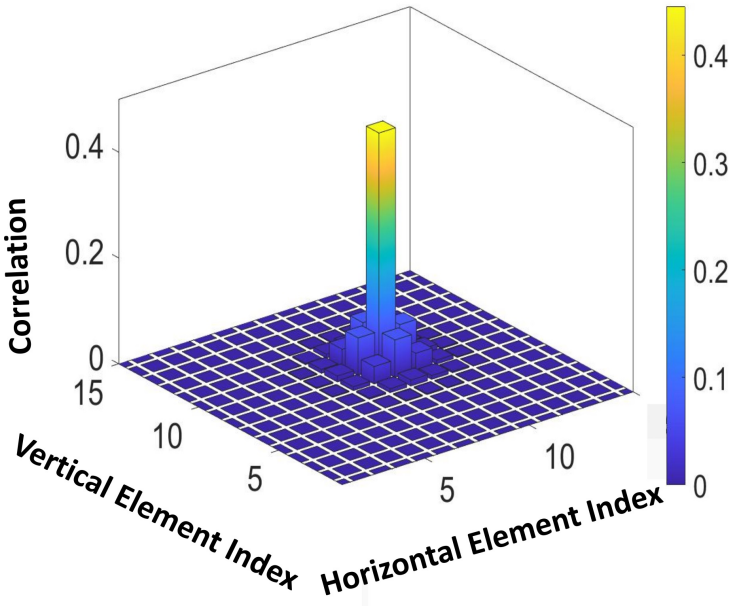

Figure 2.9: Actual capacitance of the RIS element at row 10 and column 10 is correlated with the intended capacitances of itself and the neighbouring elements

to element i and C_n is the actual capacitance of element n. Hence, we may expect that studying parameters like hardware impairments, MC, and discrete phase shifts in the wireless communication aided RIS will not only enhance the system performance in general but also establish a new era of communication research based on robust foundations that will end eventually with reliable technology.

The deployment of the RIS in [185] was near the user equipment's however, the authors in [186] studied the distributed and centralized deployments of the RIS in the wireless network. Under symmetric channel topology, it has been proved that centralised deployment outperforms scattered deployment in terms of achievable user rates. Nevertheless, the authors in [78] analyzed and compared two interesting scenarios in a SISO system, namely a finite number of big RISs and many finite-size RISs, to illustrate which implementation technique is more favourable. Using the deterministic equivalent (DE) approach, the authors calculate the coverage probability in closed form for both instances based on statistical CSI. The ideal coverage probability is then calculated. Numerical results show, among other things, that adding more surfaces beats the design strategy of adding more elements per surface.

In contrast to the early works, [91] presents a collaborative analytical and empirical investigation to introduce a new spectrum sharing solution for interior situations based on the use of a reconfigurable reflect-array in the wireless channel. The relevant signals for each transmission pair could be improved while interferences would be suppressed by managing the phase shift of each element on the reflect-array optimally. As a result, numerous wireless users in the same room can simultaneously access the same spectrum band without interfering with one another.

Consequently, network capacity can be significantly boosted. The smart reflect-array panels are hung on the walls in the indoor setting. Even though the reflected array does not buffer or process any incoming signals, it can alter the phase of the reflected wireless signal.

The authors in [79] studied the uplink rate in the presence of restrictions such as hardware flaws, inaccurate channel estimation, and interference caused by device-specific spatially correlated Rician fading. The authors have demonstrated that studies can reliably predict the performance of a LIS surface without the use of large simulations. Furthermore, it is shown that in a LIS-based system, a channel hardening occurs, and the authors also found the asymptotic bound for the uplink data rate and demonstrated that as the number of elements rises, hardware impairments, noise, and interference due to channel estimation errors and the NLoS path become insignificant. In comparison to conventional massive MIMO, the simulation results show that a large-scale RIS can achieve greater reliability in terms of capacity expectation and variation. We noticed that the number of elements that have been used in the simulations is huge in the order of thousands (10000) which raise our concern about the MC between the adjacent elements and the practical phase-shift model considerations. In LIS systems, the authors in [80] looked at the capacity impacts of hardware impairments (HWI). The authors created a general model of the HWI based on the distance between a considered point on the LIS and its centre, with the latter serving as a reference point in hardware design. To limit the negative impacts of hardware deficiencies, the analytical and simulation results suggest dividing a largescale RIS into a succession of smaller RIS units.

Similar to [80], the authors in [81] not only did investigate the effects of transceiver HWIs and RIS-HWIs on a general RIS-assisted MU-multiple-input-single-output (MISO) system with imperfect CSI and correlated Rayleigh fading, but also proposed a novel optimization methodology for reflecting beamforming matrices (RBM) optimization with low computational cost, which is particularly useful in RIS-assisted systems with many elements. The authors were able to get the channel's linear minimum mean-square error (MMSE) estimate with transceiver-HWIs and RIS-HWIs. Furthermore, using just large-scale data, the uplink attainable sum SE with maximal ratio combining (MRC) was calculated in closed form and performed high computationally efficient optimization about the RIS-RBM. In general, the authors presented an approach that produced analytical and tractable formulations that were superior to prior efforts, as demonstrated by simulation results.

Unlike other studies that focus on capacity, the paper in [82] looks into the feasibility of employing an RIS with a large number of scattering components for terminal location. The author goes into details about the effects of deployments with a single centralized LIS and numerous smaller distributed LISs constrained to the same total surface area. Splitting the LIS into 16 smaller LISs results in minor benefits, but it also increases the overheads for different small LISs to collaborate with one another.

Scatter-MIMO is a method for delivering MIMO spatial multiplexing gain that use a smart

surface to enhance scattering in the surroundings [11]. Smart surface connects to a wireless transmitter device, such as an active access point (AP), and re-radiates the same amount of power as any active AP, resulting in virtual passive APs. By employing virtual passive APs, Scatter-MIMO eliminates the synchronization, interference, and power requirements of traditional dispersed MIMO systems, allowing its smart surface to give spatial multiplexing gain at a cheap cost. According to the simulation results, Scatter-MIMO gives a median throughput gain of 2 over the active AP alone.

From the above-mentioned references and different illustrations, we would like to refer that the RIS aided wireless communication systems can be used as a reflector, receiver and transmitter [13] by modifying the phase shifts of the RIS's scattering units. The RIS's outgoing waves can generate different radiation paradigms that can convey data if these patterns can be identified and distinguished at the receiver. This is the basic design concept of spatial modulation, which is commonly implemented using programmable antennas [83, 182]. This is very similar to wireless backscatter communications, which use load modulation to adjust the antenna's reflection coefficients [183]. It's difficult to get a high rate for secondary users (SU) user in cognitive radio (CR) communication systems when there is a lot of cross-link interference with the primary users (PU) user. The authors in [86] used the recently developed RIS to solve this problem in their research. In particular, the authors investigate an RIS-assisted CR system, in which an RIS is used to help with spectrum sharing between a PU and an SU link. By combining SU transmit power and RIS reflect beamforming to optimise the feasible SU rate for a particular SINR target for the PU connection. The authors used the alternating optimization (AO) algorithm to solve the SU rate maximization problem via the joint transmit power control and RIS reflect beamforming. Simulation findings demonstrate that the RIS-assisted CR is effective for secondary transmissions, even in the tough scenario when the secondary transmitter is much closer to the PU.

RIS-enhanced energy detection is investigated in depth in [87] for single-user spectrum sensing, cooperative spectrum sensing, and diversity reception. For each example, a performance analysis is presented, as well as an analysis for the average probability of detection and false alarm. Monte Carlo simulations are used to verify the validation of his results. It is believed that RIS can significantly increase detection performance.

The authors in [88] investigate RIS concept in the UAV enabled communications to expand network coverage and improve communication reliability and spectral efficiency of IoT networks. The authors also show that RIS-assisted UAV communication systems may achieve ten times the capacity of traditional UAV communication systems in terms of achievable ergodic capacity. The impact of imperfect phase knowledge on system capacity and BER analysis for UAVs communications assisted by flying intelligent reflecting surfaces is examined in [89, 90]. The authors in [90] take into account a multi-layer UAV network with several hops, whereas [89] only addresses a single-hop case. The obtained results demonstrate the need of correct phase

estimation for RIS-based systems, especially for systems with a limited number of reflecting elements. The results are also demonstrating the importance of the number of elements in getting a reliable performance.

2.2.2 Optimization Techniques and Algorithms

The impact of multipath on the received signal is determined by how great or small the spread of time delays associated with the LoS and other multipath components are concerning the inverted signal bandwidth. The LoS and other multipath components are often non-resolvable if the channel delay spread is minimal, leading to the narrowband fading model. The LoS and all multipath components are often resolvable into several discrete components if the delay spread is large, resulting in the wideband fading model [5]. The reflected signals can be merged coherently at the intended receiver to boost the received signal strength or destructively at the non-intended receiver to limit interference by smartly altering the phase shifts of all scattering elements, as shown in Fig.2.7. The experimental demonstration and channel measurements in [92] support this, paving the road for more theoretical research and system optimization. In the following section, we go over the most common optimization formulations and solutions for RIS-assisted narrow and wideband wireless systems for single and multi-users.

Passive Beamforming Techniques

In this part, we will investigate the passive reflection optimization for RIS-assisted wireless communications. We will assume the knowledge of direct and indirect channels for the purpose of exposition however, the channel estimation will be discussed in section 2.3. The optimization problem can be expressed generally as follows:

$$\text{(OP)} \max_{\mathbb{Q}, w_\theta} \quad f(\mathbb{Q}, w_\theta) = \left| \left(G^\top w_\theta H + h_d \right) \mathbb{Q} \right|^2 \tag{2.6}$$

s.t:

$$(C1): \ \|\mathbb{Q}\|^2 \leq p \tag{2.6.1}$$

$$(C2): \ \phi_1, \ldots, \phi_N \in [0, 2\pi) \tag{2.6.2}$$

$$(C3): \ \gamma_1, \ldots, \gamma_N = 1 \tag{2.6.3}$$

Where $\mathbb{Q}$ is the transmit beamforming vector, w_θ is the RIS matrix with unit-modular constraint on each element and $f(\mathbb{Q}, w_\theta)$ denotes the objective function. We envision that the joint beamforming optimization problem is a non-convex problem due to the fact that both $\mathbb{Q}$ and w_θ are linked to each other. Furthermore, RIS elements need unit magnitude since, unlike relays, they do not amplify or decode then transmit a received signal. The necessity for suboptimal tractable rate optimization solutions is motivated by the non-convex unit modular constraints in

the above-mentioned optimization issue. Previous works on narrowband [93–106] and wideband [107–112] RIS-assisted wireless communication systems attempt to solve the non-convex problem where the main challenge includes the unit modulus constraint. Several techniques have been used in the literature to address this constraint.

- **Alternating Optimization Method:**
  The famous alternating optimization method is examined extensively in the literature. The method style of switching between the active transmit beamforming and passive reflection gives it an advantage to deal with the active transmit beamforming as a conventional problem when the passive beamforming is fixed however, under the given active beamforming the passive beamforming is still a non-trivial exercise to tackle including the unit modular constraint on each element of the RIS. There are possible ways have been shown in the literature to deal with this constraint. For example, the semidefinite relaxations (SDR) method is applied to relax the non-convex rank-one constraint to a standard convex semidefinite program (SDP). The SDP is used then to solve the formulated non-convex quadratically constrained quadratic program (QCQP) problem. However, the relaxed problem may not result to a rank one solution which by return require obtaining the eigenvalue decomposition by using circularly symmetric complex Gaussian (CSCG) distribution methods. The SDR with large number of Gaussian randomizations will lead eventually to approximation of $\pi/4$ of the optimal objective value [99]. Consequently, the SDR approach can only provide an approximation and solving an SDP program is computationally expensive for large number of antennas and RIS elements.

- **Iterative methods:**
  The concept of the iterative algorithms is to find a locally or near optimal solution for the objective problem at a reasonable computational complexity and acceptable run time. For example the low-complexity successive refinement algorithm [93,97] to determine the optimal discrete phase shifts of different elements at RIS one by one in an iterative way. Another technique based on the fixed point iteration and manifold optimization is investigated [98]. The authors in [106] used the projected gradient method (PGM) to jointly optimize the covariance transmitted matrix and the phases of the RIS elements. The PGM method achieved the same data rate as the AO method but with less number of iterations and lower computational complexity. The authors in [112] extended the work of [106] in the wideband MIMO communication. The paper in [108] proposed the low complexity power method to compute the dominant eigenvector of the reflection coefficient matrix to configure the RIS phases. In general, all these iterative methods have shown good system performance with acceptable computational complexity and reasonable run time.

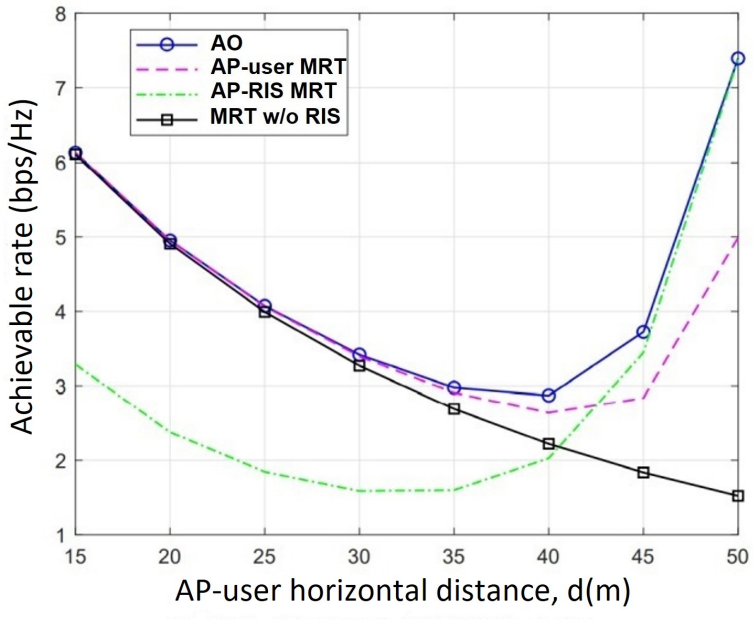

Figure 2.10: Achievable rate of RIS-aided MISO system versus AP-user horizontal distance, d [11, 152]

Active and Passive Beamforming: The State-of-The Art

The authors in [152] investigate an RIS-assisted point-to-point MISO wireless system in which one RIS is used to aid transmission from a multi-antenna AP to a single-antenna user. As a consequence, the user simultaneously receives both the signal directly from the AP and the signal reflected by the RIS. By combining the active transmitted beam at the AP with the passive reflected beam at the RIS using phase shifters, the authors aimed to optimize overall received signal power at the user. Assuming that the RIS contains global CSI, a centralised solution based on the SDR technique was proposed. Because the centralised approach includes excessive channel estimation and signal exchange overheads, a low complexity distributed technique is used, in which the AP and RIS modify the transmit beamforming and phase shifts in alternating fashion until convergence is achieved. When compared to benchmark systems, simulation results suggest that the proposed techniques can obtain high performance gains. Furthermore, it has been proven that the RIS can significantly improve link quality and coverage when compared to a traditional setup without the RIS. For example, Fig. 2.10 [3, 152] investigates four schemes 1) AO's joint transmit and passive beamforming design, 2) AP-user maximum ratio transmission (MRT) transmission, 3) AP-RIS MRT, and 4) MRT without RIS. When the user is near to the AP, the AP-user MRT system works similarly to the AO method, but suffers a considerable rate loss when the user is nearer to the RIS, as illustrated in Fig. 2.10. This is to be expected, given the AP-user direct link dominates the user received signal in the former scenario, but the RIS-user link dominates in the latter. Furthermore, the AP-RIS MRT system operates in the opposite manner when compared to the AP-user MRT counterpart. Consequently, as shown in

Fig. 2.10, if the transmit beamforming is not adequately built according to the whole channels, the achievable rate utilizing the RIS may be poorer than the conventional MRT without the RIS, for example, in the application of the AP-RIS MRT scheme for distance $d \leq 40(\text{Mtrs})$. This emphasises the significance of combining active and passive beamforming to achieve the best balance of direct transmission to the user and indirect transmission via RIS reflection in order to maximise the received signal strength at the user. For a desired SNR of 8 dB, the network coverage without the RIS is roughly 33 (Mtrs) , but when the suggested combined beamforming designs with an RIS are utilised, this value is increased to about 50(Mtrs) [152]. Another important result in [152] is that the user's receive power grows quadratically as N grows, by a factor of $\mathcal{O}\left(N^2\right)$. The transmit power can be reduced at the AP in the order of $1/N^2$ without sacrificing the receive SNR. This is due to the fact that the RIS catches an extra aperture gain of $\mathcal{O}(N)$ in the AP-RIS link in addition to the reflect beamforming gain of $\mathcal{O}(N)$ in the RIS-user link.

The power scaling in RIS and its comparison with massive MIMO (m-MIMO), are studied in the reference [153] in which the authors proved analytically that the gap between m-MIMO and RIS is enormous; an RIS requires a high number of reflecting elements to achieve SNRs equivalent to m-MIMO and by concluding such solid fact the authors disapproves of the myths and the wrong understanding of the RIS fundamental concepts.

A point-to-point MISO communication system with RIS assistance is also investigated in [154]. The beamformer at the AP and the RIS phase shifts are tuned simultaneously to improve spectral efficiency. The resultant non-convex optimization problem is handled with the help of two efficient methods that employ fixed-point iteration and manifold optimization approaches, respectively. The proposed techniques not only improve spectral efficiency but also reduce computational complexity as compared to the current state-of-the-art approach. The RIS-assisted MISO downlink model described above, as well as the heuristic AO described in [152, 154], provide a generic framework for the optimum design of RIS-assisted systems that may be used in a variety of network scenarios. Despite the fact that RISs with continuously phase shifts and maximum reflection magnitudes were explored, it was discovered that realistic RIS with discrete phase shifts and discrete reflection amplitudes satisfied the hardware criteria.

Different from the preceding sections, the authors in [155] look at an RIS-based wireless communication, in which an RIS with a limited figure of phase shifts at each element is used to enhance communication between a multi-antenna AP and many individual-antenna users. Particularly, the continuously transmitted precoder at the AP and the discrete phase shifts at the RIS were tuned together to lower transmit power at the AP while still achieving user SINR requirements. For single-user and multiuser instances, both optimum and successive refinement based suboptimal solutions were investigated. Furthermore, when the figure of reflecting elements gets asymptotically large, the performance degradation of RIS due to discrete phase shifts against the ideal scenario with continuous phase changes was investigated. Surprisingly, it was discovered that utilizing RIS with even 1-bit phase shifters can attain the same asymptotic squared power

increase as continuous phase shifts when only a constant power loss in dB is applied. In comparison to the situation without RIS, simulation results revealed that employing RIS with discrete phase shifts can save significant transmit power. Furthermore, it was shown that immediately quantizing the optimised continuous phase shifts to generate discrete phase shifts offers near-optimal performance in the single-user scenario, but that performance is significantly reduced in the multiuser case owing to substantial co-channel interference. Eventually, owing to the multiuser channel rank enhancement provided by the RIS's extra signal routes, it was proved that the zero forcing (ZF) precoder-based algorithm performs almost as well as the MMSE precoder-based method.

We looked at narrow-band communication systems with frequency-flat fading channels and a single and multiple antennas for the AP and user in the aforementioned works. Consequently, the wideband communication is important to explore in the literature. Passive RIS reflection optimization problems for MIMO systems with multiple antennas at both the AP and the user, as well as broadband OFDM systems with frequency-selective fading channels, must cater to multi-antenna channels and multi-path channels with different delays, making them more complicated and challenging to solve. The fundamental capacity limit of RIS-assisted point-to-point MIMO communication systems with multi-antenna transmitter and receiver is quantified in general by simultaneously optimising the RIS reflection coefficients and the MIMO transmit covariance matrix, which differs from previous MISO systems [156]. For frequency-flat channels, an alternate optimization approach was devised to discover a locally optimum solution by optimising one of the reflected coefficients or transmitted covariance matrix at a time while leaving the others constant, and the best possible solution were found in closed-form. Alternative, less difficult algorithms for asymptotically low and high SNR circumstances, as well as MISO and SIMO channels, were devised. Furthermore, for frequency-selective channels, a MIMO-OFDM system was investigated, in which a collection of reflection coefficients for all subcarriers must be designed. A novel AO approach used the convex relaxation technique to successively optimise a set of transmitting covariance matrices across multiple subcarriers or a common reflection coefficient for all subcarriers. Extensive numerical results reveal that the suggested algorithms outperform several benchmark methods with and without RIS in terms of rate performance. The performance gain improves as the number of elements increases.

The authors in [157] make the first efforts to investigate the wideband beamforming for RIS-assisted mm-Wave massive MIMO using a different design. For RIS-assisted mm-Wave hybrid MIMO systems, the authors present a geometric mean decomposition-based beamforming method. With the help of RIS, simulation results show that the proposed strategy can achieve good BER performance in a wideband hybrid MIMO system. To increase the system sum-rate, the authors [158] updated the source precoders and RIS phase shift matrix in the full-duplex MIMO two-way communication system. To maximise the system sum rate, the RIS phase shift matrix and source precoders are tuned jointly. The Arimoto-Blahut approach is used to divide

the non-convex optimization issue into three sub-problems that are tackled alternately. Closed-form solutions can be used to solve all the sub-problems quickly. RIS provides a performance boost equal to a relay operating at a transmission power of only 40 dBm to 35 dBm. This is related to the RIS's concern with double-fading. It's worth noting, though, that RIS does not need any transmission power.

All of the aforementioned research studies in [154, 156–158] rely on an ideal RIS with infinite phase resolution, i.e., each scattering element's phase shift may be entirely controlled. However, this is difficult to accomplish in practice, and devising precise phase control algorithms is similarly tough. Furthermore, for the RIS controller to provide precise phase control, full CSI is usually required. This implies that data sharing might be incredibly expensive, particularly for RIS that is self-sustaining due to wireless energy harvesting.

The authors in [159] presented a novel way to use the RIS to improve the attainable rate of an OFDM system. The authors developed a workable transmission protocol by assembling the RIS elements and calculating the joint channel for every group, with data transfer based on a shared RIS reflection coefficient. Then, based on the predicted channels under the recommended protocol with any defined grouping, the authors constructed a combined optimization problem of transmit power allocation and RIS reflection coefficients. The non-concave rate function was estimated utilising its concave lower limit based on the first-order taylor expansion in an efficient successive convex approximation (SCA)-based technique. The SCA-based approach guarantees that the RIS's combined reflection and transmission power optimization issue will converge to a stationary point, and it only has polynomial complexity over the number of elements and sub-carriers. The simulation results show that the improvements in the data rate is connected with the selection of the group ratio and the coherence time of the channel however, we have seen a performance degradation in the low SNR regime as the design parameters are adjusted based on the calculated CSI, the CSI obtained at low SNR is inaccurate, resulting in a larger performance degradation at both low and high grouping ratios so, we think that to maximize the obtainable rate, the grouping approach as well as the training sequence can be further improved. In addition, the author considers continuous phase and maximum amplitude equal one in the optimization schemes rather than proposing practical discrete phase shift.

To reduce complexity even more, the authors in [160] proposed a simpler approach called highest channel impulse response (CIR) maximisation, in which RIS phase changes are only aligned with the time-domain channel with the strongest path power. The authors propose a feasible transmission protocol for an RIS-enhanced OFDM system that conducts channel estimation and reflection optimization sequentially. The RIS proposes a unique reflection pattern to facilitate channel estimation at the AP based on received pilot signals from the user, for which the channel estimation error is calculated in closed-form under the unit-modulus constraint. After that, the reflection coefficients are optimised using the estimated CSI and a low-complexity approach based on the temporal domain's resolved strongest signal route. It is observed from Fig.

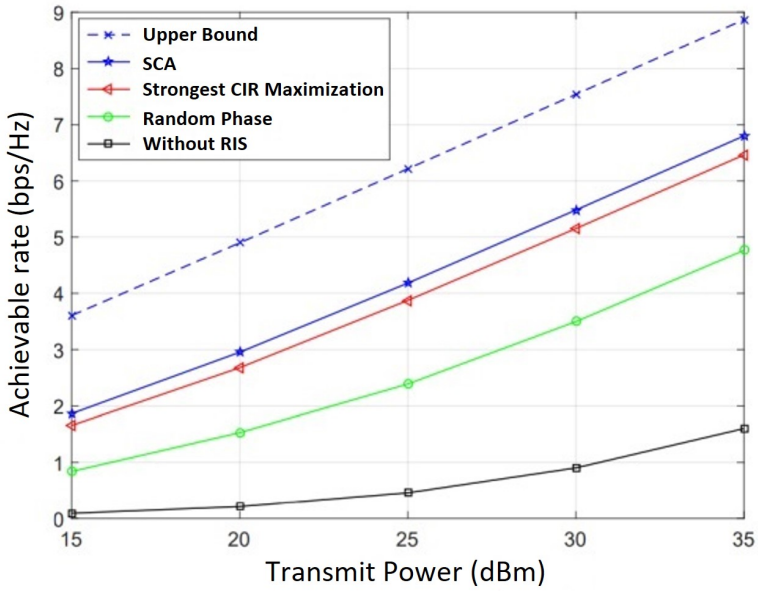

Figure 2.11: Achievable rate versus transmit power for RIS-aided OFDM system [160]

2.11 that in comparison to the OFDM system without RIS and the OFDM system with random RIS phase shifts and the related optimal transmit power allocation, the SCA-based algorithm suggested in [159] achieves a much higher rate. Furthermore, the most powerful CIR maximization algorithm provides similar results to the SCA-based method, making it a cost-effective and low-complexity option. The figure also sets a possible upper rate limit by proposing that various RIS reflection coefficients can be created ideally for various sub-carriers, resulting in a frequency-selective RIS reflection system. With the realistic frequency-flat RIS reflection, this upper rate limit greatly outperforms the SCA-based approach, and the rate difference expands as the number of sub-carriers rises. As a result of its passive functioning, RIS-aided OFDM systems have a basic weakness in the absence of frequency selectivity of the RIS reflection. Due to the necessity to cater to additional channels in both space and frequency, the RIS reflection design for rate increase is entailed in more general RIS-aided MIMO-OFDM systems where the user and AP are kitted out with more antennas. Additionally, numerous transmit covariance matrices at distinct sub-carriers must be optimised together with the RIS reflection. Consequently, the authors in [156] expanded the narrow-band MIMO situation and using the convex relaxation technique, the authors suggested an effective AO-based solution. Despite the absence of frequency selectivity, the results in [156] revealed that RIS is still useful in enhancing the systems rate of MIMO-OFDM with well-planned RIS reflection coefficients when compared to a typical system without considering RIS.

Different from the above researches, the authors in [185] investigated a wideband OFDM system supported by a practical RIS configuration with two binary states per each element as well as MC between adjacent elements. Using the dataset from [161], new channel estimation and configuration techniques have been proposed and analysed. Because of the trade-off

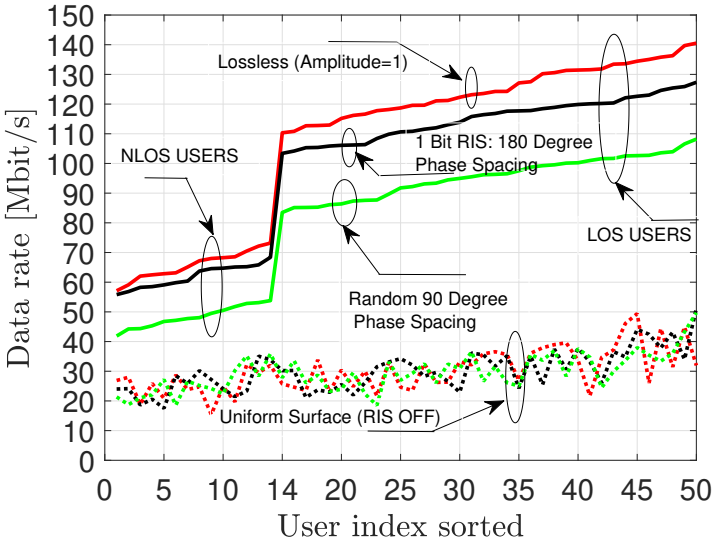

Figure 2.12: Achieved data rate using dataset in [161]

between multiple subcarriers, finding a good RIS configuration with reasonable complexity is difficult in OFDM systems.

In [160, 167], the strongest tap maximization (STM) approach is studied, to maximize the magnitude of the channel's greatest entry. This works well for LoS channels but not for NLoS channels [12] and extending it to the scenario where each RIS element has just two states is difficult. Instead, the authors aimed to optimize the total signal power received by creating a heuristic algorithm based on the iterative power method, which finds the dominating eigenvalue by iterating the computation until it converges. The simulation outcomes illustrate the achieved data rates by the 50 users in the dataset, as depicted in Fig. 2.12, organized in ascending order based on the data rates utilizing the proposed iterative power technique. Two benchmarks were employed: 1) selecting the best configuration from the N examined pilot transmission, and 2) deactivating all coefficients to model a uniform metal surface. Across all users, including those in NLoS conditions, the proposed technique consistently yields higher achievable rates. Notably, the initial 14 users among the 50 experience NLoS channels from the RIS, while users from 15 to 50 benefit from LoS links from the RIS, resulting in significantly higher data rates. This transition is evident from user 15 onwards in Fig. 2.12. In comparison to a uniform surface, the cumulative rate with an optimized RIS is 3.3 times greater, underscoring the substantial advantages of this technology even in intricate setups.

The authors in [242] studied the data rates achieved by the 50 users by setting different reflecting phase spacing per element considering the practical phase shift model. Figure 2.13 shows the importance of the RIS technology when compared with the uniform surfaces without considering the RIS configuration. The authors investigated the performance of three bits RIS to be compared with 1 bit and random phase. We noticed that the data rate increased when the phase levels assigned per each element are increased bearing in mind the equally spaces

Table 2.3: Summary of existing work in the field of RIS systems performance analysis

Ref.	Communication setup	RIS functionality	Criterion for measuring performance	Design Goal
[57]	MIMO	Transmitter	BER	Enhance the performance and boost the spectral efficiency
[58]	SISO in the presence of random objects	Reflector	Probability of being a reflector	If an item is coated in meta surfaces, the chance that it is a reflector is unaffected by its length, but it is strongly affected if Snell's law of reflection must be applied
[59]	SISO mm-Wave communications with blocked LoS	Reflector	Outage probability	Even when the links are impeded by barriers, a reflect-array deployment may provide reliable mm-Wave connections for indoor communications
[60]	MISO	Reflector	Outage Probability	The effects of several critical system factors on the ideal outage probability are analysed to uncover crucial design insights
[61]	SISO in the presence of both LoS signal blockages and reflectors	Reflector	Coverage probability	Improving the coverage in high-density networks
[64]	SISO under double Nakagami-m channels	Reflector	Bit error probability	Performance improvement
[65]	SISO under Rayleigh fading channel	Reflector and Transmitter	SEP	Increasing the received SNR
[67]	Multi-users NOMA system	Reflector	BER	Improving system performance and reliability
[70]	Multi-users MISO	Reflector	symbol error probability (SER)	Optimal SNR and increase Sum rate
[71]	mm-Wave MIMO	Reflector	Achievable Rate	High rate in low SNR
[72]	Point to point MIMO	Reflector	Achievable Rate	Rate by choosing proper RIS deployment and phases
[73]	Narrow band SISO	Reflector	Achievable data rate	Maximize data rate
[184]	Single BS-Multiusers	Reflector	Spatial throughput	Maximize spatial throughput for users
[185]	Single BS-Multiusers	Reflector	Achievable data rate	Sum Rate enhancement
[186]	Single AP- Multiuser	Reflector	Achievable user Rate	Superior rate performance of centralized over distributed
[78]	SISO	Reflector	Coverage Probability	Increasing the number of surfaces surpasses the design technique of increasing the number of elements per surface.
[79]	Uplink LIS-based large antenna-array system for single Antenna multiusers	Receiver	Ergodic Rate	Produce performance comparable to traditional massive MIMO
[80]	Uplink single user to signal processing unit	Receiver	Capacity	Reducing the impact of hardware impairments
[81]	MU-MISO	Reflector	Sum SE	Enhance sum SE
[82]	Single antenna radiating to LIS	Receiver	Coverage positioning	Distributed deployments have the ability to expand terminal placement coverage and deliver superior average Cramer–Rao lower bound (CRLB)s in all dimensions.
[162]	MISO	Reflector	Coverage probability and average throughput	Improve system coverage probability and throughput without consuming more energy.
[163]	MISO-OFDM	Reflector	Downlink rate	Downlink rate enhancement despite the lack of independent RIS phase control
[164]	Single user SISO	Reflector Array	Outage probability and the average SEP	The RIS-assisted system outperforms the AF relay system with fewer reflecting elements
[165]	Single source and two wireless sensor nodes	Reflector	average symbol error probability (ASER) and the outage probability	As the number of reflecting elements grows, the performance improves
[166]	RIS-assisted NOMA	Forward Relay	Outage probability and ergodic rate	Enhance energy efficiency compared to conventional cooperative communications.

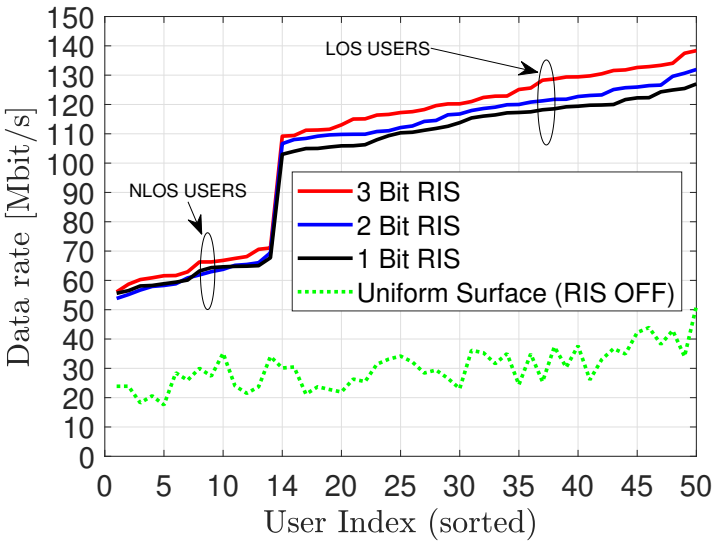

Figure 2.13: Data rates when considering different types of RIS and compared with the uniform surface (The RIS is OFF)

between the finite number of phases and the reason behind that is The reflective currents are out-of-phase with the element currents when the phase shift is approximately 180 or -180 degrees and so the electric field and current flow in the element are both reduced, resulting in least energy loss and maximum reflection amplitude. The effect of the amplitude response has been taken into account and show its impact on the gain of the data rate unlike many researchers who considered constant amplitude and ignore the related losses. Figures 2.14a and 2.14b show the impact of amplitude variations on the system data rate performance for three and one bits RIS. Therefore, considering the assumption of lossless amplitude in the literature gives promising results however, energy loss is unavoidable in practical hardware, hence, a practical phase shift model should be considered taking into account the losses.

Similar to [185], the authors in [168] investigated a wideband OFDM system for MISO MU, the authors first look at the dual-phase and amplitude squint effect of reflected signals before presenting a simplified RIS reflection model for wideband signals. Then, a wideband RIS enhanced MU MISO-OFDM system is examined. When using both continuous and discrete phase shifters, the transmit beamformer and RIS reflection are developed jointly to maximise the average sum-rate over all subcarriers. The original problem is turned into a multi-block variable problem that may be solved effectively using the block coordinate descent (BCD) approach by leveraging the relationship between sum-rate maximization and mean square error (MSE) minimization. In Both scenarios complexity and convergence are explored. When compared to the ideal RIS reflection model, simulation results demonstrate that the proposed technique may provide considerable average sum-rate augmentation, underscoring the importance of using the realistic model in wideband system design. However, the authors put the assumption that the channels were well known, but in practice, a channel estimating phase is required. Because the

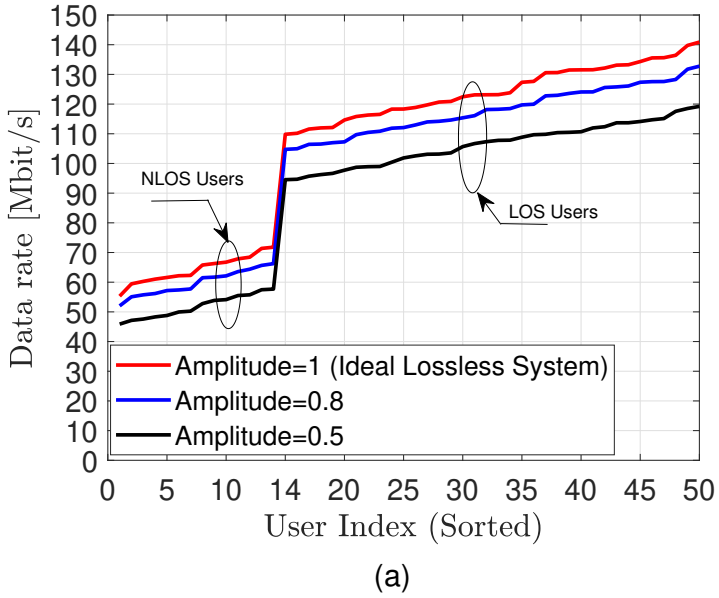

(a)

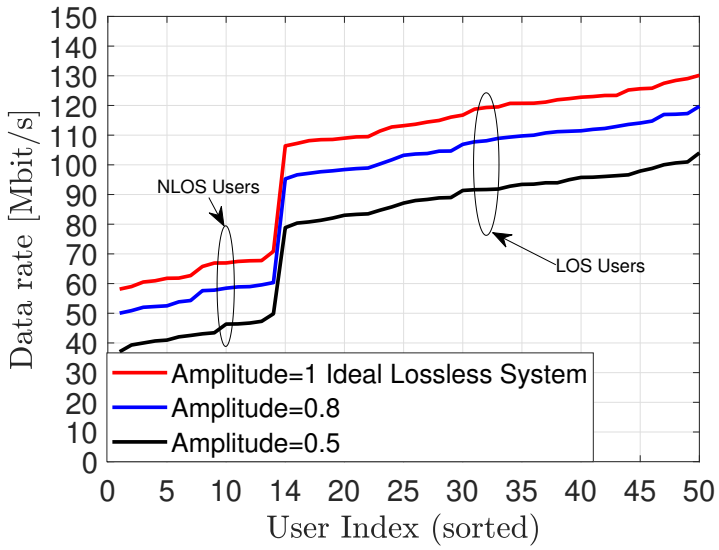

(b)

Figure 2.14: (a) 3-bits and (b) 1-bit RIS for different amplitude response

RIS is a passive device, the estimation must be done at the receiver which was not considered in addition to the proper employment of the RIS.

2.2.3 Discussions and Insightful Prospect for Section 2.2

- In summary of the performance analysis, we would like to refer that the bulk of the research papers presume that the CSI and discrete phase shifts are known at both transmitter and receiver [65]. As a result, more practical setups are needed to evaluate the effectiveness of implementing large-scale RIS cellular communications networks in practice. Furthermore, neither for indoor nor outdoor communication setups, the above-mentioned

literature pays little attention to user mobility. User mobility causes not just handoffs between RIS units, but also a geographical correlation in user distribution, which could have a significant impact on system performance. Consequently, incorporating various mobility models into performance will become a crucial study path in the future. Furthermore, the maximization of performance gain for a certain network structure problem involves a combined tuning of active transceivers and RIS passively scattering components. Passively reflected signals, which are intimately related with the active transceivers' control variables, can be thought of as the combined phase control of scattering components. Because the scattering objects in wireless environment scenarios are unpredictable and omnipresent, performance evaluation of RIS-assisted wireless systems is complicated, but it also generates new optimization challenges that demand creative methods to account for active-passive device communication [3, 12]. Table 2.3 is a summary of some of the work done in the performance system analysis considering the usage of the RIS as a reflector, receiver, and transmitter in addition to the design objectives. We believe that in order to construct genuinely widespread wireless networks that can provide continuous communication and good QoS to numerous users in such a challenging wireless environment, new and radical solutions are still required.

- In summary of the optimization techniques and algorithms, we have presented the different optimization techniques used in the literature for both narrow and wideband systems taking into consideration many communication systems parameters like capacity, rate, sum rate and SNR to study the performance and efficiency. Different system models were illustrated using single and multi-users under various channels and environments however, there are still huge subjects that need to be investigated which are not yet covered properly in the above research like the doppler shift and mobility, practical phase shift models, proper and fast channel estimations, and MC for the adjacent RIS elements. Table 2.4 summarizes the work of RIS reflection optimization studies based on the system settings analysis and optimization methodologies used.

2.3 Channel Estimation

2.3.1 Channel Estimation Protocol and Pilot Transmission

To effectively appreciate the performance advantages given by RIS, accurate CSI is necessary, which is a practical obstacle. The challenges can be summarized as follows:

- Aside from having significantly more RIS-induced channel coefficients than a conventional system without RIS, RIS channel estimation has a hurdle in that its cheap reflecting components lack active RF chains and hence are unable to broadcast pilot and training

Table 2.4: Summary of existing work of optimization techniques for narrow and wideband systems

Ref.	System Model	Algorithm	Algorithm Performance	Work Objective
[185]	Wideband MU SISO-OFDM	Power Method	Heuristic	Maximize Data Rate for 50 Users
[152]	Narrowband Single/MU MISO	AO and SDR	Near Optimal	In an RIS-assisted MU system, reduce the transmit power as much as possible
[154]	Narrowband Single User MISO	Fixed point iteration, manifold optimization	Locally Optimal	Maximize Spectral efficiency and lower computational complexity
[155]	Narrowband Single and MU MISO	ZF precoder and MMSE precoder based algorithms	Near Optimal	Combine the AP's continuous transmit precoding with the RIS's discrete reflect phase changes to reduce transmit power at the AP
[156]	Wideband Single User MIMO-OFDM	AO and convex relaxation	Locally Optimal	Capacity enhancement
[157]	Wideband Single user mm-Wave MIMO-OFDM	geometric mean decomposition (GMD) based on beamformer and combiner	Heuristic	Improve BER without sophisticated bit/power allocation
[158]	Narrowband Full-duplex MIMO	Arimoto-Blahut algorithm	Near Optimal	Maximize sum rate
[159]	Wideband Single user SISO-OFDM	SCA, AO	Near Optimal	To optimise the achievable rate, combine the transmit power allocation and the RIS passive array reflection coefficients
[160]	Wideband Single user SISO-OFDM	The strongest-CIR maximization (SCM) method	Near Optimal	Maximize the achievable date rate
[167]	Wideband Single user SIMO-OFDM	SDR, STM	Near Optimal	Improve the maximum achievable rate and data transfer latency
[168]	Wideband MU MISO-OFDM	Three-phase one-dimensional search method	Near Optimal	Determine the wideband MU-MISO-OFDM system's highest average sum-rate
[169]	Wideband Single user SISO-OFDM	AO	/	The necessity of considering practical RIS model for channel estimation
[170]	Wideband MU SISO-OFDM	Quadratic unconstrained binary optimization (QUBO) formulation	/	Assigning each RIS to a maximum of one user equipment (UE) using the allocation scheduling method for each UE
[171]	Wideband Single-user downlink OFDM	AO	High Quality Suboptimal	Optimize the transmission power allocation at the BS and the passive array reflection coefficients at the RIS to boost the user's downlink achievable rate
[172]	Wideband Multi-antenna for eavesdropper MIMO-OFDM	AO	Approximation and Suboptimal	Maximizing the sum secrecy rate
[173]	Wideband Multicell MU MISO OFDMA ultra-reliable low latency communications (URLLC)	Successive Convex Approximation and iterative rank maximization approach (IRMA)	Iterative Suboptimal	Under QoS constraints, maximise the weighted total throughput
[174]	Wideband RIS-Assisted UAV OFDMA	AO	Approximation	The employment of an RIS in UAV OFDMA transmission can boost the system's sum-rate dramatically
[175]	Wideband MU RIS assisted UAV	SCA with the Rate restriction penalty	Iterative Suboptimal	Maximize the lowest possible average rate for all users
[181]	Narrowband single user MISO	branch and bound (BnB)	Globally Optimal	Maximize spectral efficiency

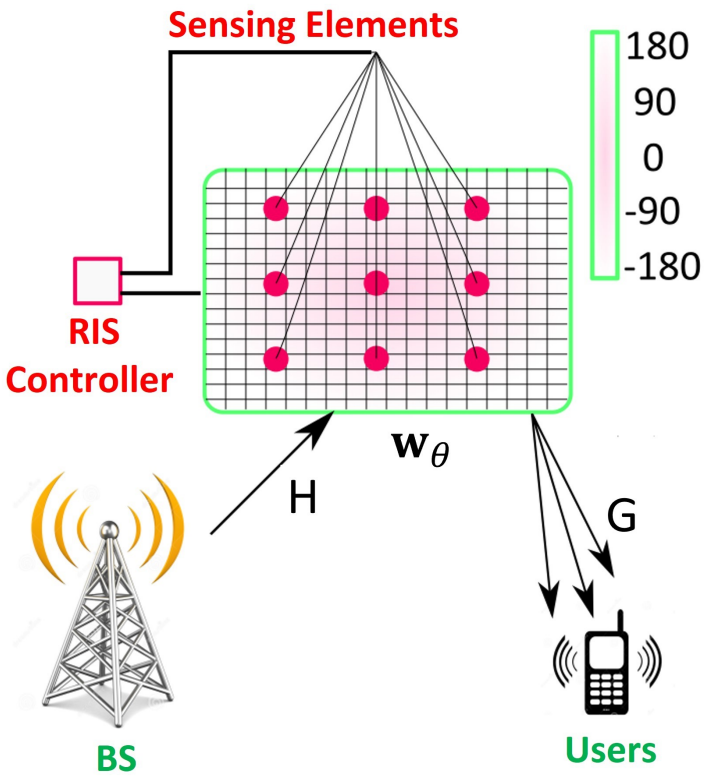

Figure 2.15: RIS assisted wireless communication with sensing elements (nearly passive RIS)

signals to facilitate channel estimate, in contrast to traditional systems' active BSs and user equipment.

- The RIS channel estimation is constructing high-dimensional channels from low-dimensional channels with approximated CSI.
- In broadband systems with frequency-selective fading channels, extra channel coefficients must be estimated due to the multi-path delay spread and subsequent convolution of the User-RIS and RIS-BS multi-path channels in each cascaded User-RIS-BS channel. Additionally, although the channels are frequency-selective, the RIS reflection coefficients are frequency-flat, making it impossible to create flexible various frequencies, such as separate sub-carriers in OFDM communications. In all SISO, MISO, MIMO, single and MU scenarios, forecasting the RIS channel for broadband frequency-selective fading channels is much more challenging than estimating the RIS channel for narrow-band flat-fading channels due to these characteristics [3].

To address the challenges, let us consider the downlink wideband SISO communication. Recall 2.1 but for the wideband system, The received signal can be represented as:

$$r = F\left(V^\top w_\theta + h_d\right) \odot x + e, \tag{2.7}$$

Where $F \in \mathbb{C}^{K\times K}$ is the DFT matrix and K is the number of subcarriers, $V = [v_1, v_2, \ldots, v_K]$ $\in \mathbb{C}^{N\times K}$ is the cascaded channels H and G to and from the RIS respectively, the configuration of the RIS is given by the diagonal matrix $w_\theta = \Gamma\Phi$ with $\Phi = \text{diag}\left(e^{-j\emptyset_1}, \ldots, e^{-j\emptyset_N}\right)$ and $\Gamma = \text{diag}(\gamma_1, \ldots, \gamma_N)$, $h_d = [h_{d1}, \ldots\ldots, h_{dK}] \in \mathbb{C}^{K\times 1}$ gathers all the uncontrollable channel components and $e \sim \mathcal{N}_{\mathbb{C}}\left(0, \sigma_e^2\right)$ is the receiver noise. Accordingly, the downlink CSI includes the number of channel coefficients to and from the RIS (i.e., H and G) equal to $(NK + NK \times N^{ant})$ where $N^{ant} = 1$ for single user antenna and the number of channel coefficients for the direct link h_d equal to $(N^{ant} \times K)$. The total number of coefficients is different for time division duplexing (TDD) and frequency division duplexing (FDD) systems. Furthermore, they are substantially more as compared to the conventional systems. It is sufficient to estimate the cascaded BS-RIS-User channel V for any RIS configuration ϕ. Suppose pilot signal x is transmitted on each of the K subcarriers. Let the RIS configuration ϕ_i where i is the index of the OFDM block. The received signal:

$$\bar{r}(i) = F_K V^\top w_\theta x + \bar{e}(i) \in \mathbb{C}^S, \tag{2.8}$$

Where F_K contains the K rows of F. There are KN unknown coefficients in V but we only get K observations from $\bar{r}(i)$. One possible way to get KN linearly independent observations, is to consider a sequence of N^{OFDM} OFDM blocks with different configurations $(\phi_1, \ldots, \phi_N)$. So, the joint received signal [113]:

$$\bar{r}[1], \ldots, \bar{r}[N] = F_K V^\top [w_{\theta 1}, \ldots, w_{\theta N}] x + \bar{e}[1], \ldots, \bar{e}[N]. \tag{2.9}$$

Let $\bar{\mathbf{r}} = \bar{r}[1], \ldots, \bar{r}[N]$, $\mathbf{w}_\theta = [w_{\theta 1}, \ldots, w_{\theta N}]$ and $\bar{\mathbf{e}} = \bar{e}[1], \ldots, \bar{e}[N]$. If $\mathbf{w}_\theta$ is invertible then we can apply the least square (LS) estimate to compute V as follows:

$$\underbrace{\frac{1}{x} F_K^{-1} \bar{\mathbf{r}} \mathbf{w}_\theta^{-1}}_{\substack{\text{Known} \\ \text{Signal}}} = \underbrace{V^\top}_{\substack{\text{Estimated} \\ \text{Composite} \\ \text{Channel}}} + \underbrace{\frac{1}{x} F_K^{-1} \bar{\mathbf{e}} \mathbf{w}_\theta^{-1}}_{\substack{\text{Noise} \\ \text{Signal}}}. \tag{2.10}$$

The challenge is when w_θ is non-invertible and the system is overdetermined to solve.

There are two basic methodologies for RIS channel estimates in the available literature, which are based on two alternative RIS configurations, depending on whether it is installed with sensing devices (receive RF chains as per Fig.2.15 or not, and are referred to as semi-passive RIS and completely passive RIS, respectively. For more details, refer to [114, 115]. One example for the full passive channel estimation method is by employing [116] the ON/OFF based RIS reflection pattern but it requires $N+1$ channel coefficients and substantial reflection power loss. An other workable method by grouping the neighbouring RIS elements into smaller RIS surfaces so, only the effective cascaded BS-RIS-User channel associated with each smaller surface needs

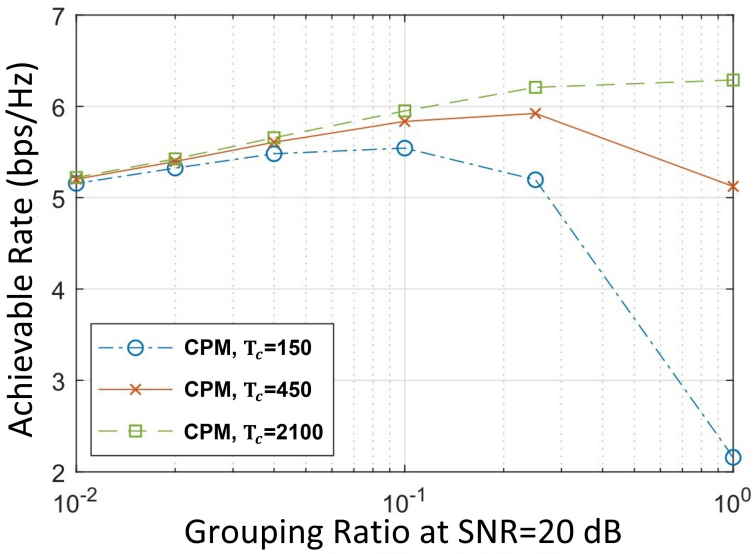

Figure 2.16: Achievable rate versus RIS Grouping [178]

to be estimated, hence significantly reducing the training overhead [107, 117].

In case of MIMO/MISO MU systems, the training overhead will be more as compared with single user SISO. To handle this, some RIS channel characteristics (such as spatial correlation, sparsity, and low rank) can be used to make the cascaded channel division easier and decrease the training overhead [118]. The authors in [119] used deep learning and searching algorithms to accelerate the training for channel estimation. The authors in [120] exploited the fact that all users share the same RIS-BS channel in the uplink to get minimum training overhead $N^{\text{user}} + N + \max\left(N^{\text{user}} - 1, \left\lceil \frac{(N^{\text{user}}-1)N}{N^{ant}} \right\rceil\right)$ where N^{user} is the number of active users and N^{ant} is the number of antennas at base station. Moreover, [121] utilized the redundancy of having more OFDM subcarriers than the number of delayed paths in designing OFDM-based pilot symbols to effectively estimate the channels of multiple users simultaneously. For instance, by exploiting the common BS-RIS channel and the LoS dominant RIS-User channels. It was demonstrated that $N^{OFDM} + 1$ OFDM symbols are required to estimate the cascaded channels of up to $\left\lceil \frac{(N+1)(K-L)}{N+L} \right\rceil + 1$ users at the same time. Where L is the number of multipath and K is the number of subcarriers.

2.3.2 Channel Estimation: The State-of- The Art

The authors in [176] examines the progression of the reflecting radio idea to RISs, as well as the RIS-assisted MISO communication model and how it differs from traditional multi-antenna communication models. For the design and study of RIS-assisted systems, a MMSE based channel estimate technique was proposed. The BS instructs the microcontroller to keep all RIS elements turned off throughout the channel estimation phase, and the BS estimates the direct channel for all users. The BS then sends a signal to the microcontroller to turn element n of the

RIS ON while leaving the other elements OFF, allowing the BS to begin estimating the cascaded channel. As a result, the microcontroller instructs the RIS's control circuit board in Fig. 2.1a to carry out the needed sequence, and so on. The MMSE estimating method is used to calculate the estimations. The BS then computes the optimal beamforming vector using the channel estimates and transmits it to the RIS microcontroller. Using the estimated channels (direct and cascaded), the phase shifts of the RIS are tuned by utilizing a gradient ascent algorithm.

Similar to [176] the authors in [177] describe a unique passive intelligent surface (PIS)-assisted energy transfer mechanism from a multi-antenna power beacon (PB) to a single-antenna energy harvesting user. A controlled LS Channel estimate protocol with binary reflection was proposed. This binary model is used because it accounts for the fact that a PIS lacks active components, forcing PB to estimate all the channel vectors on its own. The above-aforementioned works require at least $N+1$ pilot symbols for predicting the total $N+1$ channel coefficients in the system. Because only one element is turned on at a time, the ON/OFF-based RIS reflection setup suffers from considerable reflection power losses, resulting in a feeble reflected signal.

Different from the above research of work, the authors in [160, 178] developed an effective method of grouping adjacent RIS elements into a sub-surface, referred to as RIS element grouping; consequently, only the effective cascaded user RIS-BS channel connected with each sub-surface needs to be calculated, significantly decreasing the training overhead and simplifying RIS reflection configuration for transmitting data. However, it is crucial to mention that the channel coherence time has a significant impact on the appropriate grouping ratio for practical implementation. The upward and downward trend of the achievable data rate in Fig. 2.16 is an obvious example of the effect of the grouping ratio on the data rate at a high SNR regime.

Similar to [160, 178] the authors in [179, 180] studied the channel estimation for the broadband system but for MU. The authors in [179] proposed two efficient channel estimate algorithms for various channel configurations in an RIS-assisted multi-user broadband communication system using OFDMA. The sequential user channel estimation (SeUCE) scheme can sustain more users for channel estimation than the simultaneous user channel estimation (SiUCE) scheme by leveraging the advantage that all users have the same RIS-AP channel, but at the cost of increased channel estimation complexity and some decayed channel estimation performance. The authors in [180] describe a compressive sensing (CS)-based channel estimate (CE) solution for RIS-aided mm-Wave massive MIMO systems, whereby the angular channel sparsity of large-scale array at mm-Wave is used for improved CE with reduced pilot overhead. The authors develop pilot signals based on the previous knowing of the LoS-dominated transmitter-to-RIS channel as well as previous experience of the high-dimensional transmitter-to-receiver and RIS-to-receiver channels using CS techniques. To take advantage of the channel sparsity, a distributed orthogonal matching pursuit method is used. As a result, several writers [122–128] leverage RIS channel features (such as low-rank, sparsity, and spatial correlation) to simplify cascaded channel decomposition and decrease training overhead in RIS-assisted single-user

Table 2.5: Summary of existing work of channel estimation methods and techniques

Ref.	Communication Setup	Practical Phase shift model	RIS Passivity	Channel estimation protocol
[176]	MU MISO	Discrete	Full	Channel estimation procedure based on the MMSE
[131]	Point to Point MISO	Discrete	Full	LS CE protocol with binary-reflection
[183]	Single user RIS-enhanced OFDM	Continuous	Full	Interpolation based on discrete Fourier transform (DFT)/inverse discrete Fourier transform (IDFT) to estimate the channel
[182]	Single user RIS based OFDM	Discrete	Full	The RIS's on-and-off state control of reflecting elements
[179]	MU OFDMA Uplink	Continuous	Full	The sequential-user channel estimation
[180]	MU mm-Wave massive MIMO	Continuous	Full	CS-based CE solution
[122]	Single user mm-Wave MISO	Continuous	Full	CS-based channel estimation
[123]	Single-user-assisted massive MIMO system	Continuous	Full	Two-stage mixed channel estimate. The joint bilinear factorization and matrix completion (JBF-MC) method
[124]	Single-user RIS-assisted MIMO system	Continuous	Full	Tensor model with parallel factor (PARAFAC) that may be used to estimate the communication channels involved
[125]	Single-user RIS-enabled MIMO system	Continuous	Full	A bilinear adaptive vector approximate message passing (BADVAMP) method with a traditional training uplink technique
[126]	Single-user RIS-aided mm-Wave MIMO system	Continuous	Full	The channel parameters are successively estimated using an iterative reweighted technique
[127]	RIS assisted SISO	Continuous	Full	Low complexity channel information acquisition method using the channel sparsity and the position of the UE
[128]	Single-user MISO	Continuous	Full	Method for channel estimate based on compressed sensing
[129]	A RIS aided MU MIMO system	Continuous	Full	CS approaches are used to solve a sparse channel matrix recovery problem
[130]	An RIS aided MU MIMO system	Continuous	Full	Dual-link pilot transmission scheme
[131]	MU MIMO	Continuous	Full	Matrix-calibration based sparse matrix factorization
[132]	MU MISO	Continuous	Full	Method based on the PARAFAC decomposition
[133]	Single-user m-MIMO assisted RIS	Continuous	Full	Design of a hierarchical search codebook (low-complexity basis of beam training)
[134]	MU massive MIMO assisted RIS	Continuous	Full	Beam training-based cooperative channel estimation approach for RIS-assisted MIMO systems
[135]	Single-user RIS assisted MISO	Continuous	Full	deep learning (DL)-based detector, called (Deep RIS for channel estimates
[136]	MU mm-Wave massive MIMO	Continuous	Full	Deep learning bases scheme (twin convolution neural network (CNN))
[137–139]	Single-user OFDM based system	Continuous	Nearly passive	Deep Reinforcement Learning and CS Based RIS
[140]	Single user SISO	Discrete	Nearly Passive	Method for explicit channel estimation that uses AO

MIMO/MISO systems. On the other hand, the authors in [129–132] used the same channel properties to investigate the channel estimation in the MU MISO/MIMO systems.

To speed up the training process in passive RIS-aided MIMO and MISO systems, DL and hierarchical searching algorithms have been developed for channel estimation [133–136].

Different from the above-aforementioned works, the authors in [137–140] exploited some sensing elements interlaced with the passive RIS elements to provide RIS with sensing capabilities for the channel estimation process as per Fig. 2.15. Unlike the fully passive RIS channel estimation, the nearly passive RIS has two modes of operation. All the reflecting elements are kept OFF in the first mode or called sensing mode, moreover the sensing elements are powered up to receive pilot signals from the BS or users in the downlink or uplink for estimating their respective channels to RIS, whereas in the second mode or called reflection or transmission mode, the sensors are deactivated, and the RIS reflecting elements are turned on to reflect the data signals from the BS or users for improving downlink and uplink communication in both.

The authors in [137] presented a new deep reinforcement learning framework for estimating RIS reflection matrices by teaching the RIS how to anticipate optimum interaction matrices using sampling channel knowledge on its own. Unlike supervised learning-based methods, this technique does not require an initial dataset gathering step.

2.3.3 Discussions and Insightful Prospect for Section 2.3

- In summary of the above section, a detailed explanation for the various types of channel estimation in different wireless communication system environments was presented. Table 2.5 summarize to some extent good literature of channel estimation taking into consideration different communication parameters. The pilot transmission and channel estimation are not fully covered in the literature.

2.4 RIS Deployment

2.4.1 Why RIS Location is Important?

RIS works in full duplex (FD) mode with just passive reflection, avoiding amplification, processing noise and self-interference. These appealing features of RIS have prompted extensive research into using it to largely enhance the performance of wireless systems in a variety of scenarios, including MU NOMA, wireless power transfer (WPT), physical-layer security, multi-carrier communications, multi-antenna, and MEC [3, 6, 13]. In the existing literature, the RIS is usually deployed near the distributed users for the purpose of enhancement the local coverage which is completely different from that for the active relay, almost placed in the middle of the transmitter and receiver for balancing the SNRs of the two-hop links, that process and amplify the source signal before forwarding it to the receiver. Alternatively, the other deployment method is to position the RIS near the BS bearing in mind that both methods of deployments minimize the product distance path loss as per Fig. 2.17a and Fig. 2.17b. It's worth mentioning that RIS might be deployed much more widely across the network, due to its cheap price, to effectively modify signal propagation. However, this creates a considerably larger-scale de-

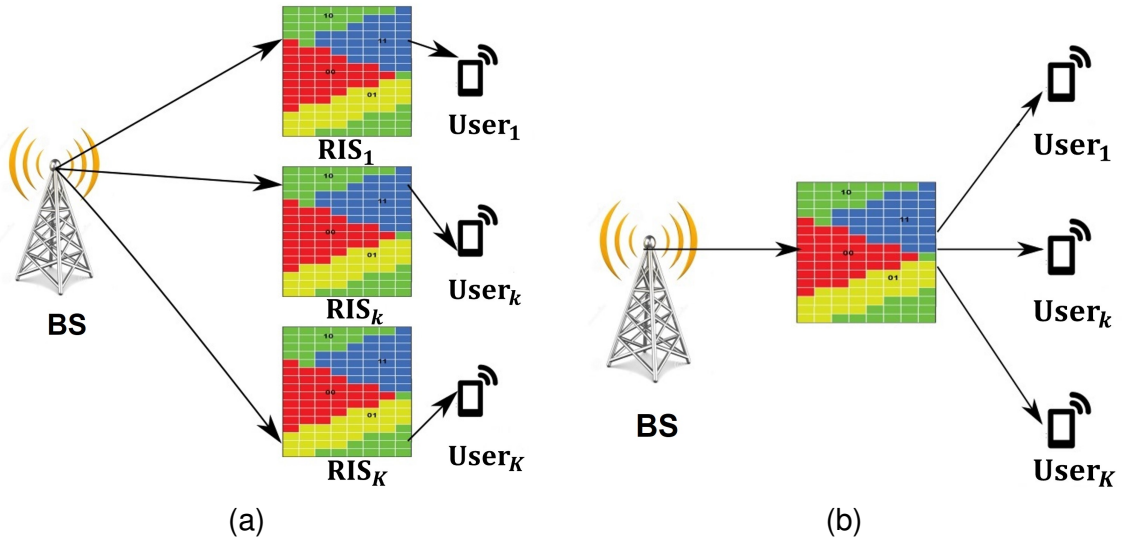

Figure 2.17: RIS deployment methods, (a) Centralized RIS deployment, (b) Distributed RIS deployment

ployment optimization challenge that is far more difficult to address in addition to the fact that because RIS is passive equipment, the strength of their reflected signals decays fast with distance; consequently, if RISs are placed far enough away, reciprocal interference is essentially non-existent, considerably simplifying their deployment design so, thanks to the RIS passivity.

2.4.2 RIS Deployment: The State-of- The Art

In this part of chapter 2, we look at the new RIS deployment problems in a variety of scenarios to get valuable insights into practical design, beamforming performance, and coverage.

The authors in [141] tackles the critical topic of how to place RISs in a wireless communication network for maximum performance. In terms of different communication performance metrics, the two traditional techniques of installing RIS at the BS or at distributed users are evaluated, and then suggest a novel hybrid RIS deployment approach that combines their cooperative benefits. An inter-RIS reflective link between both the BS-side RIS and each of the user-side RIS is included in the hybrid RIS installation proposal. When both direct and single-reflection links between the BS and its served users are significantly obstructed, the double-reflection links can be leveraged to provide alternative accessible LoS pathways between them. The double-reflection path may achieve a significantly larger asymptotic passive beamforming gain than the single-reflection channel given the same total number of reflecting elements N despite the fact that N increase of $\mathcal{O}\left(N^4\right)$ versus $\mathcal{O}\left(N^2\right)$. The simulation results show the superior performance of the proposed deployment over the conventional ones as per Fig. 2.17. Because all users may be served by at least one RIS, located whether user or BS side, under the hybrid RIS deployment, it demonstrates its increased efficacy in terms of network coverage.

The authors [142–145] employed the cooperative RIS method in their work to reap the ad-

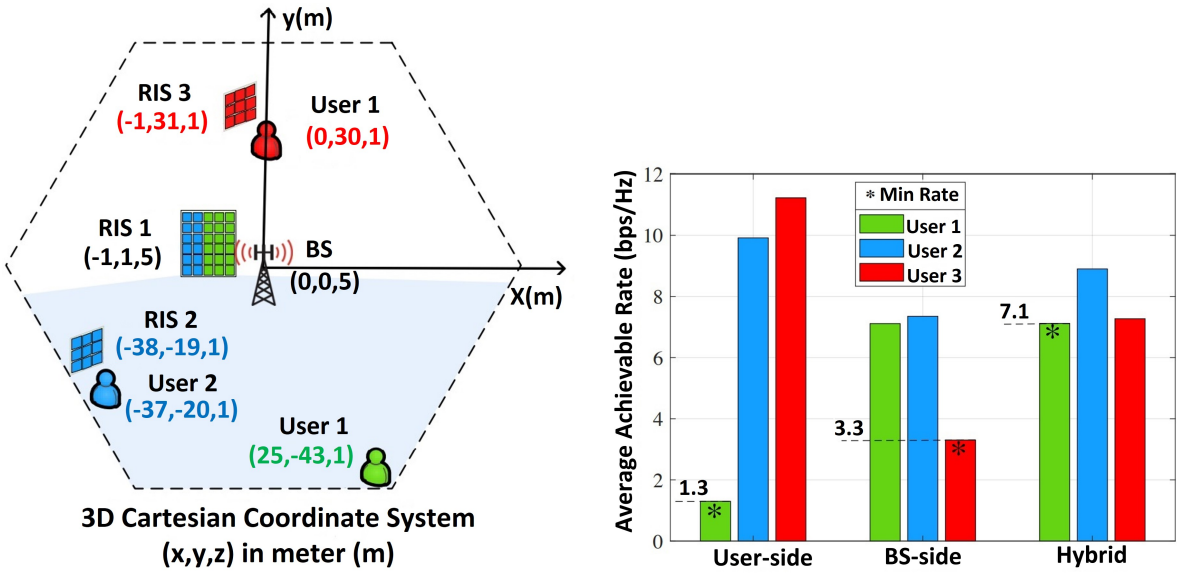

Figure 2.18: Three typical users' achievable rates, as well as their minimum rate, given various RIS deployment techniques [141], (a) System simulation setup,(b) Achievable rate versus deployment method

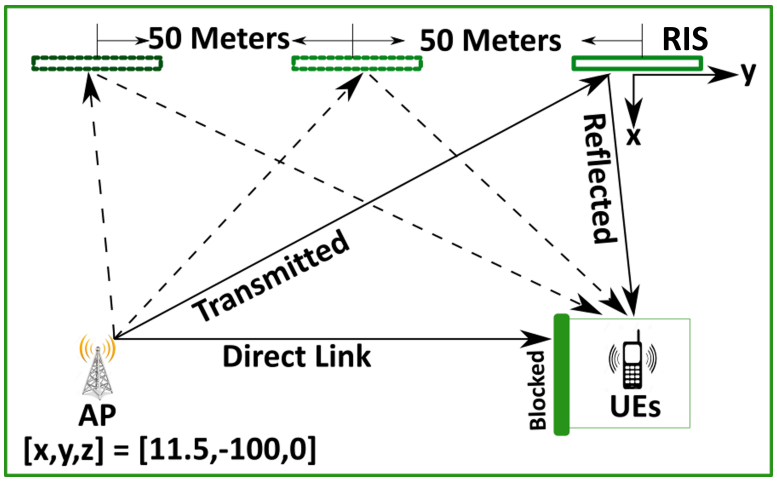

Figure 2.19: Simulation setup for different RIS deployments

vantages of placing more than one RIS near the users or BSs and to overcome the standalone RIS which suffers from gain loss if it is located far away from the base station or user equipment. In the case of standalone RIS, when situating the RIS near the user or AP it provides the highest SNR however, placing it in the midway between the user and the AP yields the lowest SNR meanwhile the two cooperative RIS case obtains a significant SNR boost When compared to the highest SNR in the single-RIS scenario.

The authors in [268] studied communication system from a single antenna source AP to many users equipments using an RIS with N reconfigurable controllable elements as per Fig. 2.19. The AP location is $[x,y,z] = [11.5,-100,0]$ while the users are placed in $[x,y,z] = [16,1,0]$

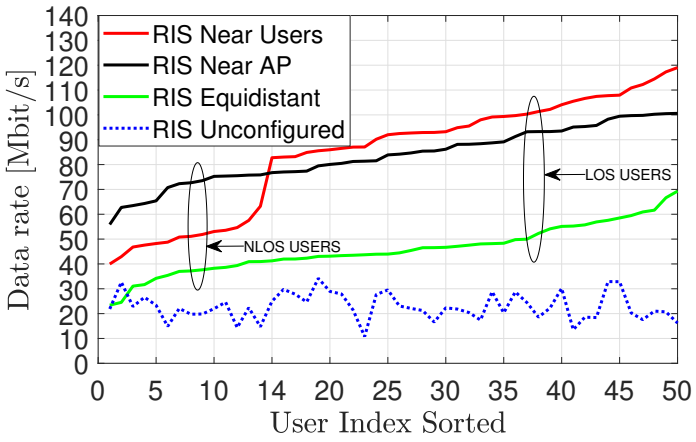

Figure 2.20: Achievable data rate for different RIS deployments

as per Fig. 2.19. The RIS is positioned in three locations to study the related data rate for all users. It is placed near the AP, near the users and in equidistant between the AP and the users. To achieve the least pathloss exponent that leads to the minimal pathloss under a given connection distance, it is practicable to put RIS under LoS conditions with AP and users. Despite a single RISs of order $\mathcal{O}\left(N^2\right)$ passive beamforming gain, the received signal strength at the users suffers from a twofold pathloss proportionate to the product of the user-RIS and RIS-AP connections' distances. The simulation Results , as per Fig. 2.20, revealed that the superior data rate for all users when placing the RIS either near the users or AP nevertheless, the data rate is degraded when the RIS is located in the middle. The reason behind that is when placing the RIS near the user or AP it yields the largest SNR while placing it around the middle between the user and AP leads to the smallest SNR.

The authors in [142] contribute to current research by proposing and assessing a wireless communication system with the double-RIS communication system. On the reasonable premise that the reflection channel from the first RIS to the second RIS is of rank one, a combined passive beamforming design for the two RISs was developed. A power increase of order $\mathcal{O}\left(N^4\right)$, may be achieved by deploying two cooperative RIS with a total of N components, which is superior than installing one ordinary RIS with a power gain of level $\mathcal{O}\left(N^2\right)$. Simulated findings demonstrate that establishing two cooperative RISs perform much better than deploying one RIS with the same total number of elements. The simulation shows that when two cooperative RISs are deployed, their performance is lower than when only one RIS is deployed. However, when the total number of elements is big, such as $N = 1600$, using two cooperatives' RISs instead of one can result in substantial performance gains. Another point to notice is that increasing the total number of elements by a factor of two, for example, from $N = 800$ to $N = 1600$, raises the received SNR of the benchmark case with one RIS by 6 dB, while increasing the received SNR of the two-RIS case with $N_1 = N_2 = N/2$ by 12 dB.

Similar to [142], the authors in [144] investigate effective channel estimation and passive

beamforming solutions for a single and MU communication system helped by a double-RISs. In [143] the authors consider a cooperative passive beamforming design for a double-RIS assisted MU MIMO that catches the inter-RIS channel's multiplication beamforming gain. The constructive received beamforming at the BS and the cooperative passive reflected beamforming at the two distributed RISs, positioned near the BS and users, respectively, are optimised in a general channel structure with both dual and single-reflection links to increase the minimum SINR of all users equipment. In the simulation, the maximum power $P = 30$ dBm was adopted to investigate the influence of channel ranking and spatially multiplexing gain on system performance for MU and found the superiority of the doubled RIS over the single in relation to achievable max-min rate data rate for the users.

The researchers in [145] proposed a wireless network consists of multiple RISs, which would help transmission between a multi-antenna BS and a large number of single-antenna cell-edge users. The authors aim to optimise the weighted sum rate of all cell-edge users by adjusting the BS's transmit beamforming and RIS's phase shifts together. For several schemes, the simulation results display the transmit power versus the weighted sum rate (WSR). To begin, all systems' WSR grows in lockstep with BS power, and when BS has a larger transmit power budget, the proposed multi-RIS with continuous phase shifts outperforms the single RIS with continuous phase shifts in terms of WSR. This is because, in multi-RIS systems, having the RIS close to the users minimises pathloss propagation, allowing the users data rate to increase due to the RIS passive beamforming gain. This exemplifies the value of using several RISs to increase system performance.

More inter-RIS reflections are created as the number of RISs in the User-AP connection grows, resulting in increased pathloss, backhaul cost, and complexity in the aforementioned activities. However, bigger multiplicative beamforming benefits may be obtained by performing cooperative passive beamforming across a large number of RISs.

The researchers in [146, 186] considered two workable RIS deployment methods that correspond to various effective channels between users and the AP: scattered deployment, in which the N elements form two RISs, each placed near one user, and centrally managed deployment, in which all of the N elements are deployed near the AP. The capacity and achievable rate regions for both deployment methods using various multiple-access algorithms are calculated considering the uplink multiple access channel (MAC). It is shown that in symmetric channel settings, the centrally controlled deployment beats the scattered deployment in terms of achievable user rates and capacity region. By exploiting the MAC broadcast duality, the results were extended to the downlink RIS-aided broadcast channel, where the performance advantage of centralized over distributed RIS deployment was also proven to be true. The advantages of centralized vs scattered RIS deployment is particularly apparent when the two users have asymmetric rate demands and channel conditions, according to numerical results. However, in practical scenarios, the assumption of the uplink and downlink channel duality for both RIS deployments may

change in terms of the LoS and the NLoS which it will by return impact performance gain of the system.

The uplink power control of an RIS-aided IoT network under the QoS limitations at each user is investigated in [147]. The objective is to reduce total user power by simultaneously optimizing RIS reflecting element phase shifts and receiving beamforming at the BS, while considering each user's unique SINR restriction. The authors used the environment diversity by installing several RISs to produce considerable improvements in energy efficiency through combined optimization of RIS phase shifts and reception beamforming. Specifically, each RIS is made up of N reflecting components that may independently reflect the incident signal with an adjustable phase shift. The simulation results reveal that when the number of RIS units rises from 1 to 8, the riemannian manifold based alternating optimization (RM-AO) algorithm saves about 4 dBm transmit power in the single-user situation. Furthermore, as the number of users grows, more transmission power can be conserved. Despite the above-mentioned efforts and advancements in link-level performance optimization for different RIS-aided wireless systems, the large-scale deployment of RISs in large size wireless networks require methods and tools to optimize the huge deployments of the multiple RIS units in the wireless network.

The authors in [148, 149, 184] offer an analytical framework for the RIS assisted hybrid network relied on stochastic geometry while the authors in [150, 151] rely on machine learning algorithms in resolving the problems joint RIS deployments, phase shift design, and power allocation in a MISO NOMA network to increase energy efficiency while considering the data needs of each individual user.

2.4.3 Discussions and Insightful Prospect for Section 2.4

Table 2.6 summarize the different RIS deployments for various communication system models for single and multiple users in addition to the purpose and the achievement of the RIS deployments. It was shown that different deployments methods can achieve tradeoff between performance improvements from one side and complexity/budget/training overhead/optimization from the other side. Moreover, the dimentional size (number of RIS elements) of RIS and the LoS path bewteen the transmitter and the RIS are essential parameters that should be taken into account in the RIS designs and deployments to ensure achieving performance gain and better channel conditions.

2.5 Future Research Directions

Various techniques, examined in this research, represent that RIS-assisted wireless networks can strongly improve the received signal power, boost the capacity and sum rate, expand network coverage, minimize transmit power, reduce interference, and provide better security layer and

Table 2.6: Summary of existing work of RIS deployment

Ref.	RIS Deployment method	Users	Achievement
[137]	Hybrid (distributed near the users and BS)	MU SISO	Minimum data rate significant improvement over the methods of placing the RIS near users or near the BS
[142]	Cooperative double RIS (near BS and user)	Single-user SISO	Improvement of the power gain of order $\mathcal{O}\left(N^4\right)$ instead of $\mathcal{O}\left(N^2\right)$
[143]	Cooperative double RIS (near BS and users)	MU MIMO	maximize the minimum SINR among all users
[144]	Cooperative double RIS (near BS and user)	Single-user SISO	The training overhead and channel estimate error are taken into consideration, resulting in significant rate improvement
[145]	Four numbers of RIS distributed uniformly at the cell edge of the base station vicinity	MU MISO	maximisation of the cell-edge users' weighted sum rate
[146, 186]	Both Distributed and Centralized	Two users SISO	the centralized deployment beats the distributed deployment in terms of possible user rates Under symmetric channel setups
[147]	Multiple RIS near the users	MU SIMO	By combining the phase shifts of RIS reflecting components with receiving beamforming at the BS, the overall user power is reduced
[148]	Hybrid active and passive OFDMA wireless network	MU	maximizes the hybrid network throughput

QoS supply to multiple users. However, from a communication aspect, the design of RIS-aided wireless communication has novel and unique issues, which are outlined below:

1. The passive reflections of all reflective elements at each RIS must be constructed in such a way that they enable coordinated signal focusing and interference elimination at the RIS's location. Meanwhile, whether or not an associated RIS is located near every user, the RIS passive reflections must be built in tandem with the BSs or users' transmissions in order to enhance their end-to-end communications across the RISs re-designed wireless channels.

2. Lacking RF chains makes it difficult to obtain the CSI between RIS and its feeding BSs or users, which is necessary for the RIS reflection optimization mentioned earlier. This is

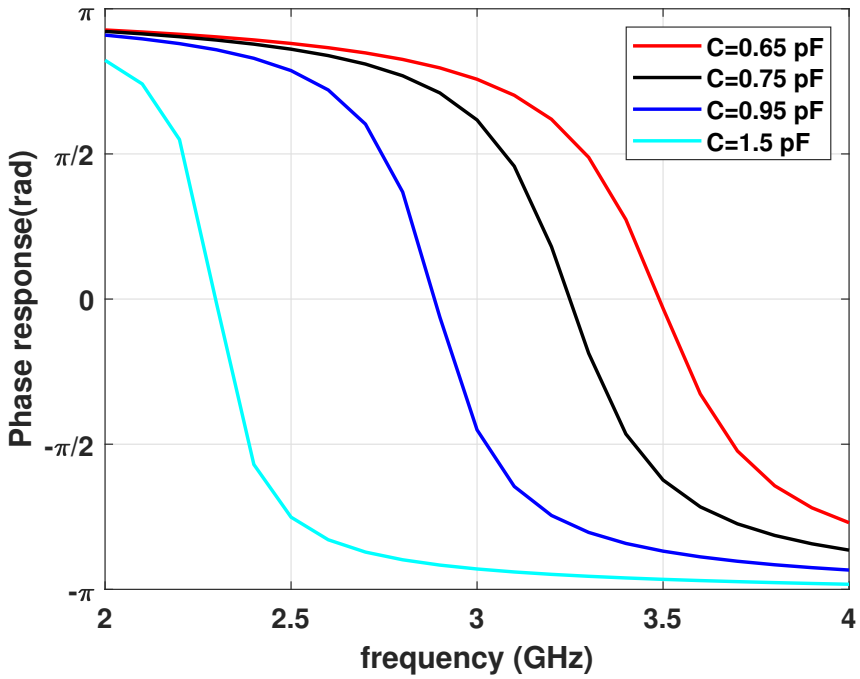

Figure 2.21: Frequency response adjustment when employing a varactor to change the effective capacitance

especially true given that RIS typically has a high percentage of reflecting elements and consequently related channel coefficients to calculate.

3. Due to their different array structures, passive versus active, operating mechanisms, and reflect versus transmit or receive, the best possible implementation method for RISs in wireless networks to achieve maximum network capacity is observed to be extremely different from that for traditional wireless networks with active BSs, APs, and relays, and thus needs to be thoroughly re-tested. In conclusion, integrating RISs into wireless networks effectively brings both new possibilities and problems, both of which need further exploration.

In this section, we will try to present some challenges of the RIS that we think that still need more studying and investigations.

- **Scaling Laws and Beyond Far-field Regime:**
  When narrowband capacity increased, the SNR with an RIS grows as $N^2 H w_\theta G$ at the time when N paths have the same propagation loss [12]. The quadratic SNR scaling does not imply that a higher SNR may be achieved than if the RIS were replaced with an equitable antenna array broadcasting at the same power level as the RIS. The SNR would be proportional to NG in the latter scenario. The SNR scaling can be factorized obtained by the RIS as $(NHw_\theta)(NG)$ to recognize the difference. The first term accounts for the

proportion of the transmitter's signal power reflected by the RIS, which is a relatively tiny amount even when N is big. As a result, the RIS can't get a higher SNR than NG. Consequently, the RIS must be large to be competitive with another enabling technology [224]. Far-field assumptions have been used in the majority of current research on RIS-enabled SRE. RISs, on the other hand, can be composed of a few square metres of geometrically large surfaces. This means that inappropriate application settings, such as interior environments, RISs can function in the near-field regime. The usage of large RISs allows for the creation of novel wireless networks that function in the near-field domain, which is not a common design assumption in wireless communications since the RIS elements incur substantial variations in propagation loss due to the different propagation distances and angles. More significantly, the near field allows the RIS to focus signals not only in a certain direction but also at a specific location within that direction, making it superior to a mirror [225]. This feature can also be exploited for enhanced localization [226]. The basic performance restrictions, design requirements, and possible uses and advantages of near-field transmissions in RIS-enabled SREs have received little attention thus far. The near-field regime is deserving of greater research because of the possible uses that may be unlocked, such as highly focused capabilities.

- **Mutual Coupling:**
  When the RIS sections on the substrate material are near together, separating them appropriately is challenging. This causes MC, in which one element's impedance is linked to the impedances of its neighbours. As a result, whereas Fig. 2.22 depicts how a RIS element acts in isolation, the frequency response will change based on the arrangement of the adjacent elements. The mutual impedance is determined using full-wave simulations, such as the method of moments, and is reliant on the physical characteristics of the components. A RIS constructed of patch or slot antennas effectively decouples the reflected wave's amplitude and phase, providing complete two-phase control. The trade-off between complexity and performance when the RIS is densified cannot be determined without adequate modelling of the mutual impedance. As a result, to capture the behaviour of RISs with closely spaced components, new modelling approaches that do not rely on the canonical minimum-scattering (CMS) assumption must be devised. Machine learning methods could be useful to solve the problem of system identification if accurate models are difficult to develop [12]. The MC will affect both algorithmic design from one side and communication and localization performance from the other side. The effect of MC on RIS-aided IoT-based applications is inevitable. The RIS is most beneficial when the number of its elements is large however when the surface is quite big (for example 4096 elements i.e., 2 Mtrs $\times$ 2 Mtrs), the MC between the adjacent elements will impact the actual response of the reflection coefficients of all elements which will end eventually in losing the reward of RIS technology in beamforming or steering the beam direction to-

wards the intended receiver. For example, if the RIS is deployed in LoS with the energy transmitters and receivers in addition to utilising their big aperture and excellent passive beamforming gains, the received power of neighbouring IoT devices can be greatly improved nevertheless, such power enhancement cannot be achieved when MC affecting the beamforming capability of the RIS.

- **Electromagnetic Interference (EMI):**
  Many researches are ignoring the EMI that is unavoidably present in any environment and instead focus only on the signals produced by the system [227]. The EMI may result from a range of natural, purposeful, or unintentional factors, such as man-made devices and background radiation from the environment. In general, every unregulated wireless transmission generates EMI [228]. The energy of the EMI waves that strike the RIS in the space in front of it is proportional to its area. When the EMI energy is radiated again by the RIS, it will reach the intended receiver resulting in degrading the end-to-end SNR of the wireless networks which are unaware of such interference effects. The SNR decline is attributed to the fact that such wireless networks/systems are simply designed to deliberately act against only the thermal noise generated by the receiver. As a result, the RIS must be aware of such damaging EMI effect by designing beamforming RIS asisted algorithms that take into consideration the uncontrollable EMI. For example, many authors [229] studied the potential of an RIS assisted wireless powered sensor networks (WPSN) where the RIS is deployed to help multiple IoT devices to enhance their energy harvesting and data transmission capabilities with intelligently adjustable phase shifts. Consequently, we will not get considerable improved throughput performance with the presence of EMI and MC effects.

- **Deployment of Large-scale Wireless Networks:**
  Due to the extensive deployment of reconfigurable metasurfaces on diverse objects in the future smart radio environment, wireless networks can benefit from a decentralized RIS system with individually programmable RIS units. The great bulk of previous research activities have focused on optimizing small scale networks, which are often networks consisting of a single RIS. This is a natural growth to start when evaluating the potential advantages of new technology. Furthermore, the evaluation of these fundamental conditions is dependent on modelling hypotheses that may or may not be realistic enough for the evaluation of sub-wavelength metamaterials. However, quantifying the performance constraints of SREs in large-scale installations is critical. This creates a difficult scenario for real-time allocation and optimization of different RISs in dynamic and heterogeneous networks to service diverse data streams. Individual transceivers can adjust their operating parameters in response to the channel state, which is determined by a stochastic model and can be predicted or estimated via a training procedure. Because of the RIS's reconfigurability, the radio environment becomes programmable and non-stationary. As a result, understanding the CSI via training becomes more challenging for individual transceivers. This suggests that the RIS-assisted networks, at least for the scattered RIS units, will be coordinated from a central location. The wireless environment becomes tractable and controlled as a result. To efficiently allocate and associate RIS units to service numerous users at the same time, a joint control method is necessary [13]. Consequently, deploying

large density RISs in a big industrial plant or even in a city's Centre to improve coverage probability or energy efficiency are becoming necessary in future wireless systems.

- **Sensing and Estimation of Energy-efficient Channels:**
  The RIS's supremacy is based on its ability to reconfigure the phase shift of each scattering element based on the channel circumstances from the transmitter to the receiver. This necessitates channel sensing and signal processing capabilities, which are difficult to come by without specific signal processing capacity at the passive scattering components. Channel estimation in an RIS-assisted system is often performed at one side of the communication process, such as the BS with superior computing capabilities or the receiver end. In channel estimation section 2.3, we overview the different existing RIS channel estimate techniques, For instance, the paper in [177], assumes that only one scattering element is active at any one time, with the rest inert. An element-by-element ON/OFF-based channel estimation technique is fundamentally too costly for a sizable RIS with massive scattering components. The RIS is underutilized because only a tiny percentage of the scattering components is active at any given moment. This reduces the precision of the channel estimate and causes a significant estimation delay. Despite the tremendous efforts exerted in [117, 121, 123, 269–271] in creating robust channel estimation algorithms to reduce the training overhead and enhancing the estimation accuracy by deviating from the ON/OFF technique and proposing other effective ones, we think that still feasible, efficient, and long-term channel estimation methods are needed to alleviate the pressure on requesting more energy consumption for exchange of information, signal processing, and computing. Consequently, the authors in [219–221] resolved the optimization problems by considering schemes without the need for computing the channel state information calculating the convex optimizations. For example, the authors in [219] optimizes beamforming without CSI at the BS and RIS by decreasing transmit power while maintaining a minimal SNR by proposing a particle swarm optimization (PSO) technique which is a stochastic optimization method inspired by some animal species' social behaviour based on updating the varying velocity and positions of the particles and then , for each particle, comparing the SNR at the user equipment with threshold to update its state and so on. While the researcher in [221] solved the optimization problem by proposing cosine similarity based low complexity algorithm to avoid the complex iterations and the huge overhead needed when using convex optimization techniques. Despite, the proposed algorithm is not powerful in comparison to convex, it is still very simple and does not require many iterations to adjust the phases of the RIS elements.

- **RIS Configuration Under Mobility:**
  Many characteristics of communication systems have been investigated under the idea that the channel is approximately piecewise time-invariant, allowing the use of linear time-

invariant (LTI) system theory, in the majority of the research employing the RIS to aid transmission however, the wireless channels are time-variant because of the mobility of the transmitter/receiver. The authors in [12, 222, 223] revealed the importance of using the RIS in reducing the delay spread and eliminating additional Doppler spread. However, the results in [222] were based on hypothetical RISs which create specular reflections with a single and very large conducting elements. While in [223] the inclusion of statistical channel model that accounts for atmospheric effects and line of sight outage were not considered in the system model and optimization of the RIS assisted low earth orbit (LEO) satellite communications. Consequently, the literature is still lacking to be enriched with practical communication models that take into consideration real and practical assumptions and parameters.

In the above-mentioned points, we tried to summarize some challenges that have been noticed while preparing this survey and the purpose of referring to them is to ensure that the research is still in its infancy and herculean efforts are required to establish strong foundation research to create strong enabling RIS technologies for beyond 5G and 6G wireless standards so, this chapter suggests some study directions for future investigation based on the existing literature review and the thorough system analysis of the present volume of researches.

- **Machine Learning for Passive Beamforming:**
  Machine learning techniques, rather than the AO techniques often used in the literature, may be more appealing to the RIS in terms of achieving flexible and light-weight phase management dependent on locally obtained radio environment data. This might reduce the quantity of data shared between the RIS and active transceivers [13, 129, 130, 142–144].

- **mm-Wave and THz Communications:**
  mm-Wave communications cannot give gigabit-per-second data rates in the future, enabling rate-demanding wireless applications (augmented/virtual reality (AR/VR) and online gaming, because of the large bandwidth available at mm-Wave frequencies (i.e., 30–300 GHz). However, because of the growing figure of operating antennas and RF chains, mm-Wave communications have significantly higher energy consumption and hardware costs [3]. Furthermore, mm-Wave communication channels are more prone to obstruction and suffer from greater propagation loss overall. When RISs are installed between base stations and end-users, the RIS's two key EM features of reflection and refraction may be leveraged to address the critical problem of dead spots by establishing LoS channels between the AP and the user equipment, allowing for high SE and data rates [211–213]. It is predicted that the RIS will be integrated with the beyond 5G, Fig. 2.22 , networks and the current massive MIMO and the mm-Wave and THz networks to enhance the network coverage and increase the capacity.

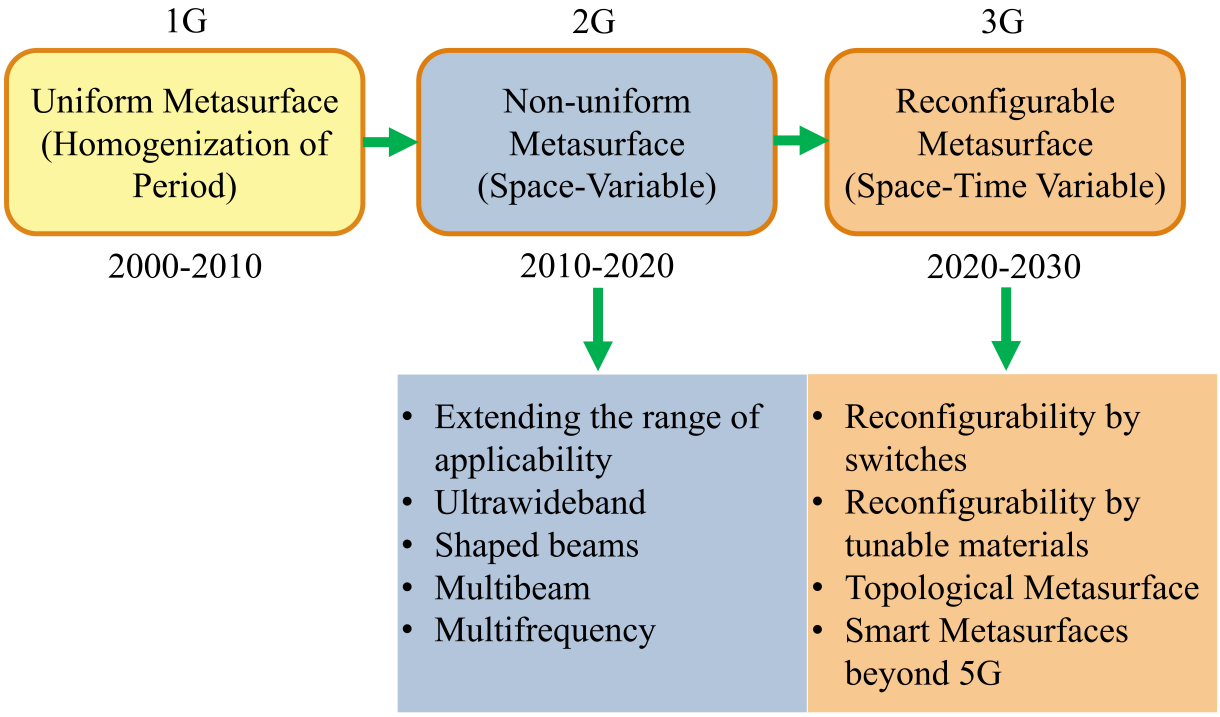

Figure 2.22: 3G Metasurfaces [6]

- **Multiple Access MEC:**
  The core premise of the MEC is that network congestion is minimized, and applications function better when applications and related processing activities are executed closer to consumers. The MEC technology is intended for use at cellular base stations and other edge nodes. It helps clients to deploy new applications and services in a flexible and timely manner, in addition, to assisting in offloading computing workloads from mobile devices to reduce latency and energy consumption. Some academics have been looking into the use of RISs in this setting recently [214–218] to enhance the computing performance gains and optimize the computing and communication operations.

- **Advanced Applications of RISs in Wireless Communications:**
  In the above discussions, the applications of RISs in wireless communications are focused on controlling the wireless channels and improving the wireless environment by reconfiguring the beam directions and beam coverages, in which the metasurfaces are not involved in the digital information modulations. Recently, digital coding and programmable metasurfaces have been presented [187–194], in which the metasurfaces are characterized digital states and controlled by FPGA. On one hand, the digital coding and programmable metasurfaces can manipulate the beam directions, beam coverages, number

of beams [187–189], polarization states [190], and the waveforms like cone beams [191] and orbital-angular-momentum vortex beams [192–194] in real time and in programmable way; and on the other hand, they can directly modulate the digital information. More recently, time-domain digital coding metasurfaces have been developed, which increase an additional degree of freedom to control the EM waves - the frequency spectral distributions [195, 196]. In this manner, the general space-time-coding digital metasurfaces have the capabilities in engineering both spatial beams and the frequency spectra simultaneously and independently, and directly modulating the digital information [197, 198]. Hence, the digital coding and programmable metasurfaces are also called as information metasurfaces [199–201], which have set up a broad link between the EM physical world and the digital world. The information metasurfaces can be regarded as advanced RISs, which will have deeper applications in wireless communications. For example, the information metasurfaces can be utilized to construct new architectures of the wireless communication systems, in which the digital-analog converters, mixers, RF devices, and antennas in the traditional transmitters are no longer required [202–208]; and the information metasurfaces can also be used to develop the EM information theory to combine the Shannon information theory and the Maxwell's equations, in which both EM information and bit-stream information are considered simultaneously [209, 210]. Based on the information metasurfaces, ambient backscatter communications were demonstrated by manipulating the commodity Wi-Fi signals, making it possible to realize secure wireless communications without any active radio components [206]. In the future, we expect that the information metasurfaces, or the advanced RISs, will push revolutionary advances of the wireless communications in basic theories, system levels and communication security for future wireless generations.

The literature is full of interesting and promising future research directions, however, this study concentrates on the conceptual and the techniques of analysis and optimization for RIS more than investigating each RIS assisted application individually.

2.6 Summary

This chapter provided a thorough overview of the RIS's architecture and uses in wireless communication networks. In the beginning, we have presented the RIS principles to throw new light on the RIS design and different types of control mechanisms that show the applied tuning methods used in various communication models. In addition to the channel correlation fading and practical pathloss models which characterize the signal and channel model in RIS-aided communications. Then, the optimization frameworks and performance analysis methodologies for RIS, are discussed. The methods have shown promises in increasing the spectral efficiency of wireless networks because of their capacity to modify the behaviours of the interacting EM waves

through intelligent manipulations of the reflections phase shifts under different wireless communication scenarios, including the SNR/data rate/secrecy rate maximization, transmit power minimization and EE/SE maximization. The chapter afterwards gives various relevant RIS deployments strategies and channel estimation algorithms to teach the RIS how to recognize the surrounding environments and enhance the system performance despite its passiveness. Finally, this work paves the way for some research limitations and future directions.

This chapter encompasses a wide range of research topics related to RIS and its uses in wireless communication, from its physical tuning, channel modelling, digital coding and information modulations to research issues from a wireless communication viewpoint, with a key goal on the optimization techniques and solution approaches for RIS-assisted wireless systems. The presented methods in the current research are still limited to certain assumptions and dropping some practical parameters and limitations. For example, the MC between the adjacent RIS elements, the impractical phase shift resolution models that describe the reflection coefficients of all RIS elements and the uncontrollable EM interference are vital, crucial and essential factors in limiting and degrading the RIS performance. In addition to the scaling laws in the near/far-field regime and the time-variant channel mobility which are still required to be explored thoroughly due to their significant effects on the performance of RIS-aided communication. The current solutions mentioned in the literature is depending mainly on the AO methods and grouping the elements to reduce the overhead and guarantee the convergence of the algorithms to locally optimal solutions nevertheless, the computational complexity and the elapsed run time are still substantially high. In the future work, by analyzing low complex and run time RIS-based algorithms using the machine learning methods for acceleration the phase management, the RIS-aided wireless systems are predicted to attain not only a higher performance gain but also it will establish for more refined and realistic communication models. Furthermore, the RIS must be aware of the MC, the uncontrollable electromagnetic interference and the practical phase shift models for the RIS coefficients to guarantee remarkable and optimum RIS performance outcome in their beamforming algorithms. Besides, the RISs provide LoS channels which can be exploited to enhance the coverage in the dead spot zones of the mm-Wave communication channels and the MEC computing performance gains in congested networks. However, the research of RIS-enhanced networks is still full of challenges and future directions not only from controlling the wireless channel and the SRE perspective but also when the RIS is involved in digital coding and information modulations which will push for revolutionary advances in security communication based RIS systems.

Chapter 3

Rate Optimization Using Low Complex Methods

With the help of a developing technology called RIS, it is possible to modify the propagation environment and boost the data rates of wireless communication networks. In this chapter, we optimized the phases of the RIS elements and performed a fair power allocation for each subcarrier over the full bandwidth in a SISO wideband system where the user and the AP are provided with a single antenna. The data rate or its equivalent channel power is maximized by proposing different low-complex algorithms. The STM and power methods are compared with the SDR method in terms of computational complexity and data rate performance. Runtime and complexity analysis of the suggested methods are computed and compared to reveal the actual time consumption and the required number of operations for each method. Simulation results show that with an optimized RIS, the sum rate is 2.5 times higher than with an unconfigured surface, demonstrating the RIS's tremendous advantages even in complex configurations. The data rate performance of the SDR method is higher than the power method and less than the STM method but with higher computational complexity, more than 6 million complex operations, and 50 minutes of runtime calculations compared with the other STM and power optimization methods.

3.1 Introduction

The use of RIS is a recent method that enhances the quality of wireless channels [6, 12, 240]. It enables the receiver to concentrate the signal due to the combined impact of reflections from all RIS elements and the direct LoS route between the transmitter and the receiver. This combination produces a focused beam in a specific direction [52]. Unlike wireless repeaters and relays, RISs have unique features such as configurability, no signal amplification requirements, and no need for complex processing, coding, and decoding techniques [53].

The literature has suggested a number of alternative optimization techniques for increasing

the data rates in RIS-assisted wireless communication systems, which aims to identify a nearly ideal solution with tolerable computational complexity and run time. Heuristic solutions, such as SDR [50,152,167,213,234–237], strongest signal path maximization in time domain [12,117] and successive convex approximations [107] are investigated by many authors in the literature. Applying the SDR and the successive convex approximation approaches require efficient optimization tools. Furthermore, the SDR needs Gaussian randomization methods to obtain the rank-one suboptimal solution. Considerable effort has been devoted to developing sophisticated algorithms that can identify high-quality solutions that are close to optimal. However, the computational complexity associated with these algorithms is often quite high, making them prohibitively expensive in practical settings where a large number of RIS elements are present. It is precisely in such situations that RIS is most valuable. [112, 239, 242].

3.1.1 Contribution and Organization of The chapter

The contributions of this chapter are highlighted as follows:

- We maximize the data rate of the SISO wideband system equipped with RIS surface and single antenna for both AP and user equipment. We formulate a joint optimization problem of the subcarriers power allocations and the phase shifts of the RIS elements. Then, we proposed an iterative power method to solve the non-convex problem resulting from the unit-modular constraint on each RIS element. It is noted that for large surfaces the reflection coefficients can be estimated by the column of the DFT matrix [232]. We used the DFT beamforming codebook to select an SNR maximizing configuration to be utilized in the proposed power method.

- To evaluate the performance of the power method in terms of the data rate and complexity computation, it is compared with the SDR method. The SDR approach handles the nonconvexunit-modulus constraint by transforming the passive beamforming vector into a rank-one and positive semidefinite matrix. The non-convex problem is transformed into a convex SDP problem by utilising the SDR technique, which may then be addressed by a variety of effective convex optimization tools. The SDR method shows a higher performance data rate than the power method but at the cost of increased computational complexity and runtime. However, it shows lower performance than the STM method. The STM chooses a configuration that is good for channel tap rather than a subcarrier, when there exits a stronger a LoS path.

- The goal of this article is to demonstrate that the heuristic approaches like power and STM methods show significantly less computational complexity than the famous SDR method and achieve comparable data rates as a state-of-the-art benchmark scheme. The performance of all the methods is validated by comparing them with the upper bound of the system.

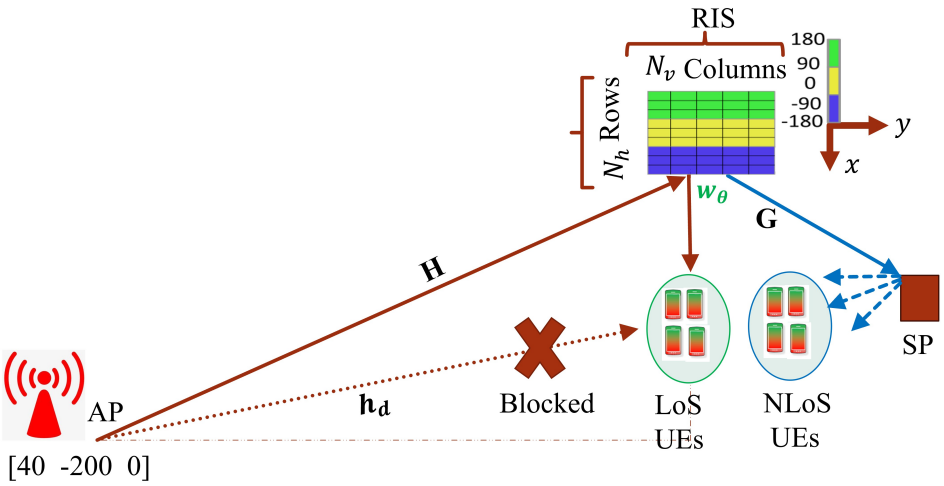

Figure 3.1: System setup illustration.

The rest of this chapter is organised as follows. The system and channel models are presented in Section 3.2, while Section 3.3 discusses the data rate optimization using different schems. Section 3.4 presents simulation results for single and MU and 3.5 gives summary for the chapter. Finally, Section **??** concludes this chapter.

3.2 System Model

A single antenna (transmitter) and a single user (receiver) are used in a SISO wideband system. As depicted in Fig. 3.1, a RIS with N reconfigurable elements is taken into consideration inside the coverage area of the transmitter and receiver. An OFDM is used for transmission. In the complex baseband domain, if $x(k)$ is the transmitted discrete-time signal, then the discrete-time received signal at the receiver can be written as [12]:

$$r[k] = \sum_{l=0}^{M-1} h_\theta[l]x[k-l] + e[k], \tag{3.1}$$

where, the wideband channel in the time-domain with the RIS configuration θ is represented as$\{h_\theta[l] : l = 0, \ldots\ldots, M-1\}$ and $e[k] \sim \mathcal{N}_\mathbb{C}\left(0, \sigma_e^2\right)$ is the receiver noise. The $h_\theta[l]$ is given by:

$$h_\theta[l] = h_d[l] + v_l^\top w_\theta, \tag{3.2}$$

where, $h_d[l]$ and $v_l \in \mathbb{C}^N$ are the AP-User uncontrollable direct channel and the AP-RIS-User controllable indirect channels via all RIS N elements respectively. The reflection coefficients of all elements is described by $w_\theta \in \mathbb{C}^N$. With $K > M$ subcarriers and a length of $M-1$ cyclic prefix, an OFDM transmission is taken into consideration. As a result, a time domain signal with a block of $K+M-1$ is transmitted to generate a block of OFDM signal with K of parallel

subcarriers by using the DFT:

$$\bar{r}[s] = \bar{h}_\theta[s]\bar{x}[s] + \bar{e}[s], \quad s = 0, \ldots, K-1. \tag{3.3}$$

The above equation (3.3) can be illustrated in vector form as follows:

$$\begin{bmatrix} \bar{r}[0] \\ \vdots \\ \bar{r}[K-1] \end{bmatrix} = \begin{bmatrix} \bar{h}_\theta[0] \\ \vdots \\ \bar{h}_\theta[K-1] \end{bmatrix} \odot \begin{bmatrix} \bar{x}[0] \\ \vdots \\ \bar{x}[K-1] \end{bmatrix} + \begin{bmatrix} \bar{e}[0] \\ \vdots \\ \bar{e}[K-1] \end{bmatrix}, \tag{3.4}$$

where, $\odot$ describes the hadamard product. The channel vector $\bar{h}_\theta$ can be realized a function of w_θ as per following:

$$\bar{h}_\theta = F \begin{bmatrix} h_d[0] + v_0^\top w_\theta \\ \vdots \\ h_d[M-1] + v_{M-1}^\top w_\theta \end{bmatrix} = F\left(h_d + V^\top w_\theta\right), \tag{3.5}$$

where, $h_d = [h_d[0], \ldots\ldots, h_d[M-1]]^\top$ and $V = [v_0, \ldots\ldots, v_{M-1}] \in \mathbb{C}^{N\times M}$ are the AP-User uncontrollable direct channel components and the AP-RIS-User controllable indirect propagation channels respectively. The channel parameters will be defined later, in the channel model. We assume that the channel models are known in the system. The $(s,k)th$ element of the DFT matrix $F \in \mathbb{C}^{K\times M}$ is $e^{-\frac{2\pi ks}{K}}$. The reflection coefficients of the RIS that accounts for the effective phase shifts $(\emptyset_1, \emptyset_2, \ldots, \emptyset_N) \in [-\pi, \pi)$ and amplitude coefficients $(\gamma_1, \gamma_2, \ldots, \gamma_N) \in [0,1]$ are included in the vector $w_\theta = [w_{\theta_1}, \ldots, w_{\theta_N}]^\top \in \mathbb{C}^{N\times 1}$. The sum data transmission rate across K subcarriers, given a specific RIS setup, assuming uniform power distribution and known channel at the receiving end, is expressed as:

$$\mathcal{R} = \frac{B}{K+M-1} \sum_{s=0}^{K-1} \log_2\left(1 + \frac{P_s \left| f_s^H h_d + f_s^H V^\top w_\theta \right|^2}{BN_o}\right) \frac{bit}{s}, \tag{3.6}$$

the channel bandwidth represented by B, the power allocated to the subcarrier s indicated by P_s, the number of channel taps referred to as M, and the f_s^H component, which corresponds to the vth row of DFT matrix F. It is worth noting that the upper bound of equation (6) is provided in [12]:

$$\mathcal{R} \leq \frac{B}{K+M-1} \sum_{s=0}^{K-1} \log_2\left(1 + \frac{P_s}{BN_o}\left(\left| f_s^H h_d \right| + \left\| f_s^H V^\top \right\|_1\right)^2\right), \tag{3.7}$$

where, $\|\cdot\|_1$ is the L_1 norm.

3.2.1 Channel Model

The uncontrollable direct channel is given by [230]:

$$h_d = \sum_{\ell=1}^{L_d} \sqrt{\beta_{d,\ell}} e^{-j2\pi f_c \tau_{d,\ell}} \begin{bmatrix} \operatorname{sinc}\left(0 + B\left(\varsigma - \tau_{d,\ell}\right)\right) \\ \vdots \\ \operatorname{sinc}\left(M - 1 + B\left(\varsigma - \tau_{d,\ell}\right)\right) \end{bmatrix}, \tag{3.8}$$

where, $\beta_{d,\ell}$ is the ℓ^{th} pathloss from the AP to the user with L_d propagation paths as per Fig. 3.1, $\tau_{d,\ell}$ is the delay of propagation and the sampling delay over the shortest path is ς. Similarly, the controllable indirect channel is presented as:

$$\begin{aligned} V = \sum_{\ell=1}^{L_a} \sum_{\ell_b=1}^{L_b} \sqrt{\beta_{H,\ell}\beta_{G,\ell_b}} e^{-j2\pi f_c\left(\tau_{H,\ell}+\tau_{G,\ell_b}\right)} \left(a\left(\varphi_{H,\ell}, \vartheta_{H,\ell}\right)\right. \\ \left.\odot a\left(\varphi_{G,\ell}, \vartheta_{G,\ell_b}\right)\right) \begin{bmatrix} \operatorname{sinc}\left(0 + B\left(\varsigma - \tau_{H,\ell} - \tau_{G,\ell}\right)\right) \\ \vdots \\ \operatorname{sinc}\left(M - 1 + B\left(\varsigma - \tau_{H,\ell} - \tau_{G,\ell_b}\right)\right) \end{bmatrix}^{\top}. \end{aligned} \tag{3.9}$$

the paths L_a and L_b represent the propagation of signals from the AP to the RIS, and from the RIS to the users, respectively. The attenuation of the combined indirect channel from the AP to the user via the RIS is denoted by $\beta_{H,\ell} \geq 0$, and $\beta_{G,\ell_b} \geq 0$, as depicted in Fig. 3.1. The time delay for propagation along the paths to and from the RIS is $\tau_{H,\ell}$ and τ_{G,ℓ_b}, respectively. The array response vector is denoted by $a(\varphi, \vartheta) = \sqrt{\mathbb{D}(\varphi, \vartheta)} \left[e^{j\mathcal{K}(\varphi,\vartheta)^{\top}\mathbb{U}_1}, \ldots, e^{j\mathcal{K}(\varphi,\vartheta)^{\top}\mathbb{U}_N}\right]^{\top}$, where $\mathbb{D}(\varphi, \vartheta)$ represents the directivity pattern of each element, and ϑ and φ denote the elevation and azimuth angles, respectively. Furthermore $\mathcal{K}$ is defined as the wavenumber, $\mathcal{K}(\varphi, \vartheta) = \frac{2\pi}{\lambda}[\cos(\vartheta)\cos(\varphi), \cos(\vartheta)\sin(\varphi), \sin(\vartheta)]^{\top}$. The location of the *nth* element is represented by $\mathbb{U}_n = [0, i(n)0.25\lambda, j(n)0.25\lambda]^{\top}$, where $i(n) = \operatorname{mod}(n-1, N_{hor})$ and $j(n) = \lfloor (n-1)/N_{hor} \rfloor$ correspond to the horizontal and vertical indices of element n. The modulus and truncate operations are represented by $\operatorname{mod}(.,.)$ and $\lfloor . \rfloor$, respectively. Finally, the vertical and horizontal spacing between the elements is $\lambda/4$.

3.3 Data Rate Optimization Using Different Methods

The need for faster data rates has grown significantly and exponentially over the past few years. The proliferation of mobile phones and the emergence of services that demand high data rates (such online gaming and video streaming) are the key factors that are continually driving up this demand. Massive MIMO and mm-Wave are enabling technologies for future communication systems. These technologies can provide wide bandwidths combined with improved beamforming and spatial-multiplexing benefits from the antenna arrays to satisfy the requirements for in-

creased data rates and accommodate an increasing range of wireless equipments [106]. Despite having potentially large possible rate improvements, these technologies typically have higher hardware and power costs, necessitating a separate evaluation of the overall benefits of their application for each user scenario. In addition, they are unable to directly control the propagation channel, whose randomness nature can occasionally limit the effectiveness of these solutions.

The sum rate in RIS-enhanced multi-user MISO downlink communications was maximised by the authors in [102]. The power allocation and the RIS reflection matrix were optimised alternatively using the majorization-minimization method by using the zero-forcing precoding at the BS. The authors in [104] also looked at the issue of weighted sum rate maximisation. Three iterative techniques were developed for optimising the reflection coefficients in terms of various kinds of RIS reflection components within the AO framework in order to produce the transmit beamforming. In [107], the authors first provide a workable transmission protocol for estimating the channels in a MIMO-OFDM system via pilot training, and they then suggest an AO algorithm for optimising the RIS phase shifts and power allocation matrix. The authors in [230] discuss the sum data increase with the presence of mutual coupling in a SISO OFDM system and provide a simple method for channel estimation and RIS construction that includes realistic reflection amplitudes and binary RIS phase shifts. In order to increase the attainable average sum rate in a RIS-enhanced multi-user system, [241] presented a two-timescale transmission protocol as opposed to optimising the passive beamforming using the instantaneous CSI. In [156], the authors used the AO approach to increase the achievable data rate of a multi-stream MIMO communication system supported by RIS. Despite being a straightforward optimisation technique to use, it may take several iterations to converge.

A more challenging RIS optimization problem arises in the wideband scenario with K orthogonal subcarriers than in the narrowband case with a single subcarrier. Estimating the ideal vector w_θ and fairly assigning the power to each subcarrier are necessary for maximizing the data rate in (3.6). In a one-bit RIS architecture, each RIS element can alternate between the phase shifts of 90 or -90 degrees. The phase matrices can be created from the DFT columns of the beamforming codebook [232].

3.3.1 Beamforming 2D-DFT Codebook

Finding the optimal configuration involves a lengthy analysis and is essentially impossible for large values of N because there are 2^N possible RIS configurations. In existing research, switching between N orthogonal configurations for a RIS with N reflecting elements depends on accurate configurations. The structure of the optimal RIS phase shifts remains compatible with the 2D-DFT codebook for a given incident and desired reflected angles [232]. Therefore, if an incoming signal is directed towards a particular beam, each column of the codebook beamformer $W_\theta = F(N_v) \otimes F(N_h) \in \mathbb{C}^{N \times N}$, (where $\otimes$ represents the Kronecker product) may correspond to a potential reflection configuration. As a result, for this codebook setup, the likelihood of

Algorithm 1: Proposed power method for optimizing $\left\|\bar{h}_\theta\right\|^2$.

1: Input: $w_{\theta_{\text{CodeBook}}}$, Ω_0, $h_{\text{equivalent}}$
2: Output: $w_{\theta_{optimized}}$
3: Select $w_{\theta_{\text{CodeBook}}}$ from the codebook $\{W_\theta\}$ that gives the maximum SNR in (11) and set $w_\theta = w_{\theta_{\text{CodeBook}}}$ so, $\Omega_0 = \begin{bmatrix} 1 \\ w_\theta \end{bmatrix}$
4: Set $n = 1$
5: **for** $n <$ maximum number of iterations **do**
6: Compute $\mathcal{H}_i = h_{\text{equivalent}}\,\Omega_i$ from the initial solution Ω_0 and let the first entry $\mathcal{H}_{i,1} = \text{sign}\left(\mathcal{H}_{i,1}^{*}\mathcal{H}_{i,1}\right)$ to ensure that the direct path is always assigned to 1 and unconnected with the RIS configurations. sign(.) is the signum function
7: Set $\Omega_{i+1} = \mathcal{H}_i$ and then quantize the current phases of all candidates $\arg\left([w_\theta]_i\right)$ where $i = 1,\ldots,N$ to be either $\left\{e^{j\pi/2} \text{ or } e^{-j\pi/2}\right\}$ if $\arg\left([w_\theta]_i\right) \in [-\pi, 0)$ and $\arg\left([w_\theta]_i\right) \in [0, \pi)$ respectively.
8: Iterate until convergence
9: **end for**
10: After convergence $w_{\theta_{\text{Optimized}}}$ is obtained.
11: Calculate the power allocation for subcarriers P_s as per (25).
12: Evaluate the data rate $\mathcal{R}$ in (6) by substituting $w_\theta = w_{\theta_{optimized}}$ and the optimized P_s resulting from (25).

obtaining a strong SNR configuration is significantly high. The DFT matrices for the columns $F(N_v)$ and $F(N_h)$ can be denoted as:

$$F(N_v) = \begin{bmatrix} 1 & 1 & 1 & \cdots & 1 \\ 1 & f_{N_v} & f_{N_v}^2 & \cdots & f_{N_v}^{N_v-1} \\ \vdots & \vdots & \vdots & \vdots & \vdots \\ 1 & f_{N_v}^{N_v-1} & f_{N_v}^{2(N_v-1)} & \cdots & f_{N_v}^{(N_v-1)(N_v-1)} \end{bmatrix}, \tag{3.10}$$

in this context, $f_{N_v} = e^{-j2\pi/N_v} = \cos(2\pi/N_v) - \sin(2\pi/N_v))$. The variables N_v and N_h correspond to the number of vertical and horizontal elements, respectively, within the RIS, as shown in Fig. 3.1. To fit the RIS design, the phase shifts produced by the codebook should be quantized. Therefore, the reflection coefficient w_θ for element i can be either $e^{j\pi/2}$ if $\arg\left([w_\theta]_i\right) \in [-\pi, 0)$ or $e^{-j\pi/2}$ if $\arg\left([w_\theta]_i\right) \in [0, \pi)$. We looked through the codebook W_θ to find the best configuration that will maximize the SNR in (11). The best phase configuration that can be created from the codebook can be represented as $w_{\theta_{\text{CodeBook}}} \in W_\theta$. It is considered the standard or reference point for achieving the maximum SNR:

$$SNR = \frac{P\left|\bar{h}_\theta\right|^2}{BN_o}. \tag{3.11}$$

Algorithm 1 utilizes the optimal configuration with the highest SNR, which is determined by evaluating P across all numbers of subcarriers.

3.3.2 Problem Formulation

The objective of this research is to enhance the sum rate received by the user by optimizing the transmit power P and reflection coefficient vector w_θ across all the RIS elements. The optimization problem (OP1) can be formulated mathematically to represent the problem of maximizing the sum rate:

$$\text{(OP1)} \max_{P, w_\theta} \quad \mathcal{R}(P, w_\theta) = \sum_{s=0}^{K-1} \log_2 \left(1 + \frac{P_s \left| f_s^H h_d + f_s^H V^\top w_\theta \right|^2}{BN_o} \right),$$

$$\begin{aligned} &\text{s.t:} \\ &(C1): \left| [w_\theta]_i \right| = 1, \quad \forall i \in N, \\ &(C2): \frac{1}{K} \sum_{s=0}^{K-1} P_s \leq P, \\ &(C3): P_s \geq 0 \quad \forall_v \in K. \end{aligned} \tag{3.12}$$

The first constraint (C1) confirms that there is no pathloss in the reflection of each RIS element. It is necessary to use unit magnitude elements as RIS elements do not amplify or decode signals like relays. Constraint (C2) specifies that power allocations across all subcarriers must not exceed the power budget of the base station and should be ≥ 0, as indicated in constraint (C3). It is important to note that the non-convexity of the (OP1) over the unit modular constraint (C1) for all RIS elements [107] is addressed by iteratively utilizing the power method until convergence is achieved, leading to the optimal w_θ that can impact all subcarriers. Furthermore, the power in constraint (C2) is allocated to each subcarrier using the well-established water-filling algorithm.

3.3.3 Proposed Solutions

Power Method

In order to optimize the RIS phase shifts, we employ the power method to identify a low-complex solution. It determines the channel power's dominating eigenvector. The channel power is given as follows:

$$\left\|\bar{h}_\theta\right\|^2 = \underbrace{\begin{bmatrix} 1 \\ w_\theta \end{bmatrix}^H}_{\Omega^H} \underbrace{\left[h_d, V^\top\right]^H \left[h_d, V^\top\right]}_{h_{\text{equivalent}}} \underbrace{\begin{bmatrix} 1 \\ w_\theta \end{bmatrix}}_{\Omega}. \tag{3.13}$$

We consider that the channels h_d and V are known at the receiver. To initiate the power method and optimize the quadratic form of the channel $\left\|\bar{h}_\theta\right\|^2$, we select $w_{\theta_{CodeBook}}$ from the codebook $W_\theta \in \mathbb{C}^{N\times N}$ as shown in Algorithm 1. The power method determines the dominant eigenvalue by iteratively computing $\Omega_{i+1} = \frac{h_{\text{equivalent}}\,\Omega_i}{\left\|h_{\text{equivalent}}\,\Omega_i\right\|}$ from the initial solution $\Omega_0 = \begin{bmatrix} 1 \\ w_\theta \end{bmatrix}$, where we set $w_\theta = w_{\theta_{\text{CodeBook}}}$, until convergence, following the steps outlined in Algorithm 1.

Semidefinite Relaxation Method

The s-th $(s = 0, 1, \ldots, K-1)$ subcarrier has a channel gain as follows:

$$\left\|\bar{h}_\theta\right\|^2 = \sum_{s=0}^{K-1} \left| f_v^H h_d + f_v^H V^\top w_\theta \right|^2. \tag{3.14}$$

The channel gain fluctuates as a function of the passive beamforming vector w_θ. In order to increase the data rate in (3.6), we develop an optimization problem, relying on (3.14), using beamforming reflection coefficient vector w_θ and fairly allocating the power over the entire subcarriers. The optimization problem below is specifically reformulated as follows:

$$\begin{aligned} &(\text{OP2}) \max_{P, w_\theta} \sum_{s=0}^{K-1} \left| f_v^H h_d + f_v^H V^\top w_\theta \right|^2, \\ &\text{s.t:} \\ &\text{(C1): } \left|[w_\theta]_i\right| = 1, \quad \forall i \in N, \\ &\text{(C2): } \tfrac{1}{K}\textstyle\sum_{s=0}^{K-1} P_v \le P, \\ &\text{(C3): } P_v \ge 0 \quad \forall_v \in K, \end{aligned} \tag{3.15}$$

where unnecessary terms have been removed for the sake of clarity. Keep in mind that the sum channel gain maximization at the user is the optimal value of (OP2). Through the use of the semidefinite relaxation approach, we are able to solve the problem (OP2) sub-optimally. Thus, the (OP2) objective function of (3.15) is denoted as:

$$\widetilde{U} = \sum_{s=0}^{K-1} f_v^H V V^H \tag{3.16}$$

$$\tilde{u} = \sum_{s=0}^{K-1} f_v^H V h_d \tag{3.17}$$

$$\widetilde{D} = \sum_{s=0}^{K-1} \left| f_v^H h_d \right|^2 \tag{3.18}$$

where (OP2) is equivalent to:

$$\begin{aligned} \text{(OP3):} \max_{w_\theta} \; & w_\theta^H \widetilde{U} w_\theta + w_\theta^H \tilde{u} + \tilde{u}^H w_\theta + \widetilde{D} \\ & \text{s.t:} \\ & |[w_\theta]_i| = 1, \forall i = 1,2,\ldots,K \\ & \frac{1}{K} \sum_{s=0}^{K-1} P_v \leq P, \\ & p_v \geq 0 \qquad\qquad\qquad\qquad \forall_v \in K \end{aligned} \tag{3.19}$$

Problem (OP3) is easily distinguishable as a non-convex QCQP problem, which can be rewritten as a homogeneous QCQP problem. In particular, by describing:

$$Q = \begin{bmatrix} \widetilde{U} & \tilde{u} \\ \tilde{u}^H & 0 \end{bmatrix}, \widetilde{w}_\theta = \begin{bmatrix} w_\theta \\ t \end{bmatrix}, \tag{3.20}$$

where, t is an auxiliary variable. Let us define $\phi = \widetilde{w}_\theta \widetilde{w}_\theta^\top$ with rank $(\phi) = 1$. Optimization Problem (OP3) is changed into the following problem:

$$\begin{aligned} \text{(OP4)} : \max_{\phi} \; & \text{tr}(Q\phi) + \widetilde{D} \\ & \text{s.t:} \\ & [\phi]_{i,i} = 1, \quad \forall i = 1,2,\ldots,N+1 \\ & \phi \geq 0. \end{aligned} \tag{3.21}$$

It is noted that due to the rank-one constraint, (OP4) is still not convex. As a result, We apply the SDR method to overcome the rank-one constraint, transforming (OP4) into a convex SDP that can be solved effectively with the help of current convex optimization solvers like CVX [238]. It is important to note that the ideal objective value of (OP4) acts as an upper bound on that of (OP2). However, the best solution ϕ^* to (OP4) might not be a rank-one answer. As a consequence, using the Gaussian randomization method, we produce the following rank-one solution.

$$\phi^* = \Lambda \Sigma \Lambda^H \tag{3.22}$$

where $\Lambda = [\rho_1, \cdots, \rho_{N+1}]$ and $\Sigma = \text{diag}\,(\mathbb{A}_1, \cdots, \mathbb{A}_{\text{N}+1})$ are unitary and diagonal matrices, respectively, both with the size of $(N+1) \times (N+1)$. then we obtain a suboptimal solution to (OP4) as $\widetilde{w}_\theta^* = \Lambda \Sigma \mathbb{M}$ where $\mathbb{M} \in \mathbb{C}^{(N+1)\times 1}$ is a random vector generated according to $\mathbb{M} \in \mathcal{N}_\mathbb{C}\,(0, I_{N+1})$ denoting the circularly symmetric complex Gaussian (CSCG) distribution with zero mean and

covariance matrix I_{N+1}. Finally, we achieve a suboptimal solution to the issue (OP2) as ${w_\theta}^* = e^{j\angle\left([\widetilde{w}_\theta{}^*]_{1:N}/[\tilde{w}_\theta]_{N+1}\right)}$.

Strongest Tap Maximization Method

According to STM, the received signal power should be concentrated in the time domain rather than distributed over the K subcarriers. Therefore, choosing a configuration that is suitable for a single channel tap is preferable to the one which is suitable for a single subcarrier. This is especially valid if one of the LoS propagation paths is significantly more powerful than all other paths. It should be noted that the total energy of the incoming signals, computed in the frequency domain, is the objective function in (3.15). The optimization Problem (OP2) is thus equivalent to the following problem:

$$\begin{aligned} (\text{OP5}): \max_{w_\theta} \quad & \sum_{l=0}^{M-1} h_d[l] + v_l^\top w_\theta \\ \text{s.t:} \\ & |[w_\theta]_i| = 1, \quad \forall_i \in N. \end{aligned} \tag{3.23}$$

Because practical wireless communication systems have $M \ll K$, it should be noted that computing the objective function in (3.23) is more effective than calculating it in (3.15). To start, we determine the vector w_θ that increases the magnitude of every channel tap. We then select the solution resulting in the largest magnitude with respect to the channel tap index l.

$$\ell^{\text{opt}} = \underset{\ell \in \{0,\ldots,M-1\}}{\arg\max} \left| h_d[\ell] + v_\ell^{\mathrm{T}} \omega_\ell \right|^2 \tag{3.24}$$

Consequently, we obtain the following sub-optimal solution to the problem (OP2) as $w_{\theta_l} = \left[e^{\mathrm{j}(\arg(h_d[l]) - \arg([v_l]_1))}, \ldots, e^{\mathrm{j}(\arg(h_d[l]) - \arg([v_l]_N))} \right]^{\mathrm{T}}$, where the argument of a complex number is provided by $\arg(\cdot)$ and the nth entry of v_l is signified by $[v_\ell]_n$. The phase of every component in the inner product $v_l^{\mathrm{T}} \omega_l$ is rotated in this solution to line up with the phase of $h_d[\ell]$.

Water-filling Algorithm

All subcarriers $P_0, \ldots, P_{K-1}$ have a power distribution that satisfies $P = \frac{1}{K} \sum_{s=0}^{K-1} P_s$, where $P_s = E\left\{ |\bar{x}[v]|^2 \right\}$ is the power assigned to subcarrier s. The symbol $E\{.\}$ represents the expectation operator. To determine the optimal amount of power assigned to each subcarrier, the water-filling algorithm [107] can be employed.

$$P_s = \max\left(\eta - \frac{BN_o}{\left| f_s^H h_d + f_s^H V^\top w_\theta \right|^2}, 0 \right), \tag{3.25}$$

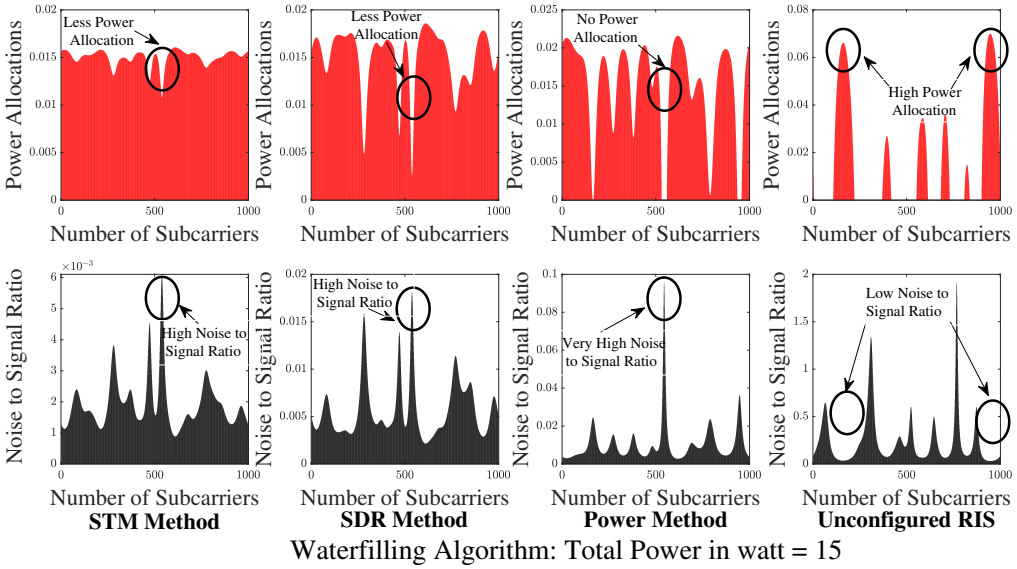

Figure 3.2: Fair Power allocations for all subcarriers in STM method, SDR method, Power method and the case when the RIS surface is unconfigured

where, the parameter $\eta \geq 0$ is chosen to satisfy $\frac{1}{K}\sum_{s=0}^{K-1} P_s = P$. Consequently, the power allocated for s^{th} subcarrier P_s is dependent on the water level parameter η and can be re-written as follows.

$$P_s = \begin{cases} \eta - \frac{BN_o}{\left|f_s^H h_d + f_s^H V^\top w_\theta\right|^2} & \text{if } \eta \geq \frac{BN_o}{\left|f_s^H h_d + f_s^H V^\top w_\theta\right|^2} \\ 0 & \text{if } \eta < \frac{BN_o}{\left|f_s^H h_d + f_s^H V^\top w_\theta\right|^2} \end{cases} \tag{3.26}$$

The water-filling algorithm is used to allocate the transmitted power fairly to all subcarriers in the different optimization methods, STM, SDR, Power method and the case when the surface is unconfigured. In Fig. 3.2, we show how the water-filling algorithm allocates the 15 Watt power for the entire number of subcarriers fairly taking into consideration the channel gain status. the black circles in the figure refer to the amount of power allocated by the algorithm to some subcarriers taking into consideration their corresponding noise to signal ratio status.

3.3.4 Computational Complexity

This section discusses the computational complexity of the proposed optimization methods for allocating fair power to all subcarriers and tuning phases of the RIS. To estimate the Big-O $(\mathcal{O})$ complexity of these methods, we followed the same procedure as in [106]. The complexity of the power method can be calculated by considering the steps in Algorithm 1. The algorithm requires $(N+1)^2$ complex multiplications for the term $h_{\text{equivalent}}$, while the term $h_{\text{equivalent}}\,\Omega_i$ necessitates $(N+1)$ complex multiplications and phases quantization demands N complex computations. Additionally, allocating power to all subcarriers requires $2(KM)$ complex multiplications. Thus,

Table 3.1: Proposed methods complexities and qualities

Method	Complexity	Objective Function	Quality
Power	$\mathcal{O}\left(\left((N+1)^2 + (N+1)+N)I_R + 2(KM)\right)\right.$	Equivalent Power of the channel	Low complex and sub-optimal solution
SDR	$\mathcal{O}\left(\left(2(N+1)^2 + (N+1)^{4.5} + 2(KM)\right)\right.$	Equivalent Power of the channel	High complex and sub-optimal solution
STM	$\mathcal{O}((N)+2(KM))$	Equivalent Power of the channel	Low complex and sub-optimal

the estimated overall complexity per iteration is denoted as $\mathcal{O}_{\text{Power}}$:

$$\mathcal{O}_{\text{Power}} = \mathcal{O}\left(\left((N+1)^2+(N+1)+N\right)I_R+2(KM)\right) \tag{3.27}$$

where, I_R represents the maximum number of iterations required to achieve the optimal data rate. The complexity of the SDR method can be determined by calculating the complex operations of the following terms. The terms Q and ϕ in (3.20) require $(N+1)^2$ complex multiplications for each of them. The gaussian randomization method needs $(N+1)^{4.5}$ complex multiplications to compute the best solution ϕ^*. Moreover, power allocation for all subcarriers, as per Fig. 3.2 SDR method, needs $2(KM)$ complex multiplications. Consequently, the overall estimated complexity is given as $\mathcal{O}_{SDR}$:

$$\mathcal{O}_{SDR} = \left(2(N+1)^2+(N+1)^{4.5}+2(KM)\right) \tag{3.28}$$

The complexity in (3.28) meets with the computational complexities estimated in [107] and [167]. The complexity in [107] is $\mathcal{O}\left(NKI_{SA}+N^{4.5}K^{3.5}I_T\right)$ where I_{SA} denotes the number of iterations that the successive approximation requires and I_T is the total time that is needed to solve the problem during the successive convex approximation algorithm. Furthermore, the complexity is calculated as $\mathcal{O}(N+1)^{4.5}$ in [167]. Consequently, the complexity in (3.28) coincides with the results in [107] and [167] in terms of the complexity degree of $\mathcal{O}(N)^{4.5}$. Furthermore, the complexity for STM method is computed using the same procedure:

$$\mathcal{O}_{STM} = \mathcal{O}((N)+2(KM)) \tag{3.29}$$

The methods complexities are compared in Table 3.1. It is obvious from Table 3.1 that the SDR complexity is the highest in terms of $\mathcal{O}(N)^{4.5}$ while the STM is the lowest in terms of $\mathcal{O}(N)$ and the power method is lying in between SDR and STM with Complexity $\mathcal{O}(N)^2$.

Table 3.2: Simulation parameters

Parameter	Value
Carrier frequency f_c	4e9 Hz
Speed of light c	3e8 m/s
Wavelength λ	0.075 m
Total number of elements N	400
Number of horizontal Elements N_{hor}	20
Number of vertical Elements N_{ver}	20
Vertical and horizontal element spacing	$\lambda/4$
AP Location in meter, Coordinates $[x,y,z]$	$\begin{bmatrix} 40 & -200 & 0 \end{bmatrix}^\top$
User Location in meter, Coordinates $[x,y,z]$	$\begin{bmatrix} 20 & 0 & 0 \end{bmatrix}^\top$
RIS Location in meter, Coordinates $[x,y,z]$	$\begin{bmatrix} 0 & 0 & 0 \end{bmatrix}^\top$
Pathloss NLoS	$34.53 + 38\log_{10}(d)$
Pathloss LoS	$30.18 + 26\log_{10}(d)$
Channel Taps M	23
Total Number of Subcarriers K	1000
Transmitted Power P	15 W
Bandwidth B	15e6 Hz

3.4 Simulation Results

We analyze the performance of our suggested approaches for increasing the RIS-aided SISO-OFDM system achievable data rate by providing numerical results from Monte Carlo simulations. The simulation parameters are considered by using the 3GPP channel model [231] and Table 3.2. In this study, we take into account an OFDM system with number of subcarriers $K = 1000$ and a more realistic multi-path channel model with channel taps $M = 23$ at random delays and an exponential power decay profile. The AP, user, RIS locations coordinates in meter are shown in Fig. 3.1. We considered LoS channels between the AP-RIS-User indirect link as per Fig. 3.1, to guarantee effective transmissions and large channel gains. However, the NLoS propagation is assumed between the AP and the user direct link. We contrast the achieved data rate of the suggested methods with the system's upper bound. For Comparison with the system upper bound, we consider the power method, SDR, STM benchmark schemes, the random phase shifts and the case when the surface is Un-configured where we replaced the RIS with a passive metal sheet causing zero phase-shifts for the entire elements. We search in the codebook W_θ for the best configuration that maximize the SNR in (3.11). Fig. 3.3 depicts the related strongest and weakest SNR with a difference of around 20 dB. The strongest SNR configuration is further utilized in Algorithm 1. The strong SNR which is achieved by the beamforming codebook increases the data rate as per Fig. 3.5 and Fig. 3.6.

In order to validate the performance of the proposed method, Fig. 3.4 shows the performance of the iterative power method and the benchmark schemes at different SNR values, with $N = 400$. It is noticed that all the schemes with RIS (SDR method, power method and random

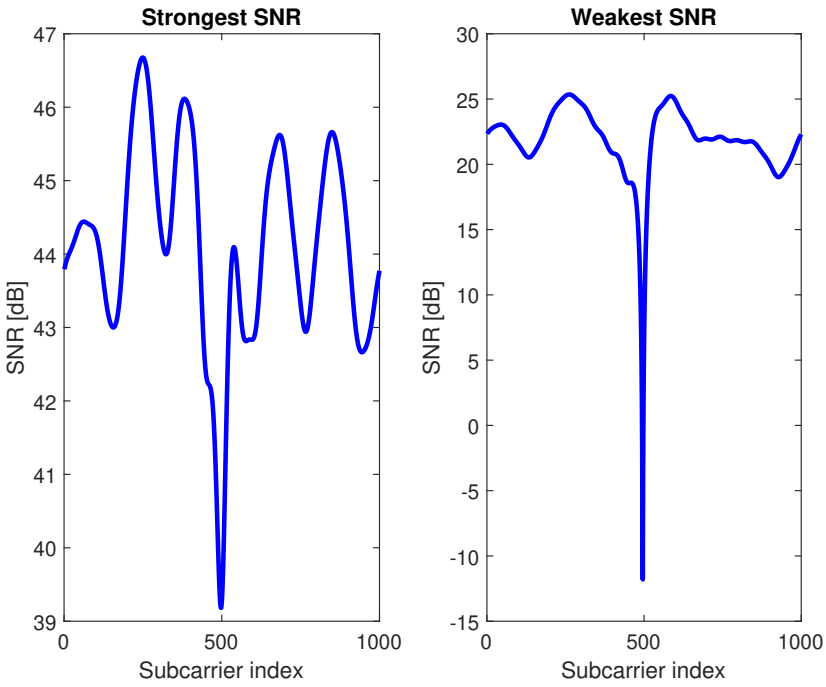

Figure 3.3: The best confguration in the codebook that gives the maximum SNR and the worst confguration that gives the minimum SNR.

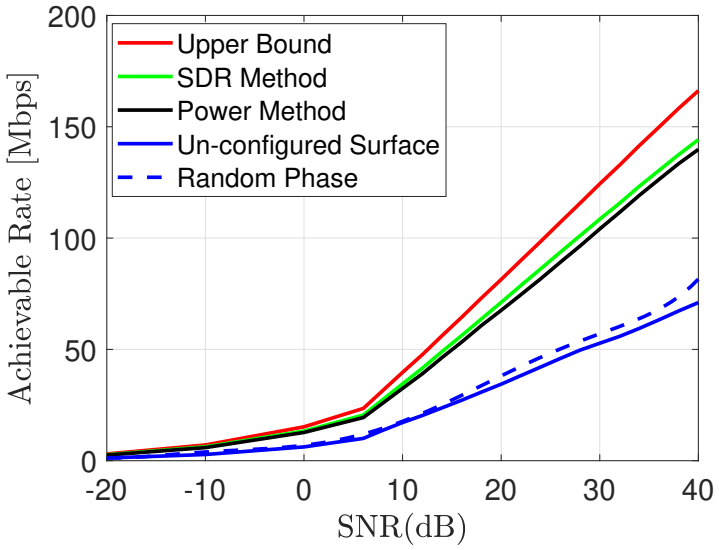

Figure 3.4: Achievable data rate versus SNR.

phase) outperform the scheme without RIS (un-configured surface), owing to the RIS-enhanced average channel power between the AP and the user. Additionally, the proposed iterative power method and the SDR scheme both significantly outperform the random phase scheme in terms of achievable rate because of the tuned RIS coefficients that help the direct and the reflecting channel to be superimposed more constructively at the receiver. The SDR method shows slightly superior performance to the power method at low and high SNR regimes. Nevertheless, the

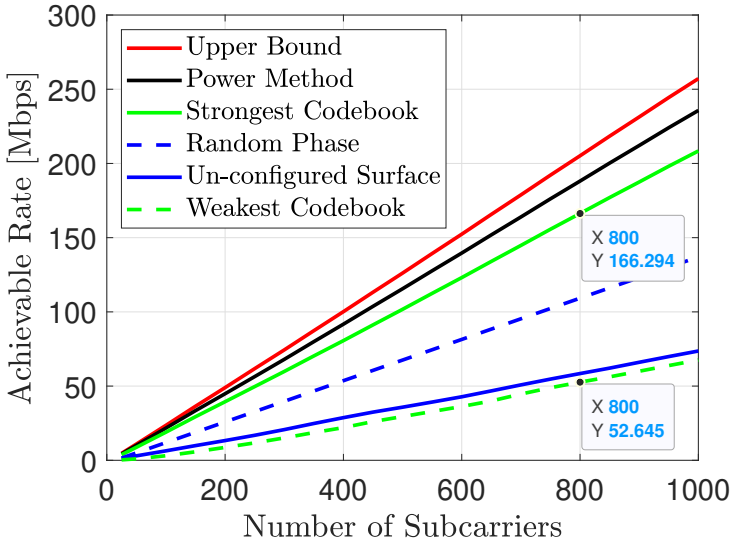

Figure 3.5: Comparison of the achievable data rate versus number of subcarriers for diferent schemes when $N = 4096$.

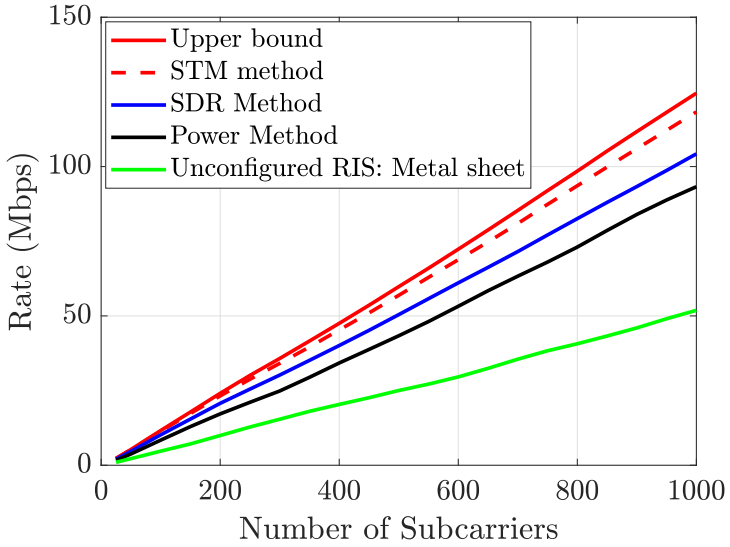

Figure 3.6: Comparison of data rate versus the number of subcarriers when considering LoS channel between the AP-RIS-User composite indirect link when $N = 400$.

performance gap between them is very small and can be sacrificed for the sake of practical implementations and lower complexity.

The data rate of the proposed methods is compared in Fig. 3.6 considering LoS channels between the AP-RIS-User indirect link as per Fig. 3.1. The heuristic STM method outperforms both the SDR and the power methods while the data rate is the lowest in case of the unconfigured RIS (metal sheet). The achievable data rate is dramatically boosted up as the range of subcarriers increases. In comparison to unconfigured RIS (metal sheet) configuration, the proposed approaches improve the sum data rate dramatically with an optimized RIS because of the

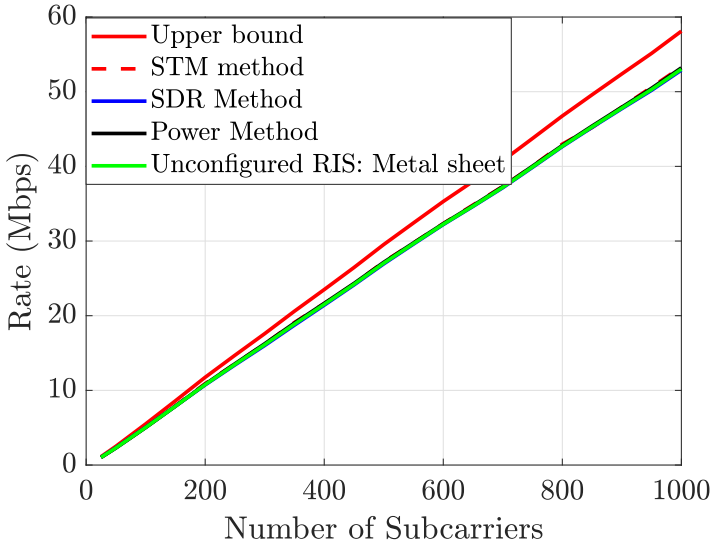

Figure 3.7: Comparison of data rate versus the number of subcarriers when considering NLoS channel between the AP-RIS-User composite indirect link.

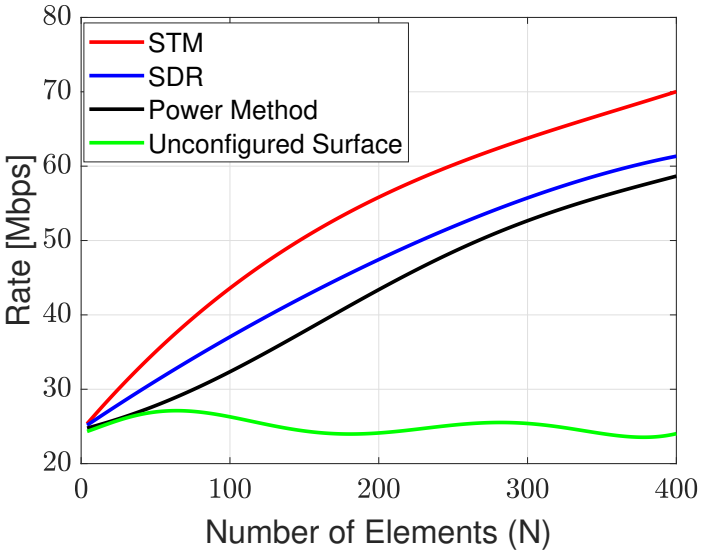

Figure 3.8: Comparison of data rates for different values of N.

adjusted RIS coefficients that allow the direct and reflecting channels to be integrated at the receiver more effectively and constructively. The power method shows the lowest data rate among the other methods however, it is a practical way to configure the RIS surface by implementing the strongest SNR configuration selected from the W_θ codebook. The SDR method outperforms the power method by optimizing the quadratic form of the channel power, however, the STM method shows the highest achievable data rate since it implements the dominant LoS in the composite AP-RIS-User channel.

Unlike the scenario in Fig. 3.6, Fig. 3.7 incorporates the example when the path to the RIS encounters an NLoS, which sheds light on two influences: There is no dominant path, and the

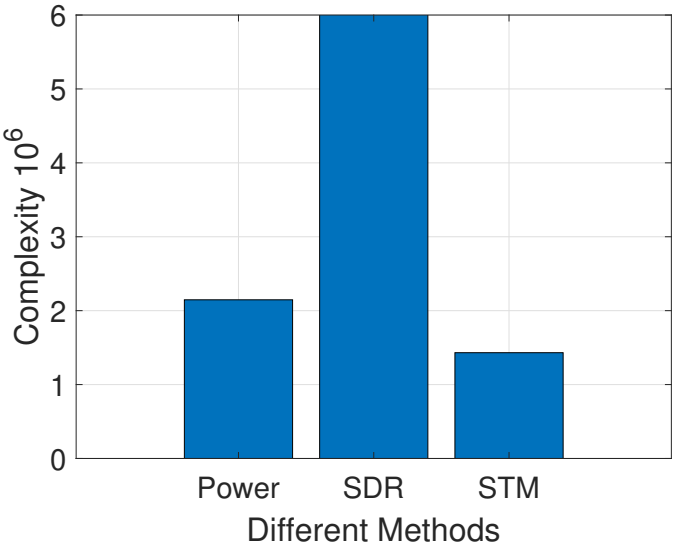

Figure 3.9: Complexity level for each optimization method when $N = 400$.

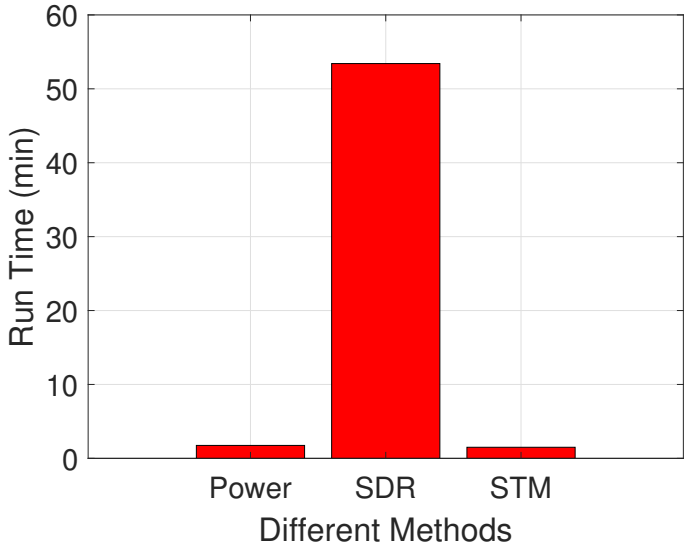

Figure 3.10: Runtime consumption for each optimization method when $N = 400$.

path via the RIS is weaker. The upper bound and the unconfigured RIS surface (metal sheet) are much closer together due to the weaker path through the RIS, whereas the absence of the dominating path leads to the impossibility to identify a single RIS configuration that works for the total number of subcarriers. Fig. 3.7 results meet with [12] when the authors demonstrated the same scenario for the STM method and the upper bound cases.

An important parameter that should be taken into account when investigating the data rate is the dimension of the RIS surface. The RIS enhances the data rate and it increases further when the surface is large are per Fig. 3.8. We compare the achievable rate of different schemes versus the number of RIS elements at SNR = 20 dB. It is clear that the rate performance of the

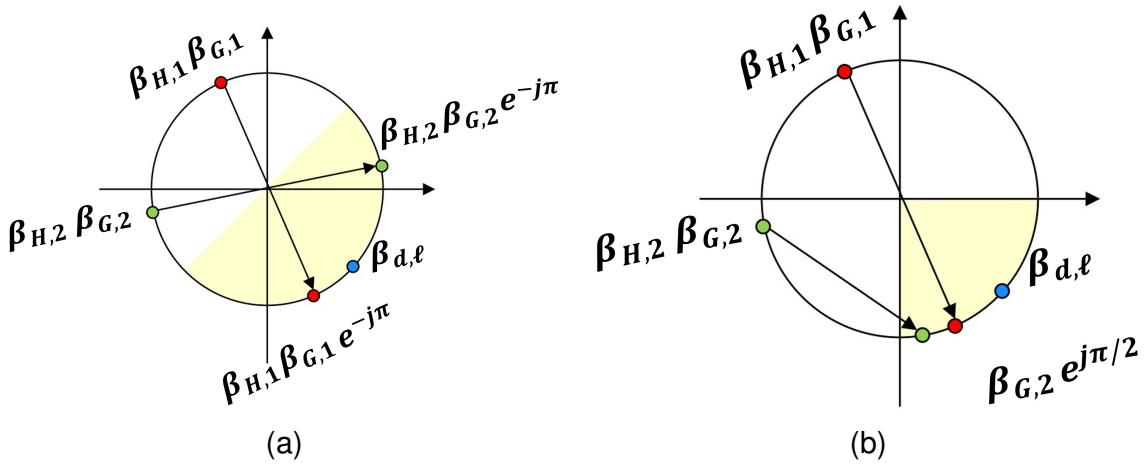

Figure 3.11: (a). Two configurations:$\theta_n \in \{0,\pi\}$ (b). Four configurations: $\theta_n \in \{0,\pi,\pi/2,-\pi/2\}$

un-configured surface (zero phase shifts) scheme at the RIS is independent of the number of elements. However, the tuned RIS phase profiles in the other schemes (STM, SDR and power method) enhanced the data rate with the increase number of RIS elements. The highest average data rate over the entire bandwidth is shown when the number of elements on the surface is $N = 400$, while the lower data rate is obtained at $N = 100$ or less.

Another crucial factor that should be considered is the complexity and runtime. Table 3.1 reveals the complexity level for each method. The complexity in SDR method is $\mathcal{O}\left(N^{4.5}\right)$ while it is very less in both power and STM methods, $\mathcal{O}\left(N^2\right)$ and $\mathcal{O}(N)$ respectively. We illustrated the complexity level and the runtime consumption for each method in Fig. 3.9 and Fig. 3.10 respectively. We noticed that the SDR method complexity is the highest (more than 6 millions of complex multiplications) with a runtime larger than 50 minutes, however, the complexity in the other two methods, STM and the power method, is less than the SDR with few minutes runtime consumption.

The above simulation results considered low finite resolution phase shift configurations. Two phase configurations (1-bit RIS) $\theta_n \in \{0,\pi\}$ or $\left\{\frac{\pi}{2},\frac{-\pi}{2}\right\}$ are used to maximize the SNR at the user. It is preferable, for more realistic and practical scenarios in the design, to select the phase shifts which are limited to a certain number of states. The higher resolutions necessitate complex RIS design with different bias voltages dedicated for each state. For example, in 2-bit RIS scenario four phase configurations are required for each RIS cell or element while the 3-bit RIS design switch over to eight-phase configurations. The channel gains $\beta_{H,\ell}$ and β_{G,ℓ_b} move along the unit circle with these phase shifts configurations while the path $\beta_{d,\ell}$ cannot be moved since it is the direct channel path as per Fig. 3.1. Consequently, if 1-bit RIS design is considered then one should select 0 or π phase shift. If 0 phase shift is selected, then the gains $\beta_{H,\ell}$ and β_{G,ℓ_b} will remain at the location where they are on the unit circle however, if π is chosen then the gains

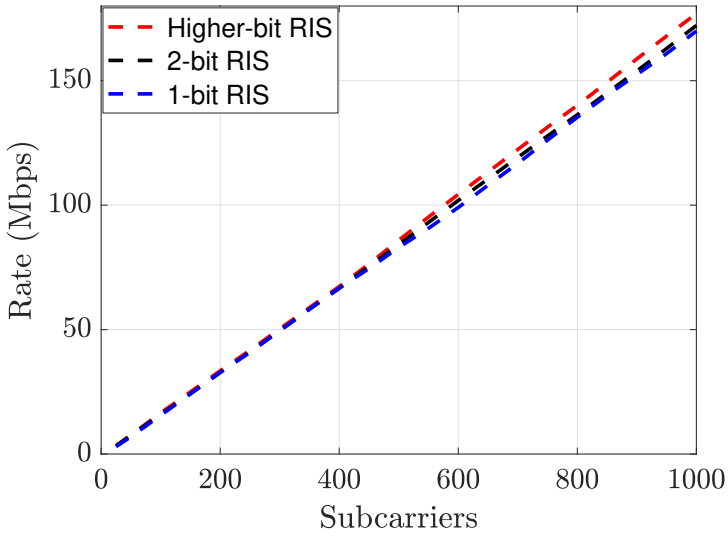

Figure 3.12: STM method for multi-bit RIS design.

will move to the opposite side of the circle. The key point is to shift theses signal gains $\beta_{H,\ell}$ and β_{G,ℓ_b} in the same half-space of the unit circle as the direct channel gain so, one can add all the terms $\left(\beta_{d,\ell}, \beta_{H,\ell} \text{ and } \beta_{G,\ell}\right)$ constructively. The same procedure can be repeated for higher resolutions of phases where all the signals are added up in the same quadrant of the unit circle as the direct path. Therefore, higher phase resolutions are not required as long as the signals can be added constructively without cancelling each other. An illustration is shown on the unit circle for two and four finite phase resolutions when the RIS has two elements only for simplicity [12]. All the signals are gathered in the same half space in the two configurations case while they are in the same quadrant in the four configurations case as per Fig. 3.11.

The finite phase resolutions for different bit-RIS designs are studied in the case of the STM scheme. The obtained results of the sum data rate in case of higher-bit RIS are very close to the 1-bit and 2-bit RIS and this is expected since the path phases of the indirect channels are aligned with the dominant LoS path of the direct channel gain in the STM method. Consequently, they are added up constructively at the receiver and hence increase the SNR and the sum rate. However, choosing higher-bit RIS design increase the complexity from $\mathcal{O}((N)+2(KM))$ to $\mathcal{O}((2N)+2(KM))$ due to assigning more phases for each RIS individual element and the switching between of them to aim the direction of the beamforming towards the receiver. Furthermore, the increase in the computational complexity $\mathcal{O}(2N)$ instead of $\mathcal{O}(N)$ is negligible and will increase the run time few seconds only. The challenge is clearly evident in the RIS hardware when higher-bit RIS is required. Generally speaking, it is required more PIN or varactor diodes for each RIS cell or element to achieve more states of phases so, it not recommended to complicate the design and increase the cost by selecting high-bit RIS while the 1-bit RIS phase profile can give comparable sum data rate performance. Fig. 3.12 shows the data rate for different bit RIS designs with slight difference in the performance for the STM scheme when $N = 900$ elements.

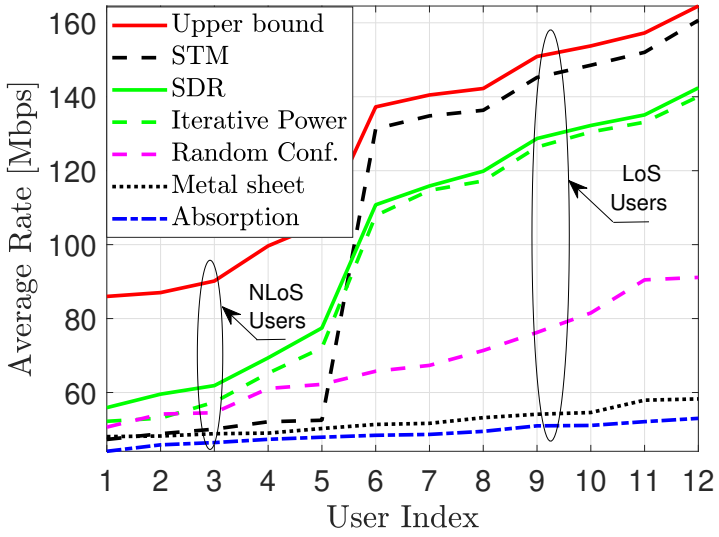

Figure 3.13: The data rates achieved for 12 users using different schemes in LoS and NLoS propagations channels.

Considering the MU scenario, in Fig. 3.13, the heuristic STM technique surpasses the SDR, the iterative power, the random and the RIS when is it is replaced by an absorbed material and passive metal sheet in terms of data rate performance. However, the data rate is at its minimum when dealing with an unconfigured RIS, represented by a absorbed material and metal sheet. Nevertheless, the STM outperforms all other methods for the users who enjoys LoS path from the RIS and the achievable rate is degraded for the NLoS users from the RIS. This is due to the fact that the STM approach of maximizing the strongest tap, aiming to enhance the magnitude of the largest element in the channel vector $h_d + V^{\mathrm{T}} w_\theta$. While effective for LoS channels, this method does not perform well for NLoS channels. Compared to an unconfigured RIS, the proposed approaches (STM,SDR and iterative power) yield a significant enhancement in the achieved data rate through the optimized RIS configurations with a $2.5\times$ increase. This improvement is due to the adjusted RIS coefficients, which facilitate a more efficient and constructive integration of both direct and reflected channels at the user. The iterative power-based algorithm, although providing a lower data rate than the SDR algorithm, offers a practical and realistic means to tune and program the RIS surface. This is achieved by applying the configuration with the strongest SNR, chosen from the w_θ codebook. The SDR algorithm surpasses both the iterative power method and the random phase case. However, it comes with the trade-off of higher computational complexity.

In Fig. 3.14, we juxtapose the achievable data rates of various strategies against the number of RIS elements, with SNR of 25 dB. Initial observations reveal two significant patterns. Firstly, it becomes evident that the rate achieved with the random phase shift approach on the RIS remains unaffected by the number of elements. This outcome is anticipated, given that this method solely relies on aperture gain, lacking any passive beamforming gain. However, the

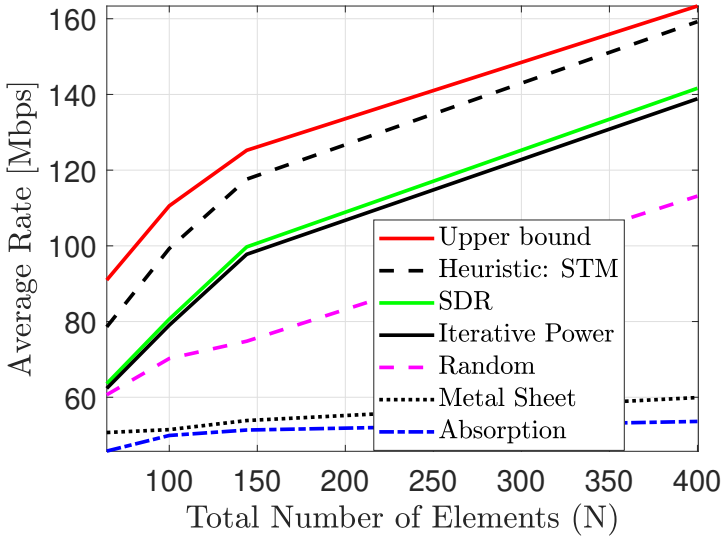

Figure 3.14: Achievable rates versus number of reflecting elements N using different schemes.

random configuration is still higher in the achieved data rates than the unconfigured metal and absorbing sheets cases. Furthermore, a distinct trend emerges: STM, SDR and iterative power-based methods exhibit better performance compared to the random phase involving the RIS, as well as the unconfigured surfaces.

3.5 Summary

In this chapter, we showed that the RIS can be configured to provide significantly higher data rates, in comparison with a uniform surface, e.g., metal sheets. The codebook approach was implemented to generate varieties of phase configurations for the RIS surface in which we searched for the best configuration to be used in the optimization process. A problem formulation is described, and a solution is presented using different optimization methods and the water-filling algorithm. The data rate which is produced by different methods is compared with the upper bound. We noticed that all methods give performance near the upper bound, however, the data rate declines with the decrease in the dimensional area of the surface (number of elements per dimension). in addition, we have proved that the STM and the power methods are simple ways to configure the RIS with lower complexity and less runtime consumption. Selecting higher-bit RIS phase resolutions enhances slightly the sum data rate but at the cost of the hardware and computational complexities. The 1-bit RIS gives performance very close to the higher-bit phases which is enough to align the direct and the indirect paths constructively at the receiver. The RIS is a promising technology and is predicted to have a significant contribution in the 6G networks so, the search for low complex algorithms with reasonable data rate outcomes is crucial and necessary for realistic communications models.

Chapter 4

Data Rate Investigation of RIS-assisted Communication Considering MC and EMI Effects

In wireless communications, various study findings have shown that a RIS may successfully alter wireless wave parameters like phase and amplitude without requiring sophisticated signal processing and decoding at the receiver. However, it is necessary to take into account designing the surface under a realistic frequency selective fading channel. Because of this, we chose a wideband OFDM multi-user communication system based on an actual RIS setup that considers MC and EMI. In this chapter, we used Hadamard matrix in the pilot transmissions to estimate the uncontrollable and the controllable channels. The best pilot configuration was selected to initialize the gradient descent method in order to calculate the optimal reflection coefficient that maximize the data rate for each user in the presence of EMI and MC. Simulation results revealed that the data rate has been degraded when considering EMI and MC for around 30 Mbits/s for each user. This confirms that both EMI and MC must be given considerable attention in our research due to their inevitable effects on the system performance.

4.1 Introduction

RISs are a recent innovation in the field of wireless communication research. The RISs are electromagnetically produced intelligent surfaces. Microelectronic circuits that are capable of wireless communication are used to regulate the materials and handling wireless propagation scenarios in a manner that was not before known [113, 114]. The RISs are made up of many tiny, inexpensive passive components (elements) that may be used to change wireless waves that impinge on them in ways that ordinary substances and materials cannot. It is important to note that prior research primarily focused on frequency flat fading channels for narrowband communications, where the reflection coefficients of the RIS are intended to modify the phase of the

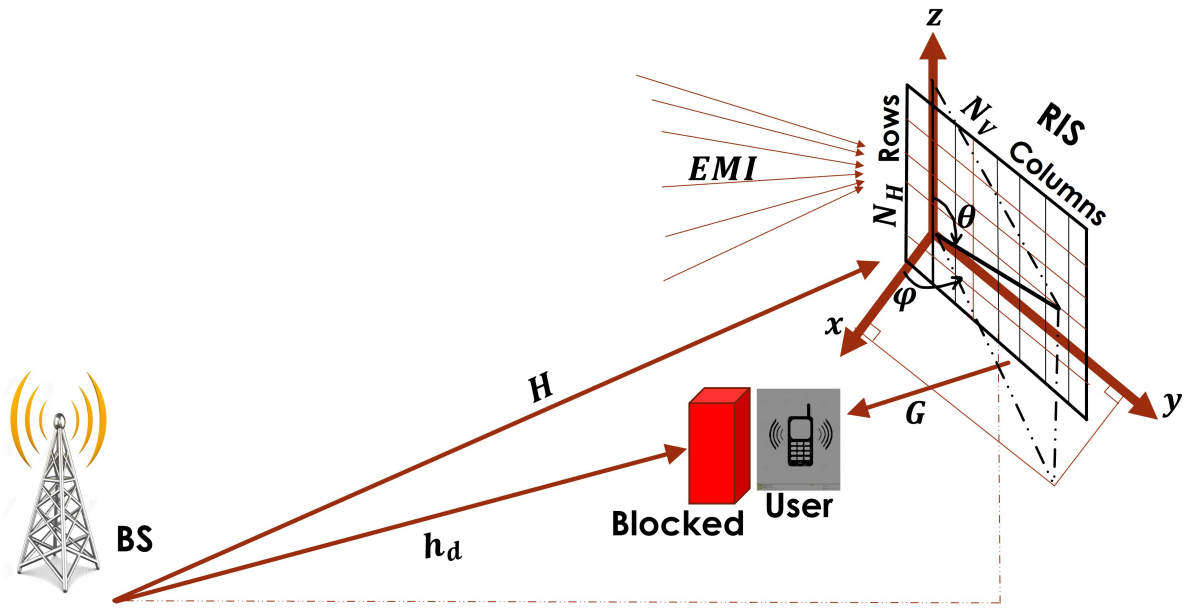

Figure 4.1: Simulation setup for multi-users OFDM aided RIS communication

BS-RIS-User reflected path with the BS-User direct path for constructive interference. The RIS reflection coefficients must, however, account for all signal paths at varying delays when channels with frequency-selective fading nature are present, making optimization challenges more difficult to resolve. In contrast, several subcarriers in OFDM systems favour various configurations over a single one, which complicates the optimization process and reduces the effectiveness of RIS [113]. Heuristic techniques of various complexity are proposed in [160, 178, 243] for coupled channel estimation and RIS configuration in OFDM setups.

However, high percentage of the previous works did not take into consideration the effects of MC and EMI on RIS performance. According to our knowledge, we notice that the literature is lacking such important parameters and most of the research obtained results are overoptimistic. We have investigated RIS setup to look at the effect on the information rate for both the users who have LoS and the NLoS users under MC and EMI in a SISO MU OFDM communication Setup. In this Chapter, we developed the gradient descent method to reach to the optimal pilot configuration for each user. Simulation results revealed the gap in performance between the ideal case (when there is no EMI and MC) and the case when they have effect on the system setup. A summary of the remaining of this chapter is given as following. The system model is introduced in Section 4.2. The EMI and channel model is the focus of Section 4.3, while section 4.4 present the phase shift model that is realistic. We show the pilot transmission and channel estimation in section 4.5. Sections 4.6 and 4.7 depict the dataset and the RIS optimization with the knowledge of EMI, respectively. Simulation results and summary for the chapter are given in section 4.8 and 4.9 respectively. Finally, section **??** list the publications resulted from this chapter.

4.2 System Model

We take into account an OFDM-based MU wireless system where a RIS is used to improve communication between a BS and a user, as shown in Fig. 4.1. We assume for the sake of explanation that both the BS and the user are outfitted with a single antenna. It is considered that the RIS consists of N passive reflecting elements which is organized into a homogeneous planar array with horizontal row elements $N_{hor} = 64$ and vertical column elements $N_{ver} = 64$. The system's entire bandwidth is evenly split into K orthogonal subcarriers (SCs), similar to a typical OFDM-based system. All subcarriers' power distributions $P_0, \ldots, P_{K-1}$ fulfil $P = \frac{1}{K}\sum_{s=0}^{K-1} p_s$ where $p_s = E\left\{|\bar{x}[s]|^2\right\}$ is the power given to subcarrier s. Let the direct channel $h_d = [h_d[0], \ldots, \ldots, h_d[M-1]]^\top \in \mathbb{C}^{M\times 1}$ describes all the direct (uncontrollable) channel coefficients. Additionally, there is a M-tap baseband equivalent multipath channel for the BS-RIS-user link via which the RIS reflects the signal that the BS transmits before it reaches the users. Consequently, let $H = [h_0, \ldots, h_{M-1}] \in \mathbb{C}^{N\times M}$ is the BS-RIS channel where $h_l \in \mathbb{C}^{N\times 1}$ corresponds to the l-th tap, $0 \leq l \leq M-1$ while $G = [g_0, \ldots, ., g_{M-1}] \in \mathbb{C}^{N\times M}$ is the RIS-User channel where $g_l^H \in \mathbb{C}^{1\times N}$ corresponds to the l-th tap, $0 \leq l \leq M-1$. When the signal is received at the RIS, each element re-scatters it with a different reflection coefficient so, $w_\theta = \text{diag}\left(e^{j\emptyset_1}, e^{j\emptyset_2}, \ldots, e^{j\emptyset_N}\right)$ is the diagonal matrix that contains the reflection coefficients of the RIS. For the sake of clarity, let us denote $V = [v_0, \ldots, v_{M-1}] \in \mathbb{C}^{N\times M}$ where $v_l^H = g_l^H \,\text{diag}\,(h_l) \in \mathbb{C}^{1\times N}$. Then we have $v_l^H w_\theta = g_l^H w_\theta h_l$ that characterizes the BS-RIS-User composite channel at the l-th tap. The received signal $z_k \in \mathbb{C}$ at the s-th subcarrier $s = 0, \ldots, K-1$ using the DFT at the RIS is given [228]:

$$z_k = H_k x_k + e_{EMI}, \tag{4.1}$$

where, x_k is the transmitted signal and $e_{EMI} \in \mathbb{C}^N$ is the EMI produced by the incoming uncontrollable waves. The received signal $r_k \in \mathbb{C}$ at the receiver is given as per Fig. 4.1:

$$r_k = z_k w_\theta G_k^H + h_d x_k + e_k, \tag{4.2}$$

where, $e_k \sim \mathcal{N}_\mathbb{C}\left(0, \sigma_e^2\right)$ is the receiver noise affecting the wave reception except for the EMI reflected by the RIS. By substituting (4.1) in (4.2).

$$r_k = \left(G_k^H w_\theta H_k + h_d\right) x_k + w_\theta G_k^H e_{EMI} + e_k. \tag{4.3}$$

Let us denote $h_\theta = \left(G_k^H w_\theta H_k + h_d\right)$ and $\mathcal{G} = w_\theta G_k^H$. We can represent (4.3) in a vector form as follows:

$$\begin{bmatrix} \bar{r}[0] \\ \vdots \\ \bar{r}[K-1] \end{bmatrix} = \begin{bmatrix} \bar{h}_\theta[0] \\ \vdots \\ \bar{h}_\theta[K-1] \end{bmatrix} \odot \begin{bmatrix} \bar{x}[0] \\ \vdots \\ \bar{x}[K-1] \end{bmatrix} \begin{bmatrix} \overline{\mathcal{G}}\bar{e}_{EMI}[0] \\ \vdots \\ \overline{\mathcal{G}}\bar{e}_{EMI}[K-1] \end{bmatrix} \begin{bmatrix} \bar{e}[0] \\ \vdots \\ \bar{e}[K-1] \end{bmatrix} \tag{4.4}$$

where, $\odot$ denotes the Hadamard product. The output of the OFDM block can be described in a short form as follows:

$$\bar{r} = \bar{h}_\theta \odot \bar{x} + \bar{\mathcal{G}}\bar{e}_{EMI} + \bar{e}. \tag{4.5}$$

We notice that the channel frequency response of $\bar{h}_\theta$ is:

$$\bar{h}_\theta = F \begin{bmatrix} h_d[0] + v_0^H w_\theta \\ \vdots \\ h_d[M-1] + v_{M-1}^H w_\theta \end{bmatrix} = F\left(h_d + V^H w_\theta\right) \tag{4.6}$$

where, F is a $K \times M$ DFT matrix. At each s-th SC, the channel frequency response is characterised as follows:

$$h_{\theta_k} = f_s^H h_d + f_s^H V^H w_{\theta,} \quad s = 0, \ldots, K-1, \tag{4.7}$$

where, f_s^H describes the k-th row of the DFT matrix F. Consequently for all subcarriers K with equal power distribution, we can represent the total sum information rate for a known w_θ configuration and complete channel knowledge as follows:

$$\mathcal{R} = \frac{B}{K+M-1} \sum_{s=0}^{K-1} \log_2 \left(1 + \frac{P\left|f_s^H h_d + f_s^H V^H w_\theta\right|^2}{A\sigma^2 \mathcal{G}^H R \mathcal{G} + \sigma_e^2}\right) \tag{4.8}$$

where, the total bandwidth is B , P is the radiated power in watt, M is the channel taps and the term $A\sigma^2\mathcal{G}^H R\mathcal{G}$ is the interference term that will be considered as a noise in this chapter. We will define and explain the channel and the EMI parameters in section 4.3.

4.3 EMI and Channel Model

RIS-enhanced communications is a burgeoning area of interest drawing considerable attention, with numerous studies highlighting potential advantages in spectral and energy efficiency. However, it's common practice to solely focus on the signals generated by the system, overlooking the EMI or "noise" inherent in any environment. This EMI can stem from various sources, including natural phenomena, deliberate actions, or unintentional emissions such as those from man-made devices or background radiation. Essentially, any uncontrolled wireless signal contributes to EMI. Despite its ubiquitous presence in wireless communication systems, EMI can

significantly impact system performance. When EMI impinges on the RIS, it is absorbed proportionally to its area and then re-radiated. Although the re-radiated EMI may not be directed towards the intended receiver, a substantial portion of its energy, owing to the extensive surface area of the RIS, may still reach it, thereby degrading the system's end-to-end Signal SNR, typically optimized under the assumption of only thermal noise presence.

4.3.1 EMI Model

A cline of incoming plane waves from external sources are superimposed to create the EMI e_{EMI}. The e_{EMI} is modelled as in [228] and distributed as $e_{EMI} \sim \mathcal{N}_{\mathbb{C}}\left(0, A\sigma^2 R\right)$ where A is the RIS element area, σ^2 is the interference variance and the (n,m)-th unit of R is given by:

$$[\mathbf{R}]_{n,m} = \iint_{-\pi/2}^{\pi/2} e^{j\mathcal{K}(\varphi,\vartheta)^{\mathrm{T}}(\mathbb{U}_n - \mathbb{U}_m)} f(\varphi,\vartheta) d\varphi d\vartheta, \tag{4.9}$$

where, $\mathcal{K}(\varphi,\vartheta) = \frac{2\pi}{\lambda}[\cos(\vartheta)\cos(\varphi), \cos(\vartheta)\sin(\varphi), \sin(\vartheta)]^{\mathrm{T}}$ is the wave number that describes the phase changes of the plane waves in relation to its three Cartesian coordinates. $f(\varphi,\vartheta)$ is the power angular density with $\iint_{-\pi/2}^{\pi/2} f(\varphi,\vartheta) d\varphi d\vartheta = 1$ and $\mathbb{U}_n = [0, i(n)d_v, j(n)d_h]^{\mathrm{T}}$ is the location of the n-th element with $n \in [1,N]$. d_v and d_h are the vertical and horizontal elements spacing where, $d_v^2 = d_h^2 = A$ and $i(n)$ and $j(n)$ are the horizontal and vertical indices of element n. Under circumstances of isotropic distribution (i.e. uniform distribution from all angles), (4.9) can be reduced to [37]:

$$\left[R^{\mathrm{iso}}\right]_{n,m} = \mathrm{sinc}\left(\frac{2\left\|\mathbb{U}_n - \mathbb{U}_m\right\|}{\lambda}\right), \tag{4.10}$$

where, $\|\cdot\|$ is the Euclidean norm.

4.3.2 Channel Model

The propagation models used in this research are more realistic because it considers multipath and can be represented by array response vectors rather than narrow flat fading channel. The channels are determined by the shape of the RIS and environment. Particularly, the wideband channel of [113] is implemented, where the BS-User direct uncontrollable link is given as:

$$h_d = \sum_{\ell=1}^{L_d} \sqrt{\beta_{d,\ell}} e^{-j2\pi f_c \tau_{d,\ell}} \begin{bmatrix} \mathrm{sinc}\left(0 + B\left(\varsigma - \tau_{d,\ell}\right)\right) \\ \vdots \\ \mathrm{sinc}\left(M - 1 + B\left(\varsigma - \tau_{d,\ell}\right)\right) \end{bmatrix}, \tag{4.11}$$

where, L_d is the number of propagation paths, $B_{d,\ell} \geq 0$ is the pathloss of the l-th path, $\tau_{d,\ell}$ is the propagation delay and ς is the sampling delay over the shortest path. Similarly, it is worth mentioning that explicit knowledge of individual channels h_l and g_l^H are not needed and the controllable composite link BS-RIS-User is given by:

$$V = \sum_{\ell=1}^{L_a} \sum_{\ell_b=1}^{L_b} \sqrt{\beta_{H,\ell}\beta_{G,\ell_b}} e^{-j2\pi f_c\left(\tau_{H,\ell}+\tau_{G,\ell}\right)} \Bigg) \left(a\left(\varphi_{H,\ell},\vartheta_{H,\ell}\right)\right.$$
$$\left.\odot a\left(\varphi_{G,\ell_b},\vartheta_{G,\ell_b}\right)\right) \begin{bmatrix} \operatorname{sinc}\left(0+B\left(\varsigma-\tau_{H,\ell}-\tau_{G,\ell_b}\right)\right) \\ \vdots \\ \operatorname{sinc}\left(M-1+B\left(\varsigma-\tau_{H,\ell}-\tau_{G,\ell_b}\right)\right) \end{bmatrix}^{\top}, \tag{4.12}$$

where, L_a and L_b are the propagation paths from the BS to the RIS and from the RIS to the users, respectively. $B_{H,\ell} \geq 0$, and $B_{G,\ell_b} \geq 0$, are the pathlosses from the BS to the RIS and from the RIS to the user, respectively. $\tau_{H,\ell}$ and τ_{G,ℓ_b} are the propagation delays to and from the RIS and $a(\varphi,\vartheta)$ is the array response vector with φ and ϑ are the azimuth and elevation angles. We perform pilot transmission in section V to estimate the channels h_d and V at the receiver however, accurate knowledge of the channel link G between the RIS and the users is needed to calculate the uncontrollable EMI so, we will assume the knowledge of G at the receiver. The simulations parameters are considered based on 3GPP channel models [161, 231].

4.4 Practical Phase Shift Model

The corresponding model for the n-th reflecting element impedance is provided by [23]:

$$\mathbb{Z}_n\left(C_n,\Omega_n^{ohm}\right) = \frac{j2\pi f_c I_1\left(j2\pi f_c I_2 + \frac{1}{j2\pi f_c c_n} + \Omega_n^{ohm}\right)}{j2\pi f_c I_1 + \left(j2\pi f_c I_2 + \frac{1}{j2\pi f_c c_n} + \Omega_n^{ohm}\right)}. \tag{4.13}$$

The bottom layer inductance, top layer inductance, effective capacitance, effective resistance, and carrier frequency of the incident signal are represented as $I_1, I_2, C_n, \Omega_n^{ohm}$ and f_c respectively. The reflection coefficient describes the portion of the reflected electromagnetic wave that is attributable to the discontinuity in impedance between the element $\mathbb{Z}_n\left(C_n,\Omega_n^{ohm}\right)$ and free space impedance $\mathbb{Z}_o$:

$$\Gamma_n = \frac{\mathbb{Z}_n\left(C_n,\Omega_n^{ohm}\right) - \mathbb{Z}_o}{\mathbb{Z}_n\left(C_n,\Omega_n^{ohm}\right) + \mathbb{Z}_o}. \tag{4.14}$$

Γ_n being a function of C_n, Ω_n^{ohm} and f_c, allows us to control and programme the reflected electromagnetic waves by changing the values of C_n, Ω_n^{ohm} and f_c. C_n has values that vary from 0.15 pF to 1.5 pF, $\Omega_n^{ohm} = 1$ ohm, $\mathbb{Z}_o = 377$, and $f = 4$GHz. The RIS element will scatter a sinusoidal signal impinging at frequency f with an amplitude of $|\Gamma_n|$ and a phase shift of $\arg(\Gamma_n)$. For example, in the case of a one-bit RIS, one PIN diode is required per RIS element, and more diodes are needed for more resolution but at the cost of complex design. Consequently, the RIS is adjusted by using multiple PIN diodes numbers assigned to every element. Two alternative capacitance values can be used with each PIN diode. In this investigation, we look at the in-

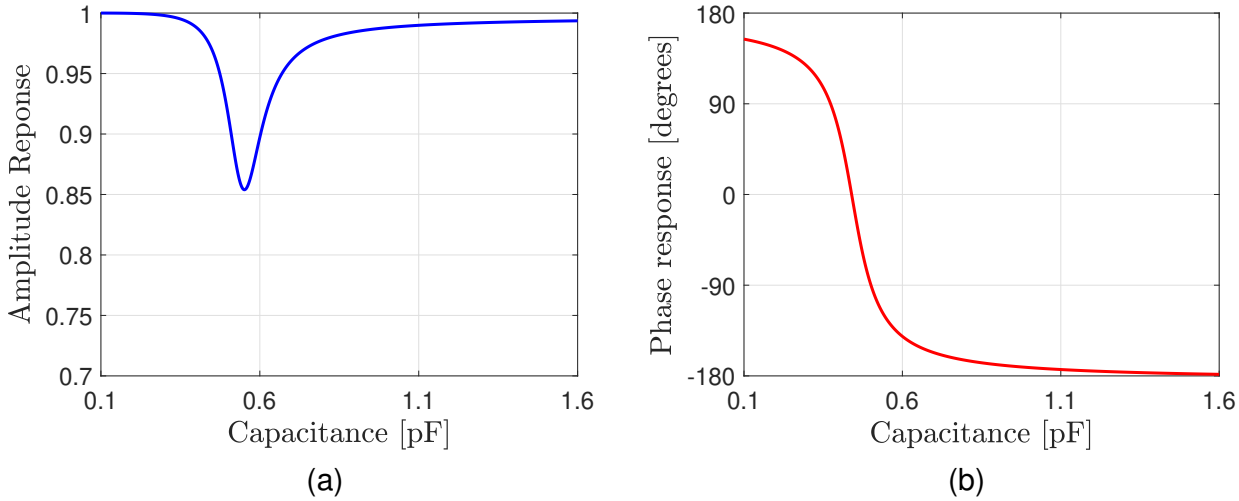

Figure 4.2: a) Amplitude and b) Phase responses versus C_n

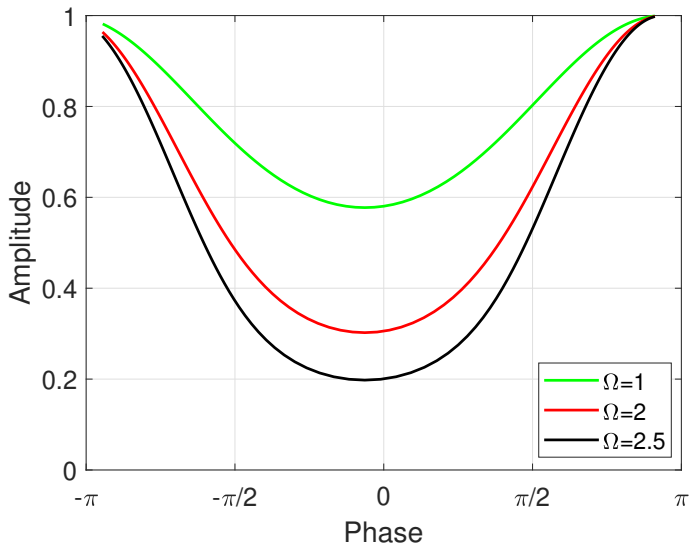

Figure 4.3: Reflected amplitude vs. phase shift for RIS element

formation rate for users for different capacitance value pairs that correlate to varying reflecting phase shifts per RIS element. Fig. 4.2 illustrates the responses of amplitude and phase for different values of capacitances. It was found that because the amplitude response and phase shifts of the reflecting element are typically non-linearly linked, they cannot be controlled separately. The reflection amplitude , as illustrated in Fig. 4.3, achieves a modest value at phase shift equals zero, but it grows consistently as the phase shift reaches 180 or -180 degrees and asymptotically approaches one. As a consequence, it is incorrect for many earlier research to assume that the amplitude response value is one.

The reflecting phase shift provided by each capacitance value varies. For instance, the capacitance values of 0.5011 pF and 0.3732 pF correspond to phases of -90 and 90 respectively,

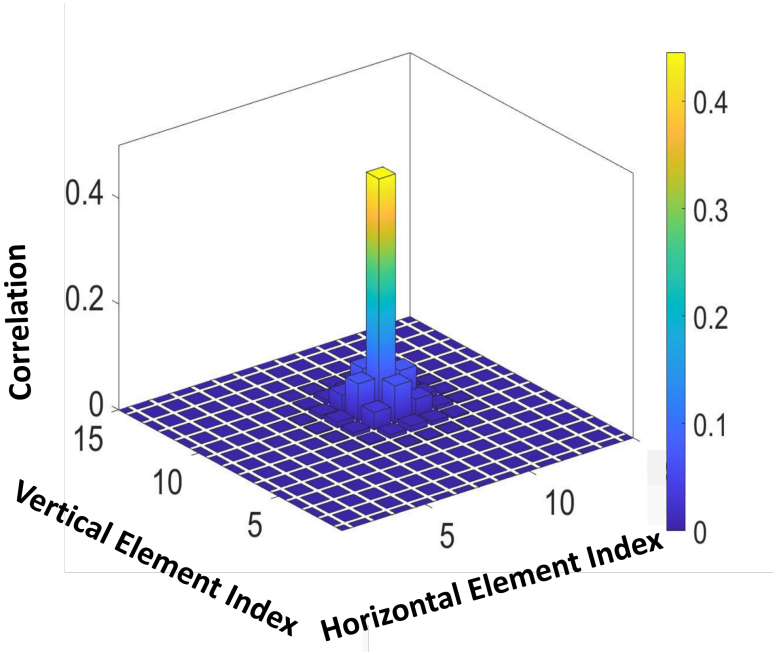

Figure 4.4: Assigned capacitance of itself and its surrounding elements is correlated with the actual capacitance of the RIS element at row 10 and column 10.

and will provide a 180 phase shift spacing per element. When RIS is included, the reflection coefficients can be expressed as follows [185]:

$$w_\theta = \begin{bmatrix} \Gamma(C_1, f_c) \\ \vdots \\ \Gamma(C_N, f_c) \end{bmatrix}, \tag{4.15}$$

where, $C_n \in \{C_1, \ldots, C_N\}$ is the actual capacitance value of element n. We used the statistical correlation model of the coupling effect in [185] to study the effect of MC on the performance:

$$C_n = \sum_{i=1}^{N} C_{i,\theta}^{\sim} \frac{100^{\frac{-d_{n,i}}{\lambda}}}{\sum_{j=1}^{N} 100^{\frac{-d_{n,i}}{\lambda}}}, \tag{4.16}$$

where, $d_{n,i}$ is the distance between element n and element i, $C_{i,\theta}^{\sim}$ is the capacitance assigned to element i and λ is the wavelength. By examining the element in row 10 of column 10, the factor multiplied by $C_{i,\theta}^{\sim}$, in (4.16) for the various elements is shown in Fig. 4.4. We see that the assigned capacitance of the element and the intended capacitance of its neighbours both affect the actual capacitance to 45% and 55%, respectively. The more closely two elements are together, the more they effect one another [185]. The effect of MC on the reflection coefficient phase response at the carrier frequency f_c = 4 GHz is illustrated in Fig. 4.5. The assigned capacitance value for the element is changed due to the MC effect and hence the corresponding phase is changed accordingly. For example in the case without MC, the assigned values of capacitance 0.37 pF and 0.5 pF are corresponding to phase shifts 90 and -90 degrees. However,

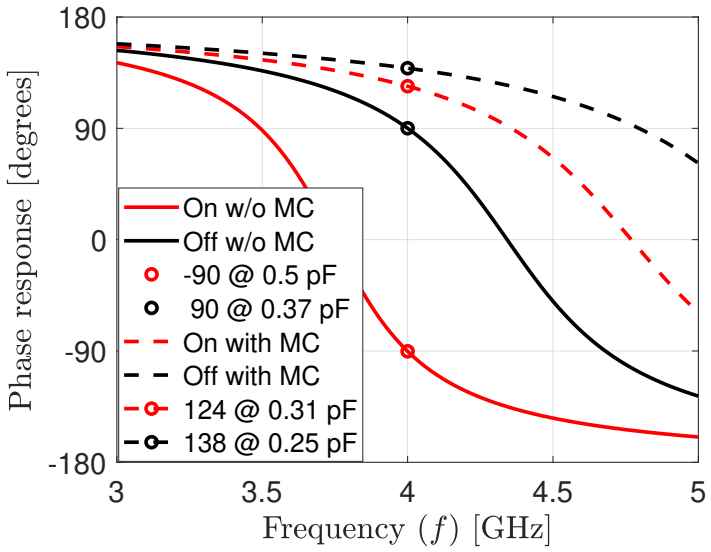

Figure 4.5: Reflection coefficients phase response in (4.14) considering mutual coupling at 4GHz frequency.

when considering MC, the actual values of capacitance will be 0.31 pF and 0.25 pF and that lead to a deviation in the phase shifts from 90 and -90 degrees to 138 and 124 degrees. We will show the effect of the MC on the achievable data rate in the next sections.

4.5 Pilot Transmission and Channel Estimation

The pilot signaling will be based on employing the columns of a Hadamard matrix, whose entries are either +1 or 1, with a scheme that makes the columns mutually orthogonal [243]. The received signal from the pilot transmission will be expressed as in [185] with extra step that add the EMI e_{EMI} in the received signal in addition to the receiver noise. EMI is seen as noise in the context of wireless communications due to the fact that EMI is produced by uncontrolled signals.

$$\begin{aligned} r &= xF\left(h_d[1,\ldots\ldots,1] + V^{\top}[w_{\theta_1},\ldots\ldots,w_{\theta_N}]\right) + \mathcal{G}e_{EMI} + e \\ &= xF\left[h_d, V^{\top}\right]\begin{bmatrix} 1,\ldots\ldots,1 \\ \mathcal{P} \end{bmatrix} + \mathcal{G}e_{EMI} + e, \end{aligned} \tag{4.17}$$

where, $r = [\bar{r}_1,\ldots\ldots,\bar{r}_N] \in \mathbb{C}^{N\times N}$ contains all the received signals, and the term $\mathcal{G}e_{EMI} = \left[\overline{\mathcal{G}}\bar{e}_{EMI_1},\ldots\ldots\overline{\mathcal{G}}\bar{e}_{EMI_N}\right] \in \mathbb{C}^{N\times N}$ is the interference matrix, $e = [\bar{e}_1,\ldots\ldots,\bar{e}_N] \in \mathbb{C}^{N\times N}$ is the noise matrix and $\mathcal{P} = [w_{\theta_1},\ldots\ldots,w_{\theta_N}]$ gathers all the RIS configurations. The assigned matrix $\widehat{\mathcal{P}} = \mathcal{P} + E$ where E is the unknown hardware mismatch. Let $\dagger$ represents the Moore-Penrose inverse, then the least square (LS) estimate of the received signal in 4.17 can be calculated as

follows [113]:

$$\frac{1}{x}F^{\dagger}r\begin{bmatrix}1,\ldots,1\\ \hat{\mathcal{P}}\end{bmatrix}^{\dagger}=\left[h_d,V^H\right]\begin{bmatrix}1,\ldots,1\\ \hat{\mathcal{P}}\end{bmatrix}\begin{bmatrix}1,\ldots,1\\ \hat{\mathcal{P}}\end{bmatrix}^{\dagger}+\underbrace{\left[h_d,V^H\right]\begin{bmatrix}0,\ldots,0\\ E\end{bmatrix}\begin{bmatrix}1,\ldots,1\\ \hat{\mathcal{P}}\end{bmatrix}^{\dagger}}_{\text{Hardware Mismatch}}$$
$$+\underbrace{\frac{1}{x}F^{\dagger}\mathcal{G}e_{EMI}\begin{bmatrix}1,\ldots,1\\ \hat{\mathcal{P}}\end{bmatrix}^{\dagger}}_{\text{Interference}}+\underbrace{\frac{1}{x}F^{\dagger}e\begin{bmatrix}1,\ldots,1\\ \hat{\mathcal{P}}\end{bmatrix}^{\dagger}}_{\text{Noise}}, \tag{4.18}$$

where, $\left[h_d,V^H\right]$ is the desired channel term. The number of pilot signals is sufficient to obtain a unique LS estimate for the channel coefficients. However we can reduce the dimension of the estimation problem by taking the advantage that the channel components within each column of the RIS are equal so, equation (4.17) can be expressed as:

$$r=xF\left[h_d,V_{row}^H\right]\begin{bmatrix}1,\ldots.,1\\ \mathcal{A}^H\mathcal{P}\end{bmatrix}+Ge_{EMI}+e, \tag{4.19}$$

where, $\mathcal{A}=(1_{N_{\mathrm{V}}}\otimes I_{N_{\mathrm{H}}})\in\mathbb{C}^{N\times N_{\mathrm{H}}}$, is the projection matrix and $\otimes$ denotes the Kronecker product. $V_{\mathrm{row}}\in\mathbb{C}^{N_{\mathrm{H}}\times M}$ is the reduced dimension channel coefficients for RIS rows. Consequently, it is possible to compute the LS estimate as follows:

$$\left[\hat{h}_d,\hat{V}_{\mathrm{row}}^{\top}\right]=\frac{1}{x}F^{\dagger}r\begin{bmatrix}1,\ldots\ldots,1\\ \mathcal{A}^H\hat{\mathcal{P}}\end{bmatrix}^{\dagger}. \tag{4.20}$$

It is necessary to choose the optimal vector $\hat{\mathcal{P}}$ in order to maximize $\hat{h}_d$ and $\hat{V}_{\mathrm{row}}^{\top}$ with regard to the RIS configurations. We must identify a considerable tradeoff among all K subcarriers to optimize the RIS. In the academia, there are heuristic methods that rely on successive convex approximation, semidefinite relaxation, and strongest tap maximization (STM) in the time domain [160, 178]. However, we will use the same methodology in [185] but the gradient descent instead of the power method in order to ensure that it works for LoS and NLoS channels as shown in Algorithm 2. The gradient descent method starts with the initial solution $\bar{a}_0$ and ending with calculating the optimized reflection coefficient vector w_{θ} for each user. The output of Algorithim 1 is to get the optimized $w_{\theta_{\mathrm{optimized}}}$ in order to achieve the maximized information rate for each user.

4.6 Dataset

We used the Dataset-2 of [185] which takes into account 50 users and contains N received OFDM signal blocks for each user obtained with the pilot transmission $\widehat{\mathcal{P}}$ with additional mod-

Algorithm 2: Gradient descent method for optimizing the data rate $\mathcal{R}$

1: Select $w_{\theta_{\text{pilot}}} \in [w_{\theta_1}, \ldots\ldots, w_{\theta_N}]$ from the received signal r in (4.17) that gives the maximum data rate in (4.8) and set $w_\theta = w_{\theta_{\text{pilot}}}$
2: Let $\mathcal{V} = \left[\hat{h}_d, \hat{V}_{\text{row}}^\top\right]^H \left[\hat{h}_d, \hat{V}_{\text{row}}^\top\right]$ and $\bar{a}_0 = \begin{bmatrix} 1 \\ w_{\theta_{\text{pilot}}} \end{bmatrix}$
3: Compute $\mathcal{V}\bar{a}_i$
4: Set $n = 1$
5: **for** $n <$ Maximum number of iterations **do**
6: set $\mu = \gamma/\lambda \left(\sqrt{\mathcal{V}}^H \sqrt{\mathcal{V}}\right)$ with $\gamma \in [0,1]$ [228] and λ is the wavelength
7: Update $\bar{a}_{i+1} = \bar{a}_i + \mu \mathcal{V}\bar{a}_i$
8: Set $a_{i+1} = e^{j \arg(\bar{a}_{i+1})}$
9: Rotate the solution to ensure that the 1st entry is 1 for the direct channel h_d (uncontrollable)
10: Quantize phases of a_{i+1} to be 1 or -1 to get the optimized $w_{\theta_{\text{pilot}}}$ vector.
11: **end for**
12: We get $w_{\theta_{\text{Optimized}}}$
13: Evaluate the new data $\mathcal{R}_{new}$ with $w_{\theta_{\text{Optimized}}}$ according to (4.8) by setting $w_\theta = w_{\theta_{\text{optimized}}}$

ifications that include the EMI and MC. We considered the EMI term $w_\theta G_k^H e_{EMI}$ in (4.3) to the received signals of all 50 users to study the effect of interference on the information rate for users. Moreover, we set the correlation matrix in the Dataset-2 for the capacitance to unity matrix I_N to compare the achievable data rate with and without MC using the statistical model defined in (4.16).

4.7 RIS Optimization with The Knoweledge of EMI

In this part of the chapter, we give an example of enhancing the data rate for a single user when the RIS is aware of the EMI, we look at the issue of maximizing the sum data rate at the user by finding the optimal transmit power P to be distributed across all subcarriers based on the power limitation for each subcarrier and the optimal phase matrix w_θ for all RIS elements. However, It is worthwhile to optimize if configuring the RIS relies on the EMI and the awareness of the spatial correlation matrix $\mathcal{R}$ would result in a higher data rate. The SNR cab be represented as follows:

$$SNR = \frac{P\left|\bar{h}_\theta\right|^2}{A\sigma^2 \mathcal{G}^H R \mathcal{G} + \sigma_e^2} = \frac{P\left|h_d + V^H w_\theta\right|^2}{A\sigma^2 \mathcal{G}^H R \mathcal{G} + \sigma_e^2} \tag{4.21}$$

We deliberately mention the signal to noise ratio because we consider the interference as a noise. Let us neglect the direct channel and rewrite (4.21) as follows:

$$SNR = \frac{P}{\sigma_e^2} \frac{w_\theta^H \mathcal{A} w_\theta}{w_\theta^H q w_\theta + 1} \tag{4.22}$$

Table 4.1: Simulation Parameters

System Parameter	Simulation value
Carrier frequency f_c	4e9 Hz
Speed of light	3e8 m/s
Wavelength λ	0.075 m
Number of elements N	4096
BS Location in meter	$\begin{bmatrix} 40 & -150 & 0 \end{bmatrix}^\top$
User Location in meter	$\begin{bmatrix} 20 & 0 & 0 \end{bmatrix}^\top$
Pathloss Model NLoS	$34.53 + 38\log_{10}(d)$
Pathloss Model LoS	$30.18 + 26\log_{10}(d)$
L_a,L_b and L_d	100, 51 and 100 respectively
Number of channel taps M	23
Number of subcarriers K	1000
Transmit Power P	15 Watt
Bandwidth B	15e6 Hz

where $\mathcal{A} = VV^H$ and $q = \frac{A}{\sigma_e^2}\sigma^2 \mathcal{G}^H R \mathcal{G}$. Consequently, we can represent (4.22) as:

$$SNR = \frac{P}{\sigma_e^2} \frac{w_\theta^H \mathcal{A} w_\theta}{w_\theta^H \mathcal{C} w_\theta} \tag{4.23}$$

where $\mathcal{C} = q + I_N$. So, it is necessary to address the following problem in order to maximise the SNR in (4.23):

$$\begin{aligned} \max_{P, w_\theta, \bar{w}_\theta} \quad & \left(\bar{w}_\theta^H \mathcal{D} \bar{w}_\theta\right) \\ \text{s.t} \quad & |[w_\theta]_i| = 1, \qquad \forall_i \in N \\ & \bar{w}_\theta = \mathcal{C}^{1/2} w_\theta \\ & \tfrac{1}{K} \textstyle\sum_{s=0}^{K-1} p_s \leq P, \\ & p_s \geq 0, \qquad \forall_k \in K \end{aligned} \tag{4.24}$$

where $\mathcal{D} = \left(\mathcal{C}^{-1/2}\right)^H \mathcal{A} \mathcal{C}^{-1/2}$. The optimization problem is non-convex over the unit modular constraint on all RIS elements and the vector w_θ does not vary with the subcarrier index k. This constraint ensures that each RIS element's reflection has no pathloss. Furthermore, unlike relays, RIS components do not amplify or decode then convey a received signal, necessitating the use of unit magnitude RIS elements. The initial solution can be selected to be the best configuration and then compute $\mathcal{D}\bar{w}_{\theta_i}$ and after that quantize phases of all candidates $\arg([w_\theta]_i)$ where $i = 1, \ldots, N$ to be either $\left\{e^{j\pi/2} \text{ or } e^{-j\pi/2}\right\}$ if $\arg([w_\theta]_i) \in [-\pi, 0)$ and $\arg([w_\theta]_i) \in [0, \pi)$ respectively. Finally iterate until convergence.

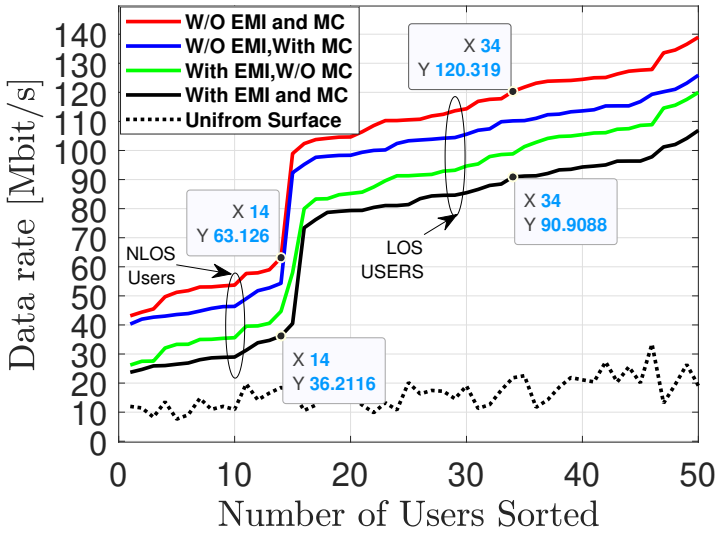

Figure 4.6: The Data rate achieved with the presence of both MC and EMI.

Water-Pouring Algorithm

Moreover, the power P should be optimized all over the subcarriers. The power distribution for all subcarriers $p_0, \ldots, p_{K-1}$ are satisfying $P = \frac{1}{K}\sum_{s=0}^{K-1} p_s$ where $p_s = E\left\{|\bar{x}[s]|^2\right\}$ is the power related to subcarrier s. Taking into account the EMI, The power allocation for the subcarriers can be optimized by the water-pouring algorithm.

$$p_s = \max\left(\mu - \frac{A\sigma^2 \mathcal{G}^H R \mathcal{G} + \sigma_e^2}{\left|f_v^H H_d + f_v^H V^\top w_\theta\right|^2}, 0\right) \tag{4.25}$$

Where the parameter $\mu \geq 0$ is chosen to fulfil $\frac{1}{K}\sum_{s=0}^{K-1} p_s = P$. Consequently, the power allocated for s-th subcarrier p_s is dependent on the water level parameter μ.

The water-pouring algorithm is used to allocate the transmitted power fairly to all subcarriers where the weak channel gain is allocated less power while the strong channel gain is allocated more power however, the total allocated power should not exceed the total power (15 Watt) as per Fig. 4.7. In Fig. 4.7, we show comparison for the power allocation between the cases with and without EMI to demonstrate how the algorithm allocate the power to each subcarrier taking into consideration the channel gain status.

4.8 Simulation Results

Figure 4.6 displays the data rates attained by the 50 users in various configuration scenarios. The case without EMI and MC is the reference that we will compare the other setups with. We investigated the effect of MC and EMI together and separately on the system performance and

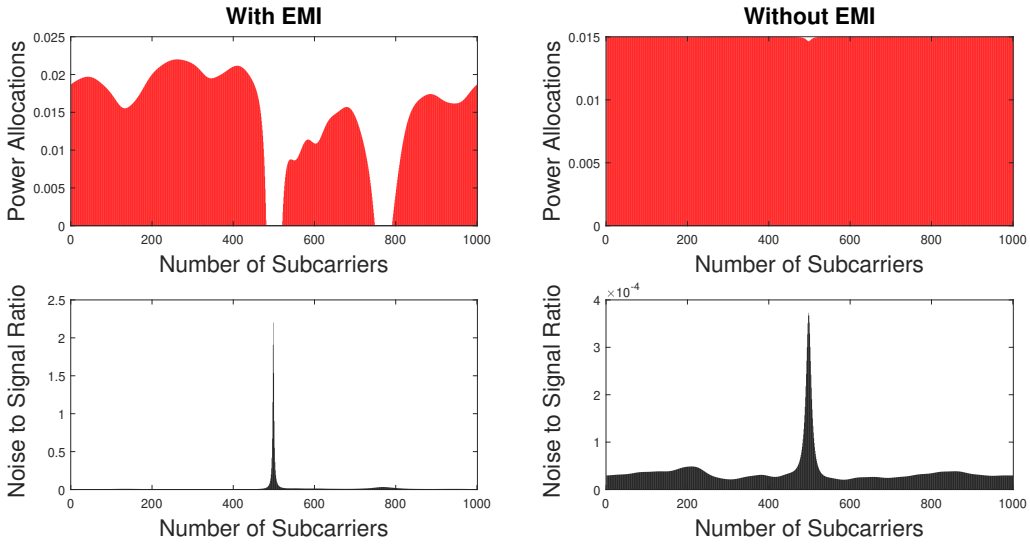

Figure 4.7: Power allocation for subcarriers in two cases: with and without EMI

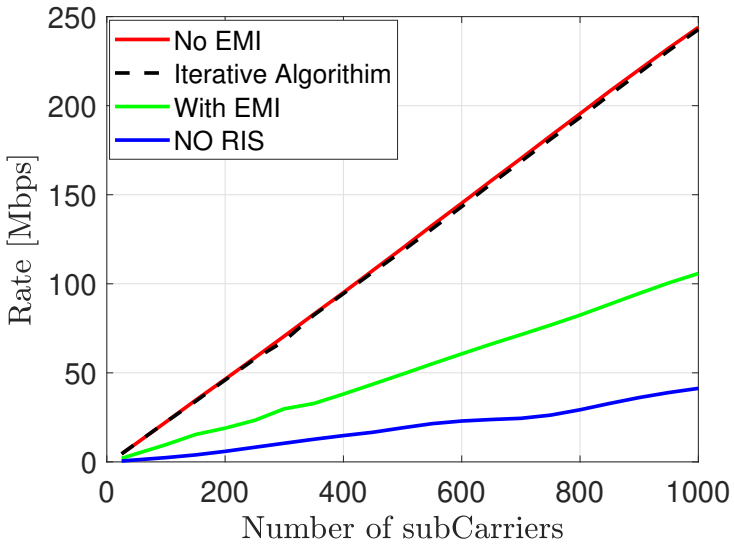

Figure 4.8: Data rate against number of subcarriers with and without EMI

notice that the data rate is dramatically declined with the presence of both MC and EMI. We select user 14 among the NLoS users and user 34 from the LoS users to calculate the gap in the data rate between the ideal reference case and the case that includes both MC and EMI. We notice a degradation of 30 Mbits/s for each user and this confirms that MC and EMI are parameters that we should consider in RIS design especially when the surface is large which exactly corresponds to the situation when the RIS is most beneficial.

In this part, we provide simulation results to assess the performance of the data rate when the RIS is aware of the EMI. Table I shows the system parameters used in the Monte Carlo simulations.

In Fig. 4.8, we considered the case when there is no EMI is the reference to be compared with the cases with EMI and uniform surface (NO RIS). There is a remarkable difference between the cases with and without EMI so the iterative algorithm enhanced the rate to be very close to the case without EMI. Consequently, the RIS must be aware of EMI in order to get higher data rate for the user.

4.9 Summary

In this research, we demonstrated the effect of EMI and MC on the achievable data rate for each user. The pilot transmission is utilized to estimate the direct and the indirect channels. A gradient descent algorithm 2 is developed to allocate the best and the high quality configuration to enhance the information rate per each LoS and NLoS user. Since RIS technology and 6G research are intertwined, it is now important to find improved communication models that can take advantage of electromagnetic characteristics and be compatible with practical applications.

Chapter 5

Near-field Localization with RIS-assited Communication

This chapter focuses on examining the problem of localizing UE in the uplink scenario using RIS based lens. We carry out a thorough analysis of the Fisher information matrix (FIM) and assess the influence of various RIS-based lens configurations using an actual RIS phase-dependent amplitude variations model. Furthermore, to reduce the complexity of the maximum likelihood (ML) estimator, a simple localization algorithm-based angular expansion is presented. Simulation results show superior localization performance when prior location information is available for directional and positional channel configurations. The position error bound (PEB) and the root mean square error (RMSE) are studied to evaluate the localization accuracy of the user utilizing the realistic RIS phase-dependent amplitude model in the near-field region. Furthermore, the achievable data rate is obtained in the same region using the realistic RIS phase-dependent amplitude model. It is noticed that adopting the actual RIS phase-dependent amplitude model under the near-field channel increases the localization error and degrades the data rate performance for amplitude value less than one so, the unity assumption of the RIS phase shift model used widely in the literature is inaccurate.

5.1 Introduction

In the realm of wireless communication networks, radio localization presents a feasible substitute for acquiring user location data within environments where global positioning system (GPS) signals are unavailable [244]. With each successive generation of mobile communication, novel features are introduced to facilitate high-speed communication, while simultaneously enhancing the precision of localization capabilities [245, 254]. Radio localization techniques operate under the fundamental concept that the radio signals contain valuable information regarding the positional data of network nodes. In fourth-generation (4G) systems, users make use of the time-of-arrival (ToA) estimation [256] in relation to each BS. This estimation relies on factors

such as the distance between the user and the BS, as well as the clock bias at the user. Using ToA from at least four LoS BSs, users can calculate three-time difference of arrival (TDoA) measurements to determine their 3D location. In 5G systems that operate in mm-Wave frequency bands, both the BS and potentially the user are equipped with multiple antennas. In this scenario, the channel is characterized by both delays and angles. The receiver determines the angle-of-arrival (AoA), while the transmitter determines the angle-of-departure (AoD). This parameterization of the channel considers both the spatial angle and the delay in the propagation of signals [12, 255, 259].

The growing prevalence of applications such as smart factories, automated/assisted driving, and augmented reality has led to increasingly stringent requirements for positioning accuracy in 5G and 6G communication networks. In 5G, the wider bandwidth and larger antenna arrays have improved localization accuracy, making it possible to efficiently localize devices using just one BS [246, 258]. Moreover, the reliability of localization provided by 5G and 6G communications is of utmost significance. As 5G and 6G systems can operate in high-frequency mm-Wave and THz bands, the links between devices are susceptible to obstacles. Since LoS propagation is typically necessary for precise location estimation, existing localization methods yield significant estimation errors if the LoS link is obstructed [247].

Alongside their advantages for communication purposes, RISs offer reliable and highly precise position estimation capabilities with low cost and high energy efficiency [3, 82, 240]. When the LoS link is obstructed, an RIS can establish a virtual LoS link, allowing for accurate delay measurements when utilizing wideband signals [226]. Unlike non-reconfigurable scatterers present in the environment, RISs have the ability to adjust the phase shifts of their reflecting elements, resulting in a significant beamforming gain. Additionally, RISs offer a large number of elements, further contributing to the high resolution achieved in the localization process. This capability enables RISs to provide enhanced resolution in AoA for uplink localization or AoD for downlink localization [248].

For communication and localization applications involving RISs, it is crucial to have precise and well-defined control over the RIS. This requires the development of proper and straightforward models for RIS phase control. These models should ideally incorporate various factors such as the effects of MC [185, 261], calibration, quantization [260] and power losses per element [262]. Most existing studies on RIS localization have focused on ideal phase shifters and have neglected the impairments mentioned above. As a result, it remains unknown how these proposed localization approaches would perform when these impairments are taken into account. However, understanding the impact of these impairments is essential as it can significantly influence the effectiveness and reliability of RIS-based localization methods [249, 250].

In this chapter we extended the work in [250]. Our research focuses on the exploration of 3D localization using a simplified RIS lens design, as described in reference [251]. This design incorporates adjustable RIS lenses and a sole antenna connected to a receiving RF chain. We ad-

dress the issue of RIS-aided geometric near-field localization in scenarios where LoS blockage is present. To tackle this challenge, we adopt a practical RIS amplitude model [23], which is based on the corresponding circuit setup of a single RIS element. We examine the impact of the mismatch between the ideal, lossless RIS amplitudes and the actual phase-dependent amplitudes on the accuracy of localization. This investigation is carried out by evaluating the PEB and assessing the RMSE analysis to quantify the degradation in localization performance. Furthermore, we have investigated the realistic RIS phase-dependent amplitude model on the communication system by evaluating the achievable data rate in the near-field channel. The achievable data rate degrades with distance in the near-filed region and this coincides with localization error behavior which increases gradually with distance from the RIS. Both achievable data rate and localization error show inferior performance when adopting the RIS phase-dependent amplitude model for amplitude value less than one so, the unity assumption of the RIS phase shift model used widely in the literature leads to over-optimistic and incorrect localization and communication performance results.

The rest of the chapter is organized as follows: Section 5.2 presents the system model which includes the signal and the RIS models in addition to the problem statement. The FIM analysis is given in Section 5.3, while the location estimation is shown in Section 5.4. Section 5.5 discusses the achievable data rate in the near-field regime. Section 5.6 represents the derivation of FIM and PEB at the presence of EMI. The simulation results and the summary are given in Sections 5.7 and 5.8, respectively. Finally, section **??** lists the publications resulted from this chapter

5.2 System Model

5.2.1 Geometry and Signal Model

We provide a detailed description of the system model utilized for localization in 3D with the help of the RIS lens. Additionally, we will introduce the near-field channel and the realistic amplitude-dependent phase model to evaluate the performance of the PEB, RMSE and the achievable data rate.

We examine a wireless setup comprising of a single user transmitting from position $p = [x,y,z]^\top$, and an N-element RIS lens positioned in the XY plane with reference point $[0,0,0]^\top$. The RIS lens is placed near a single antenna equipped with a corresponding RF chain for reception. The antenna is located at $p_{\text{ant}} \in \mathbb{R}^3$. In Fig. 5.1a, the system setup is depicted to present the components of the communication system, while Fig. 5.1b presents the 3D coordinate system that shows the positional and angular information of the user and RIS. The spacing between the horizontal and vertical elements is set to $\lambda/2$ where, λ is the wavelength of the carrier frequency. The n^{th} element of the RIS lens is located at $\mathcal{E}_n = [x_n, y_n, 0]^\top \in \mathbb{R}^3$ which is equivalent to the spherical coordinate $\mathbb{L}_n [\cos\Psi_n, \sin\Psi_n, 0]^\top \in \mathbb{R}^3$. The $\mathbb{L}_n$ refers to the element's distance

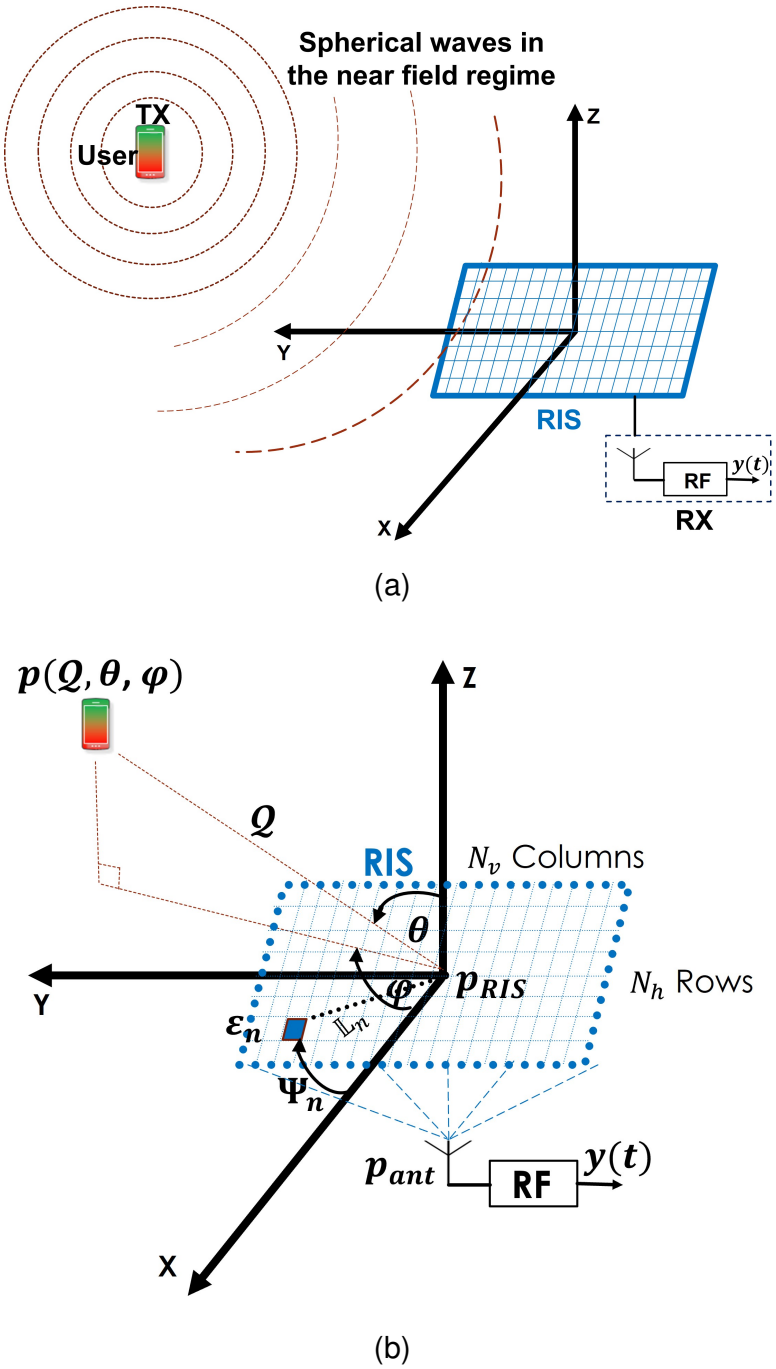

Figure 5.1: (a). System setup (b). Coordinate system

from the RIS origin to the element n and Ψ_n is the n^{th} element azimuth angle as illustrated in Fig. 5.1b. Each element exhibits a directivity pattern described by $\mathcal{D}(\vartheta,\varphi) = \cos^2(\varphi)\cos(\vartheta)$, where $\varphi \in [0, 2\pi]$ represents the azimuth angle between the X-axis and the vertical projection of p on the XY plane and $\vartheta \in [0, \pi/2]$ represents the elevation angle between the Z-axis and the user location p. From this point forward, we will refer to the AoAs as ϑ and φ. We define the wave vector $k(\varphi,\vartheta) = \frac{2\pi}{\lambda}[\cos(\vartheta)\cos(\varphi), \cos(\vartheta)\sin(\varphi), \sin(\vartheta)]^\top$. To express the unknown position vector of the user, p, we can utilize the wave vector. It can be represented as

$p = -\lambda \mathcal{Q} k(\vartheta, \varphi)/2\pi$, where $\mathcal{Q}$ is the Euclidean distance between p and the reference location of the RIS, denoted as $\mathcal{Q} \triangleq \|p\|$. Additionally, we model the prior knowledge of the user's location as a Gaussian probability density function (PDF) $f(p)$. This PDF is characterized by a mean, $\mathbb{Y}_p \in \mathbb{R}^3$, and a covariance matrix $\mathbb{V}_p \in \mathbb{R}^{3\times 3}$. In the given scenario, the user transmits a narrowband signal x_t over a series of T transmissions to the receive antenna through the RIS elements. The transmitted signal follows the requirements that the $\mathbb{E}\left\{|x_t|^2\right\} = E_s$. In general, we presume that $x_t = \sqrt{E_s}$ for any given transmission t. The received signal at the output of the RF receiver can be represented mathematically for each time instance t as:

$$r_t = e^{j\theta} h_{\text{ant}}^{\top} \mathbf{w}_{\theta t} (\mathcal{W}(p) \odot \mathcal{S}(p)) x_t + e_t, \tag{5.1}$$

where, $\mathbf{w}_{\theta t} = \text{diag}\left(w_{\theta t,0} \dots w_{\theta t,N-1}\right)$ is the reflection coefficients for N RIS lens elements at time t and $w_{\theta t,n}$ represents the amplitude $\in (0,1]$ and phase shift $\in [0, 2\pi)$ for RIS element n at time t. The practical RIS phase shift model is provided next. Furthermore, $\theta = -\frac{2\pi\mathcal{Q}}{\lambda} + \theta_{\text{sync}}$ represents the phase synchronization between the receiver and transmitter. The vector $h_{\text{ant}} \in \mathbb{C}^{N\times 1}$ comprises the gains of the propagation channels from the RIS to the receiver. The vector $\mathcal{W}(p) \geq \mathbf{0}_N$ represents the amplitudes of the propagation channels between the RIS elements and the transmitter while, the channel phases can be represented by the vector $\mathcal{S}(p) \in \mathbb{C}^{N\times 1}$. The noise vector e_t represents uncorrelated zero-mean additive Gaussian noise with a variance of $N_0/2$ per real dimension. By introducing $u_t = \mathbf{w}_{\theta t} h_{\text{ant}}$, we can define $U = [u_1, u_2, \dots, u_T] \in \mathbb{C}^{N\times T}$. Additionally, $\mathbf{x} = [x_1, x_2, \dots, x_T]^{\top}$ and $\mathbf{e} = [e_1, e_2, \dots, e_T]^{\top}$. In this context, the measurement vector $\mathbf{r} = [r_1, r_2, \dots, r_T]^{\top}$ can be represented as:

$$\mathbf{r} = e^{j\theta} \,\text{diag}(\mathbf{x}) U^{\top} (\mathcal{W}(p) \odot \mathcal{S}(p)) + \mathbf{e}. \tag{5.2}$$

The model employed in signal processing literature for the localization of objects in the near-field is essentially the far-field model of electromagnetics, or a closely related approximation [264]. This work neglects the consideration of electromagnetic near-field effects within the Fraunhofer distance. In the near-field channel model, the steering vector $\mathcal{S}(p)$ for a specific position p is defined as:

$$[\mathcal{S}(p)]_n = \exp\left(-j\frac{2\pi}{\lambda}\left(\|p - \mathcal{E}_n\| - \mathcal{Q}\right)\right), \tag{5.3}$$

and the amplitude $\mathcal{W}(p) = \mathcal{W}\mathbf{1}_N$ is constant for all RIS elements. In the improved near-field channel model, however, the upper bound of the amplitudes $\mathcal{W}(p)$ can be presented as per [224]:

$$[\mathcal{W}(p)]_n^2 = (4\pi)^{-1} \sum_{\substack{\mathrm{x}\in\mathcal{X}_n \\ \mathrm{y}\in\mathcal{Y}_n}} \frac{\mathrm{xy}}{(\mathrm{y}^2 + z^2)\,\mathcal{B}(\mathrm{x},\mathrm{y})} + 2\tan^{-1}\left(\frac{\mathrm{xy}}{z^2\mathcal{B}(\mathrm{x},\mathrm{y})}\right), \tag{5.4}$$

where, the terms, $\mathcal{X}_n = \{d_h/2 + (x_n - x), d_h/2 - (x_n - x)\}$, $\mathcal{Y}_n = \{d_h/2 + (y_n - y), d_h/2 - (y_n - y)\}$

and $\mathcal{B}(\mathrm{x},\mathrm{y}) = \sqrt{x^2/z^2 + y^2/z^2 + 1}$. Furthermore, $d_h = d_v = \lambda/2$ is the spacing between RIS elements so each n^{th} element of the RIS lens, with $n = 1, 2, \ldots, N$, have the size $A = d_h \times d_v$.

The model described in (5.3) represents the conventional near-field model, wherein the amplitude remains unchanged, but the phase changes according to the distance from each element of the RIS. On the other hand, the model presented in (5.4) corresponds to an enhanced near-field model, as proposed in [224]. In this improved model, the element's amplitude is determined by its relative position to the location of the user, while the phase remains unchanged, as in (5.3). In comparison to the conventional and enhanced near-field channels, the phase in the far-field channel is given by $[\mathcal{S}(p)]_n = \exp\left(-j\mathcal{E}_n^{\top} k(\vartheta, \varphi)\right)$, while the amplitude remains unchanged for all RIS elements $\mathcal{W}(p) = \mathcal{W}\mathbf{1}_N$.

5.2.2 RIS Phase Shift Model

Amplitude Variations

We adopt the practical model proposed in [23] which describes the fundamental relationship between the reflection amplitude and the phase shift of the RIS. Consequently, we examine the near-field localization aided by RIS by incorporating an actual RIS amplitude model, which is based on the corresponding circuit setup of single RIS elements. More specifically, the performance loss in localization resulting from the discrepancy between the ideal and the actual model responses will be explored in this work. The actual model considers variations in the amplitude, which are, in turn, determined by the phase, contrary to the commonly held assumption in the literature, which assumes a constant amplitude. In the term, $\mathbf{w}_{\theta t} = \text{diag}\left(w_{\theta t,0} \ldots w_{\theta t,N-1}\right)$, let $w_{\theta t,n} = \beta_{t,n}(\Theta_{t,n})\, e^{j\Theta_{t,n}}$ where, $\Theta_{t,n} \in [-\pi, \pi)$ is the phase shift and $\beta_{t,n}(\Theta_{t,n}) \in [0,1]$ is the amplitude. The amplitude as a function of the phase can be represented as:

$$\beta_{t,n}(\Theta_{t,n}) = (1 - \beta_{\min}) \left(\frac{\sin(\Theta_n - \nabla) + 1}{2}\right)^{\Delta} + \beta_{\min}\,. \tag{5.5}$$

The constants $\beta_{\min} \geq 0$, $\nabla \geq 0$, and $\Delta \geq 0$, are parameters associated with the particular circuit implementation being considered. It should be noted that when $\beta_{\min}$ is equal to 1 (or Δ is equal to 0), (5.5) is essentially the same as the ideal phase shift model with unity amplitude. Figure 5.2 shows the amplitude variations for different values of $\beta_{\min}$. It is evident from Fig. 5.2 that when $\beta_{\min} = 1$, the amplitude response is one while, it fluctuates as a sine wave when $\beta_{\min}$ is set to 0.1.

Design of Phase Profile

The accuracy of determining the user location relies on the selection of the profiles of the RIS phases $\mathbf{w}_{\theta t}$, while the amplitudes are not assumed to be one as mentioned widely in the literature, however, they are distributed from $[0,1]$. To eliminate the impact of phases in the channel h_{ant},

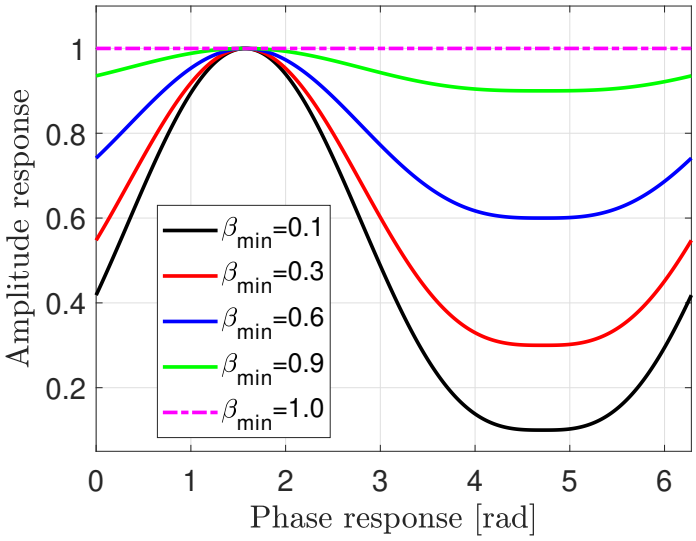

Figure 5.2: Amplitude variations for different values of $\beta_{\min}$, $\Delta = 0$ and $\nabla = 1.5$.

we assign $\mathbf{w}_{\theta t} = \mathbf{w}_{\text{ant}}\tilde{\mathbf{w}}_{\theta} t$, where the known phases $\mathbf{w}_{\text{ant}} = \text{diag}\left(u_{\text{ant},0}, \ldots, u_{\text{ant},N-1}\right)$ are chosen such that $\left[h_{\text{ant}}^{\top}\mathbf{w}_{\text{ant}}\right]_n = \left|\left[h_{\text{ant}}^{\top}\right]_n\right|, \forall n$ [52]. Where $u_{\text{ant},n} = \left[\left(h_{\text{ant}} / |h_{\text{ant}}|\right)^*\right]_n$. This approach leverages the information about h_{ant} to ensure the desired outcome. We are now left with the task of designing $\tilde{\mathbf{w}}_{\theta} t = \text{diag}\left(\tilde{w}_{\theta t,0}, \ldots, \tilde{w}_{\theta t,N-1}\right)$. We examine three configurations for $\tilde{w}_{\theta t,n}, \forall n, t$. Firstly for the random configuration, we assign $\tilde{w}_{\theta t,n} = \exp\left(j\Psi_{t,n}\right)$ where, $\Psi_{t,n} \sim \mathcal{U}(0, 2\pi)$ are independently and randomly distributed for every n^{th} RIS element and t^{th} time instant. Secondly, we set the directional phase configuration as $\tilde{w}_{\theta t,n} = \exp\left(+j\mathcal{E}_n^{\top} k\left(\vartheta^{(k)}, \varphi^{(k)}\right)\right)$. The priori PDF $f(p)$ is used to generate the phase samples of $\vartheta^{(k)}$ and $\varphi^{(k)}$. Lastly, the positional phase configuration is obtained as $\tilde{w}_{\theta t,n} = \exp\left(+j\frac{2\pi}{\lambda}\left(\left\|p^{(k)} - \mathcal{E}_n\right\| - \mathcal{Q}^{(k)}\right)\right)$. We use the $f(p)$ to extract the position $p^{(k)}$ and the distance $\mathcal{Q}^{(k)}$ samples.

To show the effect of the actual phase shift model in (5.5) on the SNR, we assume a priori position distribution with $\mathbb{Y}_p = [-0.1, -0.1, -0.1]^{\top} \in \mathbb{R}^3$ and $\mathbb{V}_p = 0.01 I_3 \in \mathbb{R}^{3\times 3}$. Figure. 5.3 shows the random, directional, and positional SNR for different values of $\beta_{\min} = \{0.1, 1\}$. Generally, in the random scenario, we notice that the SNR remains consistent across all locations with decreased SNR near the outer edges of the RIS subject to the pathloss. However, higher SNR is attained in the selected direction for both directional and positional cases with decreased SNR in the other areas compared to the random scenario. Furthermore, when $\beta_{\min} = 0.1$, the SNR degrades in all three scenarios in comparison with the case of the ideal lossless model $\beta_{\min} = 1$. The SNR dB levels at the location (-1,1.5) is shown for different values of $\beta_{\min}$ for the random, directional and positional cases. The SNR can be given as follows:

$$\text{SNR} = \frac{1}{T}\sum_{t=1}^{T} \frac{E_s \mathcal{W}^2}{N_0}\left|u_t^{\top}\mathcal{S}(p)\right|^2. \tag{5.6}$$

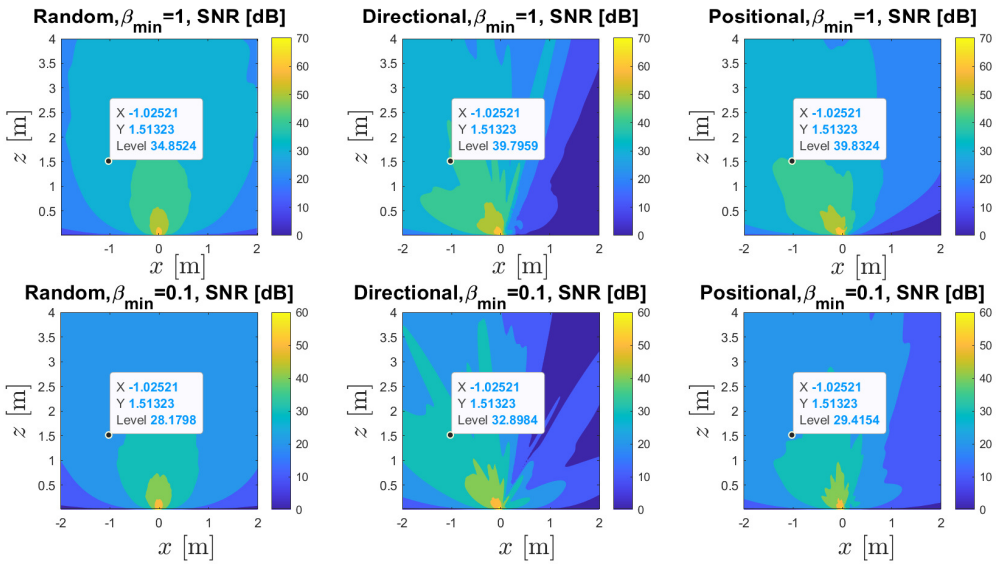

Figure 5.3: SNR in dB for Random, Directional and Positional Phase profile at $\beta_{\min} = \{0.1, 1\}$.

5.2.3 Problem Statement

Our objective is to develop the PEB and create a simplified algorithm for the estimation of the user position p, along with the unknown channel gain $\mathcal{W}$, based on the T transmission instances and the observations r_t mentioned in (5.1). We assume that the practical model in (5.5) and its associated RIS parameters, $\beta_{\min}$, ∇, and Δ are known. In this paper, we put the assumption that these parameters are available for the case of the uplink single-user scenario when the RIS act as lens [250]. In addition to localization and unlike the widely used far-field model in the literature, we have investigated the effect of the practical phase shift model on the achievable data rate in the near-field regime taking into consideration the random, directional and positional RIS phase profiles.

5.3 Fisher Information Matrix (FIM) Analysis

Considering the practical phase shift model in section II.B, the baseband observations at the receiver for the transmitted pilots after time t in the near field regime can be rewritten using (5.1) and (5.2) as:

$$r_t = \mathcal{W} e^{j\theta} \sum_{n=1}^{N} [\mathfrak{S}(p)]_n u_{t,n} x_t + e_t, \tag{5.7}$$

where, $u_{t,n} = v_{t,n} [h_{ant}]_n = \left(\beta_{t,n}(\Theta_{t,n}) e^{j\Theta_{t,n}}\right) [h_{ant}]_n$ and the amplitude $\beta_{t,n}(\Theta_{t,n})$ is defined in (5.5). The model in (5.7) can be represented in a vector form.

$$\mathbf{r} = \sqrt{E_s} \mathcal{W} e^{j\theta} U^{\top}(\Omega) \mathfrak{S}(p) + \mathbf{e}, \tag{5.8}$$

where, $U(\Omega) = [u_1(\Omega)\dots u_T(\Omega)] \in \mathbb{C}^{N\times T}$ is the matrix of the RIS profile, depending on the values of the RIS amplitude circuit parameters $\Omega = [\beta_{\min}, \nabla, \Delta]^\top$ in (5.5). Considering the noise free vector $\xi = \sqrt{E_s}\mathcal{W}e^{j\theta}U^\top(\Omega)\mathcal{S}(p)$ and the 8×1 vector of unknown parameters $\Upsilon = \left[\mathcal{W}, \theta, p^\top, \beta_{\min}, \nabla, \Delta\right]^\top$, the FIM $J(\Upsilon) \in \mathbb{R}^{8\times 8}$ is defined as [252].

$$J(\Upsilon) = \frac{2}{N_0}\Re\left\{\left(\frac{\partial\xi}{\partial\Upsilon}\right)^{\mathrm{H}}\frac{\partial\xi}{\partial\Upsilon}\right\}. \tag{5.9}$$

The FIM diagonal and off-diagonal elements can be generated from the partial derivatives. However, we put the assumption that the RIS phase profile and the related amplitude circuit parameters are known at the receiver so, the 8×1 vector of unknown parameters $\Upsilon = \left[\mathcal{W}, \theta, p^\top, \beta_{\min}, \nabla, \Delta\right]^\top$ can be reduced to $\Upsilon = \left[\mathcal{W}, \theta, p^\top\right]^\top$. We can represent (5.9) as follows:

$$J(\Upsilon) = \begin{bmatrix} J_{\mathcal{W},\mathcal{W}} & J_{\mathcal{W},\theta} & J_{\mathcal{W},p} \\ J_{\theta,\mathcal{W}} & J_{\theta,\theta} & J_{\theta,p} \\ J_{p,\mathcal{W}} & J_{p,\theta} & J_{p,p} \end{bmatrix}, \tag{5.10}$$

where, $J_{\mathcal{W},\mathcal{W}} \triangleq [J(\Upsilon)]_{1,1}$ is the first diagonal element of $J(\Upsilon)$, $J_{\theta,\theta} \triangleq [J(\Upsilon)]_{2,2}$ is the second diagonal element and $J_{p,p} \triangleq [J(\Upsilon)]_{3:5,3:5}$ are the third, fourth and fifth diagonal elements of $J(\Upsilon)$. The off-diagonal elements above and below the main diagonal are $\begin{bmatrix} J_{\mathcal{W},p} & J_{\theta,p}\end{bmatrix}^\top \triangleq [J(\Upsilon)]_{1:2,3:5}$ and $\begin{bmatrix} J_{p,\mathcal{W}} & J_{p,\theta}\end{bmatrix} \triangleq [J(\Upsilon)]_{3:5,1:2}$ respectively. To determine the diagonal and off-diagonal elements of the FIM $J(\Upsilon)$, we need to calculate the partial derivatives $\partial\xi/\partial\mathcal{W} = \sqrt{E_s}e^{j\theta}U^\top\mathcal{S}(p)$, $\partial\xi/\partial\theta = \sqrt{E_s}\mathcal{W}je^{j\theta}U^\top\mathcal{S}(p)$ and $\partial\xi/\partial p = \sqrt{E_s}\mathcal{W}e^{j\theta}U^\top\mathcal{F}(p)$, where $\mathcal{F}(p)$ cab be expressed such as, $\mathcal{F}(p) \triangleq \frac{\partial\mathcal{S}(p)}{\partial p} = j\frac{2\pi}{\lambda}\left(\mathrm{diag}(\mathcal{S}(p))W^\top + \mathcal{S}(p)\frac{p^\top}{d}\right) \in \mathbb{C}^{N\times 3}$ and $W = [w_0, w_1, \dots, w_{N-1}]$ with $w_n = (\mathcal{E}_n - p)/\|\mathcal{E}_n - p\|$. Consequently, the elements inside the FIM can be written as follows:

$$J(\Upsilon) = \frac{2E_s}{N_0}\begin{bmatrix} \mathcal{S}^{\mathrm{H}}(p)\Xi\mathcal{S}(p) & \mathcal{W}\mathcal{S}^{\mathrm{H}}(p)\Xi\mathcal{S}(p) & \mathcal{W}\Re\left(\mathcal{S}^{\mathrm{H}}(p)\Xi\mathcal{F}(p)\right) \\ \mathcal{W}\left(\mathcal{S}^{\mathrm{H}}(p)\Xi\mathcal{S}(p)\right) & \mathcal{W}^2\mathcal{S}^{\mathrm{H}}(p)\Xi\mathcal{S}(p) & \mathcal{W}^2\Im\left(\mathcal{S}^{\mathrm{H}}(p)\Xi\mathcal{F}(p)\right) \\ \mathcal{W}\Re\left(\mathcal{S}^{\mathrm{H}}(p)\Xi\mathcal{F}(p)\right) & \mathcal{W}^2\Im\left(\mathcal{S}^{\mathrm{H}}(p)\Xi\mathcal{F}(p)\right) & \mathcal{W}^2\Re\left(F^{\mathrm{H}}(p)\Xi\mathcal{F}(p)\right) \end{bmatrix}, \tag{5.11}$$

where $\Re(.)$ and $\Im(.)$ are the real and imaginary of a complex number and the positive semidefinite matrix $\Xi = U^*U^\top$.

Definition 1 Equivalent FIM (EFIM): Given a parameter vector $\Phi \triangleq \left[\Phi_1^\top, \Phi_2^\top\right]^\top$ with related FIM.

$$\mathbf{J}_\Phi = \begin{bmatrix} \mathbf{J}_{\Phi_1} & \mathbf{J}_{\Phi_1\Phi_2} \\ \mathbf{J}_{\Phi_1\Phi_2} & \mathbf{J}_{\Phi_2} \end{bmatrix}. \tag{5.12}$$

Then, the EFIM of Φ_1 is given by Schur complement as [253, 257]

$$\mathbf{J}^{\mathrm{e}}_{\Phi_1} = \mathbf{J}_{\Phi_1} - \mathbf{J}_{\Phi_1\Phi_2}\mathbf{J}^{-1}_{\Phi_2}\mathbf{J}^\top_{\Phi_1\Phi_2}. \tag{5.13}$$

As per this definition, it should be noted that $\mathbf{J}_{\Phi_1}$ is the FIM of Φ_1 under the assumption that Φ_2 is known. Additionally, $\mathbf{J}_{\Phi_1\Phi_2}\mathbf{J}_{\Phi_2}^{-1}\mathbf{J}_{\Phi_1\Phi_2}^{\top}$ quantifies the amount of information lost due to the uncertainty surrounding Φ_2. Taking into account definition 1, the equivalent FIM of the user position is given as:

$$\begin{aligned} J(p) &= [J(\Upsilon)]_{3:5,3:5} - [J(\Upsilon)]_{3:5,1:2}[J(\Upsilon)]_{1:2,1:2}^{-1}[J(\Upsilon)]_{1:2,3:5} \\ &= \frac{2\mathcal{W}^2 E_s}{N_0}\Re\left\{\mathcal{F}^{\mathrm{H}}(p)\left[\Xi - \frac{\Xi\mathcal{S}(p)\mathcal{S}^{\mathrm{H}}(p)\Xi}{\mathcal{S}^{\mathrm{H}}(p)\Xi(p)}\right]\mathcal{F}(p)\right\}. \end{aligned} \tag{5.14}$$

Consequently, the PEB is represented as:

$$\mathrm{PEB} = \sqrt{\mathrm{trace}\left(\left[J^{-1}(\Upsilon)\right]_{3:5,3:5}\right)}. \tag{5.15}$$

The RMSE of any unbiased estimator $\hat{p}$ can be bounded by an inequality:

$$\mathrm{PEB} \leq \mathrm{RMSE} \triangleq \sqrt{\mathbb{E}\{\|\hat{p}-p\|^2\}}. \tag{5.16}$$

5.4 Low Complexity Estimation

5.4.1 Maximum Likelihood (ML) Estimation

The joint PDF can be expressed as [252, 263]:

$$f(r \mid \Upsilon) = \left(\frac{1}{\pi N_0}\right)^{T} \exp\left(-\frac{1}{N_0}\|r-\xi(\Upsilon)\|^2\right), \tag{5.17}$$

where the noise free term $\xi(\Upsilon) = \mathcal{L}\sum_{n=1}^{N}[\mathcal{S}(p)]_n u_{t,n} x_t$, $\mathcal{L} = \mathcal{W}e^{j\theta}$ and $u_{t,n}$ is defined as per (5.7). Consequently, the ML estimate of the channel gain and user location:

$$\begin{aligned} [\hat{\mathcal{L}}, \hat{p}] &= \arg\max_{\mathcal{L},p} f(r \mid \mathcal{L}, p) \\ &= \arg\min_{\mathcal{L},p} \underbrace{\left\| r - \sqrt{E_s}\mathcal{L}U^{\top}\mathcal{S}(p)\right\|^2}_{d(\mathcal{L},p)}. \end{aligned} \tag{5.18}$$

Differentiating the term $d(\mathcal{L},p)$ and set equal to zero, yields to the estimate that maximize the likelihood function $\frac{\partial d(\mathcal{L},p)}{\partial \mathcal{L}} = 0$. Consequently, solving for $\mathcal{L}$ will lead to the estimate as a function of p.

$$\hat{\mathcal{L}}(p) = \frac{\mathcal{S}^{\mathrm{H}}(p)U^{*}r}{\sqrt{E_s}\left\|U^{\top}\mathcal{S}(p)\right\|^2}. \tag{5.19}$$

Therefore, the estimate p can be computed as:

$$\hat{p} = \arg\min_{p} \left\| r - \sqrt{E_s}\hat{\mathcal{L}}(p)U^{\top}\mathbb{S}(p) \right\|^2. \tag{5.20}$$

5.4.2 Simple User Localization

The framework of the user localization problem in spherical coordinates is used to solve (5.20). This framework gives rise to a three-step estimation process outlined below. Initially, we represent each exponential term in the far-field, $\mathbb{S}(\varphi,\vartheta) = \left[e^{-\mathrm{j}k(\varphi,\vartheta)^{\top}\mathcal{E}_1}, \ldots, e^{-\mathrm{j}k(\varphi,\vartheta)^{\top}\mathcal{E}_N}\right]$ as $[\mathbb{S}(\varphi,\vartheta)]_n = \exp\left(-j\frac{2\pi}{\lambda}\mathbb{L}_n \sin(\vartheta)\cos(\varphi-\Psi_n)\right)$. We utilize Jacobi-Anger expansion method [250] to express $[\mathbb{S}(\varphi,\vartheta)]_n$ as:

$$[\mathbb{S}(\vartheta,\varphi)]_n \approx \sum_{m=-L}^{L} j^m \mathcal{J}_m\left(-\frac{2\pi}{\lambda}\mathbb{L}_n \sin(\vartheta)\right) e^{jm(\varphi-\Psi_n)}, \tag{5.21}$$

where $L > \frac{2\pi}{\lambda}\mathbb{L}_{\max}\sin\vartheta$ is the number of terms in the expansion that gives sufficient precision for high-quality approximation. Consequently, $T \geq T_{\text{thr}} = 2L+1$ is adopted for low complexity solution as per algorithm 3. Furthermore, $\mathcal{J}_m(\cdot)$ is the m-th order Bessel function of the first kind. The expansion in (5.21) can be represented as:

$$[\mathbb{S}(\vartheta,\varphi)]_n = g_n^{\top}(\vartheta)h(\varphi), \tag{5.22}$$

where $[g_n(\vartheta)]_m = j^m \mathcal{J}_m\left(-\frac{2\pi}{\lambda}\mathbb{L}_n\sin(\vartheta)\right)e^{-jm\Psi_n}$ and $[h(\varphi)]_m = e^{jm\varphi}$. It can be readily confirmed that $\mathbb{S}(\vartheta,\varphi) \approx \mathbb{G}^{\top}(\vartheta)h(\varphi)$, where $\mathbb{G}(\vartheta) = [g_0(\vartheta)\ldots g_{N-1}(\vartheta)]$. Subsequently, the response vector $\mathbb{S}(\vartheta,\varphi)$ has independent structure in the angles ϑ and φ. We begin with three-stage estimating method to estimate $\hat{p} = p(\hat{\Omega},\hat{\vartheta},\hat{\varphi})$. We rewrite the system in (5.8) as:

$$\mathbf{r} = \sqrt{E_s}\mathcal{L}U^{\top}\mathbb{G}^{\top}(\vartheta)h(\varphi) + \mathbf{e}. \tag{5.23}$$

By defining the vector b as $b = \sqrt{E_s}\mathcal{L}h(\varphi)$ based on (5.23), the estimation of b as a function of ϑ can be represented by $\hat{b}(\vartheta) = \left(\left(U^{\top}\mathbb{G}^{\top}(\vartheta)\right)^{\top}U^{\top}\mathbb{G}^{\top}(\vartheta)\right)^{-1}\left(U^{\top}\mathbb{G}^{\top}(\vartheta)\right)^{\top}\mathbf{r}$. Therefore, the estimation for the angle ϑ can be applied as:

$$\hat{\vartheta} = \arg\min_{\vartheta} \left\| \mathbf{r} - U^{\top}\mathbb{G}^{\top}(\vartheta)\hat{b}(\vartheta) \right\|^2. \tag{5.24}$$

Using the estimated value $\hat{\vartheta}$, (5.23) can be rewritten as:

$$\mathbf{r} = \sqrt{E_s}\mathcal{L}U^{\top}\mathbb{G}^{\top}(\hat{\vartheta})h(\varphi) + \mathbf{e}. \tag{5.25}$$

For each value of φ, we estimate $\mathcal{L}$ in a similar manner as in (5.19), but instead of using $\mathbb{S}(p)$, we substitute it with $\mathbb{G}^{\top}(\hat{\vartheta})h(\varphi)$, resulting in the estimation $\hat{\mathcal{L}}(\varphi)$

Algorithm 3: User Location Estimate $p(\hat{\mathcal{Q}}, \hat{\vartheta}, \hat{\varphi})$ in RIS-assisted Near-Field Localization.

Input: Observations signals r as in (5.7), T_{thr} and RIS amplitude model parameters $\Omega = [\beta_{\min}, \nabla, \Delta]^{\top}$.
Output: User Location $\hat{p}$
if $T \geq T_{\text{thr}}$ **then**
    Calculate the elevation $\hat{\vartheta}$ by solving (5.24).
    Using $\hat{\vartheta}$, calculate the azimuth $\hat{\varphi}$, by solving (5.27).
    Using $\hat{\vartheta}$ and $\hat{\varphi}$, calculate the distance $\hat{\mathcal{Q}}$ by solving (5.28).
else
    Increase the number of observations to facilitate finding the initial estimates $\hat{\vartheta}$ and $\hat{\varphi}$ by solving 3D research in (5.20) using the simple user localization method.
end if
Calculate the location estimate as per (5.29)

$$\hat{\mathcal{L}}(\varphi) = \frac{h(\varphi)\mathbb{G}^{*}(\hat{\vartheta})U^{*}\mathbf{r}}{\sqrt{E_s \left\| U^{\top}\mathbb{G}^{\top}(\hat{\vartheta})h(\varphi) \right\|^2}}. \tag{5.26}$$

Therefore, we solve for φ:

$$\hat{\varphi} = \arg\min_{\varphi} \left\| \mathbf{r} - \sqrt{E_s}\hat{\mathcal{L}}(\varphi)U^{\top}\mathbb{G}^{\top}(\hat{\vartheta})h(\varphi) \right\|^2. \tag{5.27}$$

With the estimated angles $\hat{\vartheta}$ and $\hat{\varphi}$, we define the position as a function of distance as $p(\mathcal{Q}) = \mathcal{Q}\begin{bmatrix} \sin\hat{\vartheta}\cos\hat{\varphi} & \sin\hat{\vartheta}\sin\hat{\varphi} & \cos\hat{\vartheta} \end{bmatrix}^{\top}$, which allows us to determine $\hat{\mathcal{L}}(p(\mathcal{Q}))$, as described in (5.19). Finally, we proceed to solve the optimization problem.

$$\hat{\mathcal{Q}} = \arg\min_{\mathcal{Q}} \left\| \mathbf{r} - \sqrt{E_s}\hat{\mathcal{L}}(p(\mathcal{Q}))U^{\top}\mathcal{S}(p(\mathcal{Q})) \right\|^2. \tag{5.28}$$

Now we can calculate the user estimate as:

$$\hat{p} = \hat{\mathcal{Q}}\begin{bmatrix} \sin\hat{\vartheta}\cos\hat{\varphi} & \sin\hat{\vartheta}\sin\hat{\varphi} & \cos\hat{\vartheta} \end{bmatrix}^{\top}. \tag{5.29}$$

Algorithm 3 summarizes the steps of estimating the user localization.

5.5 Achievable Data Rate in The Near-field Regime

The designs that aim to minimize the PEB differ from those that prioritize communication-related metrics like capacity optimization. While both types of designs exhibit improved performance in high SNR conditions, the accuracy of localization is also influenced by factors such as geometric considerations and the possibility of distinguishing signals from various paths rather than merely aligning them [12]. In this section of the paper, we study the performance loss on

the achievable data rate in the near field channel when the realistic RIS phase profile is adopted. The achievable data rate can be represented as per [52].

$$\begin{aligned} R_{\text{RIS}} &= \max_{\Theta_{t,n},\beta_{t,n}} \log_2(1+SNR) \\ &= \log_2\left(1+\frac{1}{T}\sum_{t=1}^{T}\frac{E_s\mathcal{W}^2}{N_0}\left|u_t^{\top}\mathfrak{S}(p)\right|^2\right). \end{aligned} \tag{5.30}$$

The maximum data rate is selected when the phase shifts are tuned. Recall that the term $u_{t,n} = w_{\theta t,n}[h_{ant}]_n = \left(\beta_{t,n}(\Theta_{t,n})e^{j\Theta_{t,n}}\right)[h_{ant}]_n$ for each n^{th} element at time instant t. As a result, at the random case, we adopt $\Theta_{t,n} = \exp(j\Psi_{t,n})$ where $\Psi_{t,n} \sim \mathcal{U}(0,2\pi)$, while in both directional and positional scenarios, we respectively assign the phases $\Theta_{t,n} = \exp\left(+j\mathcal{E}_n^{\top}k\left(\vartheta^{(k)},\varphi^{(k)}\right)\right)$ and $\Theta_{t,n} = \exp\left(+j\frac{2\pi}{\lambda}\left(\left\|p^{(k)}-\mathcal{E}_n\right\|-\mathcal{Q}^{(k)}\right)\right)$. The amplitude varies as $\beta_{t,n} = \in (0,1]$.

5.6 FIM and PEB at The Presence of EMI

The received signal at the RF chain can be expressed mathematically for each time instance t considering the EMI:

$$r_t = \underbrace{e^{j\theta}h_{\text{ant}}^{\top}\mathbf{w}_{\theta t}(\mathcal{W}(p)\odot\mathfrak{S}(p))x_t}_{\substack{\text{Interference and noise}\\ \text{free term}}} + \underbrace{\mathbf{w}_{\theta t}^{\top}h_{\text{ant}}^{\top}I}_{\substack{\text{Interference}\\ \text{term, } g_t}} + \underbrace{e_t}_{\substack{\text{Noise}\\ \text{term}}}. \tag{5.31}$$

The vector $h_{\text{ant}} \in \mathbb{C}^{N\times 1}$ comprises the channel link between the RIS and the receiving antenna as per Fig. 5.4. The vector $\mathcal{W}(p) \geq \mathbf{0}_N$ represents the amplitudes of channel link between the RIS and the transmitting user. On the other hand, the vector $\mathfrak{S}(p) \in \mathbb{C}^{N\times 1}$ represents the channel phases. The noise vector $\mathbf{e}_t$ represents uncorrelated zero-mean additive Gaussian noise with a variance of $N_o/2$ per real dimension and $I \in \mathbb{C}^N$ is the EMI, generated by the arriving, uncontrollable electromagnetic waves. By introducing $u_t = \mathbf{w}_{\theta t}h_{\text{ant}}$, we can define $\mathbf{U} = [u_1,u_2,\ldots,u_T] \in \mathbb{C}^{N\times T}$. Additionally, $\mathbf{x} = [x_1,x_2,\ldots,x_T]^{\top}$, $\mathbf{g} = [g_1,g_2,\ldots,g_T]^{\top}$ and $\mathbf{e} = [e_1,e_2,\ldots,e_T]^{\top}$. The received vector, $y = [r_1,r_2,\ldots,r_T]^{\top}$ can be represented as:

$$\mathbf{r} = e^{j\theta}\,\text{diag}(\mathbf{x})\mathbf{U}^{\top}(\mathcal{W}(p)\odot\mathfrak{S}(p)) + \mathbf{g} + \mathbf{e}. \tag{5.32}$$

5.6.1 Fisher Information Analysis

5.6.2 Fisher Information Matrix (FIM)

The baseband observations at the receiver for T transmitted pilots in the standard near-field regime can be re-written using (5.32) as:

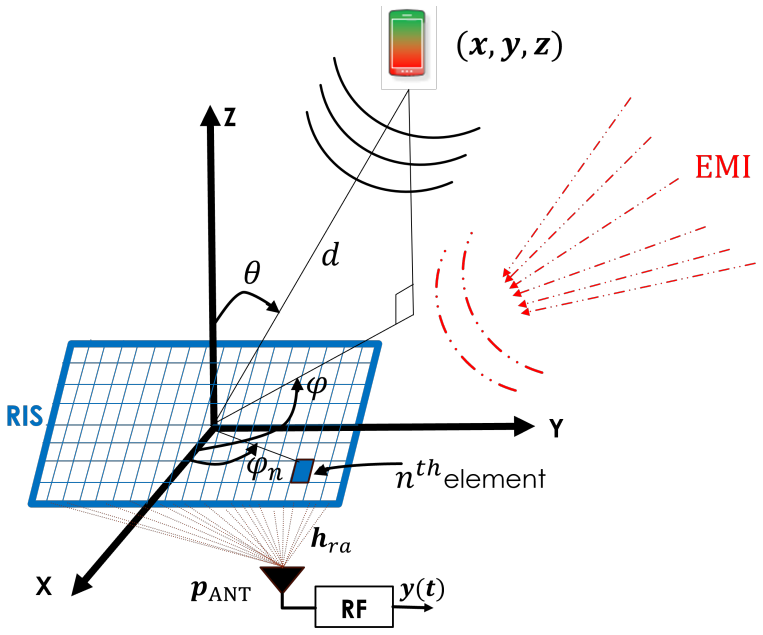

Figure 5.4: System model when a user located at $p = [x, y, z]^\top$ transmits through RIS-based lens to the receiving antenna located at p_{ANT} incorporating EMI.

$$\mathbf{r} = \sqrt{E_s}\mathcal{W}e^{j\theta}\mathbf{U}^\top \mathcal{S}(p) + \mathbf{g} + \mathbf{e}. \tag{5.33}$$

Considering the noise free term $\xi = \sqrt{E_S}\mathcal{W}e^{j\theta}U^\top \mathcal{S}(p)$ and the unknown $\rho = \left[\mathcal{W}, \theta, p^\top\right]^\top$, the FIM $J(\rho) \in \mathbb{R}^{5\times 5}$ is defined as [12, 13, 16, 24].

$$J(\rho) = \frac{2}{N_o + \sigma_g^2}\Re\left\{\left(\frac{\partial \xi}{\partial \rho}\right)^{\text{H}} \frac{\partial \xi}{\partial \rho}\right\}, \tag{5.34}$$

where, σ_g^2 is the power of the interference term, g_t mentioned in (5.31). Let us introduce $\mathcal{T} = \mathbf{w}_{\theta t}^\top h_{\text{ant}}$, then $\sigma_g^2 = A\sigma_{\text{EMI}}^2 \mathcal{T}^\top R\mathcal{T}$. Consequently, using (5.34) and denoting $\mu =$ PEB, the PEB is given as follows:

$$\mu = \sqrt{\text{trace}\left(\left[J^{-1}(\rho)\right]_{3:5,3:5}\right)}, \tag{5.35}$$

where, the notation $J_{o:q,\tilde{o}:\tilde{q}}$ refers to a matrix that consists of rows o through q and columns $\tilde{o}$ through $\tilde{q}$, taken from matrix J.

5.6.3 PEB Analysis

The partial derivatives can be used to derive both the diagonal and non-diagonal elements of the FIM. To find the diagonal and non-diagonal components of the FIM $J(\rho)$, we must compute the partial derivatives $\partial\xi/\partial\mathcal{W} = \sqrt{E_s}e^{j\theta}\mathbf{U}^\top\mathcal{S}(p)$, $\partial\xi/\partial\theta = \sqrt{E_s}\mathcal{W}_J e^{j\theta}\mathbf{U}^\top\mathcal{S}(p)$ and $\partial\xi/\partial p = \sqrt{E_s}\mathcal{W}e^{j\theta}\mathbf{U}^\top\mathcal{F}(p)$, where $\mathcal{F}(p) \triangleq \frac{\partial\mathcal{S}(p)}{\partial p} \in \mathbb{C}^{N\times 3}$ and can be calculated as $\mathcal{F}(p) =$

$j\frac{2\pi}{\lambda}\left(\text{diag}(\mathcal{S}(p))\mathbf{O}^{\top}+\mathcal{S}(p)\frac{p^{\top}}{d}\right)$. Furthermore, $\mathbf{O}=[O_0,O_1,\ldots,O_{N-1}]$ with O_n vector of $O_n=(\mathcal{E}_n-p)/\|\mathcal{E}_n-p\|$. Consequently, the diagonal and off-diagonal elements inside the FIM can be written as follows:

$$J(\rho)=\frac{2E_S}{N_{0+}\sigma_g^2}\left[\begin{array}{ccc} J_1(\rho) & J_2(\rho) & J_3(\rho)\end{array}\right], \tag{5.36}$$

And, $J_1(\rho)$, $J_2(\rho)$, and $J_3(\rho)$ are defined as follows:

$$J_1(\rho)=\left[\begin{array}{c} \mathcal{S}^{\mathrm{H}}(p)\Xi\mathcal{S}(p) \\ -\mathcal{W}\mathfrak{J}\left(\mathcal{S}^{\mathrm{H}}(p)\Xi\mathcal{S}(p)\right) \\ \mathcal{W}\mathfrak{R}\left(\mathcal{S}^{\mathrm{H}}(p)\Xi\mathcal{F}(p)\right)\end{array}\right], \tag{5.37}$$

$$J_2(\rho)=\left[\begin{array}{c} \mathcal{W}\mathcal{S}^{\mathrm{H}}(p)\Xi\mathcal{S}(p) \\ \mathcal{W}^2\mathcal{S}^{\mathrm{H}}(p)\Xi\mathcal{S}(p) \\ \mathcal{W}^2\mathfrak{J}\left(\mathcal{S}^{\mathrm{H}}(p)\Xi\mathcal{F}(p)\right)\end{array}\right], \tag{5.38}$$

$$J_3(\rho)=\left[\begin{array}{c} \mathcal{W}\mathfrak{R}\left(\mathcal{S}^{\mathrm{H}}(p)\Xi\mathcal{F}(p)\right) \\ \mathcal{W}^2\mathfrak{J}\left(\mathcal{S}^{\mathrm{H}}(p)\Xi\mathcal{F}(p)\right) \\ \mathcal{W}^2\mathfrak{R}\left(\mathcal{F}^{\mathrm{H}}(p)\Xi\mathcal{F}(p)\right)\end{array}\right], \tag{5.39}$$

where, $\mathfrak{R}(.)$ and $\mathfrak{J}(.)$ are the real and imaginary of complex number. Furthermore, the semidefinite matrix $\Xi=K^*K^{\top}$, where $(.)^*$ is the conjugate complex of a matrix. The equivalent FIM (EFIM) of the user location is given as:

$$\begin{aligned} J(p)&=[J(\rho)]_{3:5,3:5}-[J(\rho)]_{3:5,1:2}[J(\rho)]^{-1}_{1:2,1:2}[J(\rho)]_{1:2,3:5} \\ &=\frac{2\mathcal{W}^2E_s}{N_o+\sigma_g^2}\mathfrak{R}\left\{\mathcal{F}^{\mathrm{H}}(p)\left[\Xi-\frac{\Xi\mathcal{S}(p)\mathcal{S}^{\mathrm{H}}(p)\Xi}{\mathcal{S}^{\mathrm{H}}(p)\Xi\mathcal{S}(p)}\right]\mathcal{F}(p)\right\}. \end{aligned} \tag{5.40}$$

By knowing the equivalent FIM for the user location, we can now determine the PEB, and rewriting (5.35) as follows:

$$\text{PEB}\ =\sqrt{\text{trace}\left(\mathfrak{R}\left\{\mathcal{F}^{\mathrm{H}}(p)\left[\Xi-\frac{\Xi\mathcal{S}(p)\mathcal{S}^{\mathrm{H}}(p)\Xi}{\mathcal{S}^{\mathrm{H}}(p)\Xi\mathcal{S}(p)}\right]\mathcal{F}(p)\right\}^{-1}\right)}. \tag{5.41}$$

5.6.4 Data Rate Analysis

Typically, designs with the objective of minimizing the PEB differ from those that prioritize metrics related to communication, such as optimizing capacity. Although both design types demonstrate enhanced performance under high SNR conditions, the accuracy of localization is also affected by factors like geometric considerations and the ability to distinguish signals from various paths rather than simply aligning them. The achievable data rate in the improved

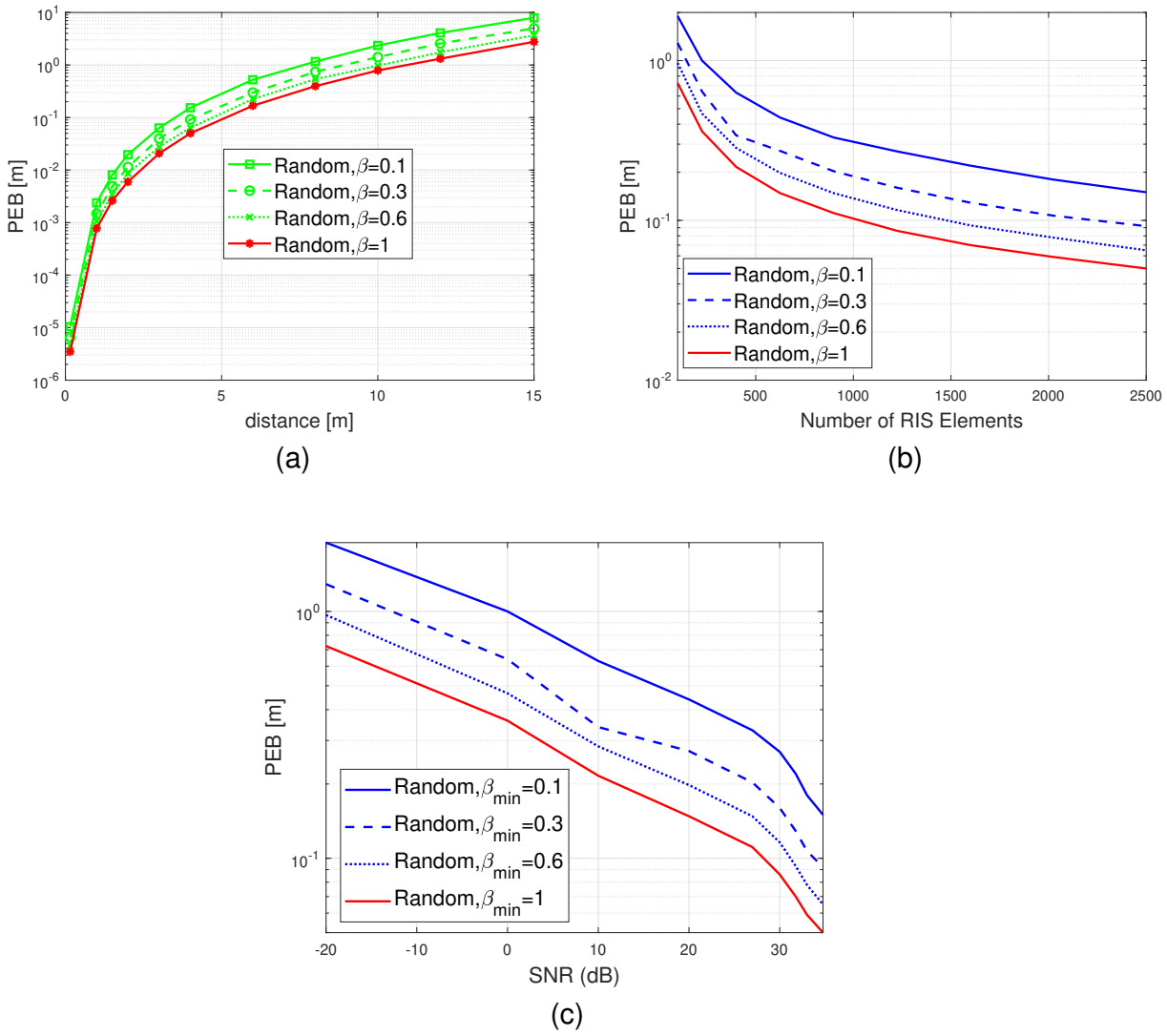

Figure 5.5: (a). PEB as a function of distance to the RIS lens, $\beta_{\min} \in \{0.1, 0.3, 0.6, 1\}$ (b). PEB as a function of Number of RIS elements (c). PEB versus SNR (dB)

near-field channels when employing the RIS phase profile, is represented as a function of the EMI:

$$\begin{aligned} r_{\text{RIS}} &= \max_{\mathbf{v}} \log_2(1+\text{SNR}) \\ &= \log_2(1+\underbrace{\frac{1}{T}\sum_{t=1}^{T}\frac{E_s \mathcal{W}^2}{N_o+\sigma_g^2}\left|u_t^T \mathfrak{S}(p)\right|^2}_{\text{SNR}}). \end{aligned} \tag{5.42}$$

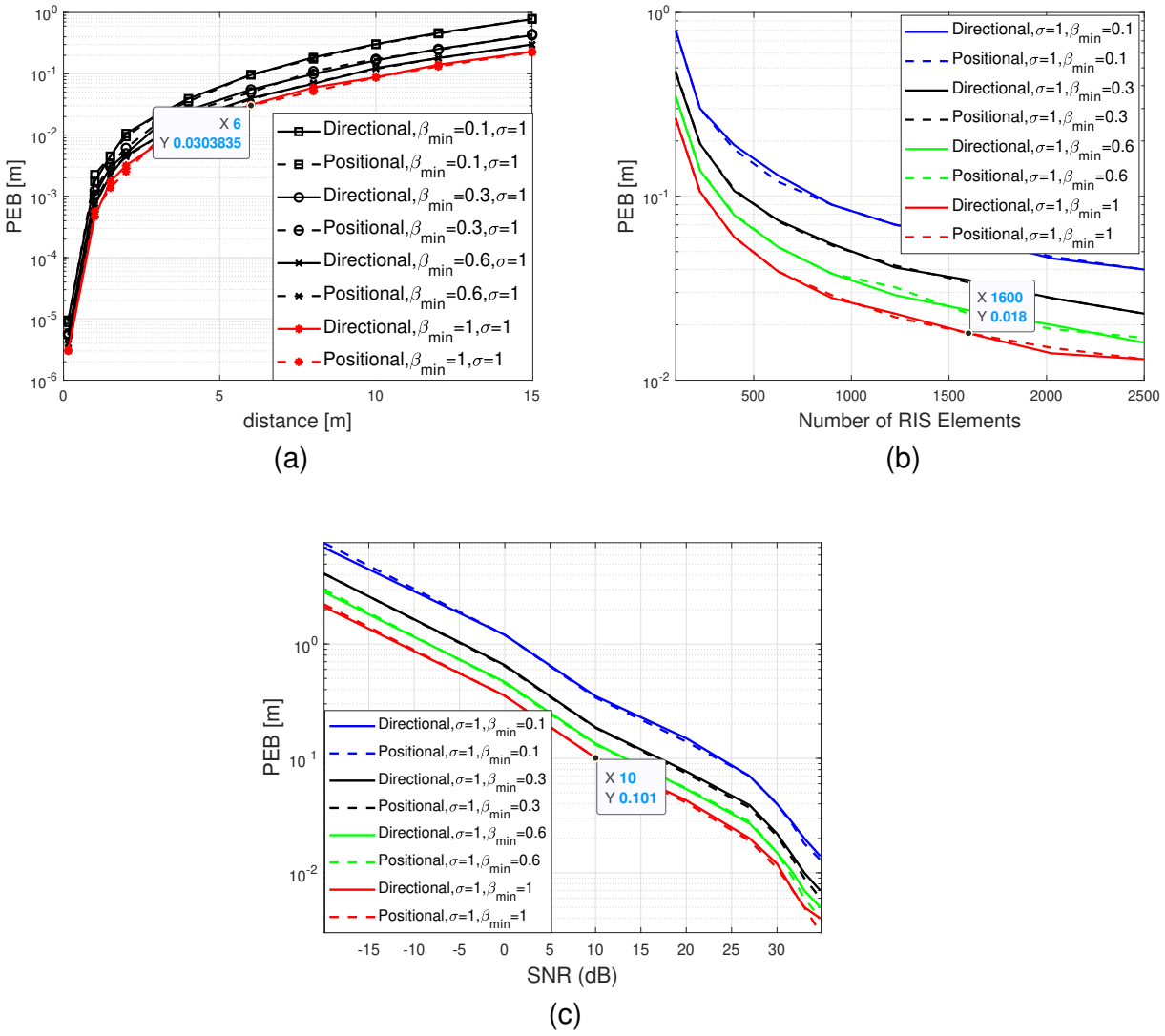

Figure 5.6: (a). PEB as a function of distance to the RIS lens,$\sigma = 1$, and $\beta_{\min} \in \{0.1, 0.3, 0.6, 1\}$ (b). PEB as a function of Number of RIS elements $\sigma = 1$, and $\beta_{\min} \in \{0.1, 0.3, 0.6, 1\}$ (c). PEB versus SNR (dB) $\sigma = 1$, and $\beta_{\min} \in \{0.1, 0.3, 0.6, 1\}$

5.7 Simulation Results

We used the simulation parameters provided in [250] but with the realistic RIS phase shift model as in Section II.B, so, $\Omega = [\beta_{\min}, \nabla, \Delta]^\top$. We select the range of values for $\beta_{\min} \in [0, 1]$ and fixed the constants ∇ and Δ to 0 and 1.5 to study the performance loss not only on the localization but also in the communication. We examine a RIS composed of $N = 2500$ elements arranged in $N_v \times N_h$ grid, where $N_v = N_h = 50$, at a frequency of 28 GHz with $\lambda/2$ and $\lambda^2/4$ element spacing and area, respectively. The receive antenna is positioned at coordinates $[0, 0, -\lambda]^\top$. The transmit power, the noise power spectral density, and the reception noise figure are set to 1mW, -174 dBm/Hz and 8 dB, respectively. The total pilot transmissions $T = 200$ and the bandwidth is fixed to 1 MHz. In our analysis, we focus on a user who possesses a wavevector

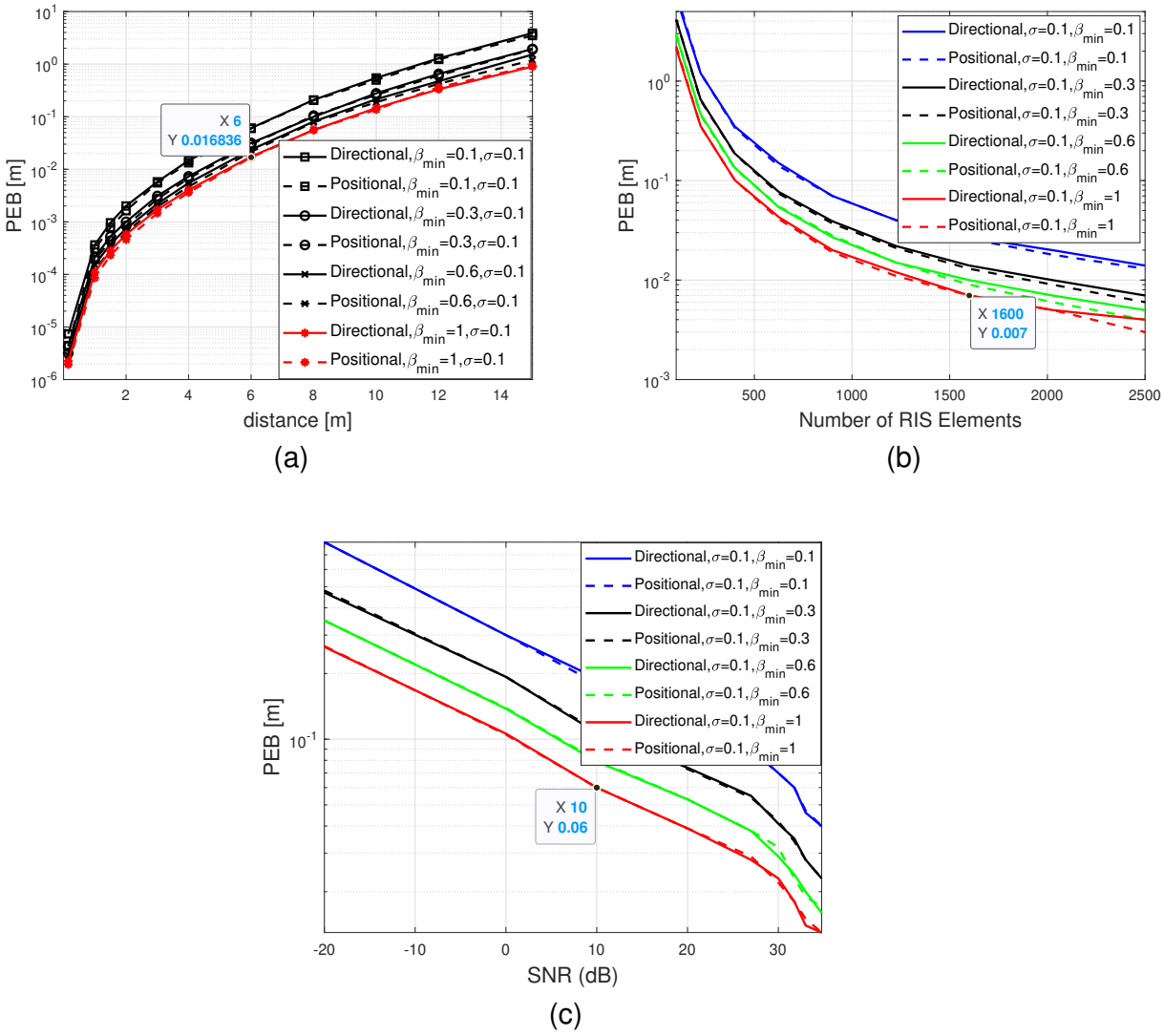

Figure 5.7: (a). PEB as a function of distance to the RIS lens,$\sigma = 0.1$, and $\beta_{\min} \in \{0.1, 0.3, 0.6, 1\}$ (b). PEB as a function of Number of RIS elements $\sigma = 0.1$, and $\beta_{\min} \in \{0.1, 0.3, 0.6, 1\}$ (c). PEB versus SNR (dB) $\sigma = 0.1$, and $\beta_{\min} \in \{0.1, 0.3, 0.6, 1\}$

k oriented in the direction $[1,1,1]^\top$. The channel gains to and from the RIS are set according to (5.3) and (5.4). The prior knowledge about the user's location is represented by the PDF as $f(p) = \mathcal{N}(p; \mathbb{Y}_p, \mathbb{V}_p)$, where $\mathbb{V}_p = \sigma^2 I_3$. It is solely employed for designing the directional beams of the RIS, and it is not utilized during the localization process or in the calculation of the PEB. The standard deviation in each dimension (XYZ) of the prior covariance of the user position is set to $\sigma \in \{0.1, 1\}$ m to evaluate the localization performance in the random, directional, and optional phase profiles. In (5.21), the number of the terms in the expansion $L = 5$ is used for low complexity estimation. Figures 5.5,5.6 and 5.7 illustrate the PEB as a function of distance in meters, number of RIS elements and SNR (dB). The figures display the PEB for the three selected designs of the RIS phase profiles, i.e., random, directional and positional, considering various values of standard deviation $\sigma \in \{0.1, 1\}$ and amplitude variation

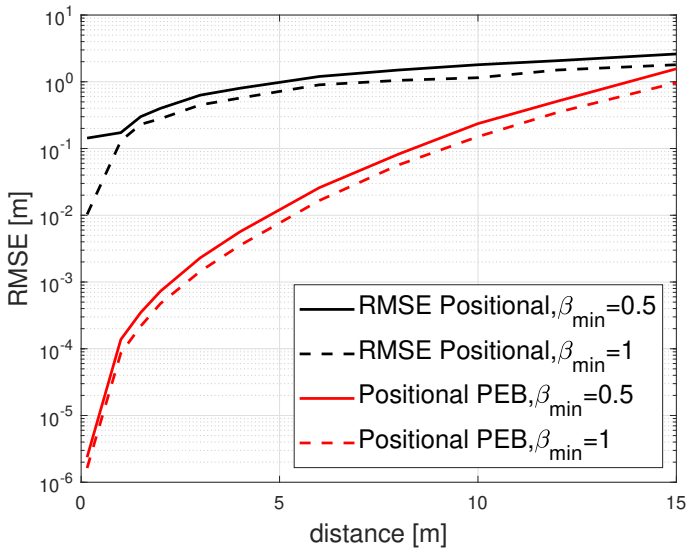

Figure 5.8: RMSE as a function of distance to the RIS lens., $\sigma = 0.1$ and $\beta_{\min} \in \{0.5, 1\}$

$\beta_{t,n} =\in (0,1]$. In Fig. 5.5a, it is noticed that by using a basic random phase configuration, we can achieve relatively low PEB, specifically below 1 meter, for user positions within a 10-meter distance from the RIS lens and at different values of $\beta_{\min}$. Figure 5.5b demonstrates the impact of varying RIS sizes on the PEB limit at different values of $\beta_{\min}$ when the UE distance is 5 meters. It is evident that for all the curves under consideration for different $\beta_{\min}$, the reduction in PEB is directly proportional to N. This relationship arises from the boost in SNR in the reflected path from the RIS to the receive antenna, which is directly proportional to the RIS's different dimensional sizes N. Consequently, Fig. 5.5c shows the PEB performance in the low and high SNR regimes. Additionally, the absence of significant beamforming gain is attributed to the randomness of phase shifts.

Figure 5.6 demonstrates that by employing directional or positional phase profiles ($\sigma = 1$ and $\beta_{t,n} =\in (0,1]$), it is possible to significantly decrease the PEB. The positional phase profile exhibits slightly superior performance compared to the directional phase profile, although the disparity between the two is negligible. Similarly, in Fig. 5.6a, we observe that employing directional or positional phase profile allows us to achieve relatively enhanced PEB, specifically below 1 meter, for user positioned within a 10-meter range from the RIS lens, regardless of the value of $\beta_{\min}$. Figure 5.6b illustrates how the PEB limit is affected by varying RIS sizes at different $\beta_{\min}$ values when the distance between the user and the RIS is 5 meters. It is clear that for all the plotted curves corresponding to different $\beta_{\min}$ values, the reduction in PEB is directly proportional to N. This correlation stems from the boost in SNR in the reflected path, which is directly proportional to N, as depicted in Fig. 5.6c. Moreover, the substantial beamforming gain is ascribed to the directional and positional phase shifts directed towards the user's location. Furthermore, the positional and directional phase profiles in Fig. 5.6 exhibit superior PEB performance compared to the random phase profile in Fig. 5.5 because of the tuned RIS coeffi-

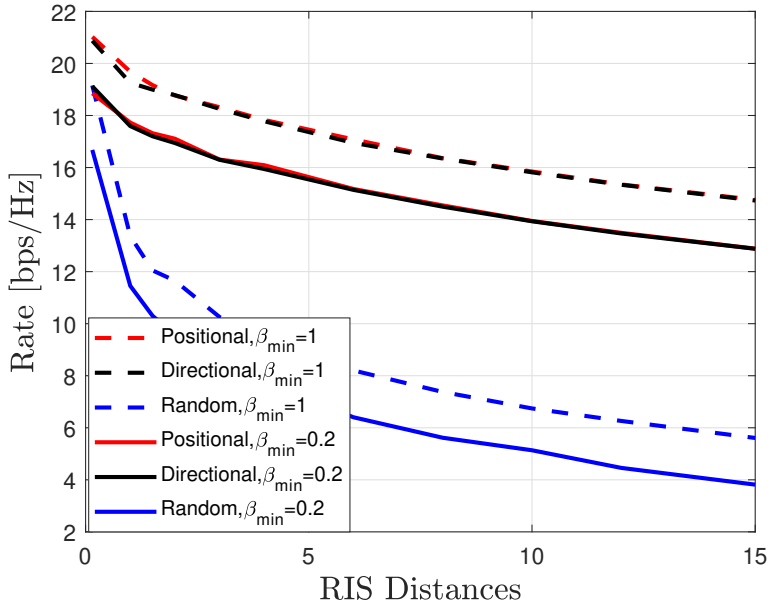

Figure 5.9: Data Rate versus RIS Distance, $\beta_{\min} \in \{0.2, 1\}$

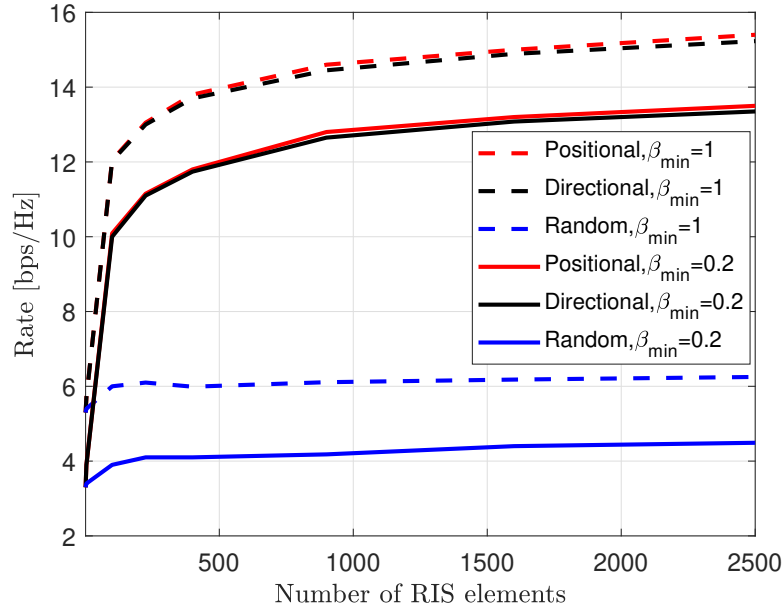

Figure 5.10: Data Rate versus Number of RIS Elements, $\beta_{\min} \in \{0.2, 1\}$

cients that help the direct and the reflecting channel to be superimposed more constructively at the receive antenna.

Similar to Fig. 5.6, Fig. 5.7 studies the PEB against distance from RIS, RIS different sizes and finally the SNR regimes but for a smaller value of standard deviation σ. Consequently, it is evident that having more precise a priori information (i.e., a smaller value for $\sigma = 0.1$) results in improved PEB. For example, the PEB in Fig. 5.7a for the positional case, $\sigma = 0.1$ and $\beta_{\min} = 1$

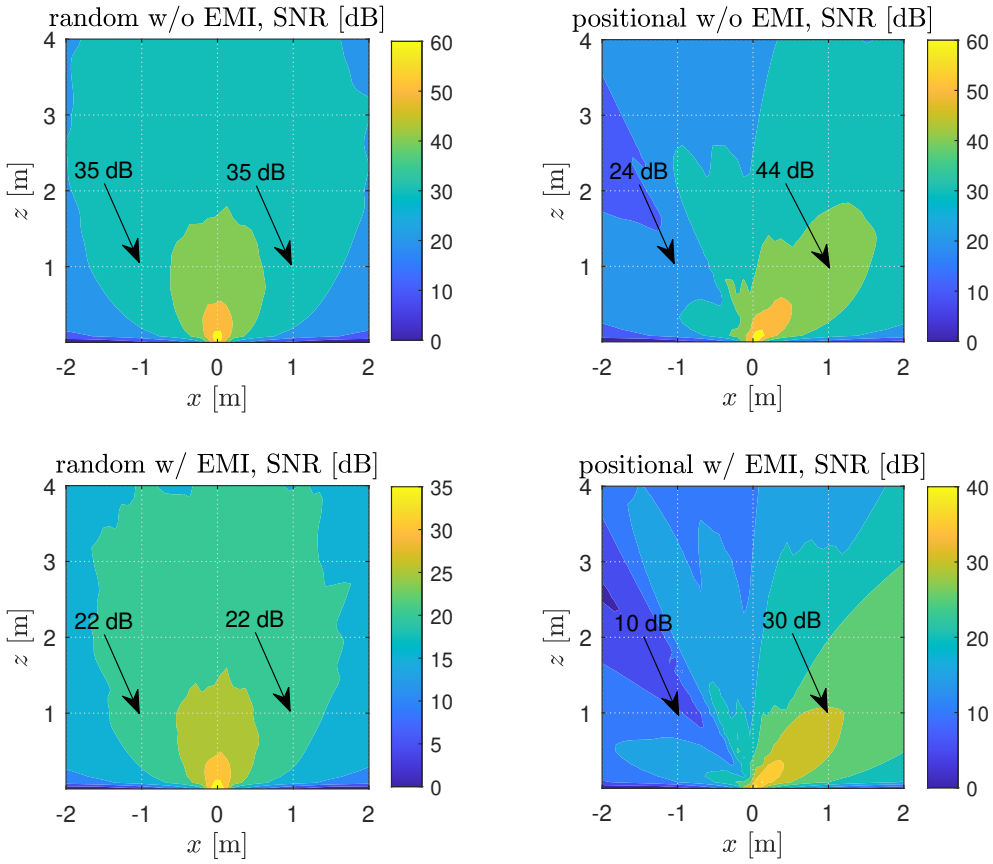

Figure 5.11: SNR in dB for random and positional phase profile with $m_p = [0.1, 0.1, 0.1]^\top$ and $\mathbb{V}_p = 0.01 I_3$.

at distance 6 m is 0.017 m however, the corresponding value in Fig. 5.6a at the same distance is 0.03 m. Furthermore, the PEB in Fig. 5.7b for the positional case, $\sigma = 0.1$ and $\beta_{\min} = 1$ at RIS number of elements 1600 is 0.007 m while its corresponding value in Fig. 5.6b is 0.018 m. the same study can be compared between Fig. 5.7c and Fig. 5.6c for the SNR scenario. The PEB is 0.101 at 10 dB when the standard deviation $\sigma = 1$, while it is 0.06 when $\sigma = 0.1$ as illustrated in Fig. 5.6c and Fig. 5.7c respectively.

Figure 5.8 illustrates the RMSE of three-stage localization algorithm, plotted against the distance from the RIS in meters. We notice how the RMSE performance is affected by adopting the true RIS phase shift model considering $\beta_{\min} = 0.5$. Due to the adoption of a definite limit of the angle and delay resolutions (360 bins for φ, 90 for ϑ, and 1000 for $\mathfrak{Q}$), coupled with the limitation that the far-field presumed in the initial stages of the algorithm is not applicable for small distances, it becomes impractical to achieve the desired RMSE in the far-field regime. However, considering these factors, the performance of the positional RMSE remains far from the positional PEB, resulting in a performance that is significantly worse than what was forecasted by the bounds. This phenomenon can be justified by the following: The positional phase pro-

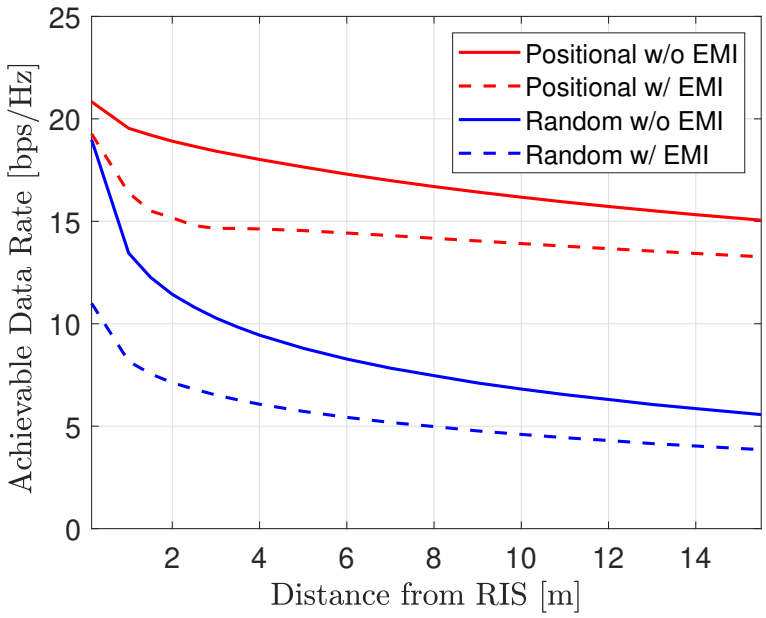

Figure 5.12: Achievable data rate as a function of RIS distance for random and positional phase profiles under the effect of EMI.

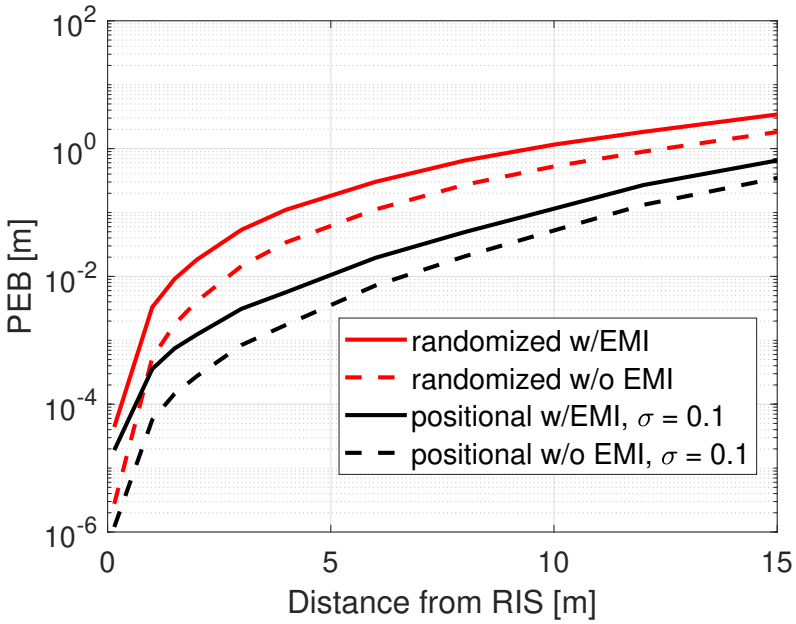

Figure 5.13: PEB as a function of distance to the RIS elements.

files concentrate energy towards the user's direction, resulting in the majority of locations, apart from the true location, having a value of $\left\|U^{\top}\mathcal{S}(p)\right\|^2 \approx 0$. Consequently, the objective function (5.20) remains nearly consistent across various positions, displaying very slender peaks around the actual position. Due to the limited precision of the estimators, there is a high probability of missing this narrow peak, which can result in a deteriorated positional RMSE.

Figure 5.9 shows the data rate against the distance to the RIS. Generally, the data rate is

inversely proportional with the distance, and this is due the decrease in SNR in the reflected path, which is inversely proportional to the distance from the RIS. The realistic RIS phase shift model is adopted, and the data rate performance gap is evident when $\beta_{\min}$ is changed from the ideal case which is $\beta_{\min} = 1$ to the actual case which is $\beta_{\min} = 0.2$. We notice that the achievable data rate in the positional phase profile exhibits slightly better performance than the directional phase profile, although the difference between the two is negligible. Nevertheless, both of them outperform the random phase case and this is expected since the random phase has only an aperture gain with no passive beamforming gain enhancement.

Figure 5.10 illustrates the achievable data rates for various phase configurations in relation to the number of RIS elements at SNR of 25 dB and a distance of 12 meters from the RIS. Our investigation focuses on assessing the impact of the amplitude-phase shift model for different $\beta_{\min}$ values, specifically $\beta_{\min} \in \{0.2, 1\}$, on the achievable data rate. In general, we observe a decline in the achievable rate when $\beta_{\min} < 1$. Firstly, it is evident that the performance of the random phase shift approach at the RIS remains unaffected by the number of elements. This result aligns with expectations, given that random phase shifts only contribute to aperture gain without any passive beamforming gain. Secondly, it is notable that both positional and directional phase configurations exhibit superior performance compared to the scheme employing random phase shifts. As the number of elements increases, we observe a consistent rise in achievable rates. This trend is logical, as the passive beamforming performance steadily improves with the increasing number of elements.

We will study the effect of EMI on the SNR in relation to the location in the Y = X plane and the achievable data rate as a function of the distance from the RIS for different RIS phase profiles in (5.42). We intentionally employ SNR, as opposed to signal-to-interference-plus-noise ratio (SINR), to emphasize that EMI should be considered noise within the context of wireless communication. This is because EMI arises from uncontrollable signals. Figure 5.11 shows the random and positional SNRs under the effect of EMI. Generally, in the random scenario, we notice that the SNR remains consistent across all locations with decreased SNR near the outer edges of the RIS subject to the pathloss. For example, SNR value at the location grid $(-1, 1)$ and $(1, 1)$ is 35 dB when there is no EMI and 22 dB with EMI. However, Higher SNR is attained in the selected direction for positional case with lower SNR in the other areas contrasted to the random scenario. For instance, the SNRs at the location grids $(-1, 1)$ and $(1, 1)$ are 24 dB and 44 dB respectively when there is no EMI while the values are reduced to 10 dB and 30 dB respectively with the presence of EMI.

Figure 5.12 shows the achievable data rate against the distance to the RIS. In general, the achievable data rate tends to decrease as the distance increases. This decrease is attributed to the diminishing SNR in the reflected path from the RIS, which also inversely correlates with the distance from the RIS. The effect of EMI is noticeable in both random and positional configurations. For example, the achievable data rate is degraded from 8 bps/Hz to around 5 bps/Hz

at a distance of 6 [m] in the random configuration while the degradation difference at the same distance for the positional configuration is around 2.5 bps/Hz.

Figure 5.13 demonstrates the PEB as it varies with the distance to the RIS, considering both random and positional phase profiles. It is observed that by using a basic random phase configuration, we can achieve relatively low PEB, specifically below 1 meter, for user positions within a 10-meter distance from the RIS elements. By employing the positional phase profiles with $\sigma = 0.1$, it is possible to significantly decrease the PEB.

5.8 Summary

We addressed the task of localizing the user in a 3D space using a RIS-based lens with a practical phase-shift model. By leveraging the curved nature of the wavefront, it is possible to estimate the location of the user by utilizing multiple phase configurations of the RIS. Fisher information analysis offers valuable insights into the design of these phase configurations taking into consideration the actual RIS phase shift model. Additionally, we have introduced a low-complexity 3D localization algorithm that simplifies the problem by decoupling the main 3D problem into 3 1D problems using the angular expansion approach. The advantage of this work shows the realistic results when using the practical phase-dependent amplitude model. The literature is saturated with RIS-related communication and localization works with overoptimistic results and far-field assumptions so, we tried in our work to prove that considering the lossless (ideal phase shift model) is not accurate in measuring the performance of localization (such as PEB and RMSE) and communication (such as achievable data rate). There are various potential research directions that can be explored further. One such direction involves mutual coupling and electromagnetic interference. This could provide additional accurate information and insights for proper positioning. These areas offer promising opportunities for advancing localization techniques and enhancing their performance in practical scenarios.

Chapter 6

Indoor Field Measurements

Recently, both academics and industry have paid close attention to the potential of adopting the prototyping of a RIS-aided wireless communication. In this chapter, we present a novel RIS prototype operating in the 3.75 GHz range with 4096 configurable elements. We propose a realistic receiver-RIS Wi-Fi feedback link and an effective method for configuring the RIS over the air by taking advantage of the geometrical array features. Our 1-bit RIS prototype offers an 18 dB power gain over the case when it is replaced with a metal plate. The indoor measurements have been carried out where the transmitter and receiver are separated by a concrete wall.

6.1 Introduction

Recent years have been a rapid expansion of research into wireless communications employing RISs. New wireless transceiver architectures have been realized using RISs, which may result in a paradigm change in transceiver design and lower the hardware cost of next wireless communication systems. In addition, RISs can modify the environment for electromagnetic wave propagation [92]. Consequently, it is worth mentioning that RIS might be deployed much more widely across the wireless network, due to its inexpensive price, to effectively modify signal propagation. There has been a significant amount of research on the theoretical modelling of the RIS, however there are currently relatively few test-bed systems that have been developed to assess the RIS's functionality in a real-world setting [265]. The main contributions of our research are as follows:

- We have developed and tested a unique feedback-based adaptive reflection coefficient optimization algorithm that enables smart reflection without changing the current communication standards.
- We have performed indoor NLoS trials and demonstrated an 18 dB channel gain improvement compared to a metal plate reference case.

The RIS implementation, beamforming and simulation results are presented under RIS-assisted wireless communication systems in section 6.2. Sections 6.3 and 6.4 give simulation results and summary for the chapter. Finally, **??** refer to the publication resulted from this chapter.

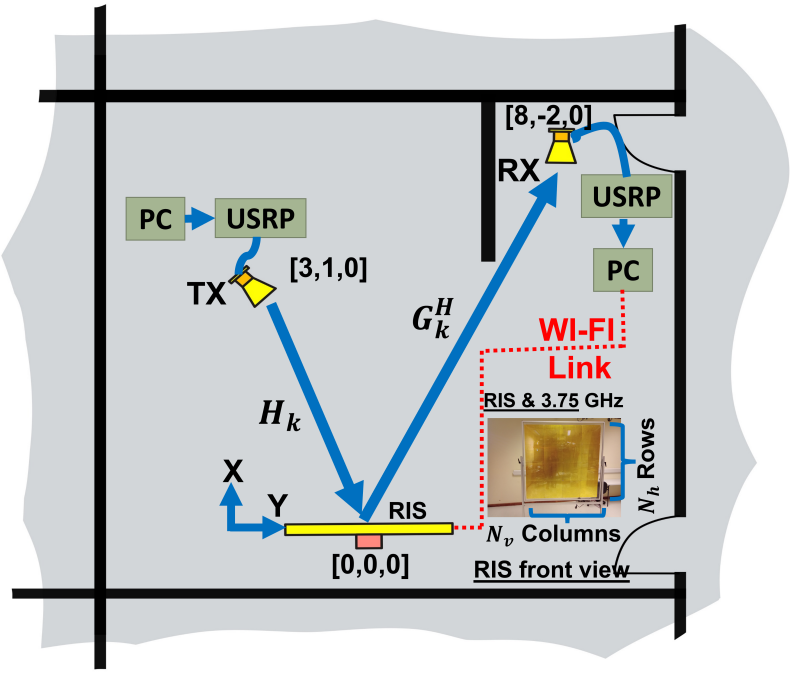

Figure 6.1: Indoor measurement setup at MAST lab

6.2 RIS-Assisted Wireless Communication System

This section describes the prototype of the RIS-aided wireless communication system seen in Fig. 6.1, which is made up of Personal Computers (PCs), universal software radio peripheral (USRP)s, a RIS, and the real-time RIS-UE feedback module. The key parts of the transmitter are the host computer, a USRP, and an antenna. The receiver has the same essential parts. These transceivers represent a UE and an access AP or BS, respectively. The locations of the Transmitter, Receiver and RIS are measured in metres. A single passive antenna on the transmitter is used to transmit 64-subcarriers OFDM signal. The USRP is used to transport the data. The receiver decodes the data stream, and the host computer recover the transmitted OFDM signal. The RIS element structure can create a 180-degree phase difference in the entire bandwidth aoround the centre frequency, for instance, employing capacitance values of 1.3 pF and 1.4 pF, for which the phase shifts are around $\pi/2$ and $-\pi/2$, respectively. Fig. 6.2 illustrates the behaviour of the amplitude and the phase shift, respectively, for different values of capacitance. It is observed that although a reflecting element is capable of achieving almost 2π full phase

tuning, its phase shift and reflection amplitude both vary with capacitance values in general. One can also observe that the minimum amplitude occurs near zero phase shift and approaches unity (the maximum value) at the phase shift of π or -π

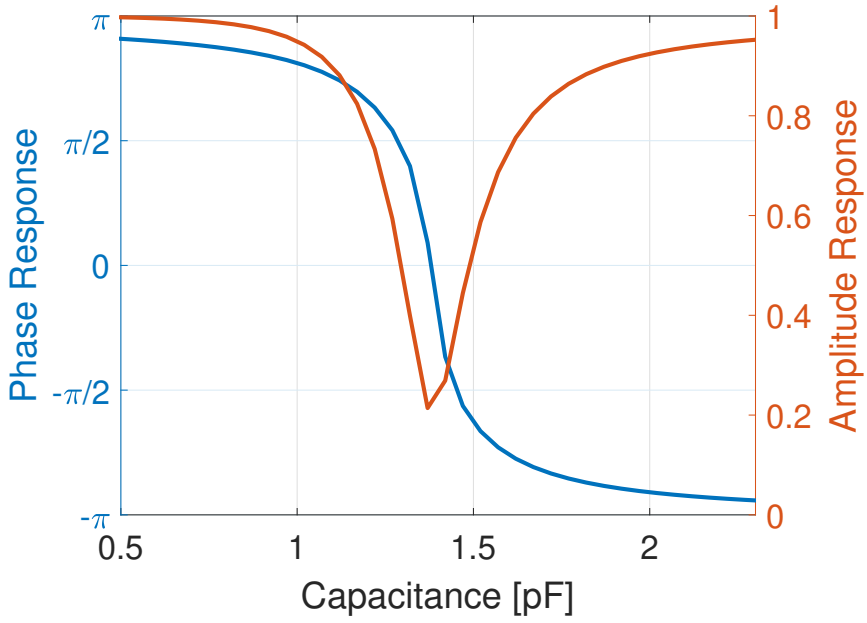

Figure 6.2: RIS element response versus different capacitance values of the PIN diode at $f =$ 3.75 GHz

6.2.1 Implementation

The fabricated RIS has a 64x64 elements grid with a square size of 192 cm x 192 cm. The front view of the RIS board is shown in Fig. 6.1. We have created a 1-bit prototype with a phase difference between the two states of about 180 degrees. A continuous OFDM Transmission is tested with Two Ettus Research Universal Software Radio Peripheral USRP X300 at the transmitter and receiver connected with standard horn antenna for each of them. Fig. 6.3 shows the RIS response of the entire band around the centre frequency. The gap of the response between the switched-off state and the achieved gain is large and this reveals the remarkable gain improvement that can be obtained by the RIS technology.

6.2.2 RIS-aided Beamforing

The RIS will either scatter or reflect the incident wave depending on its configurations. The SNR measures the communication performance where both transmitter and receiver are equipped with a horn single-antenna as per Fig. 6.1. Consequently, the RIS can help the communication system by maximizing the power of the received signal by optimizing its reflection coefficients.

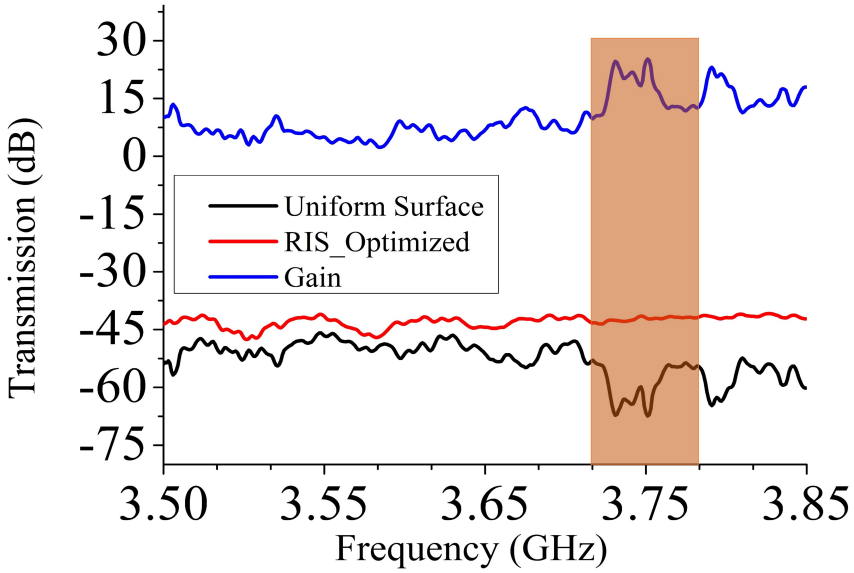

Figure 6.3: Measured transmission response when RIS is unconfigured, optimized state and achieved gain

The 2D-DFT codebook is still consistent with the structure of the optimal RIS phase shifts for a given incident angle and a specified reflecting angle [232]. The received signal $r_k \in \mathbb{C}$ can be represented as follows:

$$r_k = \left((\mathrm{G}_k \odot \mathrm{H}_k)^{\mathrm{T}} w_\theta + h_d \right) x_k + e_k \tag{6.1}$$

where $x_k \in \mathbb{C}$ is the transmitted signal, $\odot$ denotes the Hadamard product and $e_k \sim \mathcal{CN}\left(0, \sigma_e^2\right)$ is the white Gaussian noise with variance σ_e^2. The vector $w_\theta \in \mathbb{C}^N$ contains the actual reflection coefficients of the RIS that determine the amplitude losses and phase shifts. The end-to-end power gain without the direct path can be presented as:

$$\left| (\mathrm{G}_k \odot \mathrm{H}_k)^{\mathrm{T}} w_\theta \right|^2 = \beta_a \beta_b \left| a\left(\varphi_{\beta_a}, \theta_{\beta_a}\right) \odot a\left(\varphi_{\beta_b}, \theta_{\beta_b}\right) w_\theta \right|^2 \tag{6.2}$$

where $\beta_a \geq 0$ and $\beta_b \geq 0$ are the pathlosses from the AP to the RIS and from the RIS to the user respectively. $a(\varphi, \theta)$ is the steering vector while φ and θ are the azimuth and elevation angles respectively. The best approach chooses phase-shifts such that all RIS elements' reflected signals arrive in phase to the receiver. The optimal phase vector $w_{\theta_c} = \underset{|[w_\theta]_i|=1}{\operatorname{argmax}} \left| (\mathrm{G}_k \odot \mathrm{H}_k)^{\mathrm{T}} w_\theta \right|^2$ can be approximated by the columns of the DFT matrix when the RIS surface is large. Consequently, each column of the codebook beamform $W_{\theta_N} = F(N_v) \otimes F(N_h) \in \mathbb{C}^{N \times N}$ can be a possible reflection configuration for an incident signal in a certain beam direction. Let $\otimes$ denotes the Kronecker product. We searched in the codebook for the best configuration that maximize the received signal power in (6.1).

Algorithm 4: DFT Codebook Algorithm

1: Initialize the configuration vector $w_{\theta_0} \in \mathbb{C}^{N\times 1}$ from the codebook $\{W_{\theta_N} \in \mathbb{C}^{N\times N}\}$
2: Receive initial feedback of the RX signal power y_0.
3: Search in the codebook W_{θ_N}
4: **for** $w_{\theta_n}, n \in [1, N]$ **do**
5: $w_{\theta_N} \leftarrow [w_{\theta_1}, w_{\theta_2}, \ldots, w_{\theta_N}]$ where w_{θ_n} is the n-th column of the codebook matrix W_{θ_N}.
6: Receive the signal power y_n using configuration w_{θ_n}
7: **if** $y_{n-1} \geq y_n$ **then**
8: $w_{\theta_n} \leftarrow w_{\theta_{n-1}}$
9: **end if**
10: **end for**
11: Evaluate the received signal power with the new configuration.

6.3 Simulation Results

Fig. 6.4 shows the measurements of the received signal power against different configurations at 3.75 GHz. It is compared with the received power when the RIS surface is unconfigured. Algorithm 4, using the feedback iterations, searches in the codebook $\{W_{\theta_N}\}$ for the configuration that increases the received signal power. It is noticed that there are some configurations in the codebook that gives the same power gain and this explains the flat response in Fig. 6.4 at certain configurations. A power enhancement of 18 dB is obtained and this reveals the benefits of RIS technology in wireless communications.

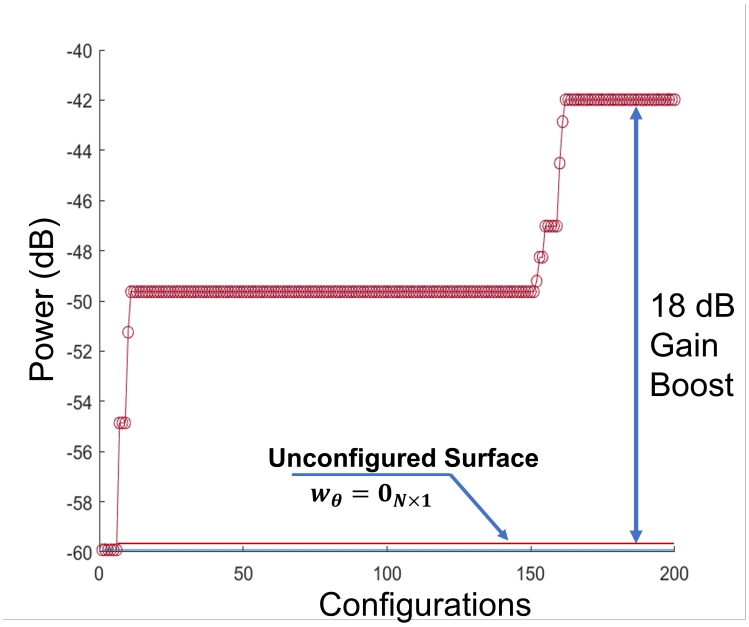

Figure 6.4: Signal power measurements at 3.75 GHz.

6.4 Summary

RIS is a promising technology and efforts are recommended towards test-bed implementations in order to demonstrate real and actual communication models.

Chapter 7

Conclusion and Future Work

This thesis presents practical and theoretical findings from research conducted in the active areas of communication and localization, with particular emphasis on assessing the communication and localization performance in sub 6 GHz with the support of RISs. In this chapter, we summarize the key outcomes related to the questions raised in the thesis (as outlined in chapter 1 Section 1.2.1) and propose potential avenues for future research.

7.1 Conclusion

RISs have recently emerged as an innovative method for enhancing wireless channel characteristics. The receiver can experience signal concentration by leveraging the constructive superposition of the LoS path between the transmitter and receiver, along with reflections from all RIS elements. This combination generates a focused beam in a specific direction. Unlike wireless repeaters and relays, RISs possess unique features: they can be configured, eliminating the need for signal amplification, intricate processing, and coding/decoding methods. Utilizing an RIS enables the customization of the wireless channel, enhancing link capacity while minimizing power consumption for point-to-point communications. Implementation of an RIS results in more effective interference reduction, leading to enhanced signal performance for end users at the cell's edge. In MU cellular networks, RISs enable the separation and sharing of scattering components, optimizing data transfer for multiple users. Consequently, an RIS-assisted wireless network has the potential to enhance QoS provisioning, sum-rate performance, and max-min fairness among users. In addition to their communication benefits, RISs provide reliable and highly accurate position estimation capabilities at a low cost and with high energy efficiency. When the LoS connection is obstructed, an RIS can establish a virtual LoS link, facilitating precise delay measurements with wideband signals. Unlike non-reconfigurable scatterers found in the environment, RISs can modify the phase shifts of their reflective elements, resulting in a substantial beamforming gain. Moreover, the abundance of elements in RISs significantly contributes to achieving high resolution in the localization process. This feature allows RISs to offer

improved resolution in terms of AoA for uplink localization or AoD for downlink localization.

The performance of multi-bits RIS is well investigated in the literature. It is noticed that the data rate increased when the phase levels assigned per each element are increased bearing in mind the equally spaces between the finite number of phases. However, choosing higher-bit RIS design increase the complexity due to assigning more phases for each RIS individual element and the switching between of them to aim the direction of the beamforming towards the receiver. The challenge is clearly evident in the RIS hardware when higher-bit RIS is required. Generally speaking, it is required more PIN or varactor diodes for each RIS cell or element to achieve more states of phases so, it not recommended to complicate the design and increase the cost by selecting high-bit RIS while the 1-bit RIS phase profile can give comparable sum data rate performance. In the current body of literature, RISs are typically placed in close proximity to distributed users, aiming to improve local coverage. This deployment strategy contrasts with that of active relays, which are typically positioned near the midpoint between the transmitter and receiver. The goal in active relay deployment is to balance SNRs in the two-hop links. Active relays process and amplify the source signal before forwarding it to the receiver. Alternatively, another deployment approach involves siting the RIS near the base station. It's worth noting that both deployment methods share the common objective of minimizing pathloss over the product distance.

The literature has proposed various alternative optimization methods to enhance data rates in RIS-assisted wireless communication systems. The goal is to find an almost perfect solution with acceptable computational complexity and runtime. Many authors have explored heuristic approaches like SDR, maximizing the strongest signal path in the time domain, and successive convex approximations. Efficient optimization tools are necessary for implementing SDR and successive convex approximation methods. Additionally, SDR relies on Gaussian randomization techniques to achieve a suboptimal rank-one solution. Despite considerable efforts to develop advanced algorithms for identifying high-quality solutions close to optimal, their computational complexity is often prohibitively high, especially in practical scenarios with a large number of RIS elements. This is precisely the context in which RIS proves most valuable. This thesis aims to illustrate those heuristic approaches, specifically power and STM methods, exhibit substantially lower computational complexity compared to the renowned SDR method while achieving data rates comparable to those of a state-of-the-art benchmark scheme. The performance of all these methods is assessed by comparing them against the upper bound of the system. A significant portion of prior studies did not account for the impact of MC and EMI on the performance of RIS. Based on our understanding, it is evident that existing literature lacks consideration of these crucial factors, leading to overly optimistic results in most research outcomes. Our investigation focuses on an RIS setup, specifically examining the influence of mutual coupling and electromagnetic interference on the information rate for both users with LoS and those without NLoS in a SISO multi-user OFDM communication setup. In the realm of communication

and localization applications involving R RISs, precise and well-defined control over the RIS becomes paramount. Achieving this necessitates the development of accurate and straightforward models for RIS phase control. These models should ideally encompass various factors, including the effects of mutual coupling, calibration, quantization, and power losses per element. Unfortunately, most existing studies on RIS localization have primarily focused on ideal phase shifters, disregarding the mentioned impairments. Consequently, the performance of proposed localization approaches under real-world conditions, accounting for these impairments, remains unknown. However, comprehending the impact of these impairments is crucial, as they can significantly influence the effectiveness and reliability of RIS-based localization methods.

The central achievement of this thesis lies in establishing a foundational comprehension of how the RIS technology can serve as a catalyst for exceptionally high communication performance and precise localization. By exploring theoretical performance boundaries, we have gained insights into the conditions under which the communication performance and accurate localization is viable, the optimal design principles for the RIS-based communication and localization systems, and the symbiotic relationship between localization and communication. This thesis underscores the pivotal role of RIS, particularly with communication and localization, in optimizing communication networks and enhancing the localization accuracy. It emphasizes that such advancements unlock opportunities that were previously inaccessible within conventional networks.

7.2 Future Research Directions

- **Scaling Laws and Beyond Far-field Regime:**
  The prevailing approach in current research on RIS-enabled SRE involves utilizing far-field assumptions. However, RISs, despite being composed of geometrically large surfaces spanning a few square meters, can operate in the near-field regime, particularly in settings like interior environments. Leveraging large RISs opens up the possibility of creating innovative wireless networks functioning in the near-field domain—an unconventional design assumption in wireless communications. This departure from the norm is noteworthy as RIS elements exhibit significant variations in propagation loss due to varying propagation distances and angles. Moreover, the near-field capability allows RISs not only to focus signals on a specific direction but also at a precise location within that direction, providing a superiority over conventional mirrors. This unique feature can be harnessed for enhanced localization. Despite these advantages, the near-field regime in RIS-enabled SREs has received limited attention in terms of understanding basic performance constraints, design requirements, and potential applications. There is a notable gap in research focusing on the near-field regime, which holds promise for unlocking capabilities like highly focused transmissions. Therefore, further investigation into the near-field

aspects of RIS-enabled SREs is warranted to explore the untapped potential and advantages it may offer.

- **Real World Implementation:**
  In recent years, there has been a rapid expansion of research in the field of wireless communications utilizing RISs. The deployment of new wireless transceiver architectures incorporating RISs holds the potential to bring about a paradigm shift in transceiver design, leading to reduced hardware costs in the next generation of wireless communication systems. Moreover, RISs have the capability to modify the electromagnetic wave propagation environment, opening up the possibility of a widespread deployment across wireless networks due to their cost-effectiveness in signal propagation modification. While there has been a considerable amount of theoretical modeling of RIS, the development of practical test-bed systems to assess RIS functionality in real-world settings has been relatively limited. This gap highlights the need for more test-bed systems to validate the extensive theoretical research conducted in this area.

- **EMI, MC and Realistic RIS Amplitude Variations Model:**
  Numerous research efforts are overlooking the presence EMI inherent in any environment. Instead, the focus tends to be solely on the signals generated by the system. EMI can arise from various sources, whether natural, intentional, or unintentional, including man-made devices and background radiation in the environment. Essentially, any unregulated wireless transmission produces EMI. The energy of EMI waves impinging on the space in front of the RIS is directly proportional to its area. When the RIS re-radiates this EMI energy, it reaches the intended receiver, leading to the degradation of the end-to-end SNR in wireless networks that are oblivious to such interference effects. The decline in SNR is attributed to the fact that these wireless networks/systems are primarily designed to counteract only the thermal noise generated by the receiver deliberately. Consequently, to address this issue, the RIS should incorporate awareness of the detrimental effects of EMI. This can be achieved through the design of beamforming RIS-assisted algorithms that specifically account for the uncontrollable presence of EMI. Another challenge is the MC, when the sections of RIS on the substrate material are in close proximity, effectively separating them poses a challenge. This proximity gives rise to mutual coupling, a phenomenon in which the impedance of one element becomes interlinked with the impedances of its neighbouring elements. Lastly, the assumption of the unity phase shift model for the RIS is inaccurate and a practical model that considers the amplitude is required to achieve realistic performance for communication and localization scenarios.

Bibliography

[1] 3GPP 2021. *First 5G NR Specs Approved,3GPP,a global Initiative, 2021*. Available at:https://www.3gpp.org/news-events/3gpp-news/1929-nsa.

[2] Saad, W., Bennis, M. and Chen, M., 2019. A vision of 6G wireless systems: Applications, trends, technologies, and open research problems. *IEEE network*, 34(3), pp.134-142.

[3] Wu, Q., Zhang, S., Zheng, B., You, C. and Zhang, R., 2021. Intelligent reflecting surface-aided wireless communications: A tutorial. *IEEE Transactions on Communications*, 69(5), pp.3313-3351.

[4] Samsung Research 2020. *The Vision of 6G, Samsung Research, 14 July 2020*. Available at:https://news.samsung.com/global/samsungs-6g-white-paper-lays-out-the-companys-vision-for-the-nextgeneration-of-communications-technology.

[5] Goldsmith, A., 2005. Wireless communications. Cambridge university press.

[6] Di Renzo, M., Zappone, A., Debbah, M., Alouini, M.S., Yuen, C., De Rosny, J. and Tretyakov, S., 2020. Smart radio environments empowered by reconfigurable intelligent surfaces: How it works, state of research, and the road ahead. *IEEE journal on selected areas in communications*, 38(11), pp.2450-2525.

[7] Subrt, L. and Pechac, P., 2012, March. Controlling propagation environments using intelligent walls. In 2012 6th European Conference on Antennas and Propagation (EUCAP) (pp. 1-5). IEEE.

[8] Welkie, A., Shangguan, L., Gummeson, J., Hu, W. and Jamieson, K., 2017, November. Programmable radio environments for smart spaces. In Proceedings of the 16th ACM Workshop on Hot Topics in Networks (pp. 36-42).

[9] Liaskos, C., Nie, S., Tsioliaridou, A., Pitsillides, A., Ioannidis, S. and Akyildiz, I., 2018. A new wireless communication paradigm through software-controlled metasurfaces. *IEEE Communications Magazine*, 56(9), pp.162-169.

[10] Liaskos, C., Tsioliaridou, A., Nie, S., Pitsillides, A., Ioannidis, S. and Akyildiz, I.F., 2019. On the network-layer modeling and configuration of programmable wireless environments. IEEE/ACM transactions on networking, 27(4), pp.1696-1713.

[11] Dunna, M., Zhang, C., Sievenpiper, D. and Bharadia, D., 2020, April. ScatterMIMO: Enabling virtual MIMO with smart surfaces. In Proceedings of the 26th Annual International Conference on Mobile Computing and Networking (pp. 1-14).

[12] Björnson, E., Wymeersch, H., Matthiesen, B., Popovski, P., Sanguinetti, L. and de Carvalho, E., 2022. Reconfigurable intelligent surfaces: A signal processing perspective with wireless applications. IEEE Signal Processing Magazine, 39(2), pp.135-158.

[13] Gong, S., Lu, X., Hoang, D.T., Niyato, D., Shu, L., Kim, D.I. and Liang, Y.C., 2020. Toward smart wireless communications via intelligent reflecting surfaces: A contemporary survey. IEEE Communications Surveys & Tutorials, 22(4), pp.2283-2314.

[14] Wymeersch, H., He, J., Denis, B., Clemente, A. and Juntti, M., 2020. Radio localization and mapping with reconfigurable intelligent surfaces: Challenges, opportunities, and research directions. IEEE Vehicular Technology Magazine, 15(4), pp.52-61.

[15] Bourdoux, A., Barreto, A.N., van Liempd, B., de Lima, C., Dardari, D., Belot, D., Lohan, E.S., Seco-Granados, G., Sarieddeen, H., Wymeersch, H. and Suutala, J., 2020. 6G white paper on localization and sensing. arXiv preprint arXiv:2006.01779.

[16] Chen, H.T., Taylor, A.J. and Yu, N., 2016. A review of metasurfaces: physics and applications. Reports on progress in physics, 79(7), p.076401.

[17] Liu, F., Pitilakis, A., Mirmoosa, M.S., Tsilipakos, O., Wang, X., Tasolamprou, A.C., Abadal, S., Cabellos-Aparicio, A., Alarcón, E., Liaskos, C. and Kantartzis, N.V., 2018, May. Programmable metasurfaces: State of the art and prospects. In 2018 IEEE International Symposium on Circuits and Systems (ISCAS) (pp. 1-5). IEEE.

[18] Turpin, J.P., Bossard, J.A., Morgan, K.L., Werner, D.H. and Werner, P.L., 2014. Reconfigurable and tunable metamaterials: a review of the theory and applications. International Journal of Antennas and Propagation, 2014.

[19] Costa, F., Monorchio, A., Talarico, S. and Valeri, F.M., 2008. An active high-impedance surface for low-profile tunable and steerable antennas. IEEE Antennas and Wireless Propagation Letters, 7, pp.676-680.

[20] Huang, D., Poutrina, E. and Smith, D.R., 2010. Analysis of the power dependent tuning of a varactor-loaded metamaterial at microwave frequencies. Applied Physics Letters, 96(10).

[21] Katko, A.R., Hawkes, A.M., Barrett, J.P. and Cummer, S.A., 2011. RF limiter metamaterial using pin diodes. IEEE Antennas and Wireless Propagation Letters, 10, pp.1571-1574.

[22] Nayeri, P., Yang, F. and Elsherbeni, A.Z., 2018. Reflectarray antennas: theory, designs, and applications.

[23] Abeywickrama, S., Zhang, R., Wu, Q. and Yuen, C., 2020. Intelligent reflecting surface: Practical phase shift model and beamforming optimization. IEEE Transactions on Communications, 68(9), pp.5849-5863.

[24] Kaina, N., Dupré, M., Lerosey, G. and Fink, M., 2014. Shaping complex microwave fields in reverberating media with binary tunable metasurfaces. Scientific reports, 4(1), p.6693.

[25] Tan, X., Sun, Z., Jornet, J.M. and Pados, D., 2016, May. Increasing indoor spectrum sharing capacity using smart reflect-array. In 2016 IEEE International Conference on Communications (ICC) (pp. 1-6). IEEE.

[26] Hu, S., Rusek, F. and Edfors, O., 2017, June. The potential of using large antenna arrays on intelligent surfaces. In 2017 IEEE 85th vehicular technology conference (VTC Spring) (pp. 1-6). IEEE.

[27] Liaskos, C., Nie, S., Tsioliaridou, A., Pitsillides, A., Ioannidis, S. and Akyildiz, I., 2019. A novel communication paradigm for high capacity and security via programmable indoor wireless environments in next generation wireless systems. Ad Hoc Networks, 87, pp.1-16.

[28] Nie, S. and Akyildiz, I.F., 2020, May. Beamforming in intelligent environments based on ultra-massive MIMO platforms in millimeter wave and terahertz bands. In ICASSP 2020-2020 IEEE International Conference on Acoustics, Speech and Signal Processing (ICASSP) (pp. 8683-8687). IEEE.

[29] Najafi, M., Schmauss, B. and Schober, R., 2021. Intelligent reflecting surfaces for free space optical communication systems. IEEE transactions on communications, 69(9), pp.6134-6151.

[30] Del Hougne, P., Fink, M. and Lerosey, G., 2019. Optimally diverse communication channels in disordered environments with tuned randomness. Nature Electronics, 2(1), pp.36-41.

[31] Karasik, R., Simeone, O., Di Renzo, M. and Shitz, S.S., 2020, June. Beyond max-SNR: Joint encoding for reconfigurable intelligent surfaces. In 2020 IEEE International Symposium on Information Theory (ISIT) (pp. 2965-2970). IEEE.

[32] Zappone, A., Di Renzo, M., Shams, F., Qian, X. and Debbah, M., 2020. Overhead-aware design of reconfigurable intelligent surfaces in smart radio environments. IEEE Transactions on Wireless Communications, 20(1), pp.126-141.

[33] Tang, W., Dai, J.Y., Chen, M.Z., Wong, K.K., Li, X., Zhao, X., Jin, S., Cheng, Q. and Cui, T.J., 2020. MIMO transmission through reconfigurable intelligent surface: System design, analysis, and implementation. IEEE journal on selected areas in communications, 38(11), pp.2683-2699.

[34] Kern, D.J., Wilhelm, M.J., Werner, D.H. and Werner, P.L., 2004, June. A novel design technique for ultra-thin tunable EBG AMC surfaces. In IEEE Antennas and Propagation Society Symposium, 2004. (Vol. 2, pp. 1167-1170). IEEE.

[35] Sheng, Z. and Varadan, V.V., 2007. Tuning the effective properties of metamaterials by changing the substrate properties. Journal of applied physics, 101(1).

[36] Lu, H., Zeng, Y., Jin, S. and Zhang, R., 2020, June. Enabling panoramic full-angle reflection via aerial intelligent reflecting surface. In 2020 IEEE International Conference on Communications Workshops (ICC Workshops) (pp. 1-6). IEEE.

[37] Björnson, E. and Sanguinetti, L., 2020. Rayleigh fading modeling and channel hardening for reconfigurable intelligent surfaces. IEEE Wireless Communications Letters, 10(4), pp.830-834.

[38] Basar, E., Di Renzo, M., De Rosny, J., Debbah, M., Alouini, M.S. and Zhang, R., 2019. Wireless communications through reconfigurable intelligent surfaces. IEEE access, 7, pp.116753-116773.

[39] Tang, W., Chen, M.Z., Chen, X., Dai, J.Y., Han, Y., Di Renzo, M., Zeng, Y., Jin, S., Cheng, Q. and Cui, T.J., 2020. Wireless communications with reconfigurable intelligent surface: Path loss modeling and experimental measurement. IEEE Transactions on Wireless Communications, 20(1), pp.421-439.

[40] Özdogan, Ö., Björnson, E. and Larsson, E.G., 2019. Intelligent reflecting surfaces: Physics, propagation, and pathloss modeling. IEEE Wireless Communications Letters, 9(5), pp.581-585.

[41] Di Renzo, M., Danufane, F.H., Xi, X., De Rosny, J. and Tretyakov, S., 2020, May. Analytical modeling of the path-loss for reconfigurable intelligent surfaces–anomalous mirror or scatterer?. In 2020 IEEE 21st International Workshop on Signal Processing Advances in Wireless Communications (SPAWC) (pp. 1-5). IEEE.

[42] Garcia, J.C.B., Sibille, A. and Kamoun, M., 2020. Reconfigurable intelligent surfaces: Bridging the gap between scattering and reflection. IEEE Journal on Selected Areas in Communications, 38(11), pp.2538-2547.

[43] Ellingson, S.W., 2021, September. Path loss in reconfigurable intelligent surface-enabled channels. In 2021 IEEE 32nd Annual International Symposium on Personal, Indoor and Mobile Radio Communications (PIMRC) (pp. 829-835). IEEE.

[44] Khawaja, W., Ozdemir, O., Yapici, Y., Erden, F. and Guvenc, I., 2020. Coverage enhancement for NLOS mmWave links using passive reflectors. IEEE Open Journal of the communications Society, 1, pp.263-281.

[45] Wu, Q. and Zhang, R., 2019. Towards smart and reconfigurable environment: Intelligent reflecting surface aided wireless network. IEEE communications magazine, 58(1), pp.106-112.

[46] Yu, X., Xu, D. and Schober, R., 2019, August. MISO wireless communication systems via intelligent reflecting surfaces. In 2019 IEEE/CIC International Conference on Communications in China (ICCC) (pp. 735-740). IEEE.

[47] Huang, C., Zappone, A., Alexandropoulos, G.C., Debbah, M. and Yuen, C., 2019. Reconfigurable intelligent surfaces for energy efficiency in wireless communication. IEEE transactions on wireless communications, 18(8), pp.4157-4170.

[48] Tang, W., Chen, X., Chen, M.Z., Dai, J.Y., Han, Y., Di Renzo, M., Jin, S., Cheng, Q. and Cui, T.J., 2022. Path loss modeling and measurements for reconfigurable intelligent surfaces in the millimeter-wave frequency band. IEEE Transactions on Communications, 70(9), pp.6259-6276.

[49] Usman, M., Rains, J., Cui, T.J., Khan, M.Z., Kazim, J.U.R., Imran, M.A. and Abbasi, Q.H., 2022. Intelligent wireless walls for contactless in-home monitoring. Light: Science & Applications, 11(1), p.212.

[50] Cui, M., Zhang, G. and Zhang, R., 2019. Secure wireless communication via intelligent reflecting surface. IEEE Wireless Communications Letters, 8(5), pp.1410-1414.

[51] Yu, X., Xu, D., Sun, Y., Ng, D.W.K. and Schober, R., 2020. Robust and secure wireless communications via intelligent reflecting surfaces. IEEE Journal on Selected Areas in Communications, 38(11), pp.2637-2652.

[52] Björnson, E., Özdogan, Ö. and Larsson, E.G., 2019. Intelligent reflecting surface versus decode-and-forward: How large surfaces are needed to beat relaying?. IEEE Wireless Communications Letters, 9(2), pp.244-248.

[53] Di Renzo, M., Ntontin, K., Song, J., Danufane, F.H., Qian, X., Lazarakis, F., De Rosny, J., Phan-Huy, D.T., Simeone, O., Zhang, R. and Debbah, M., 2020. Reconfigurable intelligent surfaces vs. relaying: Differences, similarities, and performance comparison. IEEE Open Journal of the Communications Society, 1, pp.798-807.

[54] Zhao, H., Shuang, Y., Wei, M., Cui, T.J., Hougne, P.D. and Li, L., 2020. Metasurface-assisted massive backscatter wireless communication with commodity Wi-Fi signals. Nature communications, 11(1), p.3926.

[55] Nemati, M., Ding, J. and Choi, J., 2020, May. Short-range ambient backscatter communication using reconfigurable intelligent surfaces. In 2020 IEEE Wireless Communications and Networking Conference (WCNC) (pp. 1-6). IEEE.

[56] Xu, C., Yang, L. and Zhang, P., 2018. Practical backscatter communication systems for battery-free Internet of Things: A tutorial and survey of recent research. IEEE Signal Processing Magazine, 35(5), pp.16-27.

[57] Khaleel, A. and Basar, E., 2020. Reconfigurable intelligent surface-empowered MIMO systems. IEEE Systems Journal, 15(3), pp.4358-4366.

[58] Di Renzo, M. and Song, J., 2019. Reflection probability in wireless networks with metasurface-coated environmental objects: An approach based on random spatial processes. EURASIP Journal on Wireless Communications and Networking, 2019(1), pp.1-15.

[59] Tan, X., Sun, Z., Koutsonikolas, D. and Jornet, J.M., 2018, April. Enabling indoor mobile millimeter-wave networks based on smart reflect-arrays. In IEEE INFOCOM 2018-IEEE Conference on Computer Communications (pp. 270-278). IEEE.

[60] Guo, C., Cui, Y., Yang, F. and Ding, L., 2020. Outage probability analysis and minimization in intelligent reflecting surface-assisted MISO systems. IEEE Communications Letters, 24(7), pp.1563-1567.

[61] Narayanan, A., Sreejith, T.V. and Ganti, R.K., 2017, December. Coverage analysis in millimeter wave cellular networks with reflections. In GLOBECOM 2017-2017 IEEE Global Communications Conference (pp. 1-6). IEEE.

[62] Lu, B., Wang, R. and Liu, Y., 2021. Outage probability of intelligent reflecting surface assisted full duplex two-way communications. IEEE Communications Letters, 26(2), pp.286-290.

[63] Wang, J., Zhang, W., Bao, X., Song, T. and Pan, C., 2020, December. Outage analysis for intelligent reflecting surface assisted vehicular communication networks. In GLOBECOM 2020-2020 IEEE Global Communications Conference (pp. 1-6). IEEE.

[64] Ferreira, R.C., Facina, M.S., De Figueiredo, F.A., Fraidenraich, G. and De Lima, E.R., 2020. Bit error probability for large intelligent surfaces under double-Nakagami fading channels. IEEE Open Journal of the Communications Society, 1, pp.750-759.

[65] Basar, E., 2019, June. Transmission through large intelligent surfaces: A new frontier in wireless communications. In 2019 European Conference on Networks and Communications (EuCNC) (pp. 112-117). IEEE.

[66] Assaf, T., Al-Dweik, A.J., El Moursi, M.S., Zeineldin, H. and Al-Jarrah, M., 2020. Exact bit error-rate analysis of two-user NOMA using QAM with arbitrary modulation orders. IEEE Communications Letters, 24(12), pp.2705-2709.

[67] Thirumavalavan, V.C. and Jayaraman, T.S., 2020, January. BER analysis of reconfigurable intelligent surface assisted downlink power domain NOMA system. In 2020 international conference on COMmunication systems & NETworkS (COMSNETS) (pp. 519-522). IEEE.

[68] Li, J. and Hong, Y., 2021, September. Intelligent reflecting surface aided communication systems: Performance analysis. In 2021 IEEE 32nd Annual International Symposium on Personal, Indoor and Mobile Radio Communications (PIMRC) (pp. 519-524). IEEE.

[69] Salhab, A.M. and Samuh, M.H., 2021. Accurate performance analysis of reconfigurable intelligent surfaces over Rician fading channels. IEEE Wireless Communications Letters, 10(5), pp.1051-1055.

[70] Jung, M., Saad, W., Debbah, M. and Hong, C.S., 2020, June. Asymptotic optimality of reconfigurable intelligent surfaces: Passive beamforming and achievable rate. In ICC 2020-2020 IEEE International Conference on Communications (ICC) (pp. 1-6). IEEE.

[71] He, J., Wymeersch, H., Sanguanpuak, T., Silvén, O. and Juntti, M., 2020, April. Adaptive beamforming design for mmWave RIS-aided joint localization and communication. In 2020 IEEE Wireless Communications and Networking Conference Workshops (WCNCW) (pp. 1-6). IEEE.

[72] Özdogan, Ö., Björnson, E. and Larsson, E.G., 2020, May. Using intelligent reflecting surfaces for rank improvement in MIMO communications. In ICASSP 2020-2020 IEEE International Conference on Acoustics, Speech and Signal Processing (ICASSP) (pp. 9160-9164). IEEE.

[73] Zhang, H., Di, B., Song, L. and Han, Z., 2020. Reconfigurable intelligent surfaces assisted communications with limited phase shifts: How many phase shifts are enough?. IEEE Transactions on Vehicular Technology, 69(4), pp.4498-4502.

[74] Alegría, J.V. and Rusek, F., 2019, December. Achievable rate with correlated hardware impairments in large intelligent surfaces. In 2019 IEEE 8th International Workshop on Computational Advances in Multi-Sensor Adaptive Processing (CAMSAP) (pp. 559-563). IEEE.

[75] Lyu, J. and Zhang, R., 2020. Spatial throughput characterization for intelligent reflecting surface aided multiuser system. IEEE Wireless Communications Letters, 9(6), pp.834-838.

[76] Björnson, E., 2021, November. Optimizing a binary intelligent reflecting surface for OFDM communications under mutual coupling. In WSA 2021; 25th International ITG Workshop on Smart Antennas (pp. 1-6). VDE.

[77] Zhang, S. and Zhang, R., 2021. Intelligent reflecting surface aided multi-user communication: Capacity region and deployment strategy. IEEE Transactions on Communications, 69(9), pp.5790-5806.

[78] Papazafeiropoulos, A., Pan, C., Elbir, A., Kourtessis, P., Chatzinotas, S. and Senior, J.M., 2021. Coverage probability of distributed IRS systems under spatially correlated channels. IEEE Wireless Communications Letters, 10(8), pp.1722-1726.

[79] Jung, M., Saad, W., Jang, Y., Kong, G. and Choi, S., 2020. Performance analysis of large intelligent surfaces (LISs): Asymptotic data rate and channel hardening effects. IEEE Transactions on Wireless Communications, 19(3), pp.2052-2065.

[80] Hu, S., Rusek, F. and Edfors, O., 2018, December. Capacity degradation with modeling hardware impairment in large intelligent surface. In 2018 IEEE Global Communications Conference (GLOBECOM) (pp. 1-6). IEEE.

[81] Papazafeiropoulos, A., Pan, C., Kourtessis, P., Chatzinotas, S. and Senior, J.M., 2021. Intelligent reflecting surface-assisted MU-MISO systems with imperfect hardware: Channel estimation and beamforming design. IEEE Transactions on Wireless Communications, 21(3), pp.2077-2092.

[82] Hu, S., Rusek, F. and Edfors, O., 2018. Beyond massive MIMO: The potential of positioning with large intelligent surfaces. IEEE Transactions on Signal Processing, 66(7), pp.1761-1774.

[83] Basar, E., Wen, M., Mesleh, R., Di Renzo, M., Xiao, Y. and Haas, H., 2017. Index modulation techniques for next-generation wireless networks. IEEE access, 5, pp.16693-16746.

[84] Phan-Huy, D.T., Kokar, Y., Rachedi, K., Pajusco, P., Mokh, A., Magounaki, T., Masood, R., Buey, C., Ratajczak, P., Malhouroux-Gaffet, N. and Conrat, J.M., 2019. Single-carrier spatial modulation for the Internet of Things: Design and performance evaluation by using real compact and reconfigurable antennas. IEEE access, 7, pp.18978-18993.

[85] Van Huynh, N., Hoang, D.T., Lu, X., Niyato, D., Wang, P. and Kim, D.I., 2018. Ambient backscatter communications: A contemporary survey. IEEE Communications surveys & tutorials, 20(4), pp.2889-2922.

[86] Guan, X., Wu, Q. and Zhang, R., 2020. Joint power control and passive beamforming in IRS-assisted spectrum sharing. IEEE Communications Letters, 24(7), pp.1553-1557.

[87] Wu, W., Wang, Z., Yuan, L., Zhou, F., Lang, F., Wang, B. and Wu, Q., 2021. IRS-enhanced energy detection for spectrum sensing in cognitive radio networks. IEEE Wireless Communications Letters, 10(10), pp.2254-2258.

[88] Mahmoud, A., Muhaidat, S., Sofotasios, P.C., Abualhaol, I., Dobre, O.A. and Yanikomeroglu, H., 2021. Intelligent reflecting surfaces assisted UAV communications for IoT networks: Performance analysis. IEEE Transactions on Green Communications and Networking, 5(3), pp.1029-1040.

[89] Al-Jarrah, M., Alsusa, E., Al-Dweik, A. and So, D.K., 2021. Capacity analysis of IRS-based UAV communications with imperfect phase compensation. IEEE Wireless Communications Letters, 10(7), pp.1479-1483.

[90] Al-Jarrah, M., Al-Dweik, A., Alsusa, E., Iraqi, Y. and Alouini, M.S., 2021. On the performance of IRS-assisted multi-layer UAV communications with imperfect phase compensation. IEEE Transactions on Communications, 69(12), pp.8551-8568.

[91] Tan, X., Sun, Z., Jornet, J.M. and Pados, D., 2016, May. Increasing indoor spectrum sharing capacity using smart reflect-array. In 2016 IEEE International Conference on Communications (ICC) (pp. 1-6). IEEE.

[92] Tang, W., Chen, M.Z., Chen, X., Dai, J.Y., Han, Y., Di Renzo, M., Zeng, Y., Jin, S., Cheng, Q. and Cui, T.J., 2020. Wireless communications with reconfigurable intelligent surface: Path loss modeling and experimental measurement. IEEE Transactions on Wireless Communications, 20(1), pp.421-439.

[93] Zhang, S. and Zhang, R., 2020. Capacity characterization for intelligent reflecting surface aided MIMO communication. IEEE Journal on Selected Areas in Communications, 38(8), pp.1823-1838.

[94] Huang, C., Alexandropoulos, G.C., Yuen, C. and Debbah, M., 2019, July. Indoor signal focusing with deep learning designed reconfigurable intelligent surfaces. In 2019 IEEE 20th international workshop on signal processing advances in wireless communications (SPAWC) (pp. 1-5). IEEE.

[95] Ye, J., Guo, S. and Alouini, M.S., 2020. Joint reflecting and precoding designs for SER minimization in reconfigurable intelligent surfaces assisted MIMO systems. IEEE Transactions on Wireless Communications, 19(8), pp.5561-5574.

[96] Huang, C., Zappone, A., Alexandropoulos, G.C., Debbah, M. and Yuen, C., 2019. Reconfigurable intelligent surfaces for energy efficiency in wireless communication. IEEE transactions on wireless communications, 18(8), pp.4157-4170.

[97] Wu, Q. and Zhang, R., 2019. Beamforming optimization for wireless network aided by intelligent reflecting surface with discrete phase shifts. IEEE Transactions on Communications, 68(3), pp.1838-1851.

[98] Yu, X., Xu, D. and Schober, R., 2019, August. MISO wireless communication systems via intelligent reflecting surfaces. In 2019 IEEE/CIC International Conference on Communications in China (ICCC) (pp. 735-740). IEEE.

[99] Wu, Q. and Zhang, R., 2018, December. Intelligent reflecting surface enhanced wireless network: Joint active and passive beamforming design. In 2018 IEEE Global Communications Conference (GLOBECOM) (pp. 1-6). IEEE.

[100] Chen, W., Ma, X., Li, Z. and Kuang, N., 2019, August. Sum-rate maximization for intelligent reflecting surface based terahertz communication systems. In 2019 IEEE/CIC International Conference on Communications Workshops in China (ICCC Workshops) (pp. 153-157). IEEE.

[101] Guo, H., Liang, Y.C., Chen, J. and Larsson, E.G., 2020. Weighted sum-rate maximization for reconfigurable intelligent surface aided wireless networks. IEEE transactions on wireless communications, 19(5), pp.3064-3076.

[102] Huang, C., Zappone, A., Debbah, M. and Yuen, C., 2018, April. Achievable rate maximization by passive intelligent mirrors. In 2018 IEEE International Conference on Acoustics, Speech and Signal Processing (ICASSP) (pp. 3714-3718). IEEE.

[103] Mu, X., Liu, Y., Guo, L., Lin, J. and Al-Dhahir, N., 2020. Exploiting intelligent reflecting surfaces in NOMA networks: Joint beamforming optimization. IEEE Transactions on Wireless Communications, 19(10), pp.6884-6898.

[104] Guo, H., Liang, Y.C., Chen, J. and Larsson, E.G., 2019, December. Weighted sum-rate maximization for intelligent reflecting surface enhanced wireless networks. In 2019 IEEE Global Communications Conference (GLOBECOM) (pp. 1-6). IEEE.

[105] Yu, X., Xu, D. and Schober, R., 2020, May. Optimal beamforming for MISO communications via intelligent reflecting surfaces. In 2020 IEEE 21st International Workshop on Signal Processing Advances in Wireless Communications (SPAWC) (pp. 1-5). IEEE.

[106] Perović, N.S., Tran, L.N., Di Renzo, M. and Flanagan, M.F., 2021. Achievable rate optimization for MIMO systems with reconfigurable intelligent surfaces. IEEE Transactions on Wireless Communications, 20(6), pp.3865-3882.

[107] Yang, Y., Zheng, B., Zhang, S. and Zhang, R., 2020. Intelligent reflecting surface meets OFDM: Protocol design and rate maximization. IEEE Transactions on Communications, 68(7), pp.4522-4535.

[108] Björnson, E., 2021, November. Optimizing a binary intelligent reflecting surface for OFDM communications under mutual coupling. In WSA 2021; 25th International ITG Workshop on Smart Antennas (pp. 1-6). VDE.

[109] Yang, Y., Zhang, S. and Zhang, R., 2020. IRS-enhanced OFDMA: Joint resource allocation and passive beamforming optimization. IEEE Wireless Communications Letters, 9(6), pp.760-764.

[110] Yang, Y., Zhang, S. and Zhang, R., 2019, December. IRS-enhanced OFDM: Power allocation and passive array optimization. In 2019 IEEE Global Communications Conference (GLOBECOM) (pp. 1-6). IEEE.

[111] Björnson, E., Wymeersch, H., Matthiesen, B., Popovski, P., Sanguinetti, L. and de Carvalho, E., 2022. Reconfigurable intelligent surfaces: A signal processing perspective with wireless applications. IEEE Signal Processing Magazine, 39(2), pp.135-158.

[112] Nuti, P., Balti, E. and Evans, B.L., 2022, June. Spectral efficiency optimization for mmWave wideband MIMO RIS-assisted communication. In 2022 IEEE 95th Vehicular Technology Conference:(VTC2022-Spring) (pp. 1-6). IEEE.

[113] Björnson, E., Wymeersch, H., Matthiesen, B., Popovski, P., Sanguinetti, L. and de Carvalho, E., 2022. Reconfigurable intelligent surfaces: A signal processing perspective with wireless applications. IEEE Signal Processing Magazine, 39(2), pp.135-158.

[114] Wu, Q., Zhang, S., Zheng, B., You, C. and Zhang, R., 2021. Intelligent reflecting surface-aided wireless communications: A tutorial. IEEE Transactions on Communications, 69(5), pp.3313-3351.

[115] Björnson, E., Özdogan, Ö. and Larsson, E.G., 2020. Reconfigurable intelligent surfaces: Three myths and two critical questions. IEEE Communications Magazine, 58(12), pp.90-96.

[116] Mishra, D. and Johansson, H., 2019, May. Channel estimation and low-complexity beamforming design for passive intelligent surface assisted MISO wireless energy transfer. In ICASSP 2019-2019 IEEE International Conference on Acoustics, Speech and Signal Processing (ICASSP) (pp. 4659-4663). IEEE.

[117] Zheng, B. and Zhang, R., 2019. Intelligent reflecting surface-enhanced OFDM: Channel estimation and reflection optimization. IEEE Wireless Communications Letters, 9(4), pp.518-522.

[118] He, Z.Q. and Yuan, X., 2019. Cascaded channel estimation for large intelligent metasurface assisted massive MIMO. IEEE Wireless Communications Letters, 9(2), pp.210-214.

[119] Elbir, A.M., Papazafeiropoulos, A., Kourtessis, P. and Chatzinotas, S., 2020. Deep channel learning for large intelligent surfaces aided mm-wave massive MIMO systems. IEEE Wireless Communications Letters, 9(9), pp.1447-1451.

[120] Wang, Z., Liu, L. and Cui, S., 2020. Channel estimation for intelligent reflecting surface assisted multiuser communications: Framework, algorithms, and analysis. IEEE Transactions on Wireless Communications, 19(10), pp.6607-6620.

[121] Zheng, B., You, C. and Zhang, R., 2020. Intelligent reflecting surface assisted multiuser OFDMA: Channel estimation and training design. IEEE Transactions on Wireless Communications, 19(12), pp.8315-8329.

[122] Wang, P., Fang, J., Duan, H. and Li, H., 2020. Compressed channel estimation for intelligent reflecting surface-assisted millimeter wave systems. IEEE signal processing letters, 27, pp.905-909.

[123] He, Z.Q. and Yuan, X., 2019. Cascaded channel estimation for large intelligent metasurface assisted massive MIMO. IEEE Wireless Communications Letters, 9(2), pp.210-214.

[124] de Araújo, G.T. and de Almeida, A.L., 2020, June. PARAFAC-based channel estimation for intelligent reflective surface assisted MIMO system. In 2020 IEEE 11th Sensor Array and Multichannel Signal Processing Workshop (SAM) (pp. 1-5). IEEE.

[125] Mirza, J. and Ali, B., 2021. Channel estimation method and phase shift design for reconfigurable intelligent surface assisted MIMO networks. IEEE Transactions on Cognitive Communications and Networking, 7(2), pp.441-451.

[126] He, J., Leinonen, M., Wymeersch, H. and Juntti, M., 2020, December. Channel estimation for RIS-aided mmWave MIMO systems. In GLOBECOM 2020-2020 IEEE Global Communications Conference (pp. 1-6). IEEE.

[127] Cui, Y. and Yin, H., 2019. An efficient CSI acquisition method for intelligent reflecting surface-assisted mmWave networks. arXiv preprint arXiv:1912.12076.

[128] Wang, P., Fang, J., Duan, H. and Li, H., 2020. Compressed channel estimation for intelligent reflecting surface-assisted millimeter wave systems. IEEE signal processing letters, 27, pp.905-909.

[129] Chen, J., Liang, Y.C., Cheng, H.V. and Yu, W., 2023. Channel estimation for reconfigurable intelligent surface aided multi-user mmWave MIMO systems. IEEE Transactions on Wireless Communications.

[130] Hu, C., Dai, L., Han, S. and Wang, X., 2021. Two-timescale channel estimation for reconfigurable intelligent surface aided wireless communications. IEEE Transactions on Communications, 69(11), pp.7736-7747.

[131] Liu, H., Yuan, X. and Zhang, Y.J.A., 2020. Matrix-calibration-based cascaded channel estimation for reconfigurable intelligent surface assisted multiuser MIMO. IEEE Journal on Selected Areas in Communications, 38(11), pp.2621-2636.

[132] Wei, L., Huang, C., Alexandropoulos, G.C. and Yuen, C., 2020, June. Parallel factor decomposition channel estimation in RIS-assisted multi-user MISO communication. In 2020 IEEE 11th sensor array and multichannel signal processing workshop (SAM) (pp. 1-5). IEEE.

[133] Ning, B., Chen, Z., Chen, W. and Du, Y., 2020, June. Channel estimation and transmission for intelligent reflecting surface assisted THz communications. In ICC 2020-2020 IEEE International Conference on Communications (ICC) (pp. 1-7). IEEE.

[134] Ning, B., Chen, Z., Chen, W., Du, Y. and Fang, J., 2021. Terahertz multi-user massive MIMO with intelligent reflecting surface: Beam training and hybrid beamforming. IEEE Transactions on Vehicular Technology, 70(2), pp.1376-1393.

[135] Khan, S., Khan, K.S., Haider, N. and Shin, S.Y., 2019. Deep-learning-aided detection for reconfigurable intelligent surfaces. arXiv preprint arXiv:1910.09136.

[136] Elbir, A.M., Papazafeiropoulos, A., Kourtessis, P. and Chatzinotas, S., 2020. Deep channel learning for large intelligent surfaces aided mm-wave massive MIMO systems. IEEE Wireless Communications Letters, 9(9), pp.1447-1451.

[137] Taha, A., Zhang, Y., Mismar, F.B. and Alkhateeb, A., 2020, May. Deep reinforcement learning for intelligent reflecting surfaces: Towards standalone operation. In 2020 IEEE 21st international workshop on signal processing advances in wireless communications (SPAWC) (pp. 1-5). IEEE.

[138] Taha, A., Alrabeiah, M. and Alkhateeb, A., 2019, December. Deep learning for large intelligent surfaces in millimeter wave and massive MIMO systems. In 2019 IEEE Global communications conference (GLOBECOM) (pp. 1-6). IEEE.

[139] Taha, A., Alrabeiah, M. and Alkhateeb, A., 2021. Enabling large intelligent surfaces with compressive sensing and deep learning. IEEE access, 9, pp.44304-44321.

[140] Alexandropoulos, G.C. and Vlachos, E., 2020, May. A hardware architecture for reconfigurable intelligent surfaces with minimal active elements for explicit channel estimation. In ICASSP 2020-2020 IEEE international conference on acoustics, speech and signal processing (ICASSP) (pp. 9175-9179). IEEE.

[141] You, C., Zheng, B., Mei, W. and Zhang, R., 2022. How to deploy intelligent reflecting surfaces in wireless network: BS-side, user-side, or both sides?. Journal of Communications and Information Networks, 7(1), pp.1-10.

[142] Han, Y., Zhang, S., Duan, L. and Zhang, R., 2020. Cooperative double-IRS aided communication: Beamforming design and power scaling. IEEE Wireless Communications Letters, 9(8), pp.1206-1210.

[143] Zheng, B., You, C. and Zhang, R., 2021. Double-IRS assisted multi-user MIMO: Cooperative passive beamforming design. IEEE Transactions on Wireless Communications, 20(7), pp.4513-4526.

[144] You, C., Zheng, B. and Zhang, R., 2020. Wireless communication via double IRS: Channel estimation and passive beamforming designs. IEEE Wireless Communications Letters, 10(2), pp.431-435.

[145] Li, Z., Hua, M., Wang, Q. and Song, Q., 2020. Weighted sum-rate maximization for multi-IRS aided cooperative transmission. IEEE Wireless Communications Letters, 9(10), pp.1620-1624.

[146] Zhang, S. and Zhang, R., 2021. Intelligent reflecting surface aided multi-user communication: Capacity region and deployment strategy. IEEE Transactions on Communications, 69(9), pp.5790-5806.

[147] Wu, J. and Shim, B., 2021, March. Power minimization of intelligent reflecting surface-aided uplink iot networks. In 2021 IEEE Wireless Communications and Networking Conference (WCNC) (pp. 1-6). IEEE.

[148] Lyu, J. and Zhang, R., 2021. Hybrid active/passive wireless network aided by intelligent reflecting surface: System modeling and performance analysis. IEEE Transactions on Wireless Communications, 20(11), pp.7196-7212.

[149] Kishk, M.A. and Alouini, M.S., 2020. Exploiting randomly located blockages for large-scale deployment of intelligent surfaces. IEEE Journal on Selected Areas in Communications, 39(4), pp.1043-1056.

[150] Liu, X., Liu, Y., Chen, Y. and Poor, H.V., 2020. RIS enhanced massive non-orthogonal multiple access networks: Deployment and passive beamforming design. IEEE Journal on Selected Areas in Communications, 39(4), pp.1057-1071.

[151] Jia, C., Gao, H., Chen, N. and He, Y., 2020. Machine learning empowered beam management for intelligent reflecting surface assisted MmWave networks. China Communications, 17(10), pp.100-114.

[152] Wu, Q. and Zhang, R., 2019. Intelligent reflecting surface enhanced wireless network via joint active and passive beamforming. IEEE transactions on wireless communications, 18(11), pp.5394-5409.

[153] Björnson, E. and Sanguinetti, L., 2019, December. Demystifying the power scaling law of intelligent reflecting surfaces and metasurfaces. In 2019 IEEE 8th International Workshop on Computational Advances in Multi-Sensor Adaptive Processing (CAMSAP) (pp. 549-553). IEEE.

[154] Yu, X., Xu, D. and Schober, R., 2019, August. MISO wireless communication systems via intelligent reflecting surfaces. In 2019 IEEE/CIC International Conference on Communications in China (ICCC) (pp. 735-740). IEEE.

[155] Wu, Q. and Zhang, R., 2019. Beamforming optimization for wireless network aided by intelligent reflecting surface with discrete phase shifts. IEEE Transactions on Communications, 68(3), pp.1838-1851.

[156] Zhang, S. and Zhang, R., 2020. Capacity characterization for intelligent reflecting surface aided MIMO communication. IEEE Journal on Selected Areas in Communications, 38(8), pp.1823-1838.

[157] Ying, K., Gao, Z., Lyu, S., Wu, Y., Wang, H. and Alouini, M.S., 2020. GMD-based hybrid beamforming for large reconfigurable intelligent surface assisted millimeter-wave massive MIMO. IEEE Access, 8, pp.19530-19539.

[158] Zhang, Y., Zhong, C., Zhang, Z. and Lu, W., 2020. Sum rate optimization for two way communications with intelligent reflecting surface. IEEE Communications Letters, 24(5), pp.1090-1094.

[159] Yang, Y., Zheng, B., Zhang, S. and Zhang, R., 2020. Intelligent reflecting surface meets OFDM: Protocol design and rate maximization. IEEE Transactions on Communications, 68(7), pp.4522-4535.

[160] Zheng, B. and Zhang, R., 2019. Intelligent reflecting surface-enhanced OFDM: Channel estimation and reflection optimization. IEEE Wireless Communications Letters, 9(4), pp.518-522.

[161] Björnson, E. and Marcenaro, L., 2021. Configuring an intelligent reflecting surface for wireless communications: Highlights from the 2021 ieee signal processing cup student competition [sp competitions]. IEEE Signal Processing Magazine, 39(1), pp.126-131.

[162] Yang, Z., Feng, L., Zhou, F., Qiu, X. and Li, W., 2021. Analytical performance analysis of intelligent reflecting surface aided ambient backscatter communication network. IEEE Wireless Communications Letters, 10(12), pp.2732-2736.

[163] He, M., Xu, W., Shen, H., Xie, G., Zhao, C. and Di Renzo, M., 2021. Cooperative multi-RIS communications for wideband mmWave MISO-OFDM systems. IEEE Wireless Communications Letters, 10(11), pp.2360-2364.

[164] Du, H., Zhang, J., Cheng, J. and Ai, B., 2021. Millimeter wave communications with reconfigurable intelligent surfaces: Performance analysis and optimization. IEEE Transactions on Communications, 69(4), pp.2752-2768.

[165] El Bouanani, F., Muhaidat, S., Sofotasios, P.C., Dobre, O.A. and Badarneh, O.S., 2020. Performance analysis of intelligent reflecting surface aided wireless networks with wireless power transfer. IEEE Communications Letters, 25(3), pp.793-797.

[166] Yue, X. and Liu, Y., 2021. Performance analysis of intelligent reflecting surface assisted NOMA networks. IEEE Transactions on Wireless Communications, 21(4), pp.2623-2636.

[167] Lin, S., Zheng, B., Alexandropoulos, G.C., Wen, M. and Chen, F., 2020. Adaptive transmission for reconfigurable intelligent surface-assisted OFDM wireless communications. IEEE Journal on Selected Areas in Communications, 38(11), pp.2653-2665.

[168] Li, H., Cai, W., Liu, Y., Li, M., Liu, Q. and Wu, Q., 2021. Intelligent reflecting surface enhanced wideband MIMO-OFDM communications: From practical model to reflection optimization. IEEE Transactions on Communications, 69(7), pp.4807-4820.

[169] Yang, W., Li, H., Li, M., Liu, Y. and Liu, Q., 2021, March. Channel estimation for practical IRS-assisted OFDM systems. In 2021 IEEE Wireless Communications and Networking Conference Workshops (WCNCW) (pp. 1-6). IEEE.

[170] Ohyama, T., Kawamoto, Y. and Kato, N., 2021. Intelligent reflecting surface (IRS) allocation scheduling method using combinatorial optimization by quantum computing. IEEE Transactions on Emerging Topics in Computing, 10(3), pp.1633-1644.

[171] Yang, Y., Zhang, S. and Zhang, R., 2019, December. IRS-enhanced OFDM: Power allocation and passive array optimization. In 2019 IEEE Global Communications Conference (GLOBECOM) (pp. 1-6). IEEE.

[172] Jiang, W., Chen, B., Zhao, J., Xiong, Z. and Ding, Z., 2021. Joint active and passive beamforming design for the IRS-assisted MIMOME-OFDM secure communications. IEEE Transactions on Vehicular Technology, 70(10), pp.10369-10381.

[173] Ghanem, W.R., Jamali, V. and Schober, R., 2021, March. Joint beamforming and phase shift optimization for multicell IRS-aided OFDMA-URLLC systems. In 2021 IEEE Wireless Communications and Networking Conference (WCNC) (pp. 1-7). IEEE.

[174] Wei, Z., Cai, Y., Sun, Z., Ng, D.W.K., Yuan, J., Zhou, M. and Sun, L., 2020. Sum-rate maximization for IRS-assisted UAV OFDMA communication systems. IEEE Transactions on Wireless Communications, 20(4), pp.2530-2550.

[175] Pan, Y., Wang, K., Pan, C., Zhu, H. and Wang, J., 2021. UAV-assisted and intelligent reflecting surfaces-supported terahertz communications. IEEE Wireless Communications Letters, 10(6), pp.1256-1260.

[176] Nadeem, Q.U.A., Kammoun, A., Chaaban, A., Debbah, M. and Alouini, M.S., 2019. Intelligent reflecting surface assisted wireless communication: Modeling and channel estimation. arXiv preprint arXiv:1906.02360.

[177] Mishra, D. and Johansson, H., 2019, May. Channel estimation and low-complexity beamforming design for passive intelligent surface assisted MISO wireless energy transfer. In ICASSP 2019-2019 IEEE International Conference on Acoustics, Speech and Signal Processing (ICASSP) (pp. 4659-4663). IEEE.

[178] Yang, Y., Zheng, B., Zhang, S. and Zhang, R., 2020. Intelligent reflecting surface meets OFDM: Protocol design and rate maximization. IEEE Transactions on Communications, 68(7), pp.4522-4535.

[179] Zheng, B., You, C. and Zhang, R., 2020. Intelligent reflecting surface assisted multi-user OFDMA: Channel estimation and training design. IEEE Transactions on Wireless Communications, 19(12), pp.8315-8329.

[180] Kim, I.S., Bennis, M., Oh, J., Chung, J. and Choi, J., 2023. Bayesian Channel Estimation for Intelligent Reflecting Surface-Aided mmWave Massive MIMO Systems With Semi-Passive Elements. IEEE Transactions on Wireless Communications.

[181] Yu, X., Xu, D. and Schober, R., 2020, May. Optimal beamforming for MISO communications via intelligent reflecting surfaces. In 2020 IEEE 21st International Workshop on Signal Processing Advances in Wireless Communications (SPAWC) (pp. 1-5). IEEE.

[182] Phan-Huy, D.T., Kokar, Y., Rachedi, K., Pajusco, P., Mokh, A., Magounaki, T., Masood, R., Buey, C., Ratajczak, P., Malhouroux-Gaffet, N. and Conrat, J.M., 2019. Single-carrier spatial modulation for the Internet of Things: Design and performance evaluation by using real compact and reconfigurable antennas. IEEE access, 7, pp.18978-18993.

[183] Van Huynh, N., Hoang, D.T., Lu, X., Niyato, D., Wang, P. and Kim, D.I., 2018. Ambient backscatter communications: A contemporary survey. IEEE Communications surveys & tutorials, 20(4), pp.2889-2922.

[184] Lyu, J. and Zhang, R., 2020. Spatial throughput characterization for intelligent reflecting surface aided multiuser system. IEEE Wireless Communications Letters, 9(6), pp.834-838.

[185] Björnson, E., 2021, November. Optimizing a binary intelligent reflecting surface for OFDM communications under mutual coupling. In WSA 2021; 25th International ITG Workshop on Smart Antennas (pp. 1-6). VDE.

[186] Zhang, S. and Zhang, R., 2021. Intelligent reflecting surface aided multi-user communication: Capacity region and deployment strategy. IEEE Transactions on Communications, 69(9), pp.5790-5806.

[187] Cui, T.J., Qi, M.Q., Wan, X., Zhao, J. and Cheng, Q., 2014. Coding metamaterials, digital metamaterials and programmable metamaterials. Light: science & applications, 3(10), pp.e218-e218.

[188] Liu, S., Cui, T.J., Zhang, L., Xu, Q., Wang, Q., Wan, X., Gu, J.Q., Tang, W.X., Qing Qi, M., Han, J.G. and Zhang, W.L., 2016. Convolution operations on coding metasurface to reach flexible and continuous controls of terahertz beams. Advanced science, 3(10), p.1600156.

[189] Li, L., Jun Cui, T., Ji, W., Liu, S., Ding, J., Wan, X., Bo Li, Y., Jiang, M., Qiu, C.W. and Zhang, S., 2017. Electromagnetic reprogrammable coding-metasurface holograms. Nature communications, 8(1), p.197.

[190] Ma, Q., Shi, C.B., Bai, G.D., Chen, T.Y., Noor, A. and Cui, T.J., 2017. Beam-editing coding metasurfaces based on polarization bit and orbital-angular-momentum-mode bit. Advanced Optical Materials, 5(23), p.1700548.

[191] Liu, S. and Cui, T.J., 2016. Flexible controls of terahertz waves using coding and programmable metasurfaces. IEEE journal of selected topics in quantum electronics, 23(4), pp.1-12.

[192] Zhang, L., Liu, S., Li, L. and Cui, T.J., 2017. Spin-controlled multiple pencil beams and vortex beams with different polarizations generated by Pancharatnam-Berry coding metasurfaces. ACS applied materials & interfaces, 9(41), pp.36447-36455.

[193] Shuang, Y., Zhao, H., Ji, W., Cui, T.J. and Li, L., 2020. Programmable high-order OAM-carrying beams for direct-modulation wireless communications. IEEE journal on emerging and selected topics in circuits and systems, 10(1), pp.29-37.

[194] Zhang, X.G., Jiang, W.X., Jiang, H.L., Wang, Q., Tian, H.W., Bai, L., Luo, Z.J., Sun, S., Luo, Y., Qiu, C.W. and Cui, T.J., 2020. An optically driven digital metasurface for programming electromagnetic functions. Nature Electronics, 3(3), pp.165-171.

[195] Zhao, J., Yang, X., Dai, J.Y., Cheng, Q., Li, X., Qi, N.H., Ke, J.C., Bai, G.D., Liu, S., Jin, S. and Alu, A., 2019. Programmable time-domain digital-coding metasurface for nonlinear harmonic manipulation and new wireless communication systems. National science review, 6(2), pp.231-238.

[196] Dai, J.Y., Zhao, J., Cheng, Q. and Cui, T.J., 2018. Independent control of harmonic amplitudes and phases via a time-domain digital coding metasurface. Light: Science & Applications, 7(1), p.90.

[197] Zhang, L., Chen, X.Q., Liu, S., Zhang, Q., Zhao, J., Dai, J.Y., Bai, G.D., Wan, X., Cheng, Q., Castaldi, G. and Galdi, V., 2018. Space-time-coding digital metasurfaces. Nature communications, 9(1), p.4334.

[198] Zhang, L., Chen, X.Q., Shao, R.W., Dai, J.Y., Cheng, Q., Castaldi, G., Galdi, V. and Cui, T.J., 2019. Breaking reciprocity with space-time-coding digital metasurfaces. Advanced materials, 31(41), p.1904069.

[199] Cui, T.J., Liu, S. and Li, L.L., 2016. Information entropy of coding metasurface. Light: Science & Applications, 5(11), pp.e16172-e16172.

[200] Cui, T.J., Liu, S. and Zhang, L., 2017. Information metamaterials and metasurfaces. Journal of materials chemistry C, 5(15), pp.3644-3668.

[201] Cui, T.J., Li, L., Liu, S., Ma, Q., Zhang, L., Wan, X., Jiang, W.X. and Cheng, Q., 2020. Information metamaterial systems. Iscience, 23(8).

[202] Dai, J.Y., Tang, W.K., Zhao, J., Li, X., Cheng, Q., Ke, J.C., Chen, M.Z., Jin, S. and Cui, T.J., 2019. Wireless communications through a simplified architecture based on time-domain digital coding metasurface. Advanced materials technologies, 4(7), p.1900044.

[203] Wan, X., Zhang, Q., Yi Chen, T., Zhang, L., Xu, W., Huang, H., Kun Xiao, C., Xiao, Q. and Jun Cui, T., 2019. Multichannel direct transmissions of near-field information. Light: science & applications, 8(1), p.60.

[204] Cui, T.J., Liu, S., Bai, G.D. and Ma, Q., 2019. Direct transmission of digital message via programmable coding metasurface. Research.

[205] Dai, J.Y., Tang, W., Yang, L.X., Li, X., Chen, M.Z., Ke, J.C., Cheng, Q., Jin, S. and Cui, T.J., 2019. Realization of multi-modulation schemes for wireless communication by

time-domain digital coding metasurface. IEEE transactions on antennas and propagation, 68(3), pp.1618-1627.

[206] Zhao, H., Shuang, Y., Wei, M., Cui, T.J., Hougne, P.D. and Li, L., 2020. Metasurface-assisted massive backscatter wireless communication with commodity Wi-Fi signals. Nature communications, 11(1), p.3926.

[207] Zhang, L., Chen, M.Z., Tang, W., Dai, J.Y., Miao, L., Zhou, X.Y., Jin, S., Cheng, Q. and Cui, T.J., 2021. A wireless communication scheme based on space-and frequency-division multiplexing using digital metasurfaces. Nature electronics, 4(3), pp.218-227.

[208] Chen, M.Z., Tang, W., Dai, J.Y., Ke, J.C., Zhang, L., Zhang, C., Yang, J., Li, L., Cheng, Q., Jin, S. and Cui, T.J., 2022. Accurate and broadband manipulations of harmonic amplitudes and phases to reach 256 QAM millimeter-wave wireless communications by time-domain digital coding metasurface. National science review, 9(1), p.nwab134.

[209] Wu, H., Bai, G.D., Liu, S., Li, L., Wan, X., Cheng, Q. and Cui, T.J., 2020. Information theory of metasurfaces. National science review, 7(3), pp.561-571.

[210] Wu, H., Gao, X.X., Zhang, L., Bai, G.D., Cheng, Q., Li, L. and Cui, T.J., 2020. Harmonic information transitions of spatiotemporal metasurfaces. Light: science & applications, 9(1), p.198.

[211] Tan, X., Sun, Z., Koutsonikolas, D. and Jornet, J.M., 2018, April. Enabling indoor mobile millimeter-wave networks based on smart reflect-arrays. In IEEE INFOCOM 2018-IEEE Conference on Computer Communications (pp. 270-278). IEEE.

[212] Jamali, V., Tulino, A.M., Fischer, G., Müller, R.R. and Schober, R., 2020. Intelligent surface-aided transmitter architectures for millimeter-wave ultra massive MIMO systems. IEEE open journal of the communications society, 2, pp.144-167.

[213] Wang, P., Fang, J., Yuan, X., Chen, Z. and Li, H., 2020. Intelligent reflecting surface-assisted millimeter wave communications: Joint active and passive precoding design. IEEE Transactions on Vehicular Technology, 69(12), pp.14960-14973.

[214] Mao, Y., You, C., Zhang, J., Huang, K. and Letaief, K.B., 2017. A survey on mobile edge computing: The communication perspective. IEEE communications surveys & tutorials, 19(4), pp.2322-2358.

[215] Cao, Y. and Lv, T., 2019. Intelligent reflecting surface enhanced resilient design for MEC offloading over millimeter wave links. arXiv preprint arXiv:1912.06361.

[216] Liu, Y., Zhao, J., Xiong, Z., Niyato, D., Yuen, C., Pan, C. and Huang, B., 2020. Intelligent reflecting surface meets mobile edge computing: Enhancing wireless communications for computation offloading. arXiv preprint arXiv:2001.07449.

[217] Bai, T., Pan, C., Deng, Y., Elkashlan, M., Nallanathan, A. and Hanzo, L., 2020. Latency minimization for intelligent reflecting surface aided mobile edge computing. IEEE Journal on Selected Areas in Communications, 38(11), pp.2666-2682.

[218] Hua, S., Zhou, Y., Yang, K., Shi, Y. and Wang, K., 2021. Reconfigurable intelligent surface for green edge inference. IEEE Transactions on Green Communications and Networking, 5(2), pp.964-979.

[219] Souto, V.D.P., Souza, R.D., Uchoa-Filho, B.F., Li, A. and Li, Y., 2020. Beamforming optimization for intelligent reflecting surfaces without CSI. IEEE Wireless Communications Letters, 9(9), pp.1476-1480.

[220] Abrardo, A., Dardari, D. and Di Renzo, M., 2021. Intelligent reflecting surfaces: Sum-rate optimization based on statistical position information. IEEE Transactions on Communications, 69(10), pp.7121-7136.

[221] Yigit, Z., Basar, E. and Altunbas, I., 2020. Low complexity adaptation for reconfigurable intelligent surface-based MIMO systems. IEEE Communications Letters, 24(12), pp.2946-2950.

[222] Basar, E., 2021. Reconfigurable intelligent surfaces for Doppler effect and multipath fading mitigation. frontiers in Communications and Networks, 2, p.672857.

[223] Matthiesen, B., Björnson, E., De Carvalho, E. and Popovski, P., 2020. Intelligent reflecting surface operation under predictable receiver mobility: A continuous time propagation model. IEEE Wireless Communications Letters, 10(2), pp.216-220.

[224] Björnson, E. and Sanguinetti, L., 2020. Power scaling laws and near-field behaviors of massive MIMO and intelligent reflecting surfaces. IEEE Open Journal of the Communications Society, 1, pp.1306-1324.

[225] Björnson, E., Özdogan, Ö. and Larsson, E.G., 2020. Reconfigurable intelligent surfaces: Three myths and two critical questions. IEEE Communications Magazine, 58(12), pp.90-96.

[226] Elzanaty, A., Guerra, A., Guidi, F. and Alouini, M.S., 2021. Reconfigurable intelligent surfaces for localization: Position and orientation error bounds. IEEE Transactions on Signal Processing, 69, pp.5386-5402.

[227] Loyka, S., 2004, September. Electromagnetic interference in wireless communications: behavioral-level simulation approach. In IEEE 60th Vehicular Technology Conference, 2004. VTC2004-Fall. 2004 (Vol. 6, pp. 3945-3949). IEEE.

[228] de Jesus Torres, A., Sanguinetti, L. and Björnson, E., 2021. Electromagnetic interference in RIS-aided communications. IEEE Wireless Communications Letters, 11(4), pp.668-672.

[229] Chu, Z., Zhu, Z., Zhou, F., Zhang, M. and Al-Dhahir, N., 2021. Intelligent reflecting surface assisted wireless powered sensor networks for Internet of Things. IEEE Transactions on Communications, 69(7), pp.4877-4889.

[230] Björnson, E., 2021, November. Optimizing a binary intelligent reflecting surface for OFDM communications under mutual coupling. In WSA 2021; 25th International ITG Workshop on Smart Antennas (pp. 1-6). VDE.

[231] *Spatial channel model for Multiple Input Multiple Output (MIMO) simulations (Release 16).* Available at:https://portal.3gpp.org/desktopmodules/Specifications/SpecificationDetails.aspx?specificationId=1382

[232] Pei, X., Yin, H., Tan, L., Cao, L., Li, Z., Wang, K., Zhang, K. and Björnson, E., 2021. RIS-aided wireless communications: Prototyping, adaptive beamforming, and indoor/outdoor field trials. IEEE Transactions on Communications, 69(12), pp.8627-8640.

[233] Mao, J., Gao, Z., Wu, Y. and Alouini, M.S., 2018. Over-sampling codebook-based hybrid minimum sum-mean-square-error precoding for millimeter-wave 3D-MIMO. IEEE Wireless Communications Letters, 7(6), pp.938-941.

[234] Chu, Z., Hao, W., Xiao, P. and Shi, J., 2019. Intelligent reflecting surface aided multi-antenna secure transmission. IEEE Wireless Communications Letters, 9(1), pp.108-112.

[235] Yang, G., Xu, X., Liang, Y.C. and Di Renzo, M., 2021. Reconfigurable intelligent surface-assisted non-orthogonal multiple access. IEEE Transactions on Wireless Communications, 20(5), pp.3137-3151.

[236] Zhou, G., Pan, C., Ren, H., Wang, K. and Peng, Z., 2021. Secure wireless communication in RIS-aided MISO system with hardware impairments. IEEE Wireless Communications Letters, 10(6), pp.1309-1313.

[237] Zeng, M., Li, X., Li, G., Hao, W. and Dobre, O.A., 2020. Sum rate maximization for IRS-assisted uplink NOMA. IEEE Communications Letters, 25(1), pp.234-238.

[238] Grant, M., Boyd, S. and Ye, Y., 2009. CVX: Matlab software for disciplined convex programming.

[239] Nuti, P. and Evans, B.L., 2021, June. Spectral efficiency vs complexity in downlink algorithms for reconfigurable intelligent surfaces. In 2021 IEEE International Conference on Communications Workshops (ICC Workshops) (pp. 1-7). IEEE.

[240] Hassouna, S., Jamshed, M.A., Rains, J., Kazim, J.U.R., Rehman, M.U., Abualhayja, M., Mohjazi, L., Cui, T.J., Imran, M.A. and Abbasi, Q.H., 2023. A survey on reconfigurable intelligent surfaces: Wireless communication perspective. IET Communications, 17(5), pp.497-537.

[241] Zhao, M.M., Wu, Q., Zhao, M.J. and Zhang, R., 2020. Intelligent reflecting surface enhanced wireless networks: Two-timescale beamforming optimization. IEEE Transactions on Wireless Communications, 20(1), pp.2-17.

[242] Hassouna, S., Rains, J., Kazim, J.R., Rehman, M.U., Imran, M. and Abbasi, Q.H., 2022, May. Discrete Phase Shifts for Intelligent Reflecting Surfaces in OFDM Communications. In 2022 International Workshop on Antenna Technology (iWAT) (pp. 128-131). IEEE.

[243] Amri, M.M., Tran, N.M. and Choi, K.W., 2021. Reconfigurable intelligent surface-aided wireless communications: Adaptive beamforming and experimental validations. IEEE Access, 9, pp.147442-147457.

[244] Abu-Shaban, Z., Zhou, X., Abhayapala, T., Seco-Granados, G. and Wymeersch, H., 2018. Error bounds for uplink and downlink 3D localization in 5G millimeter wave systems. IEEE Transactions on Wireless Communications, 17(8), pp.4939-4954.

[245] del Peral-Rosado, J.A., Raulefs, R., López-Salcedo, J.A. and Seco-Granados, G., 2017. Survey of cellular mobile radio localization methods: From 1G to 5G. IEEE Communications Surveys & Tutorials, 20(2), pp.1124-1148.

[246] Shahmansoori, A., Garcia, G.E., Destino, G., Seco-Granados, G. and Wymeersch, H., 2017. Position and orientation estimation through millimeter-wave MIMO in 5G systems. IEEE Transactions on Wireless Communications, 17(3), pp.1822-1835.

[247] Pan, C., Zhou, G., Zhi, K., Hong, S., Wu, T., Pan, Y., Ren, H., Di Renzo, M., Swindlehurst, A.L., Zhang, R. and Zhang, A.Y., 2022. An overview of signal processing techniques for RIS/IRS-aided wireless systems. IEEE Journal of Selected Topics in Signal Processing.

[248] Rappaport, T.S., Xing, Y., Kanhere, O., Ju, S., Madanayake, A., Mandal, S., Alkhateeb, A. and Trichopoulos, G.C., 2019. Wireless communications and applications above 100 GHz: Opportunities and challenges for 6G and beyond. IEEE access, 7, pp.78729-78757.

[249] Ozturk, C., Keskin, M.F., Wymeersch, H. and Gezici, S., 2023. RIS-aided near-field localization under phase-dependent amplitude variations. IEEE Transactions on Wireless Communications.

[250] Abu-Shaban, Z., Keykhosravi, K., Keskin, M.F., Alexandropoulos, G.C., Seco-Granados, G. and Wymeersch, H., 2021, June. Near-field localization with a reconfigurable intelligent surface acting as lens. In ICC 2021-IEEE International Conference on Communications (pp. 1-6). IEEE.

[251] Guidi, F. and Dardari, D., 2021. Radio positioning with EM processing of the spherical wavefront. IEEE Transactions on Wireless Communications, 20(6), pp.3571-3586.

[252] Kay, S.M., 1993. Fundamentals of statistical signal processing: estimation theory. Prentice-Hall, Inc..

[253] Shen, Y. and Win, M.Z., 2010. Fundamental limits of wideband localization—Part I: A general framework. IEEE Transactions on Information Theory, 56(10), pp.4956-4980.

[254] Abu-Shaban, Z., Wymeersch, H., Abhayapala, T. and Seco-Granados, G., 2020. Single-anchor two-way localization bounds for 5G mmWave systems. IEEE Transactions on Vehicular Technology, 69(6), pp.6388-6400.

[255] Larsen, M.D., Swindlehurst, A.L. and Svantesson, T., 2009. Performance bounds for MIMO-OFDM channel estimation. IEEE Transactions on Signal Processing, 57(5), pp.1901-1916.

[256] Shen, Y. and Win, M.Z., 2010. On the accuracy of localization systems using wideband antenna arrays. IEEE Transactions on Communications, 58(1), pp.270-280.

[257] Shen, Y., Wymeersch, H. and Win, M.Z., 2010. Fundamental limits of wideband localization—Part II: Cooperative networks. IEEE Transactions on Information Theory, 56(10), pp.4981-5000.

[258] Guerra, A., Guidi, F. and Dardari, D., 2018. Single-anchor localization and orientation performance limits using massive arrays: MIMO vs. beamforming. IEEE Transactions on Wireless Communications, 17(8), pp.5241-5255.

[259] Garcia, N., Wymeersch, H. and Slock, D.T., 2018. Optimal precoders for tracking the AoD and AoA of a mmWave path. IEEE Transactions on Signal Processing, 66(21), pp.5718-5729.

[260] Xu, P., Chen, G., Yang, Z. and Di Renzo, M., 2020. Reconfigurable intelligent surfaces-assisted communications with discrete phase shifts: How many quantization levels are required to achieve full diversity?. IEEE Wireless Communications Letters, 10(2), pp.358-362.

[261] Gradoni, G. and Di Renzo, M., 2021. End-to-end mutual coupling aware communication model for reconfigurable intelligent surfaces: An electromagnetic-compliant approach based on mutual impedances. IEEE Wireless Communications Letters, 10(5), pp.938-942.

[262] Pan, C., Ren, H., Wang, K., Kolb, J.F., Elkashlan, M., Chen, M., Di Renzo, M., Hao, Y., Wang, J., Swindlehurst, A.L. and You, X., 2021. Reconfigurable intelligent surfaces for 6G systems: Principles, applications, and research directions. IEEE Communications Magazine, 59(6), pp.14-20.

[263] Van Trees, H.L., 2004. Detection, estimation, and modulation theory, part I: detection, estimation, and linear modulation theory. John Wiley & Sons.

[264] Friedlander, B., 2019. Localization of signals in the near-field of an antenna array. IEEE Transactions on Signal Processing, 67(15), pp.3885-3893.

[265] Rains, J., Tukmanov, A., Cui, T.J., Zhang, L., Abbasi, Q.H. and Imran, M.A., 2022. High-resolution programmable scattering for wireless coverage enhancement: an indoor field trial campaign. IEEE Transactions on Antennas and Propagation, 71(1), pp.518-530.

[266] Sharma, S.K., Patwary, M., Chatzinotas, S., Ottersten, B. and Abdel-Maguid, M., 2015, June. Repeater for 5G wireless: A complementary contender for Spectrum Sensing intelligence. In 2015 IEEE International Conference on Communications (ICC) (pp. 1416-1421). IEEE.

[267] Liu, R., Wu, Q., Di Renzo, M. and Yuan, Y., 2022. A path to smart radio environments: An industrial viewpoint on reconfigurable intelligent surfaces. IEEE Wireless Communications, 29(1), pp.202-208.

[268] Hassouna, S., Rains, J., Kazim, J.U.R., Rehman, M.U., Imran, M. and Abbasi, Q.H., 2022, July. Investigating The data rate of Intelligent Reflecting Surface Under Different Deployments. In 2022 IEEE International Symposium on Antennas and Propagation and USNC-URSI Radio Science Meeting (AP-S/URSI) (pp. 1578-1579). IEEE.

[269] Guan, X., Wu, Q. and Zhang, R., 2020, December. Anchor-assisted intelligent reflecting surface channel estimation for multiuser communications. In GLOBECOM 2020-2020 IEEE Global Communications Conference (pp. 1-6). IEEE.

[270] Xia, S. and Shi, Y., 2020, May. Intelligent reflecting surface for massive device connectivity: Joint activity detection and channel estimation. In ICASSP 2020-2020 IEEE International Conference on Acoustics, Speech and Signal Processing (ICASSP) (pp. 5175-5179). IEEE.

[271] Jensen, T.L. and De Carvalho, E., 2020, May. An optimal channel estimation scheme for intelligent reflecting surfaces based on a minimum variance unbiased estimator. In ICASSP 2020-2020 IEEE International Conference on Acoustics, Speech and Signal Processing (ICASSP) (pp. 5000-5004). IEEE.